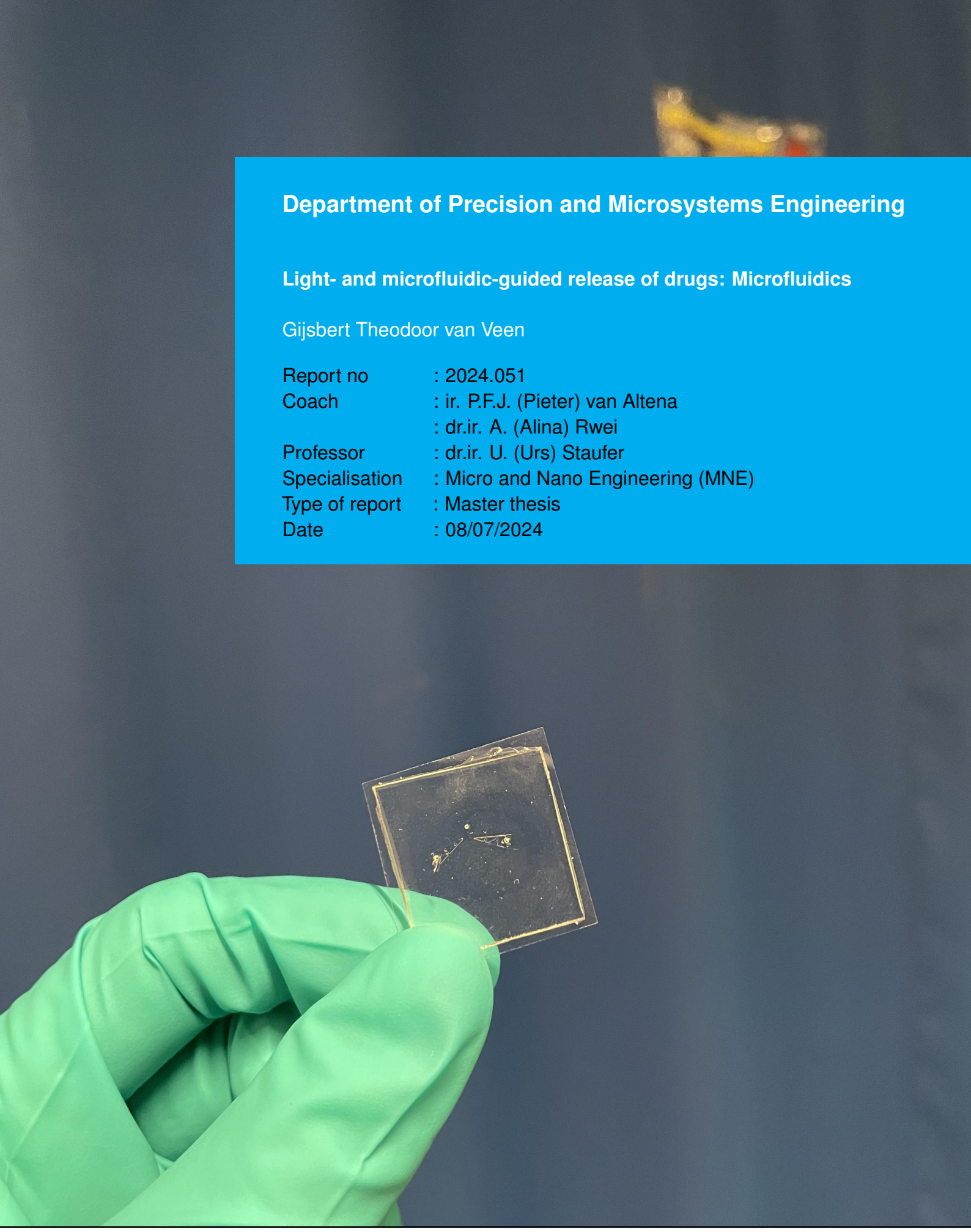

Department of Precision and Microsystems Engineering

Light- and microfluidic-guided release of drugs: Microfluidics

Gijsbert Theodoor van Veen

Report no	: 2024.051
Coach	: ir. P.F.J. (Pieter) van Altena
	: dr.ir. A. (Alina) Rwei
Professor	: dr.ir. U. (Urs) Staufer
Specialisation	: Micro and Nano Engineering (MNE)
Type of report	: Master thesis
Date	: 08/07/2024

Light- and microfluidic-guided release of drugs

Thesis report

by

Gijsbert Theodoor van Veen

to obtain the degree of Master of Science
at the Delft University of Technology,
to be defended publicly on Monday July 15^{th}, 2024 at 10:00 AM.

Student number:	4694929
Daily Assistance:	Ir. P.F.J. (Pieter) van Altena
Project Duration:	September, 2023 - July, 2024
Faculty:	Mechanical Engineering, Delft
Submission date:	July 7^{th}, 2024
Thesis commitee:	Prof.dr. U. (Urs) Staufer
	Dr. A. (Alina) Rwei
	Dr. P. (Paola) Fanzio

TU Delft

Summary

Current stroke treatments are limited to acute phase management, and there are few clinically available drugs for neuron protection or damage repair due to restrictions imposed by the blood-brain barrier. This project envisions an implantable Drug Delivery System (DDS) for precise drug dispensing to areas of the brain affected by stroke, using light-activated liposomes and microfluidic control to improve therapeutic effectiveness and minimize off-target side effects.

The ambitious goal aimed at developing a *proof-of-concept* of integrating the microfluidic system with light-actuated liposomes requires a collaborative approach between two different departments: High-Tech Engineering and Chemical Engineering. First, the High-Tech Engineering department focuses on the manipulation of liposomes within the DDS. This involves designing a microfluidic system that facilitates spatial and temporal control for precise drug release. Simultaneously, the Chemical Engineering Faculty concentrates on the chemical composition, production, and characterization of liposomes. This thesis report, which focuses on the manipulation of liposomes, tries to answer the following research question:

"How can a microfluidic system be designed such that it can repeatably release a specific amount of drugs encapsulated in liposomes with spatial and temporal control?"

Reviewing literature on microfluidic trap-and-release mechanisms, it became evident that deformable particles often tend to slip out of traps. To accurately predict this behavior, the Young's-Laplace equation and the energy stored in the liposome membrane were assessed with the use of a Matlab script. Next, microfluidic devices that were able to manipulate the liposomes to the desired trapping locations were designed and produced. The trapping behavior of liposomes has been assessed by increasing the hydrostatic pressure under a fluorescent microscope. The results show that the experimental pressure of 50-250 Pa is lower than the expected theoretical predictions and that there exists a diameter threshold of 17-18 μm for which the liposomes show lysis behavior. The proposed alterations for future experiments include ensuring that monodisperse liposomes are loaded into the system, the introduction of a bypass channel into the design, and the imaging of the liposome content rather than the membrane. Finally, the entire DDS concept has been demonstrated using a network of pores using the path-of-least-resistance approach.

Besides the contents covered in the paper, the process leading up to the final experiments has been described in detail in the appendices. Much time has been spent on production optimization. First, problems with the collapsing of more slender channels were encountered, which have been solved by increasing the curing agent to the PDMS ratio, the introduction support pillars, and increased channel height. Next, problems with the bonding of the gold electrodes on both the glass and PDMS surfaces. The issue of bonding to the glass was resolved by using a Ti intermediate layer, as suggested by various literature references. For the bonding to PDMS, the introduction of a novel chemical, 6-mercapto-1-hexanol, provided the solution. Furthermore, a custom test setup has been developed that is able to hydrostatically increase the pressure, create electro-osmotic flow, and image the behavior of the liposomes. An Arduino UNO module has been programmed to control the custom setup. Lastly, tests with water, polystyrene beads, and different designs were performed to better understand the behavior of the systems before the liposomes were available. The results of these tests, and the complete list of figures used to create the results presented in the paper, have also been included in the appendix.

Preface

The project *"Light- and microfluidic-guided release of drugs"* is a part of the Master's program in Mechanical Engineering with a specialization in High-Tech Engineering at the Delft University of Technology. Although this report can be considered a standalone research product, it belongs to a larger collaborative project involving multiple disciplines. The two contributors were the Chemical Engineering Department, which concentrated on the light-activated liposomes, and the Precision Mechanism Engineering Department, which dealt with the microfluidic aspect. The related report by Yaren Açan, titled *"Light- and microfluidic-guided drug release: light-sensitive liposomes"*, is available at `https://repository.tudelft.nl`. Several challenges were encountered during the project that could not have been overcome without the assistance of others. Therefore, I would like to express my appreciation for the help of the following individuals.

First of all, I would like to thank the following people for their help with the technical side of my project: Dr. Alina Rwei for providing her expertise on the liposomal part of the project; my daily supervisor Pieter van Althena for answering all practical questions and for the coffee breaks; the lab support of PME for assisting with practical struggles, in particular Alex van den Bogaard for addressing my countless chemical-related questions and for staying calm when I made the lab smell like a striped skunk; and Bradley But for his help with my electromechatronic questions and the design of the test setup. Lastly, I want to thank Yaren Açan for the numerous discussions on the course of the project and for providing me with many batches of liposomes for all of my (failed) experiments.

Next, I want to thank my friends and family for the support they provided me with. During countless lunch and coffee breaks, the talks with Martijn Loonen, Daan Witte, Kit van Zanten, and Bas van Geuns were a refreshing outlet.

Finally, the most important person I want to thank is my supervisor, Prof. Dr. Urs Staufer. I was enormously impressed with your level of involvement in the project. Throughout the project, you always had time for updates and discussions on the direction of the project. Every time there was a problem, you were available and open-minded about solutions. This greatly helped me in my development as a researcher, as well as in the success of the project.

Thank you all. Without your help and support, the results of this project would not have been possible!

Gijsbert Theodoor van Veen
Delft, July 2024

Contents

Abbreviations

2PP	Two Photon Polymerization
CAD	Computer Aided Design
DDS	Drug Delivery System
DiLL	Dip-in-Laser Lithography
ECoG	Electrocorticography
GUV	Giant Unilamellar Vesicle
IPA	Isopropyl Alcohol
ITO	Indium Tin Oxide
PDMS	Polydimethylsiloxane
PGMEA	Propyleenglycolmonomethyletheracetaat
SEM	Scanning Electron Microscopy
TCPFOS	Trichloro Perfluorooctyl Silane

Symbols

Symbol	Definition	Unit
A, a, B, b, C	Parameters	[-]
A, A_0	Area, initial	[m^2]
D	Diameter of channel	[m]
d	Diameter of particle	[m]
E	Young's modulus	[Pa]
E_b, E_s, E_m	Bending-, stretching, membrane energy	[J]
F_m, F_p	Membrane, pressure force	[N]
g	Gravitational constant	[$m^2/kg/s^2$]
h	Height of the microfluidic channel	[m]
K_A	Area expansion modulus	[Pa]
k_b	Bending rigidity modulus	[N m^2]
L	Length of channel/nozzle	[m]
m	Mass of particle	[m]
$\hat{n}$	Normal direction	[-]
p	Pressure	[Pa]
p_l, p_h	Laplace, hydrostatic pressure	[Pa]
Q	Flow rate	[m^3/s]
R_H	Hydraulic resistance	[Pa s/m^3]
R_1, R_2	Principle radii of curvature	[m]
R_{lip}	Radius of liposome	[m]
r	Radius of channel	[m]
S	Surface area	[m^2]
T	Temperature	[Kelvin]
t	Time	[s]
u	Velocity of fluid	[m/s]
v	Velocity of particle	[m/s]
V_i	Volume of particle	[m^3]
w	Width of channel	[m]
W_{trap}	Width of nozzle	[m]
x, y, z	Cartesian coordinates	[-]
$\alpha, \beta, \varphi, \phi$	Parameters, angles	[rad]
γ	Surface tension	[N/m]
ϵ	Elongation	[-]
η	Viscosity	[Pa s]
θ	Contact angle	[rad]
κ	Curvature	[1/m]
λ	Wavelength	[m]
ρ	Density	[kg/m^3]
σ	Stress tensor	[Pa]
τ	Shear stress	[Pa]
ω	Angular frequency	[rad s^{-1}]

1

Paper

Light- and microfluidic-guided release of drugs

G.T. van Veen and Prof.dr. U. Staufer

ABSTRACT

Current stroke treatments are limited to acute phase management, and there are few clinically available drugs for neuron protection or damage repair due to restrictions imposed by the blood-brain barrier. This project envisions an implantable DDS for precise drug dispensing to areas of the brain affected by stroke, using light-activated liposomes and microfluidic control to improve therapeutic effectiveness and minimize off-target side effects.

Reviewing literature on microfluidic trap-and-release mechanisms, it became evident that deformable particles often tend to slip out of traps. To accurately predict this behavior, the Young's-Laplace equation and energy stored in the liposome membrane have been assessed. Next, microfluidic devices that were able to manipulate the liposomes to the desired trapping locations were designed and produced. The trapping behavior of liposomes has been assessed by increasing the hydrostatic pressure under a fluorescent microscope. The results show that the experimental pressure of 50-250 Pa is lower than the expected theoretical predictions and that there exists a diameter threshold of 17-18 μm for which the liposomes show lysis behavior. Finally, the entire DDS concept has been demonstrated using a network of traps using the path-of-least-resistance approach.

1. Introduction

1.1. Motivation

Annually, strokes due to blood flow blockage in the brain result in approximately 5.5 million deaths and leave survivors with long-term disabilities, amounting to 116 million disability-adjusted life years lost [1]. Current treatments are limited to acute phase management, focusing on thrombosis removal, with limited clinically available drugs for neuron protection or damage repair. This is primarily because these compounds struggle to penetrate the blood- brain barrier in sufficiently high concentrations without inducing toxicity in other parts of the body. Consequently, the dosage of drugs that can be administered safely via conventional routes such as intravenous or intramuscular is limited. An implantable on-demand drug delivery system (DDS) that targets only the areas of the brain most affected by stroke will improve therapeutic effectiveness and minimize off-target side effects.

This paper introduces such an implantable DDS to dispense minute amounts of drug directly to a stroke-affected zone and, by integrating with Electrocorticography (ECoG) [2], the stroke-affected zone can be identified. In order to reduce interference with these measurements, no electrical signals are used to initiate and regulate the release of the drugs. Moreover, since the dosing of the drugs

should be tightly controlled for safety reasons, the drugs are encapsulated in light-sensitive liposomes and transported by microfluidic means. Drug release is controlled by light pulses that each open a well-defined number of these liposomes. A graphical concept of the proposed DDS can be found in Figure 1.1.

Although the primary motivation for developing the implantable DDS is to improve stroke therapy, its utility extends beyond that singular application. The system has the potential to revolutionize targeted drug delivery, which is a limiting factor in a variety of brain disorders. This includes, but is not limited to, neurological disorders such as Parkinson's disease [3] and epilepsy [4], or could even improve the treatment of brain tumor chemotherapy [5]. With its broad applicability, the DDS could open many possibilities for new types of medical treatment.

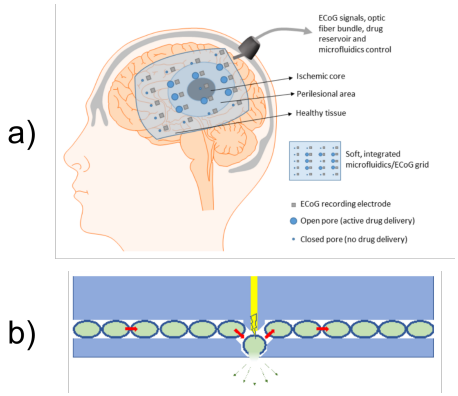

Figure 1.1: The DDS concept as proposed in this paper. **a)** Illustrative diagram of the proposed DDS as integrated within the brain. **b)** Cross-section through a conceptual microfluidic system (blue) which carries liposomes (ovals) containing a drug (green) that can be released through a light flash (yellow). The red arrows indicate the liquid flow.

1.2. Relevance

Drug delivery using microfluidic platforms has been extensively studied with systems incorporating microneedles [6], micropumps [7] and membranes [8]. However, a specific combination of light-actuated liposomes in a microfluidic system to achieve controlled drug delivery has never been demonstrated. Furthermore, the DDS provides significant progress in addressing two of the major challenges within the field of microfluidic controlled drug delivery, as recently summarized by Sanjay *et al.* [9]. Firstly, targeted drug delivery to specific cells or tissues is challenging, as drugs tend to be dispersed randomly, with only a small fraction reaching the intended sites. Secondly, existing controlled DDS' typically release drugs at fixed rates and lack the ability to adjust to changes in patient conditions once implanted.

Although the integration of microfluidics and liposomes has already been shown before, the majority of these studies focus on the production of liposomes using microfluidic flow principles [10–13]. Furthermore, liposomes have been utilized as on-demand DDS, although without the integration of a microfluidic control mechanism. Typically, two main strategies are employed [14]: passive targeting involves dispersing the particles within the patient by exploiting their ability to accumulate at sites of increased vasculature permeability; active targeting involves biochemically altering the lipid membrane to include ligands such that it predominantly binds to specific tissues. Currently, commercially available liposomes provide passive targeting at best [15, 16]. The integration of a microfluidic system would provide substantial progress by introducing enhanced spatial and temporal control. Lastly, the DDS would enable the delivery of drugs without having to cross the blood-brain barrier, which would significantly increase the effective dose delivered to the intended tissue.

1.3. State-of-the-art

Microfluidic particle control has been studied extensively [17–21]. Recently, a comparison of all different techniques has been made by Gong *et al.* [22] which categorizes them into different groups: passive physical, active physical, biochemical and hybrid mechanisms. Among them, passive physical is one of the most common techniques currently used in microfluidic particle trapping. This method uses strategic obstacle placement and geometry to generate hydrodynamic effects. According to Gong *et al.* [22] the popularity is based on low costs, fabrication time, and simple (passive) operation. Several approaches have been studied that utilize these hydrodynamic effects to isolate particles or cells, broadly categorized into microwells, microarrays and microtraps [23].

Microwells are small cavities in a microfluidic device designed to hold minute volumes of liquids, cells, or particles, usually for analysis. Several studies have been performed to improve performance and trapping efficiency, for example studies examining the optimal height-diameter ratio [24], cell density [25], and shape [26]. Microarrays, first developed by Dino *et al.* [27], utilize an array of geometrical shapes or obstacles to capture particles. Several studies have been conducted to increase the efficiency of the method, such as changing the flow orientation of the particles w.r.t. the traps to be diagonal [28], adding oscillating flow to remove

particle segregation as an effect of bridging [29] and shape optimization [30] showing that squares have the highest performance for particle-trapping probability. Microtraps, first shown by Tan and Shoji [31], use the principle of relative hydraulic resistance between a trap and bypass channel. Since this design consists of a trap with an open aperture, the situation is remarkably similar to the one encountered in the DDS. Many improvements in this design have been proposed, such as a shorter bypass channel length [32], deterministic cell trapping using the integration of burst valves [33], and increased efficiency by introducing a matrix of cell traps [34].

In order to properly trap liposomes in the DDS, the trap region of these hydrodynamic systems is especially interesting. Research by Lawrenz *et al.* [35] focused specifically on this region and looked at the effect of different shapes (triangular, square, conical and elliptical) of the trapping site for stem cells and polystyrene microspheres. They concluded that square shapes are best for cell variability, while triangular shapes are optimal for high-speed applications. In contrast, Benavante-Babace *et al.* [36] also experimentally examined the shape of traps for a microarray system that was designed to capture cells. They concluded that there is no difference between the geometries of the traps. These contradictory results should be further investigated. Furthermore, both studies [35, 36] noticed that deforming cells could squeeze through holes, which reduced the trapping efficiency. Since liposomes behave as having a flexible membrane that encapsulates a fluid, these problems need to be addressed to properly design the DDS.

Only a few studies have been published that studied microfluidic manipulation of liposomes or Giant Unilamellar Vesicle (GUV). GUVs are vesicles with a size greater than $1\mu m$, so the liposomes used in this project can be categorized into this group. Firstly, Yamada *et al.* [37] have studied the trapping and releasing of GUVs in a microwell. They concluded that the trapping results from the force balance created by the Stokes drag and the difference in the elastic energy of the membrane, which is stored in the GUV as it squeezes to enter the thin channel. Furthermore, they show that GUVs can be released by increasing the velocity of the fluid beyond a critical velocity. Next, Nuss *et al.* [38] present a microarray that is capable of trapping and releasing hundreds of GUVs. They reason that the trapping ability is dependent on the deformability of the objects, however, theoretical modeling is not present, i.e. only experimental validation has been provided. Lastly, the release of content from liposomes has currently only been studied in static suspension, without the presence of microfluidic forces [14, 39].

This paper aims to address the gap in understanding how to efficiently trap highly deformable particles and develops a modeling approach to predict trapping behavior. Next to that, it investigated under what conditions the liposomes show lysis behavior. Lastly, a design has been created that shows the envisioned principle of the DDS.

2. Theory

2.1. Trap situation

Before diving into theoretical specifics, it is important to define the situation occurring in the microfluidic trap. The deformed liposome is illustrated in Figure 1.2 with its shape divided into three regions: I) a hemi-ellipsoid with principle axis R_2, R_2 and h where h is defined as the height of the trap in the normal direction; II) a frustum of height ΔL with the base being an ellipse with principle axis h & R_2 at the bottom and h & R_1 at the top; III) a hemi-ellipsoid with principle axis R_1, R_1, h. Based on the volume of this shape, and given position x and the initial volume $V_0 = \frac{4}{3}\pi R_{lip}^3$ of a liposome with radius R_{lip}, all relevant dimensions of the deformed liposome can be determined if the fluid is assumed to be incompressible.

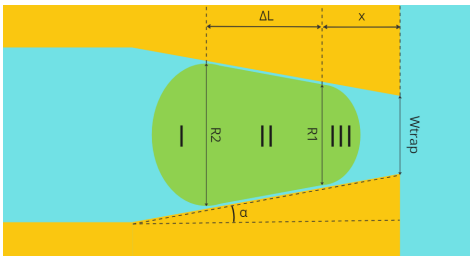

Figure 1.2: A schematic representation of a microfluidic trap containing the fluid (blue), liposome (green) and the microfluidic system (yellow). Significant features/dimensions are indicated.

2.2. Laplace pressure

Many studies have shown microfluidic platforms to trap droplets with techniques such as a microarray [40], a microtrap [41], or a Laplace trap [42]. In these studies, the pressure drop Δp_l is estimated using the Youngs-Laplace relation as can be seen in Equation 1.1a, where γ is the surface tension between the two phases and R the radius of curvature of the interface. For liposomes reported values of surface tension are in order of 10^{-6} $[N/m]$ [43]. Since the height of the microfluidic channels is equal for both front and back interface, i.e. $\frac{1}{R_{y,1}} = \frac{1}{R_{y,2}}$, the

equation can be simplified to Equation 1.1b.

$$\Delta p_l = \gamma \left(\left(\frac{1}{R_{x,1}} + \frac{1}{R_{y,1}} \right) - \left(\frac{1}{R_{x,2}} + \frac{1}{R_{y,2}} \right) \right) \tag{1.1a}$$

$$\Delta p_l = \gamma \left(\frac{1}{R_{x,1}} - \frac{1}{R_{x,2}} \right) \tag{1.1b}$$

The Laplace pressure is balanced by the hydrostatic pressure Δp_h as given by Equation 1.2, where ρ is the density of the fluid, g is the gravitational constant and h is the height of the fluid level. An illustration of the force balance can be found in Figure 1.3.

$$\Delta p_h = \rho * g * h \tag{1.2}$$

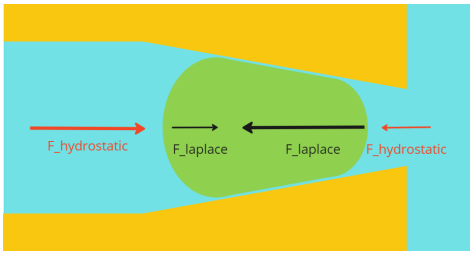

Figure 1.3: An illustration indicating the direction of the hydrostatic (red) and Laplace (black) forces acting on the liposome.

2.3. Membrane energy

For the Laplace pressure theory, the surface tension γ is considered to be constant, i.e. independent on radius R. However, several researchers [43–45] have found the membrane of liposomes behaves with a non-constant surface tension. From these studies it can be concluded the mechanical behavior of the membrane can be modeled by considering it as continuous two-dimensional surface that stores energy due to bending κ and area dilation $\frac{\Delta A}{A_0}$. The resistance to bending is characterized by the bending modulus κ_b and the resistance to area dilation by the elastic modulus K_A. The reported values of the bending modulus are in order of $20 - 30$ $\kappa_B T$ [43] and the elastic modulus in order of 150-$244 mN/m$ [44]. The relation of membrane energy based on bending and area dilation can be found in Equation 1.3a. As shown by Yamada *et al.* [37], it can be estimated that the stretching energy E_s is nearly 4 orders of magnitude higher than the bending energy E_b. Therefore it is reasonable to neglect bending energy in the calculation and simplify the energy stored in the membrane to Equation 1.3b.

$$E_m = E_b + E_s = \frac{\kappa_b}{2} \int \kappa^2 dA + \frac{K_A}{2} \left(\frac{\Delta A}{A_0} \right)^2 A_0 \tag{1.3a}$$

$$E_m = \frac{K_A}{2} \left(\frac{\Delta A}{A_0} \right)^2 A_0 \tag{1.3b}$$

By differentiating the energy stored in the membrane over the distance x it moves into the trap, the force F_m with which the liposome resists movement can be determined. This force F_m is balanced by difference in force due to hydrostatic pressure F_p (estimated using Equation 1.2) that acts on front and back of the membrane. An illustration of the force balance can be found in Figure 1.4

$$F_m = \frac{dE_m}{dx} \tag{1.4a}$$

$$F_p = \Delta p_h (A_2 - A_1) = \Delta p_h \left(\pi {R_2}^2 - \pi {R_1}^2 \right) \tag{1.4b}$$

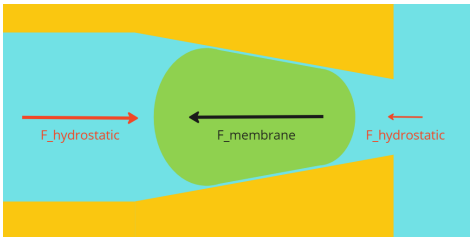

Figure 1.4: An illustration indicating the direction of the hydrostatic (red) and membrane (black) forces acting on the liposome.

2.4. Trap design

In order to properly design the trap, a Matlab script has been created to assess the influence of different parameters; specifically, the width and angle of the trap. This Matlab script evaluates both the Laplace pressure theory and the membrane energy theory as described in section 2. It should be noted that parameters such as bending rigidity and elastic modulus are dependent on the specific composition of the liposome, and therefore the figures provided below give only an indication of order of magnitude.

Effect of width

The resulting relationship between the width of the trap and the burst pressure can be found in Figure 1.5. From this figure, it can be seen that for both the Laplace and membrane energy theories, an increase in the width of the traps results in a decrease in burst pressure. However, for the membrane energy model, the decrease in burst pressure

at higher widths is greater than for the Laplace model. From this analysis, it is expected that to achieve maximal burst pressure, the width should be minimized. Furthermore, it should be noted that when designing in the lower width range of approximately 8-9μm, the membrane stretching reaches values greater than 4%. In this range of deformation, rupture tension can start to become a limiting factor according to research by Rawicz *et al.* [45], and liposomes of sufficient size are expected to rupture when they pass through the nozzle.

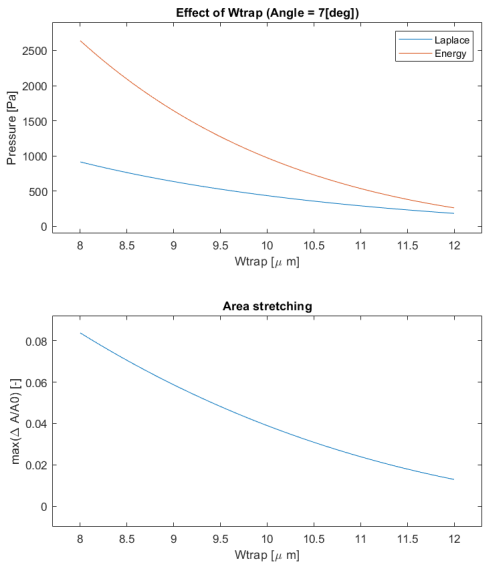

Figure 1.5: Results from the Matlab script for simulations with varying trap width showing the pressure-width relationship (top) & area stretching-width relationship (bottom).

Effect of angle

The resulting relationship between angle and burst pressure can be found in Figure 1.6. It can be seen that, when considering Laplace theory, the burst pressure increases with increasing angles. This can be explained by the fact that for high angles, the difference in radius between the front and back of the liposome is larger, thus leading to a higher Laplace burst pressure. This explains why most droplet trapping designs use an angle of approximately 45° [40–42]. However, according to the membrane energy theory, the burst pressure decreases with increasing angles. Since the rate of deformation of the liposomes from their initial shape is smaller at higher angles, the resulting burst pressure is lower. This indicates that to achieve high burst pressure for the liposomes, lower angles are preferable. Furthermore, it should be noted that when designing for lower angles, around 0-5°, the membrane stretching reaches values greater than 4%, which approaches the rupture tension of the liposomes as shown by Rawicz *et al.* [45]. Therefore, liposomes are expected to rupture when they pass through the nozzle.

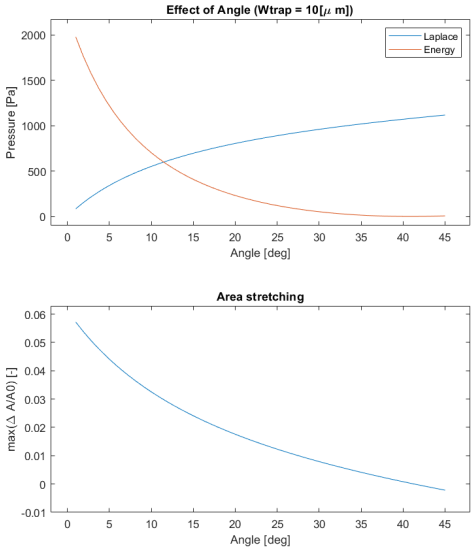

Figure 1.6: Results from the Matlab script for simulations with varying entry angles showing the pressure-angle relationship (top) & area stretching-angle relationship (bottom).

3. Microfluidic design

3.1. Requirements

In order to test the trapping behavior of the liposomes, a microfluidic system was designed to isolate individual particles at a nozzle and then gradually increase the pressure to observe the deformation. From the theoretical hyphenation as described in section 2, it was evident that the maximal pressure range was on the order of a few kPa. Therefore, hydrostatic pressure was selected as the driving mechanism. By increasing height by approximately 20 cm, a pressure increase of 2kPa (Equation 1.2) can be achieved, which perfectly aligns with the requirements. Observing the difference in the height of the water level can accurately determine the pressure in the system.

Next, another flow principle was desired to control the movement of liposomes within the system without interfering with the pressure measurements. A commonly used method to induce flow in microfluidics is electro-osmotic flow [46]. This method is popular because of its ability to provide pulsation-free flow without moving parts. Furthermore, the flow speed can be easily controlled by adjusting the applied voltage to the system.

3.2. Features

A schematic representation of the final design can be found in Figure 1.7. By applying a voltage over the gold electrodes, the liposomes can be moved from the inlet to the outlet. Once a liposome is in front of the nozzle, the hydrostatic pressure can be increased on both the in- and outlet to move the liposome into the nozzle and evaluate its behavior.

The system includes the following key design elements. First, the in- and outlet have angled edges in order to ensure that bubbles, an inherent side effect of the electro-osmotic flow, are redirected out of the system. This design feature is based on the principles provided by Heuck and Staufer [47]. Furthermore, pillars are placed at the inlet and outlet to prevent collapse of the Polydimethylsiloxane (PDMS) structure in these slender regions. Next, the height of the structure is 30 μm, except for the nozzle and the brain environment where the height is lowered to 4 μm. As the height of the channels is significantly higher compared to the median diameter of the liposomes, this ensured the stability of the particles. However, the height at the nozzle is decreased as this prevents the liposomes to deform in the z-direction, which drastically increases the resistance of the trap. Lastly, the characteristic dimensions of the specific trap, namely the minimal width and angle, have been printed to keep track of the tested design.

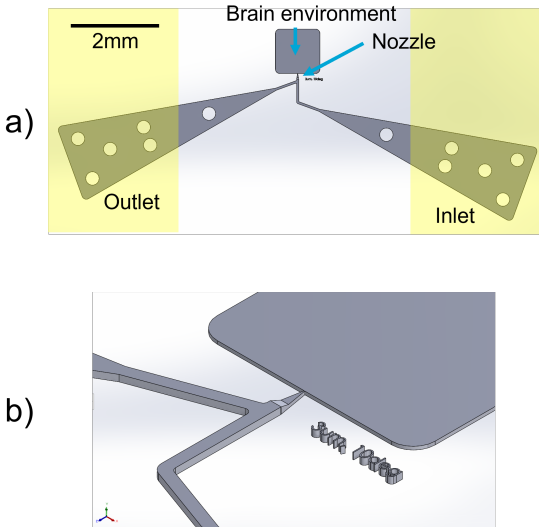

Figure 1.7: Screenshots from SolidWorks (Dassault Systèmes, SolidWorks Corp., Waltham, MA, USA), showing the design of the microfluidic system as proposed in this paper. **a)** Top view of the design. The Two Photon Polymerization (2PP)-printed structure is indicated with grey. The location of the gold electrodes is added in yellow for illustrative purposes. **b)** Zoom-in on the nozzle of the design, showing the lowering in height and the characteristic dimension.

4. Materials and methods

The fabrication of the microfluidic chip has been realized using the conventional soft lithography method [48]. A schematic overview of the production process can be found in Figure 1.8. A commercial Two Photon Polymerization (2PP) printer (Photonic Professional GT Laser Lithography System, Nanoscribe GmbH) was used to print a pattern on a silicon substrate (3D LF Dip-in-Laser Lithography (DiLL) 25mm x 25mm x 0.725mm, Nanoscribe GmbH). The mold has been coated with Trichloro Perfluorooctyl Silane (TCPFOS) to improve demolding bahavior. Next, PDMS (Sylgard 184 elastomer kit, Dow Corning, Midland, MI, USA) is poured over the mold to create microfluidic channels. After curing and demolding, the connection holes are pierced through the PDMS. Finally, the PDMS was bonded to a microscope slide coated with Ti-Au electrodes. The gold surfaces have been functionalized with 6-mercapto-1-hexanol (Sigma-Aldrich). Using air-plasma treatment, PDMS could be bonded. The general advantages of the fabrication process were the tolerances achieved (~ 2 μm) combined with a relatively short design-to-prototype time (~ 2 days).

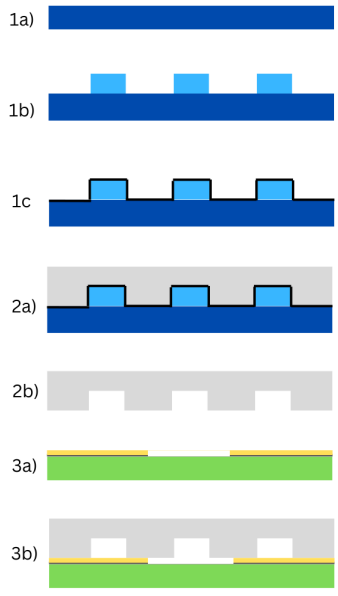

Figure 1.8: Schematic overview of the fabrication process, dimensions are illustrative. **1a)** Start with a cleaned silicon substrate (dark blue). **1b)** Print the mold features (light blue) using the 2PP approach. **1c)** Coat the mold with TCPFOS (black). **2a)** Pour the PDMS (grey) over the mold. **2b)** Remove the PDMS from the mold after curing. **3a)** Deposit the electrodes (dark grey and yellow) on the microscope glass (green). **3b)** Plasma bond the PDMS to a glass microscope slide to create the microfluidic channels (white).

4.1. Mold production

Before the 2PP printing procedure, a Computer Aided Design (CAD) model was created using Solidworks® and exported to DeScribe software (Nanoscribe GmbH) to create the job file. Several minutes before printing, the silicon substrate was cleaned by first rinsing with Aceton (Aceton, Sigma-Aldrich) followed by Isopropyl Alcohol (IPA) (Sigma-Aldrich) and demineralized water. The substrate is blown dry using filtered nitrogen gas. These procedures ensured that no residue or dust was present on the surface, reducing unwanted printing defects.

For the 2PP printing itself, DiLL configuration was used with IP-S photoresist (Nanoscribe GmbH) in combination with the 25X objective. The silicon substrate was taped to the Nanoscribe sample holder, and a droplet of the IP-S photoresist was placed onto the substrate, which was then inserted into the Nanoscribe printer. After optimization of the dose, the following parameters were used during printing.

The IP-S 25x Indium Tin Oxide (ITO) Solid (3D MF) pre-settings were used as basis, with slicing distance 1 μm, hatching distance 0.5 μm, base slice count 3, laser power 50 mW, laser power 65% and scanning speed 100000 μm/s. The most important alteration from the standard settings was a reduced dose to minimize overexposure from mirroring of the incident beam on the highly reflective silicon substrate surface and the print artifacts this creates.

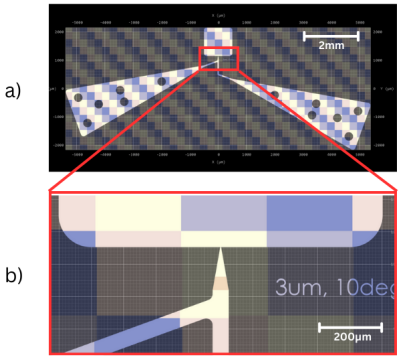

Figure 1.9: Screenshot from Describe (Nanoscribe GmbH) software. **a)** Rectangular block splitting of the mold design. **b)** Zoom-in on the critical area; showing the nozzle is not split into different blocks.

Because the dimensions of the mold exceed the maximum working area of the printing field for the 25X objective, the design is divided into rectangular blocks. The size of these blocks was 275x275x20 μm with lateral overlap 3 μm, shear angle 15° and layer overlap 1 μm. It is important to note that to ensure the quality of the print, the location of the block stitching was ensured to never overlap with the critical areas of the design (e.g., the nozzle), as can be seen in Figure 1.9.

After exposure, the 2PP print is developed by submerging it in Propyleenglycolmonomethyletheracetaat (PGMEA) (Sigma-Aldrich) for 25 minutes and IPA (Sigma-Aldrich) for 5 minutes. The PGMEA removed the unpolymerized IP-S photoresist from the substrate, whereas the IPA was used to remove the PGMEA. After this, the mold was blown dry with filtered nitrogen gas.

To improve the demolding properties of the molds, they were coated with TCPFOS (Sigma-Aldrich), a common coating chemical for soft lithography [49, 50]. This chlorosilane compound forms a superhydrophobic monolayer on the mold surface, reducing the level of adhesion. The coating procedure started with activation of the 2PP-mold surface by exposure to air plasma for 1 minute using a plasma gun. Next, a 2μL droplet of TCPFOS is deposited in a glass beaker and placed in a desiccator. The molds are positioned face down above the TCPFOS, supported by a 3D-printed holder. The pressure inside the desiccator was then reduced by approximately 800 mbar and maintained for 60 minutes, allowing the TCPFOS to vaporize and uniformly coat the mold surface. Lastly, the coated substrate is placed in an oven at 110° for 30 minutes. Afterwards, all surfaces of the glass beaker and desiccator were properly cleaned using Aceton, IPA, and water. All procedures using TCPFOS were performed within a fume hood.

4.2. Soft lithography

Soft lithography procedures are followed using coated 2PP-mold and PDMS (Sylgard 184 elastomer kit, Dow Corning, Midland, MI, USA) resulting in an optically transparent PDMS microfluidic chip. During these procedures, special care was taken with respect to contamination of uncured PDMS. Measures included the use of aluminum foil in the workspace and the frequent change of gloves.

To create PDMS structures, the two components of the Sylgard elastomer kit, PDMS and the curing agent, were mixed in a weight ratio of 7:1. Next, the stirred mixture is transferred to a desiccator to remove unwanted (air)bubbles. Here, the mixture is kept at ~ 200 mbar for 30 minutes. The desiccator is then ventilated and the sample is left untouched for 10 minutes. During this time, the remaining bubbles that have risen to the surface dissipate. Subsequently, the mixture is poured over the PDMS

mold and again transferred to the desiccator for an additional 30 minutes of degassing followed by 10 minutes of rest. Thereafter, the curing of the PDMS was realized in an oven at 80°C for 1 hour. After demolding, the connection holes are pierced through the PDMS using a puncher (Rapid-Core Microfluidic Punches, Darwin-Microfluidics).

4.3. Chip preparations

A glass microscope slide is prepared by rinsing with Aceton, IPA, and demineralized water and blowing dry with filtered nitrogen gas. Next, the electrodes are deposited using the Temescal FC-2000 e-beam evaporator from the Kavli laboratory of TU Delft. First, a 20-nm Ti layer is deposited, followed by a 100-nm Au layer. To bond the gold surface to the PDMS, it has been functionalized using 6-mercapto-1-hexanol (Sigma Aldrich). The gold surface is first rinsed with IPA and demineralized water and then blown dry with filtered nitrogen gas. Next, it is exposed to air plasma using a plasma gun for 1 minute. Thereafter, 5 μL of 6-mercapto-1-hexanol was deposited on the gold surface and left there for 3 hours. Finally, 6-mercapto-1-hexanol is removed by rinsing with IPA and blowing dry using filtered nitrogen gas. All procedures using 6-mercapto-1-hexanol were performed within a fume hood. Lastly, the demolded PDMS is exposed to air plasma for 25 seconds (Diener Electronic GmbH & Co, FEMTO Low-pressure plasma system). An exposure time of 25 seconds was selected so that the PDMS surface was properly activated while minimizing damage to the surface [51, 52]. The gold & PDMS surfaces are gently pressed onto each other and placed in an oven at 70°C for 1 hour to promote bonding.

4.4. Test setup

The test setup that has been developed to carry out the experiments can be found in Figure 1.10. This setup is required to be able to generate hydrostatic pressure-driven flow and observe the deformation of the liposomes. The hydrostatic pressure is generated by a custom-made test setup, consisting of a linear stage, 3D printed connections, and a stepper motor (NEMA 17) connected to an Arduino UNO module. To capture the deformation of the liposomes, the microfluidic chip is mounted on an optical microscope (Motic BA310MET). Later experiments replaced the optical microscope with a fluorescent microscope (Nikon Eclipse Ti2, Nikon Instruments Inc.).

5. Results

5.1. Production

An example of the resulting mold and microfluidic chip can be found in Figure 1.11. From these images, it can be seen that the gold electrode is missing from the design. Although the method described in subsection 4.3 effectively bonds the gold and PDMS surfaces, there were initial difficulties in finding an effective functionalization chemical and accompanying procedures. This, combined with time constraints, resulted in the exclusion of these features from the microfluidic chips.

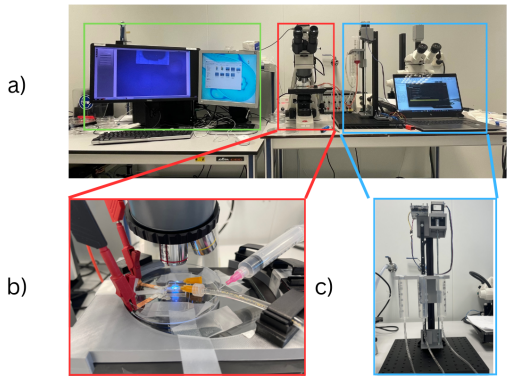

Figure 1.10: The test setup used during experiments. **a)** Picture showing the computer for monitoring and storing image (green), microscope (red) and custom-made hydrostatic pressure mechanism (blue). **b)** Zoom-in on the microscope showing the 3D printed mount (grey) and fluidic connection (tubes on the right side). **c)** Zoom-in on the custom-made hydrostatic pressure setup .

The production procedures described in section 4 resulted in a total design-to-prototype time of approximately 2 days. This time period consists of mold production (6.5 hours), soft lithography (3 hours), and chip preparation (5 hours). The microfluidic chips produced were always rested for at least 12 hours prior to use. Furthermore, because of the reusability of the molds and the scalability of the soft lithography, multiple chips could be produced simultaneously. This significantly increased the number of chips produced during the project timeline. In conclusion, this production process allowed for rapid prototyping and, throughout the process, many different microfluidic structures were produced.

The quality of the production process has been validated using a test structure that has been printed n=5 times. The 2PP mold and PDMS features were imaged using Scanning Electron Microscopy (SEM). The combined results can be found in Table 1.1, which shows the average value ± the standard deviation.

Table 1.1: Quality measurements of the production process. The results have been measured using Scanning Electron Microscopy (Joel Ltd. JSM-6010LA).

Designed nozzle width [μm]	2PP mold [μm]	Soft lithography [μm]
0.2	1.113 ± 0.031	2.061 ± 0.227
0.5	1.134 ± 0.033	2.010 ± 0.267
1	1.063 ± 0.045	2.168 ± 0.131
2	1.900 ± 0.034	4.017 ± 0.190
3	2.986 ± 0.170	4.786 ± 0.184

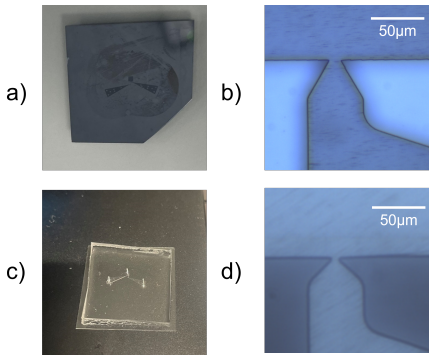

Figure 1.11: Results of the production process. **a)** Picture of a TCPFOS-coated silicon mold containing the 2PP print. **b)** Zoom-in on the nozzle of the mold using optical microscopy. **c)** Picture of a resulting microfluidic chip. **d)** Zoom-in on the nozzle of the microfluidic system using optical microscopy.

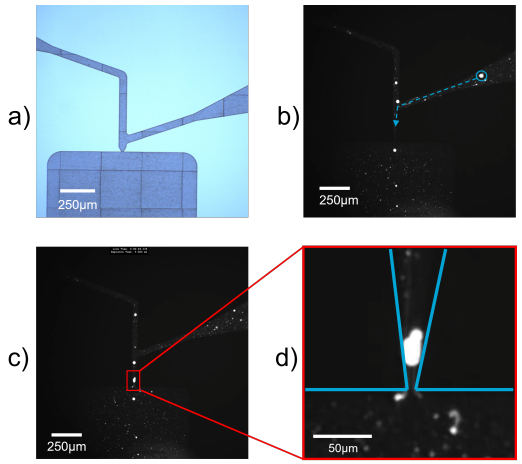

Figure 1.12: Results from trapping experiments using optical and fluorescent microscopy images. **a)** The mold used to produce the microfluidic system that is used during the experiments, the nozzle's characteristic features are a width of 4μm and angle of 10°. **b)** The liposome encircled in blue starts to move towards the nozzle. **c)** The liposome is trapped in the nozzle and the pressure is slowly increased. **d)** Zoom-in on the nozzle, showing the deformation of the liposome.

5.2. Trapping liposomes

The trapping experiments, from which screenshots of an experiment can be found in Figure 1.12, show that trapping is possible for liposomes with a diameter 7-36μm in a nozzle with a width and height of 4 μm and an angle of 10° for a pressure range of 50-250 Pa. After this pressure, the liposomes pass through the nozzle intact or rupture. Furthermore, movements in any part of the setup, such as touching the tubing and mechanical vibrations, were observed to induce movements in the fluid that could push the liposomes through the nozzle. All measurements have been plotted in Figure 1.13.

Lysis

Upon passing through the nozzle, some liposomes exhibited lysis, while others passed through without rupturing. Screenshots of a video of a ruptured liposome can be found in Figure 1.14. The experiments were analyzed to determine the parameters under which lysis occurs. The maximum diameter of the liposomes present after the nozzle is 17-18 μm measured using ImageJ [53]. These observations are consistent with the results of the video recordings as presented in Figure 1.13, all liposomes with diameter > 18 μm ruptured. However, from this figure, it is also evident that some liposomes with a smaller diameter of 13-17 μm also rupture.

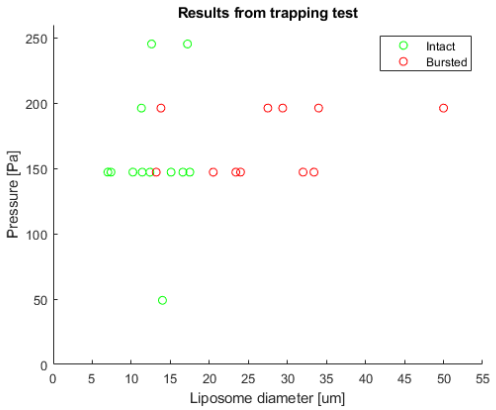

Figure 1.13: Results from the trapping experiments showing the pressure at which the liposomes escaped the trap & the diameter of the specific liposome. The videos have been analysed using ImageJ [53] software to find the diameter of the liposomes.

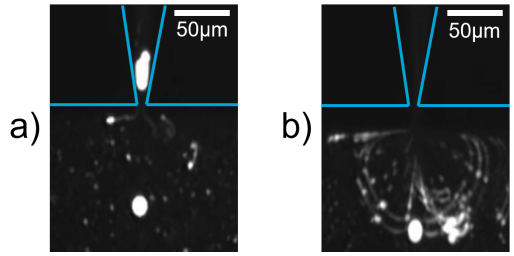

Figure 1.14: Results from trapping experiments using fluorescent microscopy. Blue lines have been added to illustrate the outline of the nozzle. **a)** Liposome before passing through the nozzle. **b)** Liposome 0.1 sec after passing through the nozzle.

Handling

During the experiments, it was found that handling could significantly impact the amount of liposomes present in the microfluidic system. In order to find what caused this discrepancy between the particle density before and after handling by the microfluidic system, the effect of the injection method has been assessed. Figure 1.15 shows the result of injecting liposome dispersion with a metal needle with a diameter of 0.79 mm. It can be seen that, before handling procedures, the dye is mainly contained within the liposomes, whereas after handling, the dye is present almost uniformly, showing that the liposomes were broken during the procedures. Due to these findings, the procedures for injecting liposomes into the system have been adjusted so that no needle or excessive pressure was necessary. The liposome solution was poured into the inlet reservoir, which already contained a 1 ml droplet of buffer solution (200 mM sucrose). By simply increasing the height of this reservoir, liposomes could be loaded into the system with a higher particle density.

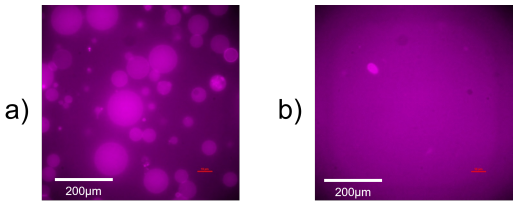

Figure 1.15: Fluorescent images of the dye taken by Y. Açan [54]. **a)** The dye before handling with a needle tip. **b)** The dye after handling with a needle tip.

5.3. Multipore demonstration

To showcase the envisioned principle of the DDS, a multipore design, as showcased in Figure 1.16a, has been produced. The prototype consists of an inlet that is connected to a pressure source and an outlet that simulates the brain environment. Between the inlet and outlet, there is a branch-shaped structure that ends in multiple nozzles (with characteristic dimensions of width and height of 4 μm and an angle of 10°) connected in a parallel configuration. If one of the nozzles does not contain a liposome, its resistance is drastically lower than when it is filled. This causes the flow speed to increase in that branch until it is filled with another liposome. Screenshots of a video that demonstrates this working principle can be found in Figure 1.16c and d.

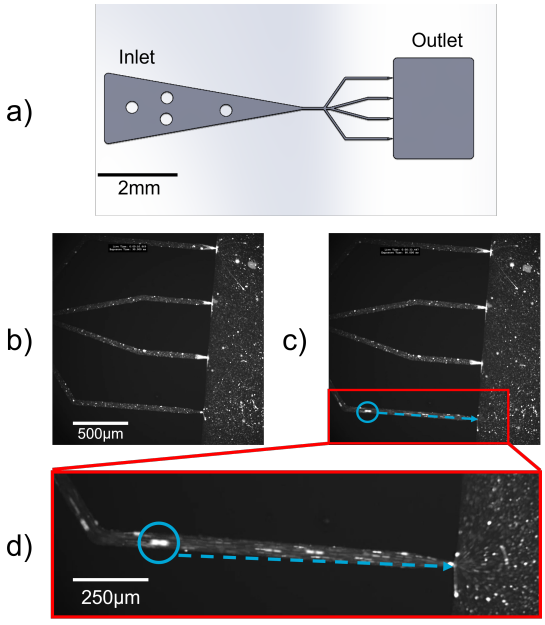

Figure 1.16: Results from the multipore experiments demonstrating the envisioned concept. **a)** The mold as designed in Solidworks (Dassault Systèmes, SolidWorks Corp., Waltham, MA, USA). **b)** The microfluidic chip with al the nozzles filled with liposomes. **c)** The bottom nozzle is opened. **d)** Zoom-in on the open nozzle branch, showing the increased flow speed.

6. Discussion

6.1. Production

From the results, it is concluded that the minimum feature size of the production process is ~ 4 μm. First, feature sizes ≤ 1 μm do not result in a decrease in width for the 2PP mold. Furthermore, when zoomed in on the SEM images, it can be seen that for these dimensions the nozzle does not always connect to the brain environment. Molds with nozzle width ≥ 2 μm show good printing quality with standard deviations < 0.170 μm. Although the Matlab model predicts a decrease in trapping pressure ~ 5%, this deviation will not significantly impact the trapping ability of the system.

However, soft lithography procedures show a difference between the desired feature size and the actual width of the trap of 1-2 μm. According to the Matlab model, changing the nozzle width

from 4 μm to 6 μm would result in a decrease in the trapping pressure ~ 48%. A possible driving mechanism for this discrepancy is that the PDMS polymerization process shrinks the structure, leaving a gap around the mold. Madsen *et al.* [55] conclude that PDMS shrinkage is present mainly at elevated curing temperature of > 60°C. To reduce the difference, they suggest lowering the curing temperature or modifying the mold to account for the shrinkage factor. Alternatively, since these measurements are made at the nozzle, which is a tight space, it could be that the PDMS does not reach this area properly [56], leaving bubbles in the corners. To find which hypothesis is true, it is proposed to use optical microscopy before and after the PDMS curing process and evaluate at which point the discrepancy between the mold and the master originates.

Lastly, within mold production there is an inherent conflict between resolution and print times, as for the nozzle it is required to have a micron feature size, whereas for manual connection points a target of a millimeter is desired. Therefore, the prints take up to 3 hours to complete; however, only a fraction of that time (around a minute) is used to print the nozzle. This could be improved by combining different printing techniques, such as SLA and 2PP, which has been shown to be effective by Altena [57].

6.2. Trapping pressure

The trapping experiments demonstrated it is possible to trap liposomes of 7-36μm for pressure ranges of 50-250 Pa with deviations exceeding 100 Pa for liposomes of similar size. This substantial variation leads to measurements that are not reliably reproducible. Furthermore, there is a deviation in the order of magnitude at which trapping is expected (~ 1-10 kPa) and the observed values (~ 50-250 Pa). Therefore, it is not possible to conclude that the theoretical hyphenation provided in section 2 provides an accurate prediction of trapping behavior. Next, it was observed that external influences on the system, such as mechanical vibrations and passing particles hitting the trapped liposome, can significantly impact the trapping behavior of the liposomes. The consequential uncontrolled release of liposomes has implications for the scalability of the concept, since such movements and shocks are difficult to avoid in the real world brain environment.

From Equation 1.3b, it is estimated that the energy accumulated within the membrane to achieve an area dilation of 0.06 is approximately 3×10^{-13} J. From the video of the outlier of 50 Pa, it can be seen that the trapped liposome is hit by another liposome with a diameter of 7 μm at a speed of around 750 μm/s. The estimated kinetic energy of this particle is thus around 4.9×10^{-20}J, which is several orders of magnitude smaller than the energy stored in the membrane and therefore unlikely to be the sole explanation for the deviation between the expected and observed release pressure. Another explanation could be that the membranes of the trapped and passing liposomes interact with each other, resulting in intermolecular forces and possibly causing the liposomes to fuse together. Since the membrane is already under tension, these interactions could significantly weaken its integrity, thus explaining the deviation.

For future experiments, two design alterations are proposed. First, the shape of the nozzle should be changed from square to round to match more closely the shape of the liposome. This will remove the open spaces in the corner and reduce the flow around the trapped liposomes. Second, the incorporation of a bypass channel could allow for the flow / particles to surpass the trapping site without interacting with the trapped liposome.

6.3. Lysis

If the area dilation is calculated using the Matlab script with the definitions found in subsection 2.1, the result is $\frac{\Delta A}{A_0} = 0.06$. Compared to references found in literature [45], this is in the range of values of 0.02 to 0.10 for which typical liposomes show lysis behavior.

From the results illustrated in Figure 1.13, it is apparent that liposomes with a diameter of 12-13 μm may also rupture while passing through the nozzle. Several studies have determined that, in addition to the critical tension of the lipid bilayers, lysis is influenced by the loading rate [45, 58, 59]. For these specific measurements, a second liposome bumps into the back of the trapped liposome before rupturing, and consequently the loading rates temporarily increase. This indicates that in future designs, the flow speed and loading rate should also be considered in the design of the DDS. Alternatively, the interaction between the two liposome membranes could introduce intermolecular forces that disrupt the integrity of the liposome.

Finally, this fragile nature of liposomes raises concerns about the practical potential of the concept. Currently, it cannot be concluded that the liposomes remain intact throughout the experiments because only the lipid bilayers have been labeled and imaged. Future experiments with liposomes filled with fluorescent labeled content are neces-

sary to verify that the liposomes have not ruptured or reformed during the experiments.

6.4. Escaping liposomes

The size distribution of the liposomes can cause problems and unwanted liposome release into the brain environment. During the experiments, it was noticed that the smaller liposomes tend to slip past the filled nozzles; this principle was illustrated in Figure 1.17a. This phenomenon suggests openings around liposomes, as illustrated in Figure 1.17b. In order to improve this, an easy solution seems to be to round the nozzle, removing the unfilled corners. However, with current production procedures, this could introduce difficulties with demolding as this creates negative draft angles. Another possibility is to ensure that a monodisperse liposome is loaded into the DDS. Methods such as microfluidic formation [60, 61], hydrodynamic filtration [62], or extrusion combined with large-pore dialysis [63] could be promising solutions to explore.

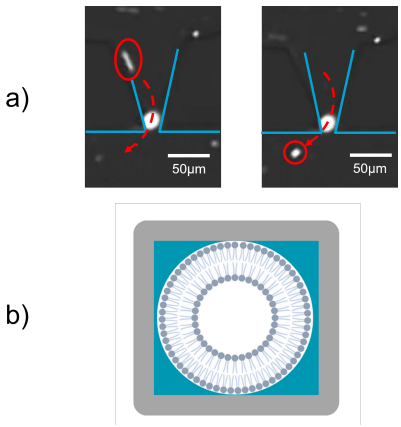

Figure 1.17: Illustration of small liposomes escaping the trap while it is filled. **a)** Screenshots of a video showing a liposome passing the filled trap. The outline of the trap has been added in blue and the location & path of the escaping liposome has been added in red. **b)** Illustration showing the top view of the trap, with in grey the microfluidic system, in white the liposome and in blue to unfilled regions through which the smaller liposomes can escape.

6.5. Lipid-PDMS adhesion

Liposomes that rupture after passing through the nozzle have been observed to leave lipids stuck on the PDMS surface, as can be seen in Figure 1.18a and b. After a short period (~ 1 minute) of using the microfluidic chip, a low-light intensity area is observed around the nozzle. After more time has passed (~ 15 minutes), this light hue turns into a high-light intensity area. This can be explained by the fact that if a membrane breaks, the hydrophobic part of the lipids might be exposed and is attracted to the hydrophobic PDMS surface. Over time, either they attract more lipids or fluorescent markers, increasing the density of the fluorescent markers and thus the intensity of light. This principle has been illustrated in Figure 1.18c.

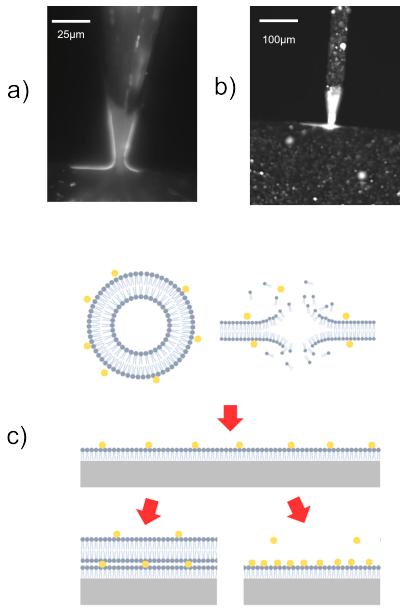

Figure 1.18: Illustration of lipids sticking to PDMS surface. **a)** Fluorescent microscopy image of the nozzle after operating for a few minutes. **b)** Fluorescent microscopy image of the nozzle after operating for over 15 minutes. **c)** The proposed mechanism underlying these observations is as follows. First the liposome, with fluorescent marker (yellow) attached to the hydrophilic head, breaks in the nozzle (top). Next the hydrophobic part is attracted to the hydrophobic PDMS (middle). Layers of lipids could stack or loose markers could be bonded to the lipid (bottom).

7. Conclusion

In this paper, microfluidic devices were produced that were able to manipulate liposomes toward desired trapping locations by means of hydrostatic pressure. The design has been shown to allow for effective trapping of pressures up to 250 kPa for liposomes of diameter 7-36 μm. However, external influences are shown to cause inaccuracies that prevent predicting the trapping behavior of liposomes by examining the energy stored in the membrane. The proposed alterations for future experiments include ensuring monodisperse liposomes, the introduction of a bypass channel into the design, and the imaging of the liposome content rather than the membrane. Next to that, it has been shown that there exists a diameter threshold of 17-18 μm for which the liposomes show lysis behavior. Lastly, a mircofluidic design that is able to passively fill open pores without the need of external forces was introduced, showing the potential of the multipore structure and the concept of using liposomes in combination with microfluidics as a drug delivery system.

References

[1] C. O. Johnson et al. "Global, regional, and national burden of stroke, 1990–2016: a systematic analysis for the Global Burden of Disease Study 2016". In: *The Lancet Neurology* 18.5 (2019), pp. 439–458. ISSN: 1474-4422. DOI: 10.1016/S1474-4422(19)30034-1.

[2] A. Palmini. "The concept of the epileptogenic zone: a modern look at Penfield and Jasper's views on the role of interictal spikes". In: *Epileptic Disorders* 8.S2 (2006), S10–S15. DOI: 10.1684/j.1950-6945.2006.tb00205.x.

[3] A. O. Pires et al. "Old and new challenges in Parkinson's disease therapeutics". In: *Progress in Neurobiology* 156 (2017), pp. 69–89. ISSN: 0301-0082. DOI: 10.1016/j.pneurobio.2017.04.006.

[4] P. Perucca and F. G. Gilliam. "Adverse effects of antiepileptic drugs". In: *The Lancet Neurology* 11.9 (2012), pp. 792–802. ISSN: 1474-4422. DOI: 10.1016/S1474-4422(12)70153-9.

[5] Y. Omidi et al. "Drug delivery and targeting to brain tumors: considerations for crossing the blood-brain barrier". In: *Expert Review of Clinical Pharmacology* 14.3 (2021), pp. 357–381. DOI: 10.1080/17512433.2021.1887729.

[6] C. Yeung et al. "A 3D-printed microfluidic-enabled hollow microneedle architecture for transdermal drug delivery". In: *Biomicrofluidics* 13.6 (Dec. 2019), p. 064125. ISSN: 1932-1058. DOI: 10.1063/1.5127778.

[7] H. Fallahi et al. "Flexible microfluidics: Fundamentals, recent developments, and applications". In: *Micromachines* 10.12 (2019), p. 830. DOI: 10.1007/s00542-019-04535-8.

[8] L. G. Aceves-Serrano et al. "Chapter 3 - Microfluidics for drug delivery systems". In: *Nanoarchitectonics in Biomedicine*. Ed. by A. M. Grumezescu. William Andrew Publishing, 2019, pp. 55–83. ISBN: 978-0-12-816200-2. DOI: 10.1016/B978-0-12-816200-2.00002-5.

[9] S. T. Sanjay et al. "Recent advances of controlled drug delivery using microfluidic platforms". In: *Advanced Drug Delivery Reviews* 128 (2018). Microfluidic Devices for Drug Delivery Systems, pp. 3–28. ISSN: 0169-409X. DOI: 10.1016/j.addr.2017.09.013.

[10] A. Jahn et al. "Microfluidic directed formation of liposomes of controlled size". In: *Langmuir* 23.11 (2007), pp. 6289–6293. DOI: 10.1021/la070051a.

[11] D. Carugo et al. "Liposome production by microfluidics: potential and limiting factors". In: *Scientific reports* 6 (May 2016), p. 25876. ISSN: 2045-2322. DOI: 10.1038/srep25876.

[12] D. van Swaay and A. deMello. "Microfluidic methods for forming liposomes". In: *Lab Chip* 13 (5 2013), pp. 752–767. DOI: 10.1039/C2LC41121K.

[13] B. Yu, R. J. Lee, and L. J. Lee. "Chapter 7 - Microfluidic Methods for Production of Liposomes". In: *Methods in Enzymology*. Vol. 465. Methods in Enzymology. Academic Press, 2009, pp. 129–141. DOI: 10.1016/S0076-6879(09)65007-2.

[14] T. M. Allen and P. R. Cullis. "Liposomal drug delivery systems: From concept to clinical applications". In: *Advanced Drug Delivery Reviews* 65.1 (2013). Advanced Drug Delivery: Perspectives and Prospects, pp. 36–48. ISSN: 0169-409X. DOI: 10.1016/j.addr.2012.09.037.

[15] A. Y. Rwei, W. Wang, and D. S. Kohane. "Photoresponsive nanoparticles for drug delivery". In: *Nano Today* 10.4 (2015), pp. 451–467. ISSN: 1748-0132. DOI: 10.1016/j.nantod.2015.06.004.

[16] U. Bulbake et al. "Liposomal Formulations in Clinical Use: An Updated Review". In: *Pharmaceutics* 9.2 (2017). ISSN: 1999-4923. DOI: 10.3390/pharmaceutics9020012.

[17] X. Wang et al. "Advances in precise single cell capture for analysis and biological applications". In: *Analytical Methods* (2022). DOI: 10.1039/D2AY00625A.

[18] Y. Deng, Y. Guo, and B. Xu. "Recent Development of Microfluidic Technology for Cell Trapping in Single Cell Analysis: A Review". In: *Processes* 8.10 (2020). ISSN: 2227-9717. DOI: 10.3390/pr8101253.

[19] Y. Lan et al. "Microfluidic based single cell or droplet manipulation: Methods and applications". In: *Talanta* 265 (2023), p. 124776. ISSN: 0039-9140. DOI: 10.1016/j.talanta.2023.124776.

[20] L. Huang et al. "Microfluidics cell sample preparation for analysis: Advances in efficient cell enrichment and precise single cell capture". In: *Biomicrofluidics* 11.1 (Feb. 2017), p. 011501. ISSN: 1932-1058. DOI: 10.1063/1.4975666.

[21] J. Nilsson et al. "Review of cell and particle trapping in microfluidic systems". In: *Analytica Chimica Acta* 649.2 (2009), pp. 141–157. ISSN: 0003-2670. DOI: 10.1016/j.aca.2009.07.017.

[22] L. Gong, A. Cretella, and Y. Lin. "Microfluidic systems for particle capture and release: A review". In: *Biosensors and Bioelectronics* 236 (2023), p. 115426. ISSN: 0956-5663. DOI: 10.1016/j.bios.2023.115426.

[23] V. Narayanamurthy et al. "Microfluidic hydrodynamic trapping for single cell analysis: mechanisms, methods and applications". In: *Anal. Methods* 9 (25 2017), pp. 3751–3772. DOI: 10.1039/C7AY00656J.

[24] J. R. Rettig and A. Folch. "Large-scale single-cell trapping and imaging using microwell arrays". In: *Analytical chemistry* 77.17 (Sept. 2005), pp. 5628–5634. ISSN: 0003-2700. DOI: 10.1021/ac0505977.

[25] M. C. Park et al. "High-throughput single-cell quantification using simple microwell-based cell docking and programmable time-course live-cell imaging". In: *Lab Chip* 11 (1 2011), pp. 79–86. DOI: 10.1039/C0LC00114G.

[26] J. Park et al. "Single cell trapping in larger microwells capable of supporting cell spreading and proliferation". In: *Microfluidics and Nanofluidics* 8.2 (Feb. 2010), pp. 263–268. ISSN: 1613-4982. DOI: 10.1007/s10404-009-0503-9.

[27] D. Di Carlo, L. Y. Wu, and L. P. Lee. "Dynamic single cell culture array". In: *Lab on a Chip* 6.11 (2006), pp. 1445–1449. DOI: 10.1039/b605937f.

[28] O. Mesdjian et al. "Enhancing the capture efficiency and homogeneity of single-layer flow-through trapping microfluidic devices using oblique hydrodynamic streams". In: *Microfluidics and Nanofluidics* 25.11 (Oct. 2021), p. 91. DOI: 10.1007/s10404-021-02492-1.

[29] Y. Yoon et al. "Clogging-free microfluidics for continuous size-based separation of microparticles". English (US). In: *Scientific reports* 6 (May 2016). ISSN: 2045-2322. DOI: 10.1038/srep26531.

[30] A. Kitagawa et al. "Microplastic particle trapping through microfluidic devices with different shaped pillars". In: *Chemical Engineering Science* 264 (2022), p. 118163. ISSN: 0009-2509. DOI: 10.1016/j.ces.2022.118163.

[31] W.-H. Tan and S. Takeuchi. "A trap-and-release integrated microfluidic system for dynamic microarray applications". In: *Proceedings of the National Academy of Sciences* 104.4 (2007), pp. 1146–1151. DOI: 10.1073/pnas.0606625104.

[32] D. Jin et al. "A microfluidic device enabling high-efficiency single cell trapping". In: *Biomicrofluidics* 9.1 (Jan. 2015), p. 014101. ISSN: 1932-1058. DOI: 10.1063/1.4905428.

[33] H. Chai et al. "A microfluidic device enabling deterministic single cell trapping and release". In: *Lab Chip* 21 (13 2021), pp. 2486–2494. DOI: 10.1039/D1LC00302J.

[34] L. Mi et al. "A fluidic circuit based, high-efficiency and large-scale single cell trap". In: *Lab Chip* 16 (23 2016), pp. 4507–4511. DOI: 10.1039/C6LC01120A.

[35] A. Lawrenz, F. Nason, and J. J. Cooper-White. "Geometrical effects in microfluidic-based microarrays for rapid, efficient single-cell capture of mammalian stem cells and plant cells". In: *Biomicrofluidics* 6.2 (Apr. 2012), p. 024112. ISSN: 1932-1058. DOI: 10.1063/1.4704521.

[36] A. Benavente-Babace et al. "Single-cell trapping and selective treatment via co-flow within a microfluidic platform". In: *Biosensors and Bioelectronics* 61 (2014), pp. 298–305. ISSN: 0956-5663. DOI: 10.1016/j.bios.2014.05.036.

[37] A. Yamada et al. "Trapping and release of giant unilamellar vesicles in microfluidic wells". In: *Soft Matter* 10 (32 2014), pp. 5878–5885. DOI: 10.1039/C4SM00065J.

[38] H. Nuss et al. "Microfluidic trap-and-release system for lab-on-a-chip-based studies on giant vesicles". In: *Lab Chip* 12 (24 2012), pp. 5257–5261. DOI: 10.1039/C2LC40782E.

[39] A. Y. Rwei et al. "Repeatable and adjustable on-demand sciatic nerve block with phototriggerable liposomes". In: *Proceedings of the National Academy of Sciences* 112.51 (2015), pp. 15719–15724. DOI: 10.1073/pnas.1518791112.

[40] A. Huebner et al. "Static microdroplet arrays: a microfluidic device for droplet trapping, incubation and release for enzymatic and cell-based assays". In: *Lab Chip* 9 (5 2009), pp. 692–698. DOI: 10.1039/B813709A.

[41] M. Courtney et al. "Droplet Microfluidic System with On-Demand Trapping and Releasing of Droplet for Drug Screening Applications". In: *Analytical chemistry* 89.1 (Jan. 2017), pp. 910–915. ISSN: 0003-2700. DOI: 10.1021/acs.analchem.6b04039.

[42] M. G. Simon et al. "A Laplace pressure based microfluidic trap for passive droplet trapping and controlled release". In: *Biomicrofluidics* 6.1 (Feb. 2012), p. 014110. ISSN: 1932-1058. DOI: 10.1063/1.3687400.

[43] Y. Shitamichi, M. Ichikawa, and Y. Kimura. "Mechanical properties of a giant liposome studied using optical tweezers". In: *Chemical Physics Letters* 479.4 (2009), pp. 274–278. ISSN: 0009-2614. DOI: 10.1016/j.cplett.2009.08.018.

[44] W. Rawicz et al. "Effect of Chain Length and Unsaturation on Elasticity of Lipid Bilayers". In: *Biophysical Journal* 79.1 (2000), pp. 328–339. ISSN: 0006-3495. DOI: 10.1016/S0006-3495(00)76295-3.

[45] W. Rawicz et al. "Elasticity, Strength, and Water Permeability of Bilayers that Contain Raft Microdomain-Forming Lipids". In: *Biophysical Journal* 94.12 (2008), pp. 4725–4736. ISSN: 0006-3495. DOI: 10.1529/biophysj.107.121731.

[46] A. Alizadeh et al. "Electroosmotic flow: From microfluidics to nanofluidics". In: *Electrophoresis* 42.7-8 (2021), pp. 834–868. DOI: 10.1002/elps.202000313.

[47] F. C. A. Heuck and U. Staufer. "Low voltage electroosmotic pump for high density integration into microfabricated fluidic systems". English. In: *Microfluidics and Nanofluidics* 10.6 (2011), pp. 1317–1332. DOI: 10.1007/s10404-010-0765-2.

[48] Y. Xia and G. M. Whitesides. "Soft lithography". In: *Annual review of materials science* 28.1 (1998), pp. 153–184. DOI: 10.1146/annurev.matsci.28.1.153.

[49] K. B. Wiles et al. "Soft lithography using perfluorinated polyether molds and PRINT technology for fabrication of 3D arrays on glass substrates". In: *Emerging Lithographic Technologies X*. Vol. 6151. SPIE. 2006, pp. 927–935. DOI: 10.1117/12.656612.

[50] M. Villegas et al. "Fabricating smooth PDMS microfluidic channels from low-resolution 3D printed molds using an omniphobic lubricant-infused coating". In: *Analytica Chimica Acta* 1000 (2018), pp. 248–255. ISSN: 0003-2670. DOI: 10.1016/j.aca.2017.11.063.

[51] S. Bhattacharya et al. "Studies on surface wettability of poly(dimethyl) siloxane (PDMS) and glass under oxygen-plasma treatment and correlation with bond strength". In: *Journal of Microelectromechanical Systems* 14.3 (2005), pp. 590–597. DOI: 10.1109/JMEMS.2005.844746.

[52] X. Jiang et al. "Polymer-on-polymer stamping: universal approaches to chemically patterned surfaces". In: *Langmuir* 18.7 (2002), pp. 2607–2615. DOI: 10.1021/la011098d.

[53] C. Schneider, W. Rasband, and K. Eliceiri. "NIH Image to ImageJ: 25 years of image analysis." In: *Nature Methods* 9 (2012), pp. 671–675. DOI: 10.1038/nmeth.2089.

[54] Y. Açan, U. Staufer, and A. Rwei. "Synthesis and characterisation of light-activated giant unilaminar vesicles." In: (2024). URL: respotitory.tudelft.nl.

[55] M. H. Madsen et al. "Accounting for PDMS shrinkage when replicating structures". In: *Journal of Micromechanics and Microengineering* 24.12 (Oct. 2014), p. 127002. DOI: 10.1088/0960-1317/24/12/127002.

[56] G. Zhuang and J. P. Kutter. "Anti-stiction coating of PDMS moulds for rapid microchannel fabrication by double replica moulding". In: *Journal of Micromechanics and Microengineering* 21.10 (Sept. 2011), p. 105020. DOI: 10.1088/0960-1317/21/10/105020.

[57] P. van Altena. "Multiscale 3D printed polymer probes for single cell experiments: A rapid prototyping method to fabricate microfluidic atomic force microscopy cantilevers for single cell studies". In: (2021). URL: https://repository.tudelft.nl/islandora/object/uuid%3A4a88ec8d-3a16-466c-906f-d9c3d367c0ea.

[58] E. Evans et al. "Dynamic tension spectroscopy and strength of biomembranes". In: *Biophysical journal* 85.4 (2003), pp. 2342–2350. DOI: 10.1016/S0006-3495(03)74658-X.

[59] D. H. Kim and J. A. Frangos. "Effects of amyloid β-peptides on the lysis tension of lipid bilayer vesicles containing oxysterols". In: *Biophysical Journal* 95.2 (2008), pp. 620–628. DOI: 10.1529/biophysj.107.114983.

[60] N.-N. Deng, M. Yelleswarapu, and W. T. Huck. "Monodisperse uni-and multicompartment liposomes". In: *Journal of the American Chemical Society* 138.24 (2016), pp. 7584–7591. DOI: 10.1021/jacs.6b02107.

[61] M. Mizuno et al. "Formation of monodisperse hierarchical lipid particles utilizing microfluidic droplets in a nonequilibrium state". In: *Langmuir* 31.8 (2015), pp. 2334–2341. DOI: 10.1021/acs.langmuir.5b00043.

[62] Y. Woo et al. "Hydrodynamic filtration in microfluidic channels as size-selection process for giant unilamellar vesicles". In: *Journal of biomedical nanotechnology* 9.4 (2013), pp. 610–614. DOI: 10.1166/jbn.2013.1543.

[63] T. F. Zhu and J. W. Szostak. "Preparation of Large Monodisperse Vesicles". In: *PLOS ONE* 4.4 (Apr. 2009), pp. 1–4. DOI: 10.1371/journal.pone.0005009.

Recommendations

Given the limited duration of a thesis project, finishing all envisioned experiments was nearly impossible, especially after the project deadline was moved up. It is unfortunate that just as you gain the most understanding of the topic at the end of the thesis, you need to conclude. Thus, this chapter offers several potential follow-up research directions based on the insights of a (somewhat) experienced master student, in addition to the suggestions discussed in the paper.

Light integration
One of the main goals of the project was to establish the release of content from liposomes; however, in the end this has not been achieved. As a result of the unavailability of light-activatable particles, the project's focus was redirected towards demonstrating the multipore design, which was feasible with the existing liposomes. However, for a complete demonstration of the concept, the integration of light-activated liposomes and a light source into the setup is essential. Furthermore, as noted in the literature review, a critical aspect missing in literature is the influence of microfluidic forces on the release of contents from a liposome. Besides determining the overall release rate and effective dose that can be administered, detailed videos of the content release profile could be investigated once the light source is included in the test setup.

Because the setup is already mounted to either a fluorescent or an optical microscope, this presents an opportunity to integrate the light source into the equipment and use the optics already present in the microscopes to control the light path to the microfluidic chip.

Nozzle design optimization
Once an experimental setup is established in which the release pressure of a specific nozzle can be determined and this corresponds to theory, it will be possible to focus on optimizing the nozzle design. By varying the width and angle of the nozzle, while constraining the maximal area dilation of the membrane, interesting contour plots can be created to find the optimal burst pressure. Examples can be found in Figure 1.19. If, on the other hand, the theory as provided in the paper is proved to be inconsistent, COMSOL multiphysics or other FEA simulations could provide an alternative solution to predict the trapping behavior of the liposomes. Lastly, it would be interesting to examine other possible nozzle shapes, such as depicted in Figure 1.20.

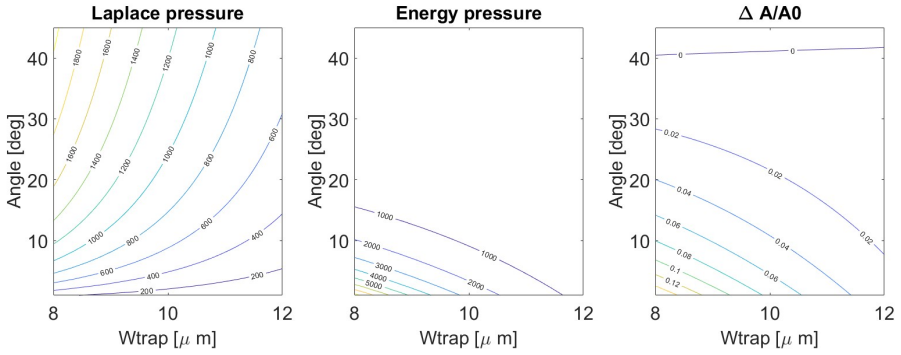

Figure 1.19: Example plots of nozzle shape optimization.

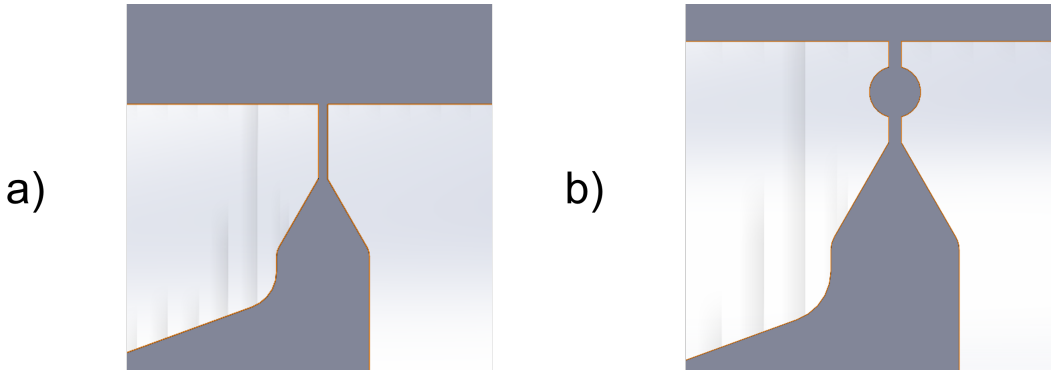

Figure 1.20: Examples of future designs. **a)** Extension tube to induce more stretching of the liposome. **b)** Inclusion of a 'relaxation' chamber to reduce lysis probability.

Optimization of release rate

Another interesting and open question remains, which is the time-sensitive part of the concept. This includes the time necessary to refill the open pores as well as the time it takes a liposome to release sufficient content. Based on the results of these experiments, the designs could be altered and optimized to ensure maximum therapeutic effectiveness.

The bigger picture; working towards implementation

Although these suggestions are not the first to be implemented, as they should only be considered once the effectiveness of the concept has been rigorously proven, they are required to realize a commercially viable product.

First, the requirement of biocompatibility should be taken into account as working within the brain environment requires this. Second, for this project, the release part of the mechanism was not part of the scope and was assumed to occur automatically due to the breakdown of the membrane during exposure to light. However, this should be verified by additional experiments. If the results show that this assumption is invalid, solutions such as the implementation of micropumps/valves to control release should be investigated. Furthermore, it will be important to ensure that it is possible to expose only certain nozzles to light, by, for example, integrating fiber optics into the DDS. Next, to accommodate the brain environment, the PDMS structure should be scaled down to a flexible thin membrane that can adapt to the shape of the brain.

Lastly, apart from the scope of the microfluidic system and the liposomes, an important yet unresolved research question concerns the types of drugs that can be utilized with this novel technique. This new approach to the delivery of on-demand drugs in the brain could potentially make new drugs effective. Once the concept has proven to be effective, research into new types of drugs should be encouraged not only to treat strokes, but also to treat other recurring brain disorders.

Personal reflection

My personal reflection...

The choice for this thesis project on microfluidics was motivated by the diversity the project offered. The combination of literature review, theory development, CAD design, production, and experiments enabled me to maintain my enthusiasm throughout the year. Every stage presented its own set of challenges and learning experiences, which I found highly rewarding.

One of the most significant lessons I learned from this project was the balance between speed and accuracy. I have always valued working quickly and efficiently. However, research (and especially microfluidics) requires a more patient and careful approach. Small vibrations can cause large disturbances, and forcing flow by hand has destroyed (too many) chips.

Daily problem solving became a big part of my work. Whether it was troubleshooting equipment, refining experimental protocols, or interpreting liposome behavior, each day presented new problems to solve. Although this was an individual project, in my opinion, support and collaboration with others were essential for success. Discussion with peers, mentors, and friends provided me with new perspectives and insights. These interactions often resulted in new ideas or helped me notice aspects that I initially overlooked.

In conclusion, my thesis journey has been a year-long learning experience. The project's diversity kept me engaged and I found a new balance between speed and precision. The technical knowledge I gained, as well as the new way of working, are skills that I am excited to apply in future projects.

Gijsbert Theodoor van Veen
Delft, July 2024

A

Theory

This section aims to provide more details on the theory described in the paper section 2. In section A.1 and subsection A.1.2 more details of the calculations are provided, whereas in section A.2 results that have not been included in the paper are discussed. Lastly, in section A.3 the Matlab code used to do the calculations and create the various figures is presented.

A.1. Shape calculations

The deformed liposome is illustrated in Figure A.1 with its shape divided into three regions: I) an ellipsoid; II) a frustum; III) an ellipsoid. From this situation follow the relations as found in Equation A.1. Furthermore, the initial volume and surface area of the liposome were calculated using Equation A.2.

$$R_1 = \frac{W_{trap}}{2} + x \tan \alpha \tag{A.1a}$$

$$\Delta L = \frac{R_2 - R_1}{\tan \alpha} \tag{A.1b}$$

$$V_0 = \frac{4}{3}\pi R_{lip}^3 \tag{A.2a}$$

$$A_0 = 4\pi R_{lip}^2 \tag{A.2b}$$

Assuming an incompressible medium inside the liposome, and given position x and initial volume of the liposome V_0, all relevant dimensions of the deformed liposome can be determined based on the volume of the deformed liposome. Details on the calculations of the new volume can be found in subsection A.1.1. Furthermore, on the basis of this new shape the difference in surface area from the initial state can also be determined. This is a necessary estimate for determining the energy stored in the membrane. More details on these calculations are provided in subsection A.1.2.

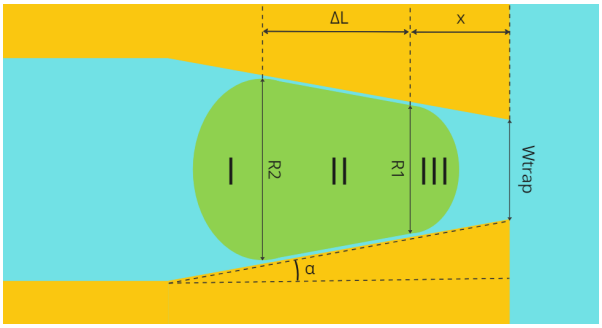

Figure A.1: A schematic representation of a microfluidic trap containing the fluid (blue), liposome (green) and the microfluidic system (yellow). Significant features/dimensions are indicated.

A.1.1. Volume

As mentioned before, it is assumed that the shape of the deformed liposome is divided into two ellipsoids and a frustum. The ellipsoids have the principle axis R_i in-plane and the principle axis $h/2$ out-of-plane, therefore their volume is calculated using Equation A.3. The volume of the frustum is calculated by integrating the surface of the base with the total height of the frustum; a sketch of the situation can be found in Figure A.2. It is important to note that one of the principal axes stays the same ($h/2$), whereas the other changes according to height y. The results of the integration can be found in Equation A.4.

$$V_{ellipsoid} = \frac{4}{3}\pi R_i^2 \frac{h}{2} \tag{A.3}$$

$$\begin{aligned} V_{frustum} &= \int_0^{\Delta L} \pi AB \, dy \\ &= \int_0^{\Delta L} \left(\pi(R_2 - y\tan\alpha)\frac{h}{2}\right) dy \\ &= \frac{\pi h}{2}\left(R_2\Delta L - \frac{1}{2}(\Delta L)^2\tan(\alpha)\right) \end{aligned} \tag{A.4}$$

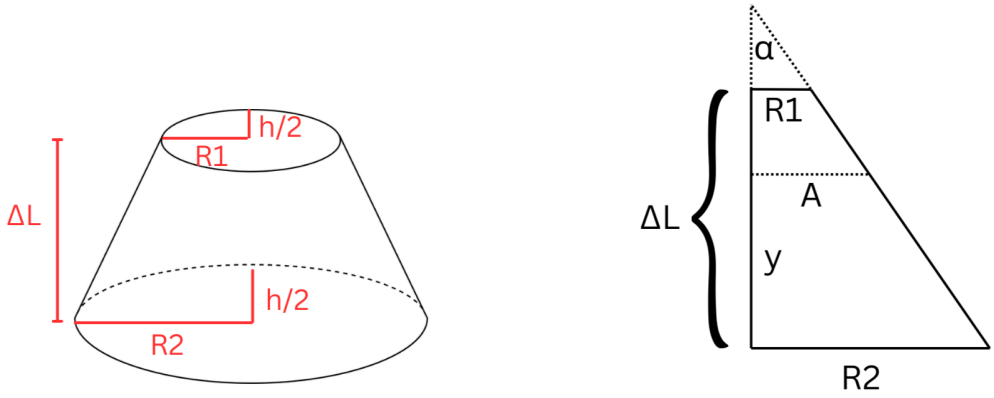

Figure A.2: Shape of the frustum.

A.1.2. Area

The area of an ellipsoid can be estimated using the Knud Thomsen approximation [1] as found in Equation A.5. This approximation has a maximal relative error of 1.061% for $p \approx 1.6075$.

$$A_{ellipsoid} = 4\pi \left(\frac{a^p b^p + a^p c^p + b^p c^p}{3} \right)^{1/p} \tag{A.5}$$

The area of the frustum can be calculated by integrating the circumference of the base of the height. Using the same terminology as in Figure A.2, this results in Equation A.6.

$$\begin{aligned} A_{frustum} &= \int_0^{\Delta L} \pi(A + B)\, dy \\ &= \int_0^{\Delta L} \left(R_2 - y \tan\alpha + \frac{h}{2} \right) dy \\ &= \pi \left((R_2 + \frac{h}{2})\Delta L - \frac{1}{2}\Delta L^2 \tan\alpha \right) \end{aligned} \tag{A.6}$$

A.2. Results

The initial Youngs' Laplace model has been based on literature, and uses the same approach as Simen *et al.* [2]. They assumed that the oil droplet in their study is deformed by a similar trap, called the Laplace trap, and that the resulting shape is composed of two ellipsoids and a frustum. However, it is assumed that the frustum has a rectangular base profile. This causes a shape where there is a non-constant interface between the ellipsoids and the frustum; a rectangular surface with characteristic length a & b touching a ellipsoid with principle axis a and b. In order to improve this, a new approach has been developed in which the frustum base is not rectangular, but also ellipsoid, resulting in a continuous shape. The differences caused by this alteration can be found in Figure A.3. It can be seen that the Laplace pressure is marginally higher when the new geometry is included. Before the distance of 5 μm, the Laplace pressure is 0, because the droplet is not yet touching the walls of the trap and is not being deformed.

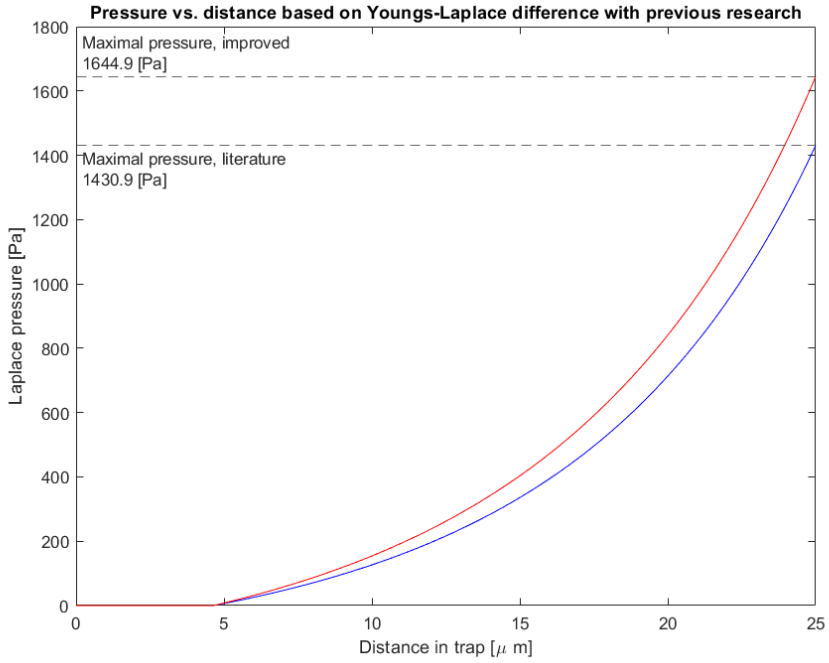

Figure A.3: Resulting graph showing the effect of the geometry improvements on the Laplace pressure. The following input parameters have been used in combination with the Matlab script as shown in section A.3: Wtrap=5e-6 m; Rlip=5e-6 m; Angle=7/180*pi rad; Gamma=15.6e-3 N/m; Ltrap=25e-6 m; h=10e-6 m.

Next, the difference between the membrane energy and the Laplace theory has been assessed. If the same trap is studied as described before, the resulting pressures can be found in Figure A.4. Interestingly, it can be seen that the pressure for the energy model is much higher, suggesting that the trap will be more effective for membrane-like particles compared to fluid droplets. However, in order to better understand the situation, a deep dive into the effect of different input parameters has been performed. The results of this investigation can be found in subsection 2.4.

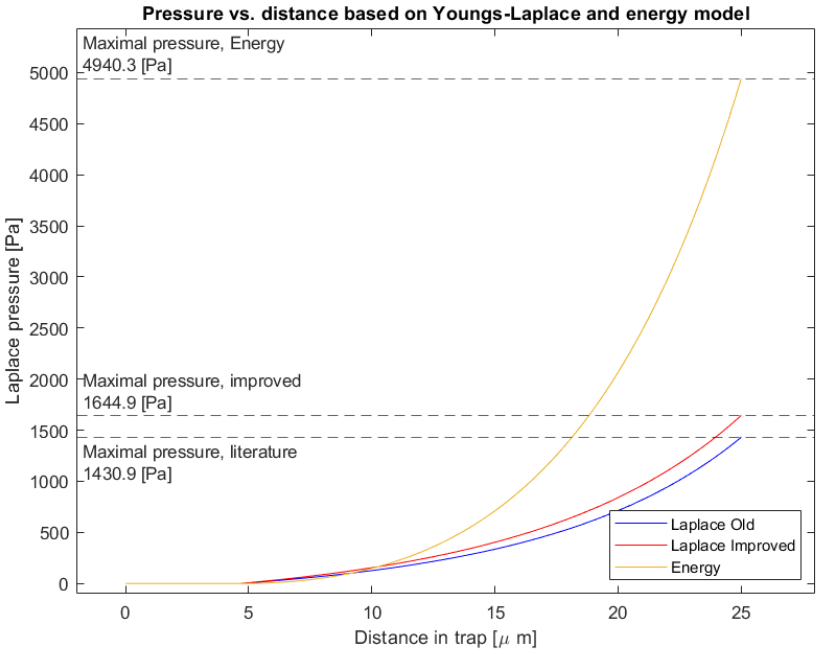

Figure A.4: Resulting graph showing the difference between the Laplace and energy approach. The following input parameters have been used in combination with the Matlab script as shown in section A.3: Wtrap=5e-6 m; Rlip=5e-6 m; Angle=7/180*pi rad; Gamma=15.6e-3 N/m; Ltrap=25e-6 m; h=10e-6 m.

A.3. Matlab code

```
clear
clc
close all


%% Parameters

Wtrap=5e-6; %width of the trap
Rlip=5e-6; %Radius of the liposome
Angle=7/180*pi; %Angle of the trap
Gamma=15.6e-3; %Surface tension of oil+water
Ltrap=25e-6; %Depth of the trap
h=10e-6; %height of the channel
Steps=1000; %Number of steps in the solver
KA = 230e-3; %Stretching moduli of liposome
Ka = 0.59e-19; %Bending moduli of liposome
Patm = 101325; %atmospheric pressure


% Initial values
V0=4/3*pi*Rlip^3; %Volume of the liposome
```

```
A0=4*pi*Rlip^2; %Surface area of the liposome
x=linspace(0,Ltrap,Steps); %Define path
S=zeros(Steps,8); %Store solver data Laplace
S2=zeros(Steps,9); %Store solver data Energy
Dlip=2*Rlip;

%% Triangular trap calculations, square channel, based on Laplace paper
for i = 1:length(x)
    Df = Wtrap + 2*x(i)*tan(Angle);
    if Df/2 > Rlip
        S(i,1) = x(i); %Location
    else
        syms Db
        eqns = pi/12*Db^2*h+pi/12*Df^2*h+h*(Db^2-Df^2)/(4*tan(Angle)) ==
            4/3*pi*Rlip^3;
        H = vpasolve(eqns, Db); %Define geometry at each point, Db = H(1)
        P = Gamma*(1/(Df/2)-1/(double(H(2))/2)); %Calculate Laplace
            pressure
        area1=ellipsoidSurfaceArea(H(2)/2, H(2)/2, h/2);
        area2=ellipsoidSurfaceArea(Df/2, Df/2, h/2);
        A = 1/2*area1+1/2*area2+(H(2)+Df)*(H(2)-Df)/2/tan(Angle)*(H(2)-Df)
            /sin(Angle)*h;%Calculate surface area
        S(i,1) = x(i); %Location
        S(i,2) = Df; %Df
        S(i,3) = H(1); %Db
        S(i,4) = (H(2)-Df)/2/tan(Angle); %delta L from solver
        S(i,5) = P; %Laplace pressure
        S(i,6) = (A-A0)^2/A0; %Delta A^2 / A0
    end
end



%% Triangular trap calculations, square channel, improved ellipsoid
for i = 1:length(x)
    Df = Wtrap + 2*x(i)*tan(Angle);
    if Df/2 > Rlip
        S2(i,1) = x(i); %Location
        S2(i,2) = Df;
    else
        syms Db
        eqns = pi/12*Db^2*h+pi/12*Df^2*h+pi*h/2*(Db/2*((Db-Df)/2/tan(Angle
            ))-((Db-Df)/2/tan(Angle))^2/2*tan(Angle)) == 4/3*pi*Rlip^3;
        H = vpasolve(eqns, Db); %Define geometry at each point, Db = H(2)
        P = Gamma*(1/(Df/2)-1/(double(H(2))/2)); %Calculate Laplace
            pressure
        DeltaL = (double(H(2))-Df)/2/tan(Angle);
        area1=ellipsoidSurfaceArea(double(H(2))/2, double(H(2))/2, h/2);
        area2=ellipsoidSurfaceArea(Df/2, Df/2, h/2);
        A = 1/2*area1+1/2*area2+pi*((double(H(2))/2+h/2)*DeltaL-DeltaL
            ^2/2*tan(Angle)); %Calculate surface area
        Es = KA/2*((A-A0)/A0)^2*A0; %Calculate stretching energy
        S2(i,1) = x(i); %Location
        S2(i,2) = Df; %Df
        S2(i,3) = H(2); %Db
        S2(i,4) = (H(2)-Df)/2/tan(Angle); %Delta L from solver
```

```
72          S2(i,5) = P; %Laplace pressure
73          S2(i,6) = (A-A0)/A0; %Delta A/A0
74          S2(i,7) = Es; %Stretching energy membrane
75      end
76  end
77
78  for i=2:length(x)-1
79          S2(i-1,8) = (S2(i,7)-S2(i-1,7))/(x(i-1)-x(i)); %Stretching force
80          S2(i-1,9) = (S2(i-1,8) * 4/pi / (S2(i-1,3)^2-S2(i-1,2)^2)); %
               Applied pressure
81  end
82
83
84
85  %% plotting
86
87  % improved ellipsoid vs old one
88  figure(1)
89
90  p1 = plot((Ltrap-S(:,1))*10^6,S(:,5),'b');
91  hold on
92  p2 = plot((Ltrap-S2(:,1))*10^6,S2(:,5), 'r');
93  hold off
94  yline(S(1,5),'--',{'Maximal pressure, old [Pa]' round(S(1,5),1)},'
       LabelHorizontalAlignment', 'left', 'LabelVerticalAlignment' , 'bottom')
95  yline(S2(1,5),'--',{'Maximal pressure, new [Pa]' round(S2(1,5),1)},'
       LabelHorizontalAlignment', 'right','LabelVerticalAlignment' , 'top')
96  legend([p1 p2],{'Old','Improved'}, 'Location','southeast')
97  ylim([-20 S(1,5)*1.3])
98  title('Pressure vs. distance according to Youngs-Laplace based on previous
        research')
99  xlabel('Distance in trap [\mu m]');
100 ylabel('Laplace pressure [Pa]');
101
102 %Laplace vs Energy
103 figure(2)
104 hold on
105 plot((Ltrap-S2(:,1))*10^6,S2(:,5));
106 yline(S2(1,5),'--',{'Maximal pressure, Laplace [Pa]' round(S2(1,5),1)},'
       LabelHorizontalAlignment', 'center')
107 ylim([-100 S2(1,5)*1.2])
108
109 plot((Ltrap-S2(:,1))*10^6,S2(:,9))
110 yline(S2(1,9),'--',{'Maximal pressure, Energy [Pa]' round(S2(1,9),1)},'
       LabelHorizontalAlignment', 'center')
111 ylim([-100 S2(1,9)*1.2])
112
113 title('Pressure vs. distance according to Laplace and Energy model')
114 xlabel('Distance in trap [\mu m]');
115 ylabel('Pressure [Pa]')
116 legend('Laplace','','Energy','')
117
118 hold off
119
120 %stretching values
121 figure(3)
```

```
plot((Ltrap-S2(:,1))*10^6,S2(:,6))
title('\Delta A/A0 vs. distance according to Energy in membrane')
xlabel('Distance in trap [\mu m]');
ylabel('Area stretching [-]');
ylim([-0.01 S2(1,6)*1.2])


%% Parameter optimization


% Angle optimization

AngleMin=1/180*pi;
AngleMax=45/180*pi;
steps2=200;
deltaX=1e-10;
Astore=zeros(steps2,7);
Angles=linspace(AngleMin,AngleMax,steps2);

for i = 1:length(Angles)
    Df=Wtrap;
    syms Db
    eqns = pi/12*Db^2*h+pi/12*Df^2*h+pi*h/2*(Db/2*((Db-Df)/2/tan(Angles(i)
       ))-((Db-Df)/2/tan(Angles(i)))^2/2*tan(Angles(i))) == 4/3*pi*Rlip^3;
    H = vpasolve(eqns, Db); %Solve, Db = H(2)
    DeltaL = (double(H(2))-Df)/2/tan(Angles(i));
    A = 1/2*ellipsoidSurfaceArea(Df/2, Df/2, h/2)+1/2*ellipsoidSurfaceArea
       (double(H(2))/2, double(H(2))/2, h/2)+pi*((double(H(2))/2+h/2)*
       DeltaL-DeltaL^2/2*tan(Angles(i))); %Calculate surface area
    Astore(i,1)= H(2); %Store Db
    Astore(i,2)= Gamma*(1/(Df/2)-1/(double(H(2))/2)); %Store Laplace
       pressure
    Astore(i,3)= KA/2*((A-A0)/A0)^2*A0; %Store energy
    Astore(i,7) = (A-A0)/A0; %Store delta A/A0
end

for i = 1:length(Angles)
    Dfd=Wtrap+2*deltaX*tan(Angles(i));
    syms Db
    eqns = pi/12*Db^2*h+pi/12*Dfd^2*h+pi*h/2*(Db/2*((Db-Dfd)/2/tan(Angles(
       i)))-((Db-Dfd)/2/tan(Angles(i)))^2/2*tan(Angles(i))) == 4/3*pi*Rlip
       ^3;
    H = vpasolve(eqns, Db); %Solve, Db = H(2)
    DeltaL = (double(H(2))-Dfd)/2/tan(Angles(i));
    A = 1/2*ellipsoidSurfaceArea(Dfd/2, Dfd/2, h/2)+1/2*
       ellipsoidSurfaceArea(double(H(2))/2, double(H(2))/2, h/2)+pi*((
       double(H(2))/2+h/2)*DeltaL-DeltaL^2/2*tan(Angles(i))); %Calculate
       surface area
    Astore(i,4) = KA/2*((A-A0)/A0)^2*A0; %Store energy new
    Astore(i,5) = abs((Astore(i,3)-Astore(i,4)))/deltaX; %Store Delta E /
       Delta X
    Astore(i,6) = Astore(i,5)*4/pi/(Astore(i,1)^2-Dfd^2); %Store pressure
end


```

```
% width optimization
WtrapMin=8e-6;
WtrapMax=12e-6;
stepAstore=50;
Wtraps=linspace(WtrapMin,WtrapMax,stepAstore);
Wstore=zeros(stepAstore,7);

for j = 1:length(Wtraps)
        Df=Wtraps(j);
        syms Db
        eqns = pi/12*Db^2*h+pi/12*Df^2*h+pi*h/2*(Db/2*((Db-Df)/2/tan(Angle
           ))-((Db-Df)/2/tan(Angle))^2/2*tan(Angle)) == 4/3*pi*Rlip^3;
        H = vpasolve(eqns, Db); %Solve, Db = H(2)
        DeltaL = (double(H(2))-Df)/2/tan(Angle);
        A = 1/2*ellipsoidSurfaceArea(Df/2, Df/2, h/2)+1/2*
           ellipsoidSurfaceArea(double(H(2))/2, double(H(2))/2, h/2)+pi*((
           double(H(2))/2+h/2)*DeltaL-DeltaL^2/2*tan(Angle)); %Calculate
           surface area
        Wstore(j,1)= H(2); %Store Db
        Wstore(j,2)= Gamma*(1/(Df/2)-1/(double(H(2))/2)); %Store Laplace
           pressure
        Wstore(j,3)= KA/2*((A-A0)/A0)^2*A0; %Store energy
        Wstore(j,7) = (A-A0)/A0; %Store delta A/A0
end

for j = 1:length(Wtraps)
    Dfd=Wtraps(j)+2*deltaX*tan(Angle);
    syms Db
    eqns = pi/12*Db^2*h+pi/12*Dfd^2*h+pi*h/2*(Db/2*((Db-Dfd)/2/tan(Angle))
       -((Db-Dfd)/2/tan(Angle))^2/2*tan(Angle)) == 4/3*pi*Rlip^3;
    H = vpasolve(eqns, Db); %Solve, Db = H(2)
    DeltaL = (double(H(2))-Dfd)/2/tan(Angle);
    A = 1/2*ellipsoidSurfaceArea(Dfd/2, Dfd/2, h/2)+1/2*
       ellipsoidSurfaceArea(double(H(2))/2, double(H(2))/2, h/2)+pi*((
       double(H(2))/2+h/2)*DeltaL-DeltaL^2/2*tan(Angle)); %Calculate
       surface area
    Wstore(j,4) = KA/2*((A-A0)/A0)^2*A0; %Store energy new
    Wstore(j,5) = (Wstore(j,3)-Wstore(j,4))/deltaX; %Store Delta E / Delta
        X
    Wstore(j,6) = Wstore(j,5)*4/pi/(Wstore(j,1)^2-Dfd^2); %Store pressure
end

%plotting
%Laplace vs energy
figure(2)
subplot(2,2,1)
plot(Angles/pi*180,Astore(:,2))
title("Effect of Angle (Wtrap = " + Wtrap*1e6 + "[\mu m])")
xlabel('Angle [deg]');
ylabel('Pressure [Pa]');
hold on
plot(Angles/pi*180,Astore(:,6))
legend('Laplace','Energy','Location','northeast')
ylim([-100 max(max(Astore(:,6)),max(Astore(:,2)))*1.1])
xlim([min(Angles)/pi*180-3 max(Angles)/pi*180+3])

```

```
%area stretching
subplot(2,2,3)
plot(Angles/pi*180,Astore(:,7))
title('Area stretching')
xlabel('Angle [deg]');
ylabel('max(\Delta A/A0) [-]');
ylim([-0.01 max(Astore(:,7))*1.1])
xlim([min(Angles)/pi*180-3 max(Angles)/pi*180+3])

%plotting
%Laplace vs energy
subplot(2,2,2)
%yyaxis left
plot(Wtraps*1e6,Wstore(:,2))
title("Effect of Wtrap (Angle = "+ Angle/pi*180 + "[deg])")
xlabel('Wtrap [\mu m]');
ylabel('Pressure [Pa]');
hold on
%yyaxis right
plot(Wtraps*1e6,Wstore(:,6))
legend('Laplace','Energy','Location','northeast')
ylim([-100 max(max(Wstore(:,6)),max(Wstore(:,2)))*1.1])
xlim([min(Wtraps)*1e6-0.3 max(Wtraps)*1e6+0.3])


%area stretching
subplot(2,2,4)
plot(Wtraps*1e6,Wstore(:,7))
title('Area stretching')
xlabel('Wtrap [\mu m]');
ylabel('max(\Delta A/A0) [-]');
ylim([-0.01 max(Wstore(:,7))*1.1])
xlim([min(Wtraps)*1e6-0.3 max(Wtraps)*1e6+0.3])
```

```
%% Function surface_area
function area = ellipsoidSurfaceArea(a, b, c)
 p=1.6075;
 area = 4*pi*((a^p*b^p+a^p*c^p+b^p*c^p)/3)^(1/p);
end
```

B

Methods and materials

To produce the microfluidic chips, significant time was spent optimizing the production process. This section outlines the selection process, steps taken, and considerations during optimization. Figure B.1 provides a complete overview of the production process, including all steps and a schematic. The process is divided into three categories: 1. Mold production, 2. Soft lithography, and 3. Chip preparations. An explanation of the selection process is found in section B.1, with detailed steps in section B.2 to section B.5. Mold production took 6.5 hours, soft lithography 3 hours, and chip preparations 5 hours, resulting in a rapid design-to-prototype time of approximately 2 days. This facilitated rapid prototyping, beneficial for future microfluidic projects. This appendix serves as a future guide for microfluidic chip production.

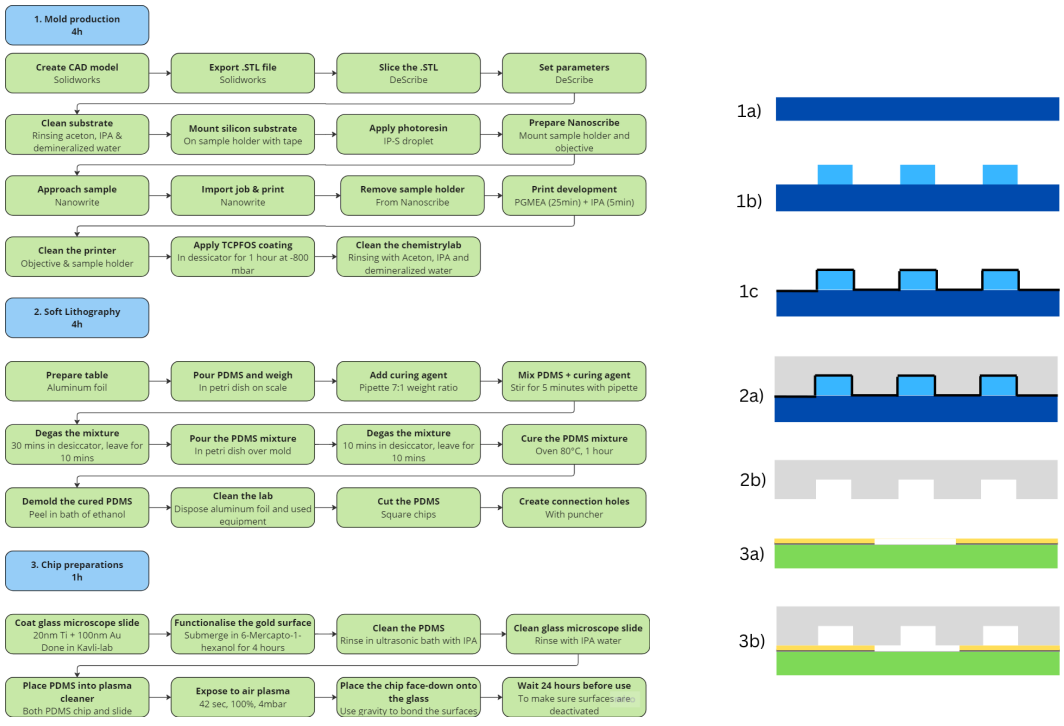

Figure B.1: Overview of the fabrication process. **a)** Complete list of all fabrication steps. 1) Steps for mold production. 2) Steps for soft lithography. 3) Steps for microfluidic chip preparations. **b)** Schematic of the fabrication process. 1a) Cleaned silicon substrate (dark blue). 1b) Creating mold features (light blue) using 2PP. 1c) Coating the mold with TCPFOS. 2a) Pouring PDMS (grey) over the mold. 2b) Removing PDMS from the mold. 3a) Coating the glass with Ti (dark grey) and Au (yellow) to create electrodes. 3b) Plasma bonding the PDMS to a glass microscope slide (green) to create the microfluidic channels (white).

B.1. Process selection

For the realization of the DDS, the choice of production technique can have a substantial impact. In addition to the limitations imposed on the dimensionality and feature size of the design, the concept-to-prototype time can be considerably different depending on the selected fabrication process. Therefore, careful consideration can lead to better designs, faster prototyping, and ultimately a better prospect on a fully functional system. This section will provide clarification on the choice of the fabrication process.

First, the requirements and wishes of the production process are determined. This resulted in the following requirements:

- feature size: sub-micron. As the size of the liposomes is around a few microns, the feature size required to design the trap need to at least less than this;
- dimensionality: at least 2.5D. As the microfluidic chip can remain relatively simple, a 2.5D dimensionality allows for enough design flexibility;
- availability: at Delft University of Technology, department of Precision and Microsystems Engineering. As the goal is to develop microfluidic chips on a regular basis during the project, the process is required to be available within reasonable time frames (~weeks);

and wishes:

- fabrication time: low. As the project is of pioneering nature, it is expected not all designs will work perfectly as intended. Therefore a low fabrication time will improve the ability to rapidly prototype and ultimately increase the chance of success;
- bio-compatible. As the DDS' application is within the brain environment, bio-compatibility is desired. However, as a proof-of-concept is included in the project proposal, this is no hard requirement;
- Young's-Modulus: low. As the DDS' application is within the brain environment, it is desired for the chip to be flexible to be compatible with the brain interface.

Based on the requirements and given the overview of the materials and fabrication processes from the literature review Appendix F, a selection of applicable processes remains as found in Table B.1. Based on the wish for low fabrication time, one of the molding techniques would provide the best solution. As the material PDMS (an elastomer that complies with the wishes of biocompatibility and low stiffness) was readily available, soft lithography proposed the best overall solution. In order to create the mold with sufficient resolution, 2PP was selected. Both SLA and 2PP approaches have been tested and the results can be found in Figure B.2. From this it was concluded the resolution of SLA (Micro2, MicroSLA Inc. USA) did not provide sufficient feature sizes to print the nozzle.

Figure B.2: The result of printing the first design with the Micro2 SLA (left) and the Nanoscribe 2PP (right) printers.

Table B.1: Overview of fabrication processes based on research from Waldbaur *et al.* [3] and combined with other references [4–7].

	Feature size	Fabrication time	Scalability	Costs	Dimens.	Materials
Injection molding [4]	Mold dependent	Low	Good	Low	3D	Polymer (Thermo-plastic)
Hot embossing [6, 7]	Mold dependent	Low	Good	Low	3D	Polymer (Thermo-plastic)
Soft lithography [7]	Mold dependent	Low	Good	Low	3D	Elastomers
SLA	μm	Medium	Low	Low	3D	Photoresists, light curable monomers
2PP	nm-μm	High	Low	High	3D	Photoresists, light curable monomers

Processes without reference have been copied from Waldbaur *et al.* [3]

B.2. Two-photon polymerization

B.2.1. Objective selection

According to the theoretical lateral and axial resolution specified by the manufacturer (Nanoscribe GmbH) and presented in Table B.2, the 25x objective met the desired feature sizes of approximately $\sim 1\mu$m, while maintaining a balance between resolution and printing duration (the 10X objective is insufficient in resolution, while the 63x objective results in slower printing speeds).

Table B.2: Description of the different objectives as provided by Nanoscribe GmbH [8].

Objective	Theoretical lateral resolution	Theoretical axial resolution	Print speed	Aspect ratio
10x	1600 nm	25400 nm	6.8 mm^3/h	16
25x	595 nm	3313 nm	0.8 mm^3/h	5.6
63x	340 nm	826 nm	0.4 mm^3/h	2.4

B.2.2. Print material selection

Several materials could be chosen for the 2PP mold production. According to the manufacturer, Nanoscribe, GmbH, two of their photoresists, IP-S and IP-PDMS, are appropriate for microfluidics. The details of both materials are provided in Table B.3. Due to the highly elastic nature of IP-PDMS, which could compromise the mold's structural integrity, and the previous experience with IP-S in soft lithography, IP-S was chosen for the mold prints. No issues were encountered later, such as incompatibility with the soft lithography method, thus there was no need to reconsider this decision.

Table B.3: Description of the different photoresists as provided by Nanoscribe GmbH.

Photoresist	Advantages	Applications
IP-PDMS	2PP printing of soft, flexible and highly elastic structures	Materials engineering, life sciences, cell and tissue engineering, microfluidics, microelectromechanical systems (MEMS)
IP-S	Biocompatible, non-cytotoxic according to ISO 10993-5 / USP 87. Smooth surfaces for micro- and mesoscale fabrication with optical-quality surface roughness and shape accuracy	Mechanical metamaterials, microoptics, integrated photonics, microfluidics, cell scaffolds

B.2.3. Print parameter optimization

In order to create smooth molds, which improve the quality of the final microfluidic system and allow better demolding, the optimal printing parameters were investigated. First, IP-S 25x ITO Solid (3D MF) pre-settings as provided by Nanoscribe GmbH were used as basis. Secondly, a dose test was performed to find the required laser power and maximize the print speed. After the dose test, from which the results can be found in Figure B.3, it was decided that the laser power should not exceed 70% in order to limit the defects. In order to have some margin future prints, we used a laser power of 60%. The scanning speed was maintained at the maximal value of 100000μm/s in order to minimize print time. The defects are caused by overheating of the resin, resulting in bubbles and locally unpolymerized photoresist.

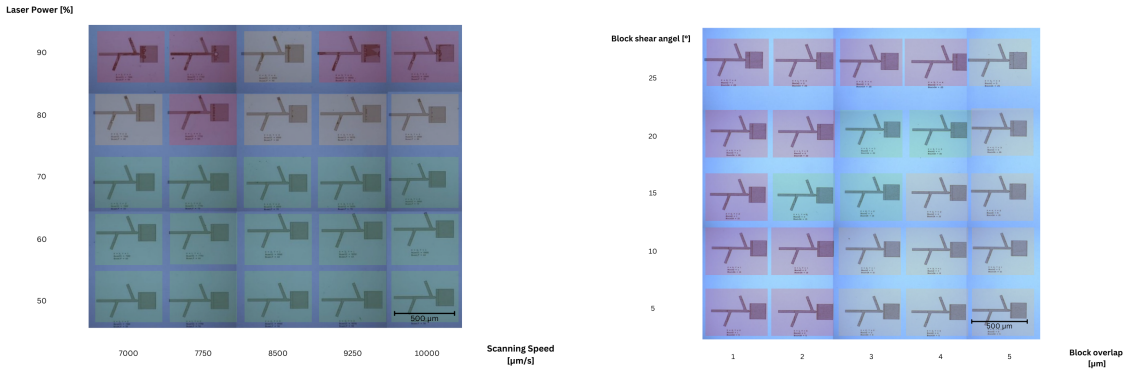

(a) Result of the dose test.

(b) Result of the stitching test.

Figure B.3: Test with IP-S resin (Nanoscribe GbmH) on silicon substrate. Green prints indicate good quality. Orange had minor defects and red has major defects.

During printing, several imperfections were noticed in the design, especially around the boundaries of the block splitting. In order to reduce these imperfections, a stitching test was performed in which the parameters used for the stitching were investigated. The results of this test can be found in Figure B.3. Based on these results, it was decided the optimal slicing parameters were; block overlap 3μm and block shear angle 15°. Although the quality of the print improved, sharp edges along the sides of the print remained. The origin of these sharp edges can be explained if it is assumed that the whole printing stage is rotated around its axis.

B.2.4. Workflow

A detailed schematic showing the steps taken during the 2PP process can be found in Figure B.4. The day before the 2PP printing procedure, a CAD model was created using Solidworks® and exported to DeScribe software (Nanoscribe GmbH) as .STL file to create the job file. In this software, the parameters used for printing are set, the .STL file is sliced/hatched and a script is created to operate the printer. Examples of slicing and hatching have been illustrated in Figure B.5a and Figure B.5b. An example code has been provided in Figure B.5c. IP-S 25x ITO Solid (3D MF) pre-settings provided by Nanoscribe GmbH were used as basis, with slicing distance 1 μm, hatching distance 0.5μm, base slice count 3, laser power 50mW, laser power 65%, Scanning speed 100000μm/s. The most important alteration from the standard settings was a reduced dose to minimize print defects and overexposure from mirroring of the incident beam on the highly reflective silicon substrate surface.

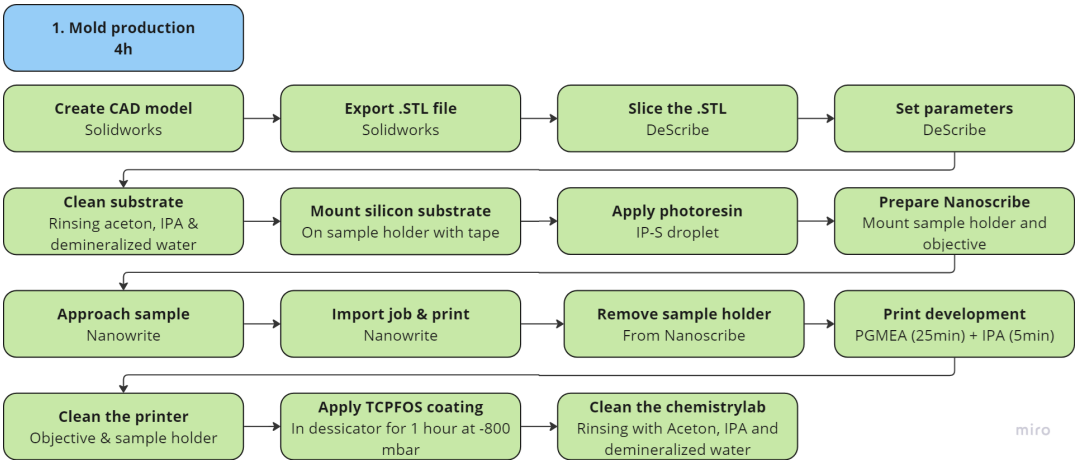

Figure B.4: A schematic of the 2PP-production process.

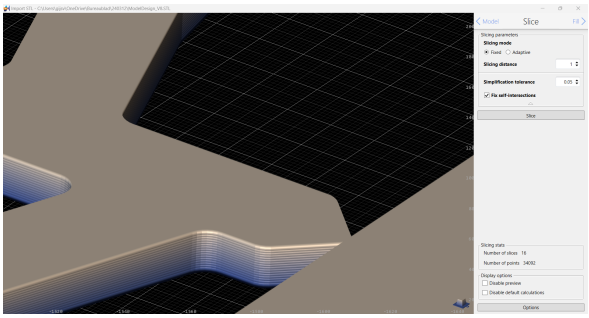

(a) Slicing the .STL file into different layers.

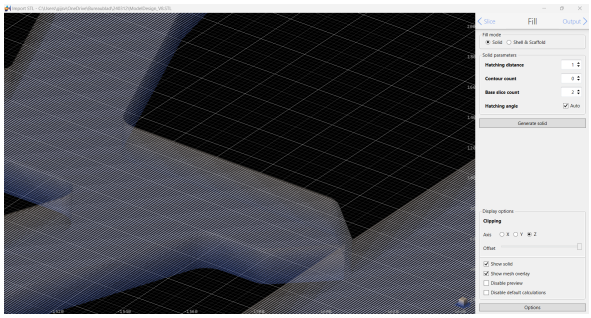

(b) Hatching the .STL into the horizontal path the laser follows.

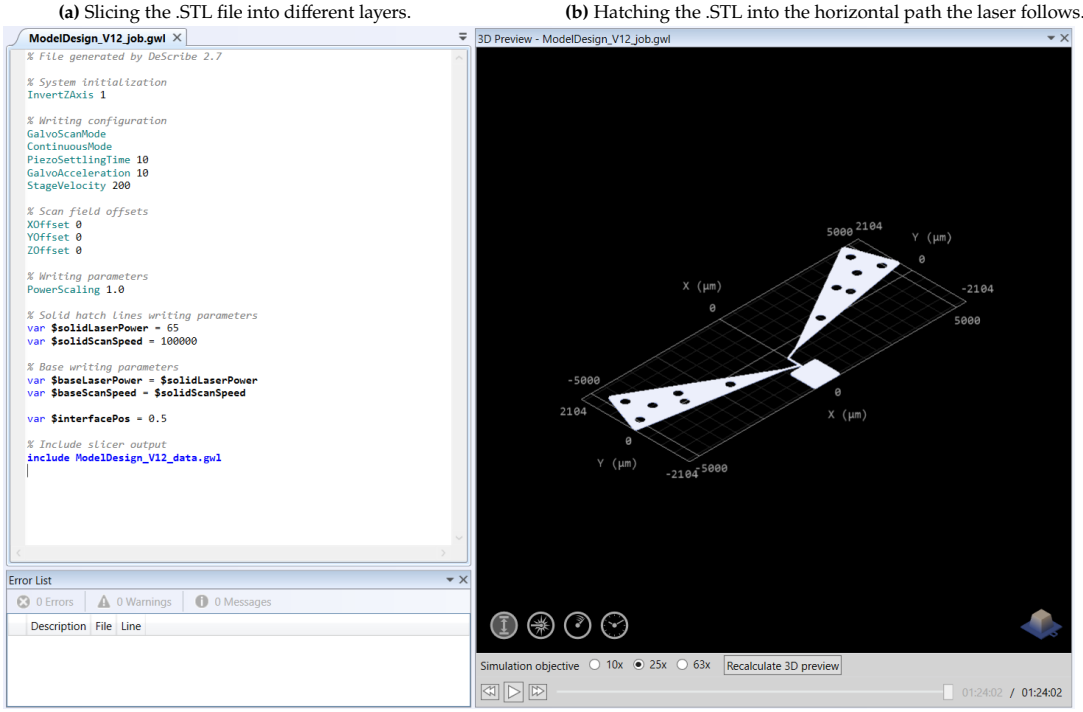

(c) A screenshot of the job file. Code can be found on the left top, errors on the left bottom and a preview of the print on the right.

Figure B.5: Screenshots of the Describe Software from Nanoscribe GmbH.

An hour before printing, the silicon substrate was cleaned by first rinsing with Aceton (Aceton, Sigma-Aldrich) followed by IPA (Isopropanol, Sigma-Aldrich) and demineralized water. The substrate was

blown dry using filtered nitrogen gas. This procedure ensured that no residue or dust was present on the surface, reducing unwanted contamination and printing errors. Finally, the substrates were placed on the sample holder and taped to ensure they remained stationary during printing. A droplet of photoresist (IP-S) was added directly onto the substrate. The result can be found in Figure B.6.

Figure B.6: A photo of the substrates with resin mounted to the sample holder.

For the 2PP printing itself, the Dip-in-Laser Lithography (DiLL) configuration was used in combination with the 25X objective. The 25x objective was installed into the correct mount inside the Nanoscribe printer and a felt ring was added to protect the printer from excessive photoresist dripping down.

Next, the software used to operate the 2PP printer was opened; Nanowrite. Within this software interface, the following steps were followed. First, the objective was lowered. The printer lid was then opened, and the sample holder including the silicon substrate(s) was installed. Once the lid was closed, the interface between the lens and the substrate was located. It is important to note that in order to find the interface, the difference in refractive index between the substrate and the resin is required to be at least 0.1 at 830 nm for the 25x objective. As the refractive index of IP-S is 1.486 and silicon 3.710, no issues were encountered during the approach. Finally, the job was selected and the print was started.

After exposure, the 2PP print is developed by submerging it in PGMEA (Propylene Glycol Monomethyl Ether Acetate, Sigma-Aldrich) for 25 minutes and IPA (Isopropanol, Sigma-Aldrich) for 5 minutes. The PGMEA removed the unpolymerized IP-S photoresist from the substrate, whereas the IPA was used to remove the PGMEA. After this, the mold was blown dry with filtered nitrogen gas.

B.3. Mold preparation

To improve the demolding properties of the molds, they were coated with Trichloro(1H,1H,2H,2H-perfluorooctyl)silane (TCPFOS). This chlorosilane compound forms a superhydrophobic monolayer on the mold surface, reducing the level of adhesion during demolding. The coating procedure started with activation of the 2PP mold surface by exposure to air plasma at 100% for 1 minute using a plasma gun. Next, a $2\mu L$ droplet of TCPFOS is deposited on a glass beaker and placed in a desiccator. The molds are positioned face down above the TCPFOS, supported by a 3D-printed holder. The pressure inside the desiccator was then reduced by approximately 800 mbar and maintained for 60 minutes, allowing the TCPFOS to vaporize and uniformly coat the mold surface. All equipment used can be found in Figure B.7. The results of the coating were verified by checking the equilibrium contact angle of water. As can be seen in Figure B.8, the angle increases significantly for the coated mold.

As TCPFOS has hazard warning "*H314 Causes severe skin burns and eye damage*", it is important to ensure proper cleaning and protection when working with this chemical. Therefore, all surfaces of the glass beaker and desiccator were properly cleaned using Aceton, IPA, and water after the procedures were

completed. Furthermore, all procedures were performed within a fume hood, and gloves were changed after completion.

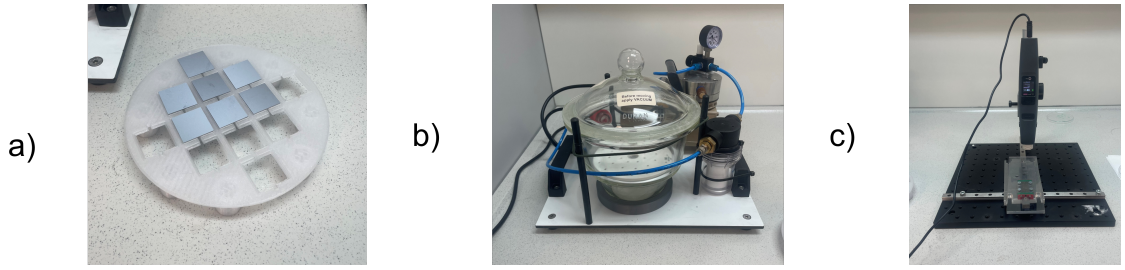

Figure B.7: Pictures of the equipment used during the coating of TCPFOS. **a)** The 3D printed substrate holder. **b)** The desiccator. **c)** The plasma gun.

Figure B.8: Picture of the result of coating the molds with TCPFOS, showing the contact angle of demineralized water. On the left is the coated substrate, while on the right is an uncoated substrate.

B.4. Soft Lithography

Soft lithography procedures are followed using the 2PP mold and PDMS (Sylgard 184 elastomer kit, Dow Corning, Midland, MI, USA) resulting in an optically transparent PDMS microfluidic stack. A schematic of the process can be found in Figure B.9. During these procedures, special care was taken with respect to contamination of uncured PDMS. These measures included the use of aluminum foil underneath the workspace and the frequent change of gloves.

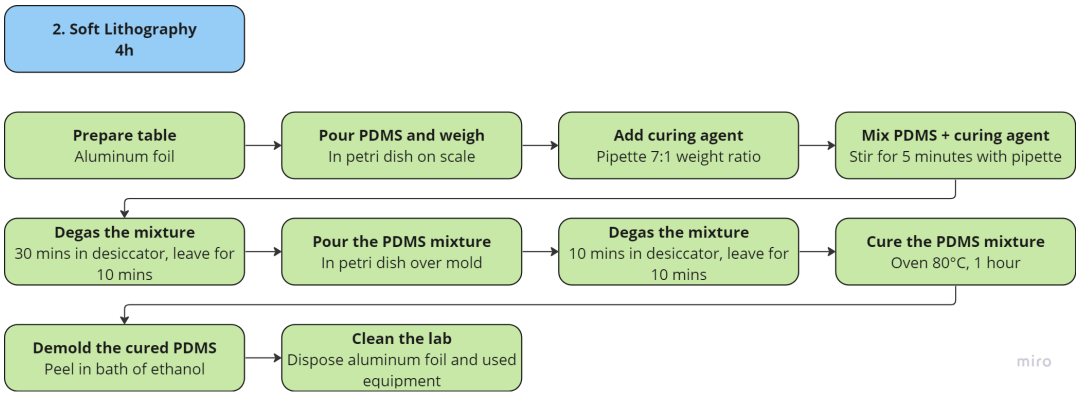

Figure B.9: A schematic of the soft lithography production process.

First, the two components of the Sylgard elastomer kit, polydimethylsiloxane and curing agent, were mixed in a weight ratio of 7:1. The ratio contained a higher amount of curing agent compared to the standard 10:1 ratio in order to increase the stiffness and reduce collapsing issues during plasma bonding with the glass, see Figure B.10a. Next, the stirred mixture is transferred to a desiccator to remove unwanted bubbles. Here, the mixture is kept in a near vacuum $\sim$ 200 mbar for 30 minutes, causing the bubbles to rise to the surface. The desiccator is then ventilated and the sample is left untouched for 10 minutes. During this time, the bubbles that have risen to the surface dissipate. Subsequently, the mixture is poured over the PDMS mold and again transferred to the desiccator for an additional 30 minutes of degassing followed by 10 minutes of rest. Thereafter, the curing of the PDMS was realized in the oven at 80°C for 1 hour. The results of these procedures can be found in Figure B.11.

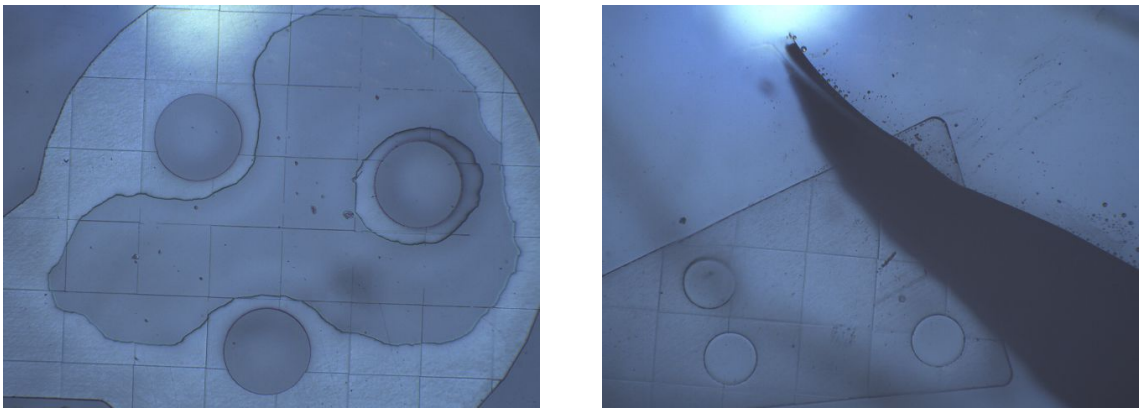

(a) The collapsing of the microfluidic channel after plasma bonding to a microscope slide.

(b) Ripped PDMS as a result of the adhesion to the mold.

Figure B.10: Photos of problems encountered during the soft lithography process.

Once the PDMS was cured, each substrate was cut out of the petri dish using a scalpel. Next, the mold was removed by gently peeling the PDMS while submerged in a bath of Ethanol (Ethyl Alcohol, Sigma-Aldrich). Ethanol was used to reduce adhesion between the mold and PDMS, which caused problems during early attempts to demold (see Figure B.10b). However, the effect was minimal and adhesion between the mold and PDMS was still causing problems. Therefore, it was necessary to coat the mold with TCPFOS. Lastly, the chemistry lab was properly cleaned with IPA and demineralized water to minimize the contamination.

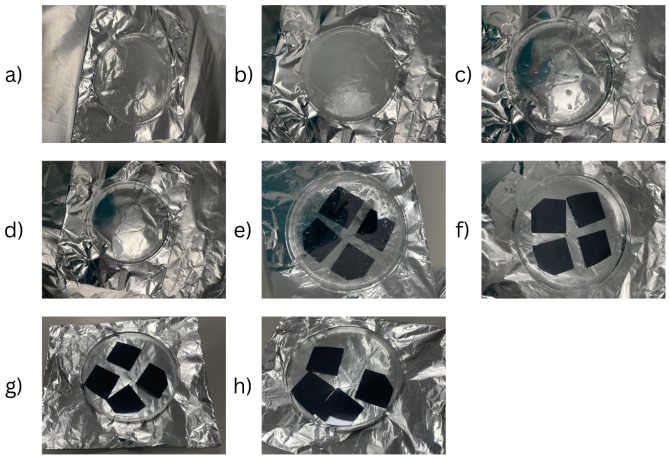

Figure B.11: Result of the soft lithography process. **a)** After stirring the PDMS+curing agent, the mixture contains many bubbles. **b)** After 10 minutes in the desiccator, the bubbles have risen to the surface. **c)** After 3 minutes in the air, most of the bubbles have disappeared. **d)** After 10 minutes in the air, all bubbles have disappeared. **e)** After pouring the mixture over the mold, again some bubbles are formed. **f)** After 10 minutes in the desiccator, the bubbles have risen to the surface. **g)** After 10 minutes in the air, the bubbles have disappeared. **h)** After curing in the oven a transparent PDMS stack remains.

B.5. Chip Preparations

Firstly, the PDMS chips are cut into squares and the connection holes are pierced through the PDMS using a puncher (Rapid-Core Microfluidic Punches, Darwin Microfluidics). Next, a glass microscope slide was prepared by subsequently rinsing with Aceton, IPA, and demineralized water and blowing dry with filtered nitrogen gas. Both the microscope slide and demolded PDMS are exposed to air plasma for 25 seconds (Diener Electronic GmbH & Co, FEMTO Low-pressure plasma system). This process creates silanol (SiOH) groups on both surfaces, which can form covalent siloxane bonds (Si-O-Si) when the material is in broad contact. The activated glass & PDMS surfaces are gently placed on top of each other, resulting in a strong bond after a few minutes. The exposure time was selected such that the PDMS surface was properly activated while minimizing damage to the surface. According to Bhattacharya *et al.* [9] changes in the wettability of the surfaces as a result of various levels of plasma exposure can be a useful parameter to evaluate bond strength. As the contact angle does not change significantly after 25 seconds of air plasma exposure [10], this indicates a properly activated surface. Interestingly, it was found that air plasma resulted in strong bonds that could withstand the experiments, whereas exposure to oxygen plasma resulted in bonding failures during the microfluidic chip operation. This contradicts the common literature that uses oxygen plasma treatment to bond the glass-PDMS interface [11–13]. In order to validate the use of air instead of oxygen, the color of the chamber during exposure, as found in Figure B.13, provides strong evidence that air was used. As there are many researchers at the department that use air plasma to create strong bonds, the cause of the problems is probably machine-specific. An alternative way to bond PDMS to glass is by using the plasma gun, a picture of this piece of equipment can be found in Figure B.7c. The settings used for bonding are: power 100% and exposure time 1 minute per surface. This method is more time efficient when only one chip has to be bonded, as it only takes 2 minutes. However, when multiple chips are produced at once, the plasma oven can expose them all at the same time.

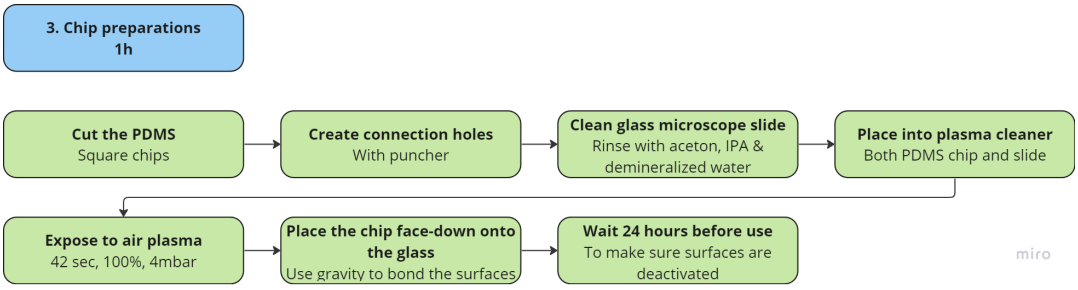

Figure B.12: A schematic of the soft lithography production process.

(a) Chamber during air plasma exposure (indicated by the purple glow). **(b)** Chamber during oxygen plasma exposure (indicated by the grey glow).

Figure B.13: Difference in colour between air and oxygen plasma exposure in the Diener Electronics Femto Low-pressure plasma system.

B.5.1. Gold electrode

In order to generate electro-osmotic flow, a potential has to be applied over the working fluid. As the electrical current causes electrolysis of the solvent, bubbles will form during the operation of the electro-osmotic flow and can cause the connection between the electrodes to break. Therefore, it is imperative that these bubbles move out of the flow direction. This can be achieved by incorporating a lg-separator as shown by Heuck and Staufer [14]. They show that in a tapered microchannel the bubble moves towards the wider side away from the electrode. The established design criteria have been implemented in the design of the microfluidic device.

To facilitate the potential that has to be applied, gold electrodes with a thickness of ~ 200[nm] have been incorporated into the chip design. These gold electrodes are deposited using a sputter coater (JOEL, JFC-1300 auto-fine coater) that has been masked with a 3D-print. The results of this process can be found in Figure B.14.

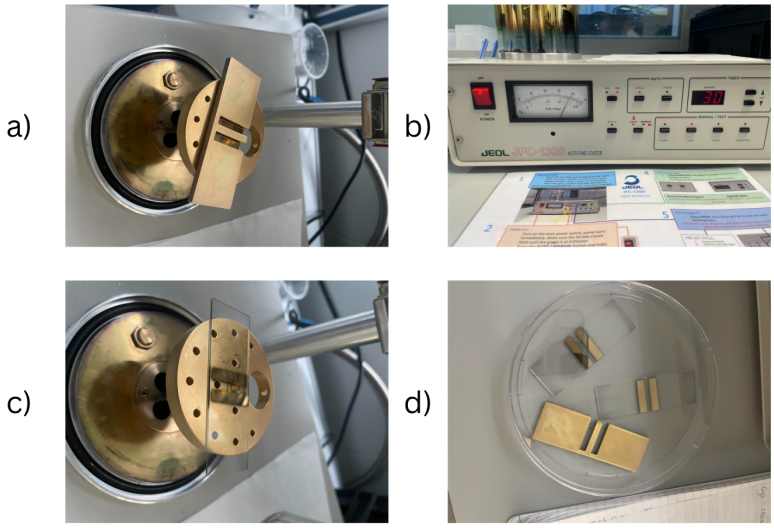

Figure B.14: The steps for creating the gold electrodes. **a)** The microscope slide together with the 3D-printed shield are placed in the JEOL JFC-1300 auto fine coater. **b)** The sputter coater is turned on and the cycle with 40mA 54s is loaded. **c)** The 3D-print is removed from the fine coater, showing the formed electrodes. **d)** Two microscope slides that are ready to be bonded to a PDMS stack.

It is commonly known that gold does not have a high bonding strength to both glass and PDMS surfaces. This causes two problems for the microfluidic system: washing away of the electrode at the glass-gold interface during operation (see Figure B.15) and leaking at the gold-PDMS interface at higher pressures.

Figure B.15: Optical microscope images of the sputter coated gold electrode after flushing of the microfluidic system. It can be seen that in regions where fluid flows over the electrode, the gold is removed.

Firstly, to promote the bond between glass and gold, typically an intermediate layer is deposited based on titanium or chromium [15–17]. As no facilities were available within our department to deposit a layer of titanium or chromium, these layers have eventually been deposited at the Kavli laboratory of Delft University of Technology using a Temescal FC-2000 e-beam evaporator. The titanium layer was deposited with a thickness of 20 nm and the gold layer was deposited with a thickness of 100 nm. The resulting slides can be found in Figure B.16.

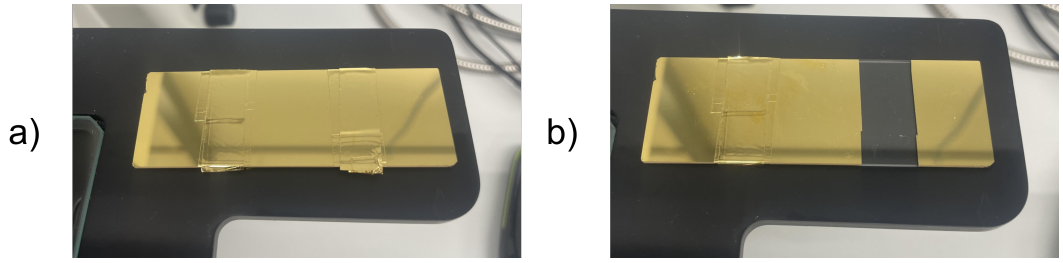

Figure B.16: The result of depositing gold electrodes at Kavli, TU Delft. **a)** Before removing tape. **b)** After removing tape, showing the seperate electrodes.

Secondly, to improve the bonding between the gold and PDMS several solutions have been attempted. Solutions provided in the literature include minimizing the electrode width by Luis *et al.* [18] and introducing carboxyl-terminated and amine-terminated silanes by Casanova-Moreno *et al.* [19]. Furthermore, talks with Alireza Tajeddin (PhD candidate at TU Delft with relevant experience) provided us with options. The following techniques have been assessed by gently peeling the PDMS chip:

1. using standard plasma-oxygen exposure (same precodures as for glass-PDMS bonding);
2. using uncured PDMS between the surfaces;
3. using chemical functionalization. Two different chemicals have been introduced: 1-octanethiol (as this was readily available in the chemistry lab) and 6-mercapto-1-hexanol.

In the end, methods 1) and 2) did not prove effective as only minimal peeling force breaks the bond between the gold and the PDMS. Furthermore, 1-octanethiol also did not provide any benefit in bonding strength. However, 6-mercapto-1-hexanol did. The mercapto group is hypothesized to bond to the gold surface, whereas the hexanol group can bond to the activated PDMS surface. During peeling tests, it was found that the gold-PDMS bonding is stronger than the titanium-glass bonding. In order to better quantify the bonding strength, further experiments are necessary in which the pressure gradually increases until failure. However, due to time constraints these have not been performed during this thesis project.

Procedures
The gold surface is first rinsed with IPA and demineralized water and then blown dry with filtered nitrogen gas. Then it is exposed to air plasma using a plasma gun for 1 minute. Thereafter, $5\mu L$ of 6-mercapto-1-hexanol is deposited on the gold surface and left there for 3 hours. Next, 6-mercapto-1-hexanol is removed by rinsing with IPA and blowing dry using filtered nitrogen gas. Lastly, the demolded PDMS is exposed to air plasma for 25 seconds (Diener Electronic GmbH & Co, FEMTO Low-pressure plasma system). The functionalized gold & activated PDMS surfaces are gently placed on top of each other and placed in an oven at 70°C for 1 hour to promote bonding. All procedures using 6-mercapto-1-hexanol were performed within a fume hood, as it is flammable and leaves a potent smell.

B.6. Test setup

The test setup that has been developed to carry out the experiments can be found in Figure B.17. The goal was to create two flow principles: electro-osmotic and hydrostatic pressure. The electro-osmotic flow is driven by a Delta Elektronika power supply in constant voltage mode. The hydrostatic pressure is generated by a custom test setup. To capture the behavior of liposomes inside the system, the microfluidic chip is mounted on an optical microscope (Motic BA310MET).

The whole setup can be divided into different parts, each with their own function:

- Microscope, to observe the behaviour of the liposomes inside the system;
- Voltage source, to induce electro-osmotic or electro-pherotic flow;
- Customer pressure setup, to generate the hydrostatic pressure to cause flow, deformation and trapping of the liposomes;
- Connection parts, to connect the reservoirs to the microfluidic chip;

- Mounting parts, to ensure the microfluidic chip stays stationary during operation.

More details on the microscope and the customer pressure setup can be found in subsection B.6.1 and subsection B.6.2, respectively.

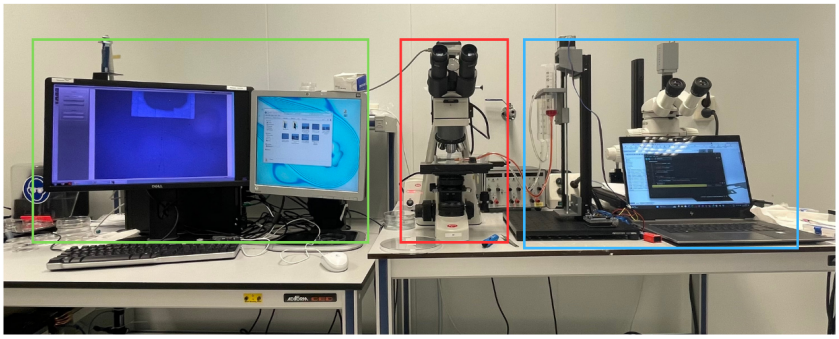

(a) Complete overview containing the computer for monitoring and storing image (green), microscope focused on the microfluidic chip (red) and custom hydrostatic pressure mechanism (blue).

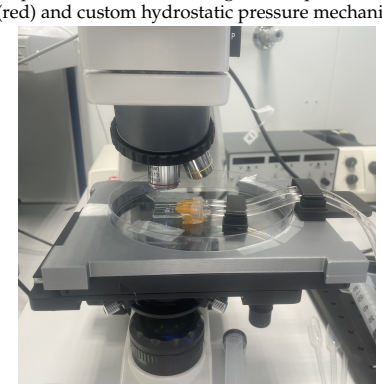

(b) Photo showing the mounting parts: Black clips and white tape.

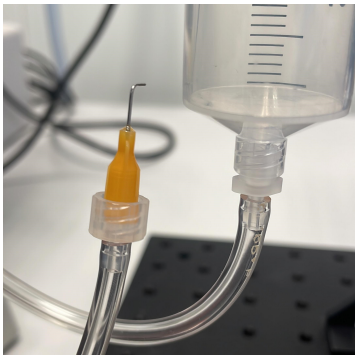

(c) Photo showing the connection parts: Luer lock connections (Darwin Microfluidics, SKU: MF-45518-02 & SKU: ID-P-858), tubing (Darwin Microfluidics, SKU: SA-ACF00005) and bend dispenser tips (Nordson EFD PN: 7018316).

Figure B.17: Photos of the test setup.

B.6.1. Microscope

Optical microscope

To gather information on the movement of liposomes within the microfluidic system, an optical microscope (Motic BA310MET) was used. On top of this microscope, a camera (Moticam A2MP) is mounted that captures the images and transfers a live feed to the computer. Because tubes that connect to the microfluidic chip might exert some force which can cause the chip to move while operating the pressure mechanism, it is important to secure both the microfluidic chip and the tubes. In order to achieve this, several measures have been taken; such as tape, clips and 3D printed components, an overview of these parts can be found in Figure B.18.

(a) Motic BA310MET

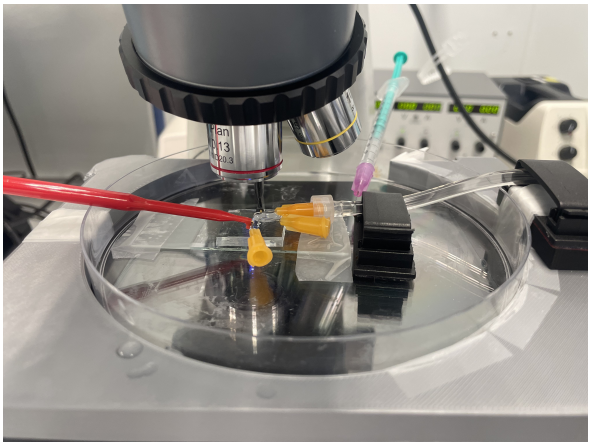

(b) Zoom-in on the microscope plate with the mounted petridish, microscope slide, tubes and clips.

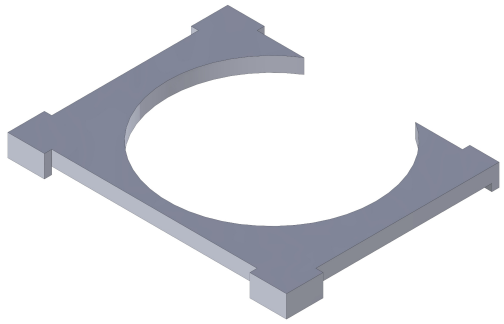

(c) The custom 3D-printed petridish holder that is attached to the microscope plate.

(d) The clips used to secure the tubing.

Figure B.18: Pictures of the microscope setup.

Fluorescent microscope

Later experiments used a fluorescent microscope to better capture the behavior/deformation of the liposomes. The model used was a Nikon Eclipse Ti2 (Nikon Instruments Inc.), a screenshot of the setup, as well as the newly designed mounting parts, can be found in Figure B.19.

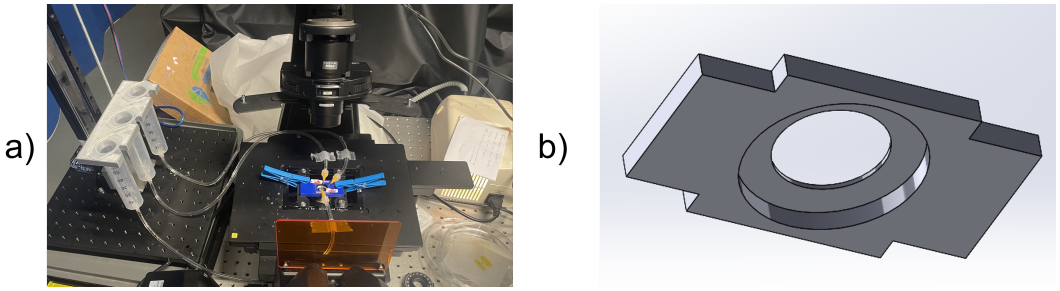

Figure B.19: Fluorescent setup used during experiments. **a)** A photo of the setup, with on the left the customer pressure mechanism and a sample mounted to the microscope. **b)** Screeenshot of Solidworks design showing the customer sample holder.

B.6.2. Custom pressure design

In order to generate pressure to drive flow in the microfluidic system, different solutions have been evaluated. During the literature review, it was found that the dominant strategies for generating flow in microfluidics are hydrostatic pressure, syringe, or centrifugal. As the pressure necessary to move the liposomes through the trap was estimated to be less than a few kPa in section 2, hydrostatic pressure was the simplest solution. The resulting design can be found in Figure B.20. It consists of a Thorlabs base plate to which an extrusion profile is mounted vertically. To create vertical movement, a stage is designed that contains a linear guide (MGN12H), a screw thread M6, a stepper motor (Nema 17), Arduino UNO, Arduino Motor Shield Rev3, a motor coupling, 2 ball bearings, and 3 custom 3D printed connection parts (see Figure B.20c to Figure B.20e). Detailed technical drawings of custom 3D parts can be found in section B.7. The code used to operate the Arduino module and thus the linear stage can be found in subsection B.6.3. Within this code, it is possible to change the speed at which the stepper motor moves and serial commands can be sent to move the stepper motor in either forward or backward direction.

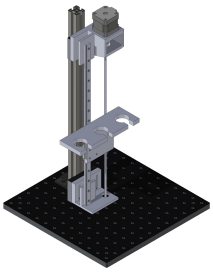

(a) Design of the complete assembly showing Thorlabs parts, 3D-printed parts and linear stage components.

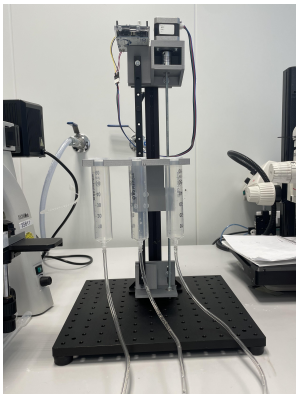

(b) physical pressure setup.

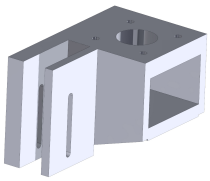

(c) 3D-printed top connection that connects the linear guide, stepper motor and coupling.

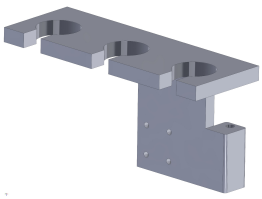

(d) 3D-printed coupling piece that hold the microfluidic reservoirs, connects the linear guide and transfers the rotational motion of the screw thread to vertical movement.

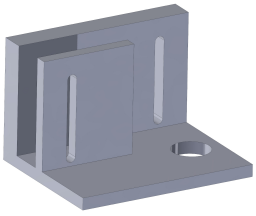

(e) 3D-printed bottom connection that connects the linear stage and screw thread.

Figure B.20: Pessure test-setup as designed and build.

B.6.3. Arduino code

```
#include "Stepper.h"

// Define number of steps per revolution:
const int stepsPerRevolution = 200;

// Give the motor control pins names:
#define pwmA 3
#define pwmB 11
#define brakeA 9
#define brakeB 8
#define dirA 12
#define dirB 13

// Initialize the stepper library on the motor shield:
Stepper myStepper = Stepper(stepsPerRevolution, dirA, dirB);

void setup() {
  // Set the PWM and brake pins so that the direction pins can be used to control the motor:
  pinMode(pwmA, OUTPUT);
  pinMode(pwmB, OUTPUT);
  pinMode(brakeA, OUTPUT);
  pinMode(brakeB, OUTPUT);

  digitalWrite(pwmA, HIGH);
  digitalWrite(pwmB, HIGH);
  digitalWrite(brakeA, LOW);
  digitalWrite(brakeB, LOW);

  // Set the motor speed (RPMs):
  myStepper.setSpeed(60);

  // Start serial communication
  Serial.begin(9600);
}

void loop() {
  if (Serial.available() > 0) {
    // Read the serial command until a newline character is received
    String serialCommand = Serial.readStringUntil('\n');

    // Extract the command and number of rotations
    char command = serialCommand.charAt(0);
    int numRotations = serialCommand.substring(1).toInt();

    switch (command) {
      case 'F':
        // Step forward by the specified number of rotations:
        myStepper.step(stepsPerRevolution * numRotations);
        break;

      case 'B':
        // Step backward by the specified number of rotations:
        myStepper.step(-stepsPerRevolution * numRotations);
        break;


      default:
        // Do nothing for other commands
        break;
    }
  }
}
```

B.7. Technical drawings

Below, the technical drawings of the 3D parts can be found.

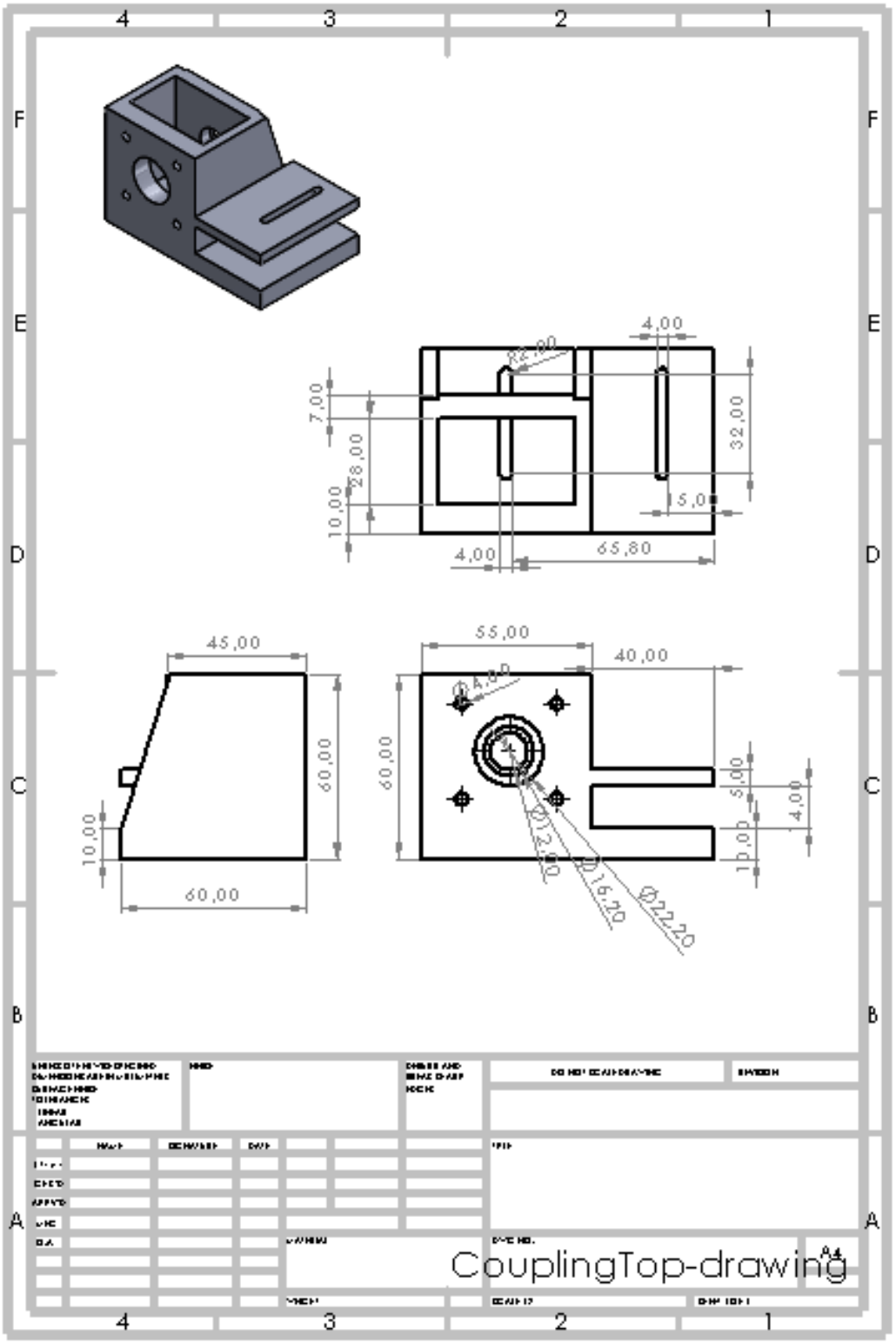

Figure B.21: Technical drawing of the top coupling part of the hydrodynamic test-setup.

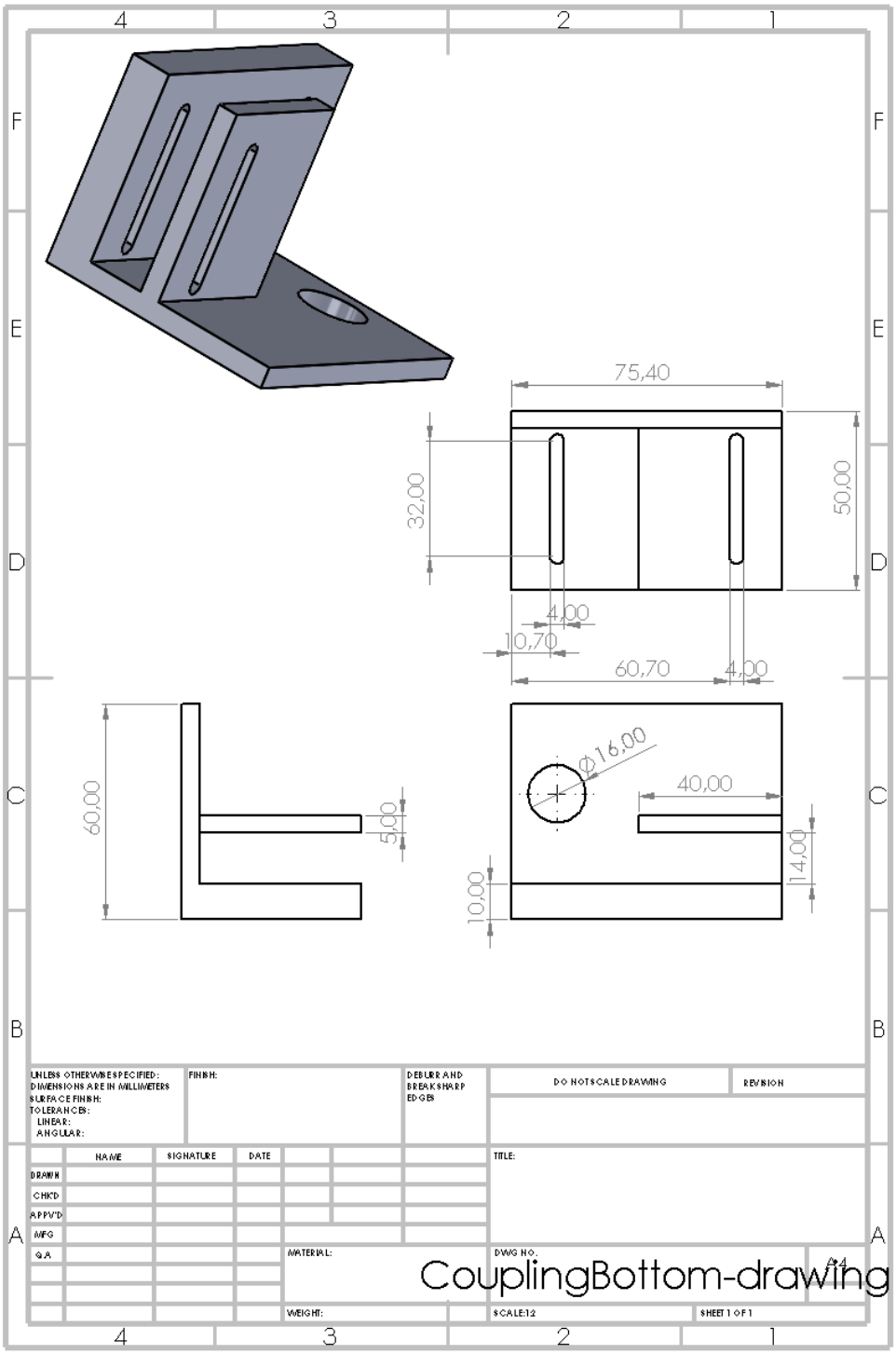

Figure B.22: Technical drawing of the bottom coupling part of the hydrodynamic test-setup.

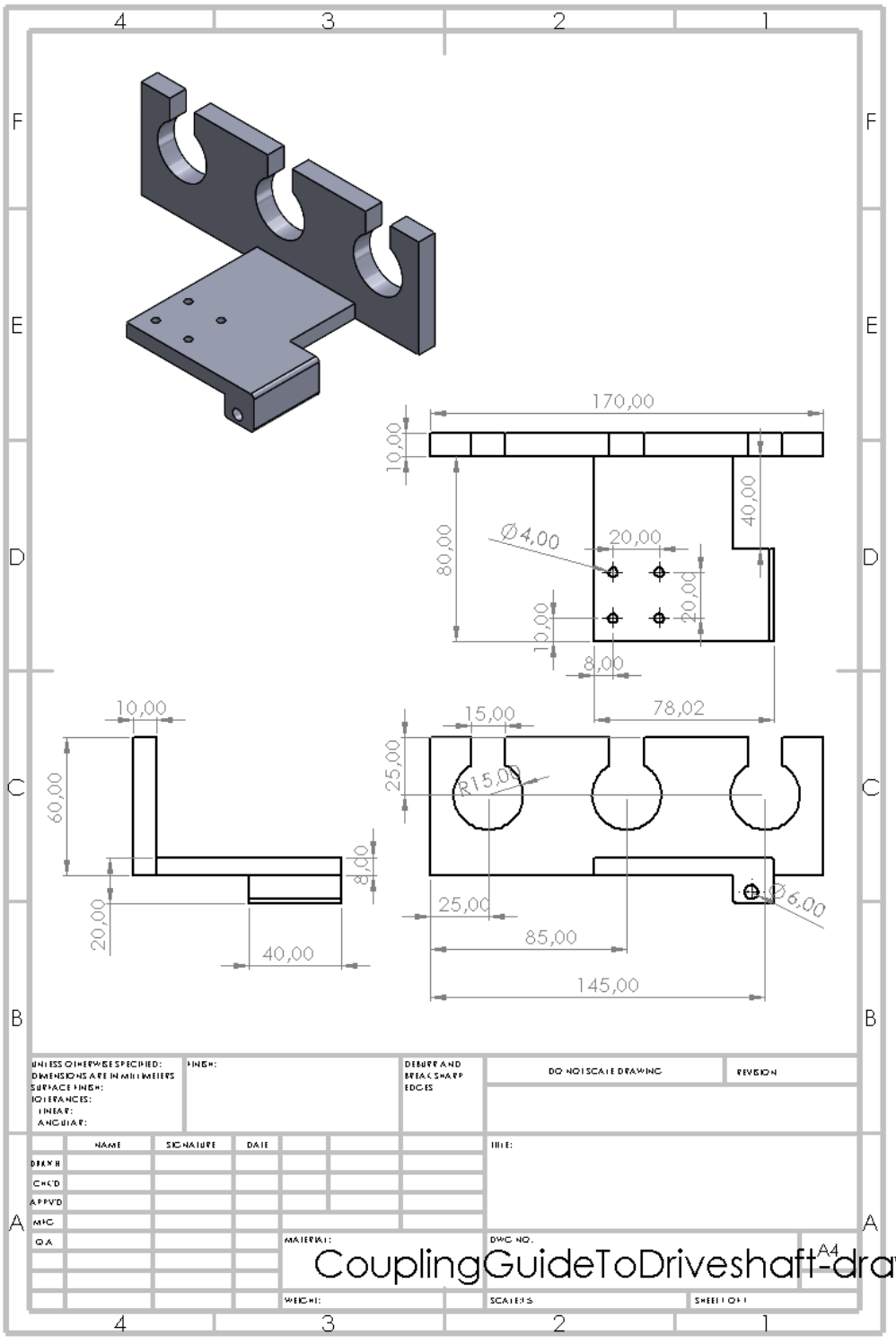

Figure B.23: Technical drawing of the coupling from the linear guide to the drive shaft of the hydrodynamic test-setup.

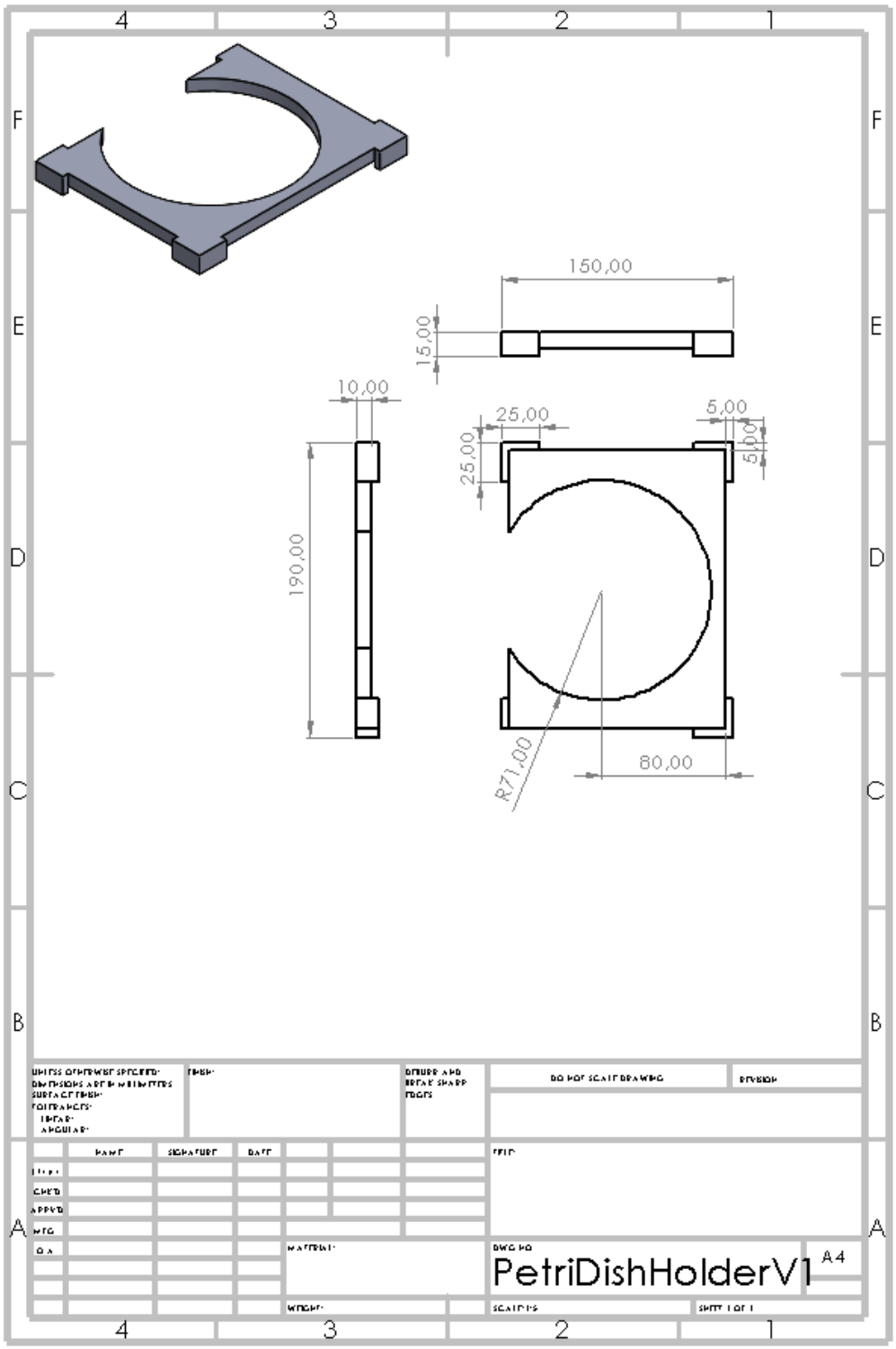

Figure B.24: Technical drawing of the petridish holder of the hydrodynamic test-setup.

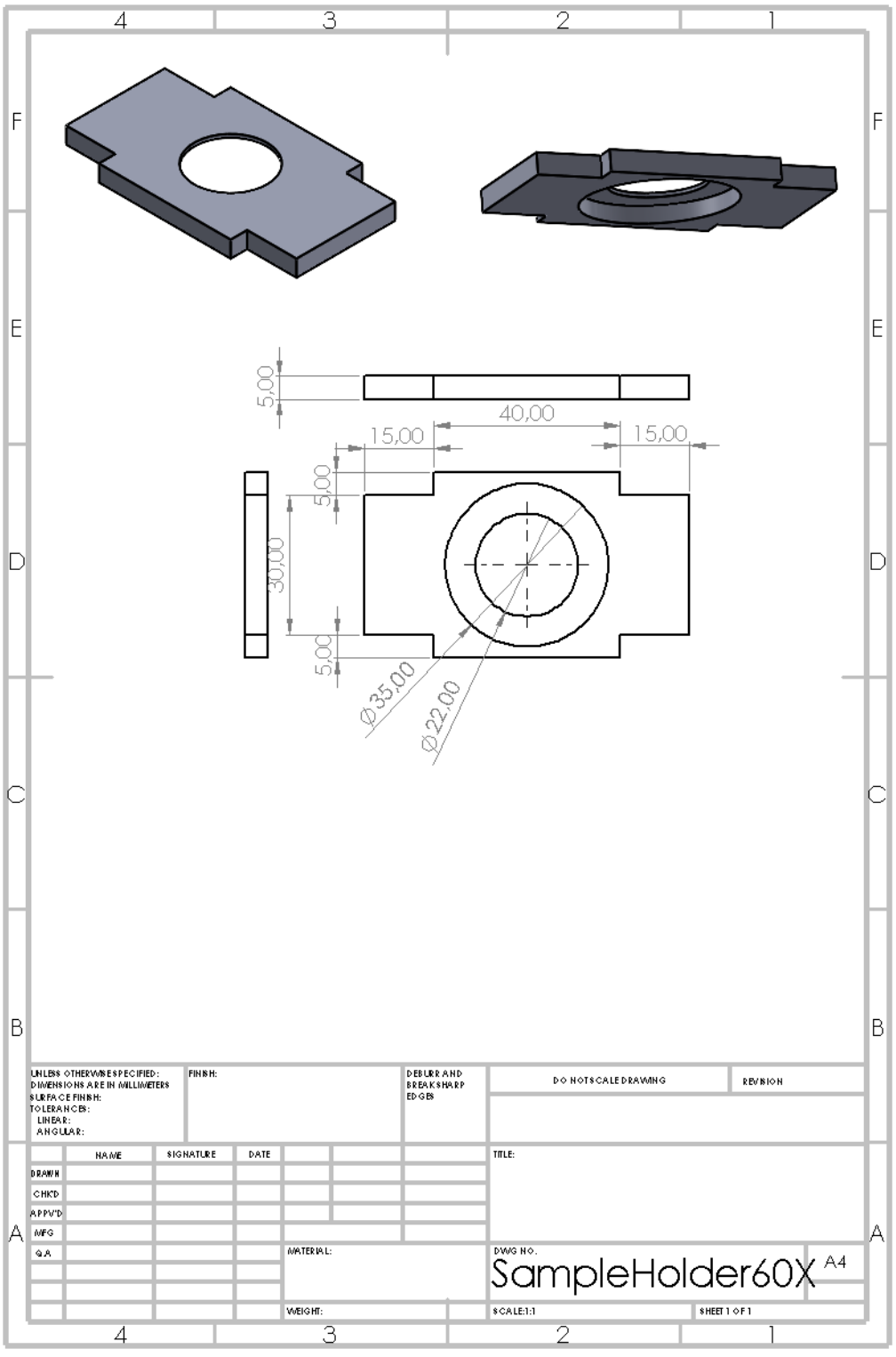

Figure B.25: Technical drawing of the sample holder for the fluorescent microscope.

C

Results

C.1. Production

To validate the quality of the procedures as described in section 4, a test structure has been assessed. Detailed descriptions of these experiments can be found in subsection C.1.1 to subsection C.1.2. The combined results can be found in Table C.1, which shows a difference from design to 2PP-print of 0.010 - 0.303 μm and a difference from 2PP-print to SL of 0.891 - 1.142 μm. These differences should be taken into account for the design. Furthermore, it highlights the importance of measuring the final width of the trap during experiments.

Table C.1: Quality measurements of the production process. Averages for n=5.

Designed feature size	2PP print	Δ Design - 2PP	Soft lithography	Δ 2PP - SL
0.2 μm	1.113 μm	0.913 μm	2.061 μm	1.861 μm
0.5 μm	1.134 μm	0.634 μm	2.010 μm	1.510 μm
1 μm	1.063 μm	0.063 μm	2.168 μm	1.168 μm
2 μm	1.990 μm	0.010 μm	4.017 μm	2.017 μm
3 μm	2.986 μm	0.014 μm	4.786 μm	1.786 μm

C.1.1. 2PP

In order to determine the resolution that could be achieved with the 2PP printing process, a test structure was designed (see Figure C.1a) and imaged using a Scanning Electron Microscope (SEM). After following the print procedures described in subsection B.2.4, the sample was coated with gold using a sputter coater (JOEL, JFC-1300 auto fine coater) at 20 mA for 20 seconds. The results of the test can be found in Figure C.7 to Figure C.10. From these results, it can be seen that the minimal feature size achieved was around 1 μm, which is close to the theoretical limit of the lateral feature size of 0.595 μm as provided by the manufacturer. However, it is also evident that for prints with a nozzle width of 1 μ m, there is a risk that the nozzle does not connect properly to the brain environment. The quality of prints with feature sizes larger than 1 μ m is good as the deviation between the desired and achieved in order of 0.01 μm, which is mainly caused by inaccuracies caused by measurement procedures. Furthermore, from Figure C.1b, it can be seen that there appear to be defects in the mold. Zooming out Figure C.1c reveals that this was caused by the SEM imaging.

C.1.2. Soft lithography

In order to assess the quality of the soft lithography procedures, a test was carried out with the mold of Figure C.1. After demolding, the PDMS sample was coated with gold using a sputter coater (JOEL, JFC-1300 auto-fine coater). The results can be found in Figure C.2. It can be seen that there is a general difference between the size of the designed feature and the demolded structure of around 1-2 μm. Furthermore, it can be seen that compared to the 2PP-mold, the corners of the nozzle are more rounded.

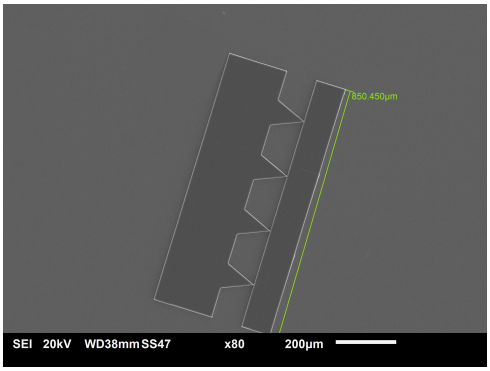

(a) An overview of the printed structure used to assess the 2PP print resolution. Each consequent nozzle had a increasing minimal width.

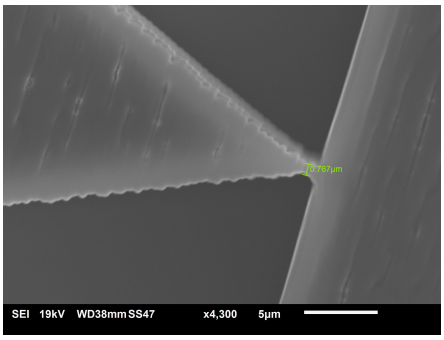

(b) Zoom-in on a nozzle with desired width of 0.5 μm. The width measurement is 0.767 μm.

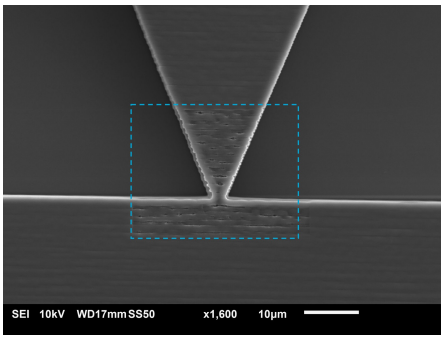

(c) Showing the result of scanning a region of the mold for a longer time period.

Figure C.1: Scanning Electron Microscope (SEM) images of a 2PP test print.

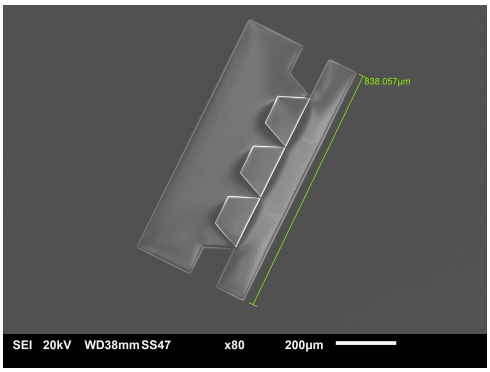

(a) An overview of the PDMS structure used to assess the production quality. Each consequent nozzle had a increasing minimal width.

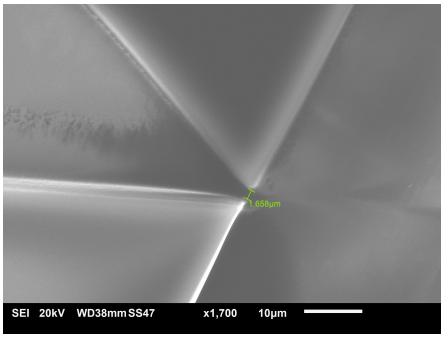

(b) Zoom-in on a nozzle with desired width of 0.5 μm. The width measurement is 1.658 μm.

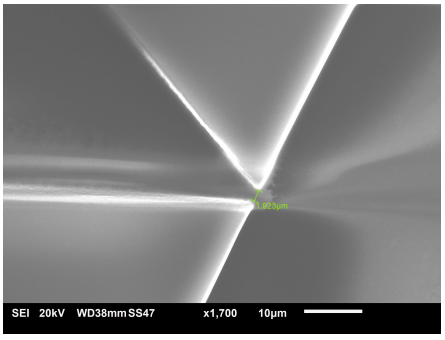

(c) Zoom-in on a nozzle with desired width of 1 μm. The width measurement is 1.923 μm.

Figure C.2: Scanning Electron Microscope (SEM) images of a PDMS test structure.

C.2. Trapping

C.2.1. Burst valve

Before the synthesized liposomes were ready, the functionality of the design was tested using water, which corresponds to the Laplace theory discussed in subsection 2.2. Based on this theory, with the trap width of 15 μ m and surface tension of the water-air interface of 72.8 mN/m, the theoretical expected burst pressure is 4.853 kPa which is reached at a water height of 49 cm. The value of the height at which the burst occurred was estimated to be around the same height, although it has not been measured exactly.

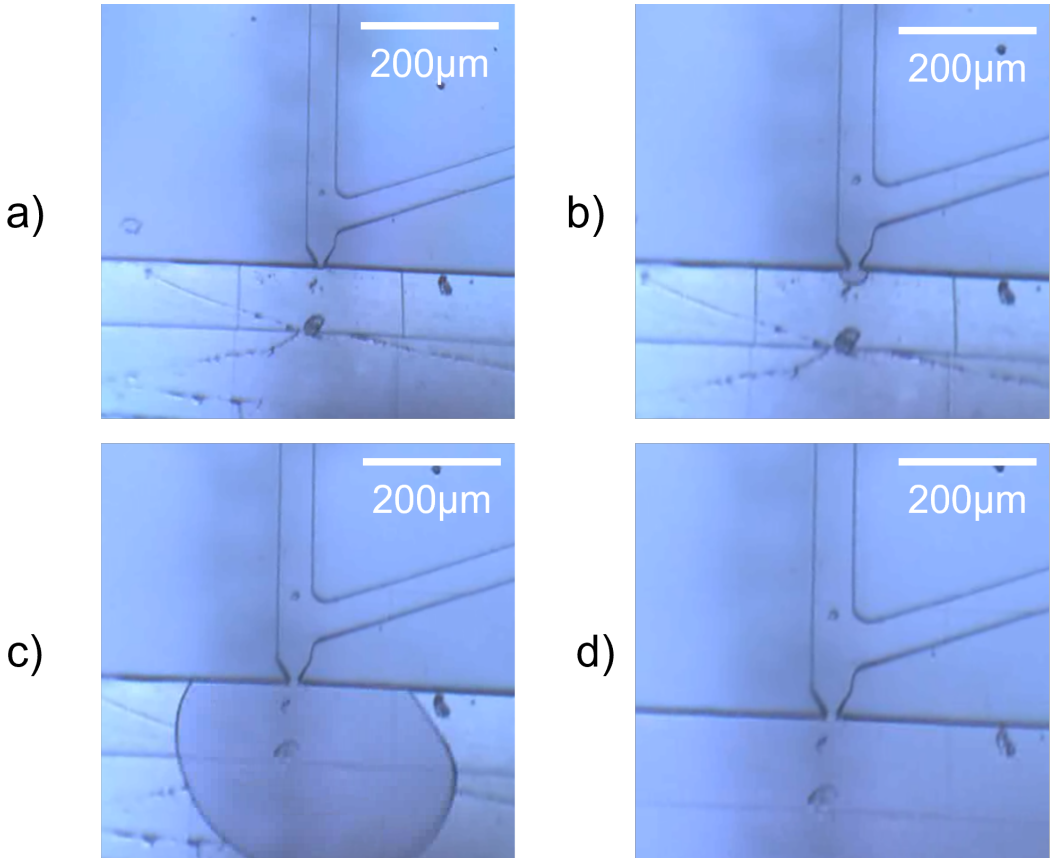

Figure C.3: Optical microscope images of the burst valve principle. Sub-figures a-d are recorded at t=0sec, t=3sec, t=4sec, t=5sec respectively.

Polystyrene beads

Next, the design was tested with standard 8.0 μm polystyrene microbeads (polystyrene monodisperse microparticles, Sigma-Aldrich). Testing with polystyrene beads at the nozzle resulted in better understanding of the systems behavior, as well as how to effectively load the particles into the system. First, just the water is loaded into the system and in order to inject the microbeads into the system, a syringe was inserted into the tubing. By increasing the pressure over both the inlet and outlet, microfluidic beads could be trapped in the nozzle.

Electro-phoresis

By using charged lipids and (non-charged) polystyrene microbeads, the different flow principles could be demonstrated. The results can be found in Figure C.4. First, a 20V potential was applied over the channel using a voltage generator, which caused the charged lipids to move. Next, the potential difference was removed and the hydrostatic pressure difference over the channel was increased, causing both the lipids and the microbeads to move.

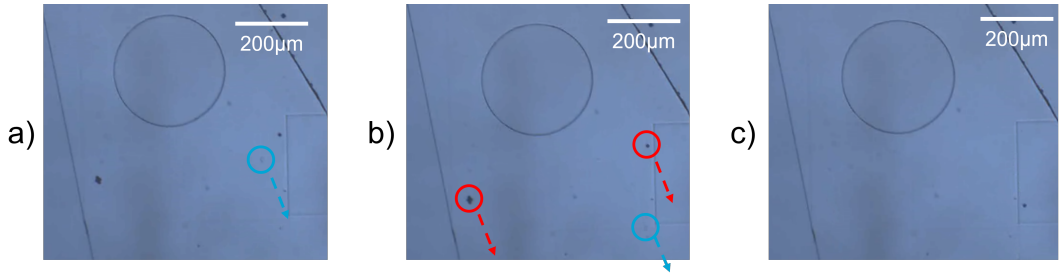

Figure C.4: Optical microscopy images of the flow in the microfluidic system. **a-b)** After turning on the potential, it can be seen the charged lipids (encircled with blue) start to move. **b-c)** After turning off the potential and increasing the pressure it can be seen both the polystyrene lipids (encircled in red) and the charged liposomes (encircled in blue) start to move.

C.3. Multipore

C.3.1. Testing with polystyrene beads

First, the design was tested using polystyrene beads. The results are promising, as the filling of pores occurs deterministically, as expected. Note that there appear to be multiple beads in each nozzle, which have been stuck in previous tests.

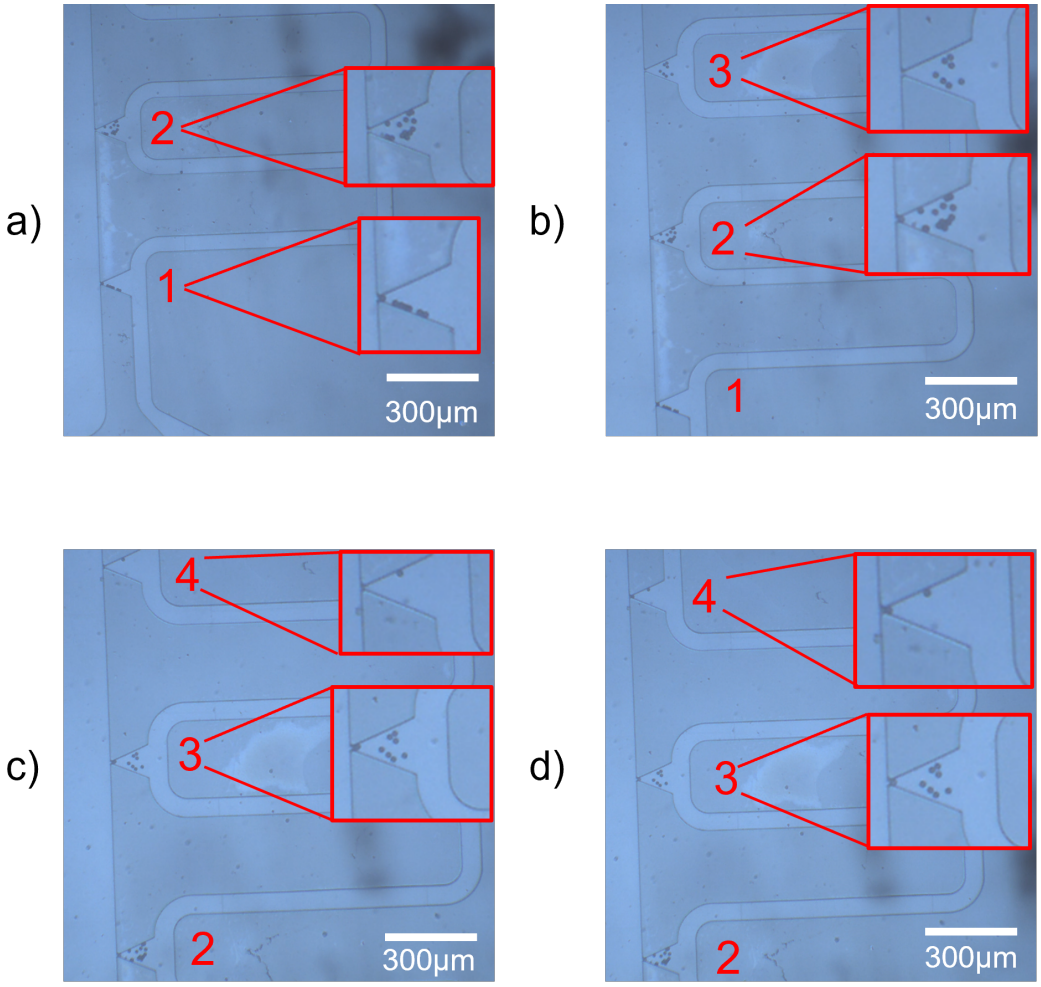

Figure C.5: Results of the multipore experiment, images taken over time. Time between each screenshot is around 15 seconds. Zoom-in on the nozzle show them being filled deterministically.

C.3.2. Testing with liposomes

Next, the design was tested with liposomes; see Figure C.6. Although trapping is effective, it can be seen that the flow is present mainly in the first two nozzles and gradually decreases along the path. This is due to flow leaking through the filled nozzles. Due to these results, the design was altered to the parallel configuration, as found in the paper.

Figure C.6: Results of the multipore experiment, images taken with fluorescent microscope.

C.4. SEM images

C.4.1. 2PP mold

See Figure C.7 to Figure C.10.

C.4.2. Soft lithography

See Figure C.11 to Figure C.14.

C.5. Trapping experiment images

See Figure C.15 to Figure C.16. The images were analyzed using ImageJ software [20]. The width of the channel is calibrated at 50 μm and then the diameter of the liposomes is measured. The liposomes are larger than the focus field of the 60X objective, causing some errors in the measurements. During the videos, the focus is pulled to ensure the best possible measurement is taken.

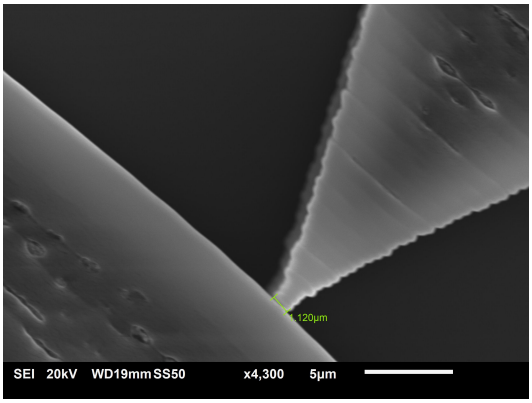

(a) Zoom-in on a nozzle with desired width of 0.2 μm. The width measurement is 1.120 μm.

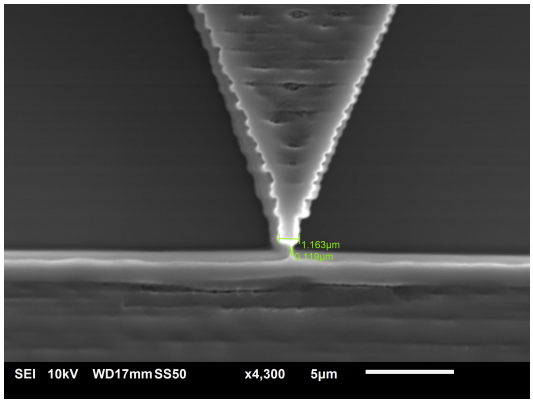

(b) Zoom-in on a nozzle with desired width of 0.2 μm. The width measurement is 1.163 μm.

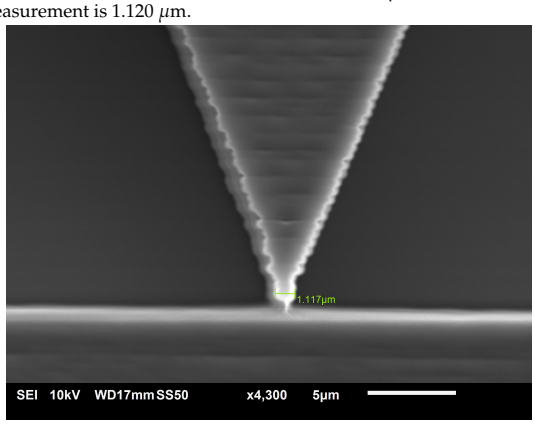

(c) Zoom-in on a nozzle with desired width of 0.2 μm. The width measurement is 1.117 μm.

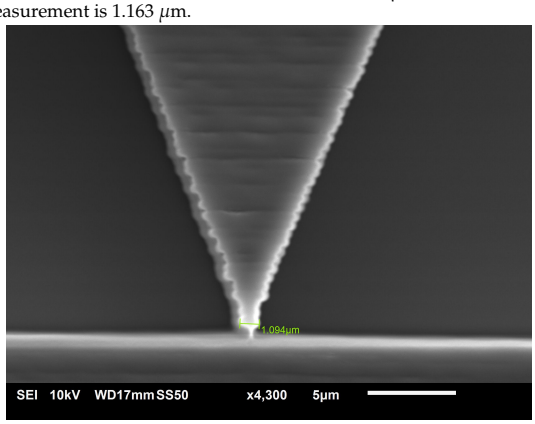

(d) Zoom-in on a nozzle with desired width of 0.2 μm. The width measurement is 1.094 μm.

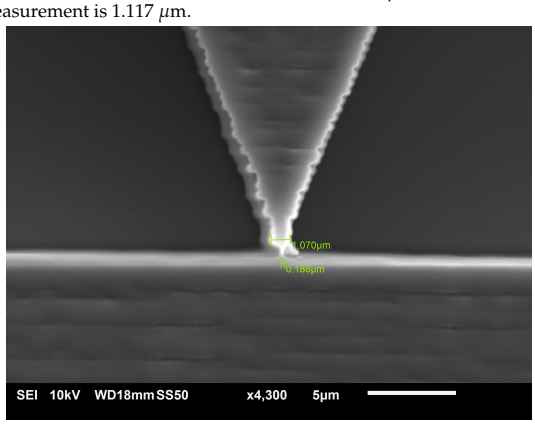

(e) Zoom-in on a nozzle with desired width of 0.2 μm. The width measurement is 1.070 μm.

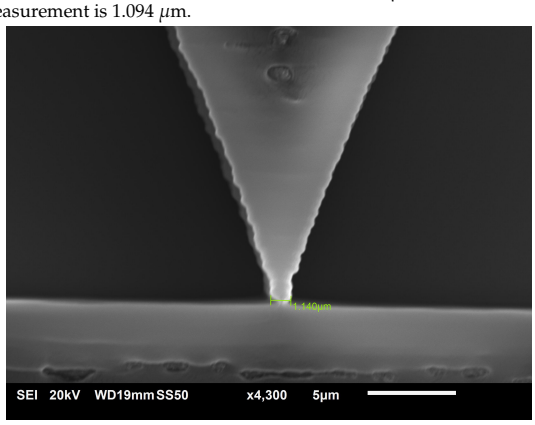

(f) Zoom-in on a nozzle with desired width of 0.5 μm. The width measurement is 1.140 μm.

Figure C.7: Scanning Electron Microscope (SEM) images of a 2PP test print (1/4).

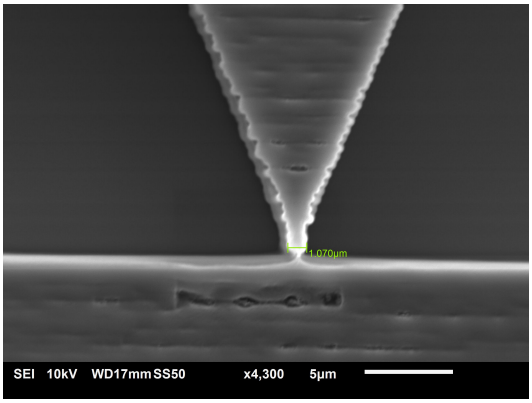

(a) Zoom-in on a nozzle with desired width of 0.5 μm. The width measurement is 1.070 μm.

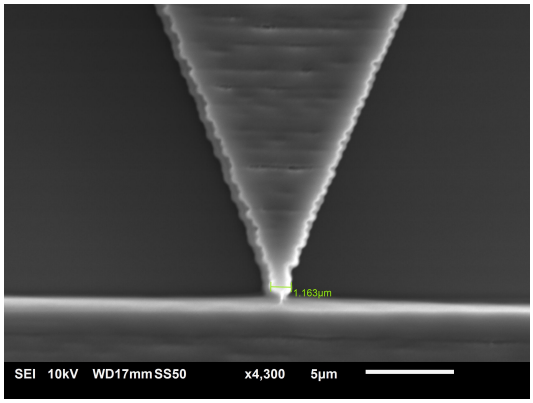

(b) Zoom-in on a nozzle with desired width of 0.5 μm. The width measurement is 1.163 μm.

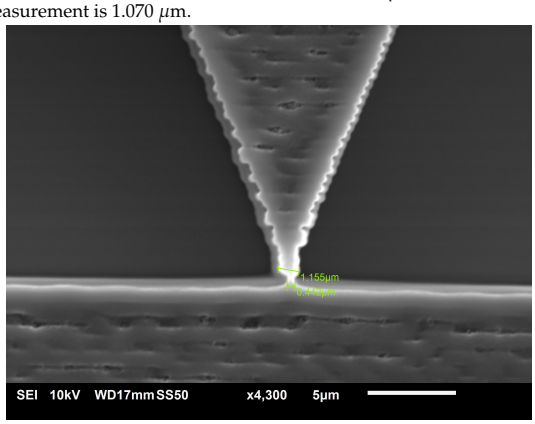

(c) Zoom-in on a nozzle with desired width of 0.5 μm. The width measurement is 1.155 μm.

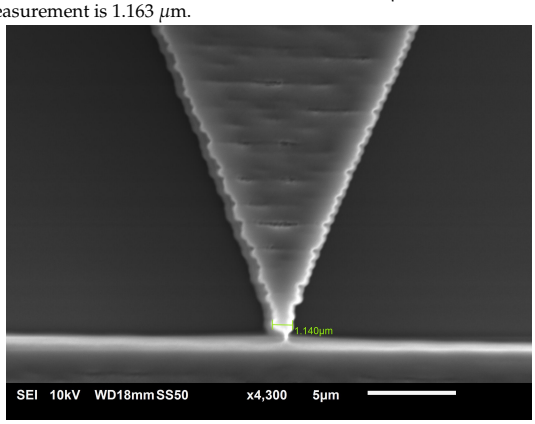

(d) Zoom-in on a nozzle with desired width of 0.5 μm. The width measurement is 1.140 μm.

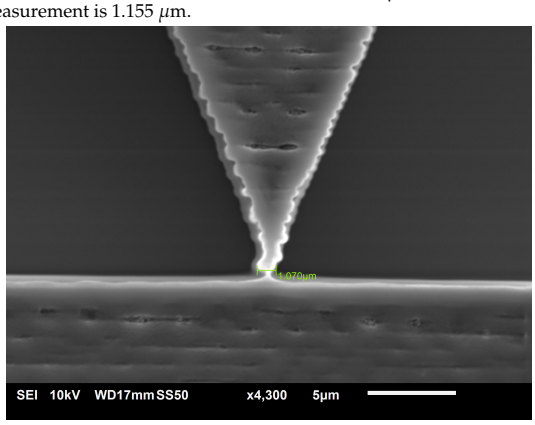

(e) Zoom-in on a nozzle with desired width of 1 μm. The width measurement is 1.070 μm.

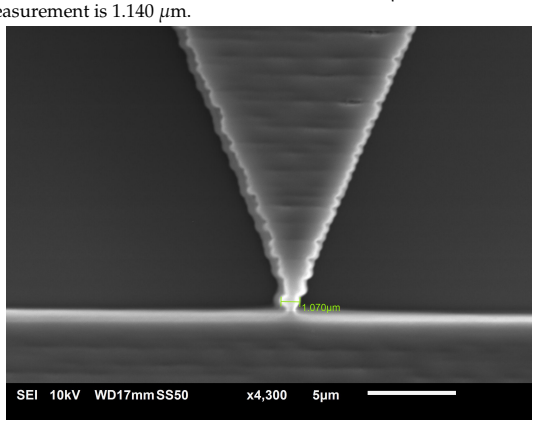

(f) Zoom-in on a nozzle with desired width of 1 μm. The width measurement is 1.070 μm.

Figure C.8: Scanning Electron Microscope (SEM) images of a 2PP test print, continued (2/4).

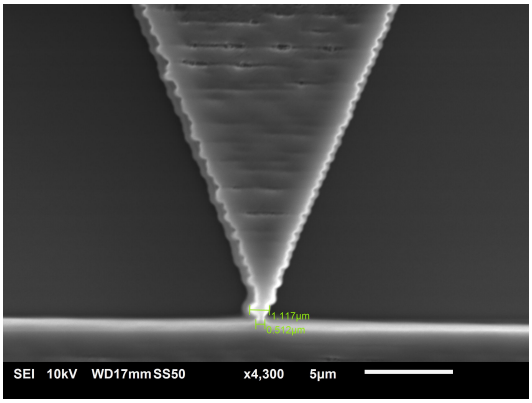

(a) Zoom-in on a nozzle with desired width of 1 μm. The width measurement is 1.117 μm.

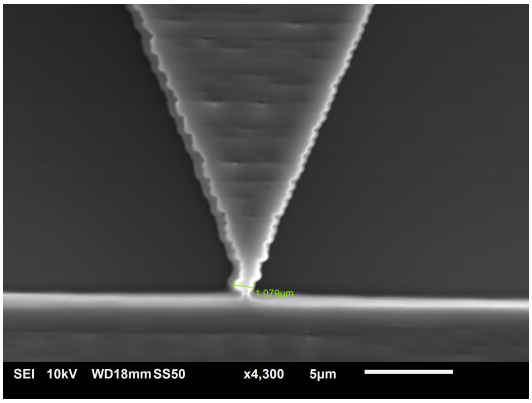

(b) Zoom-in on a nozzle with desired width of 1 μm. The width measurement is 1.079 μm.

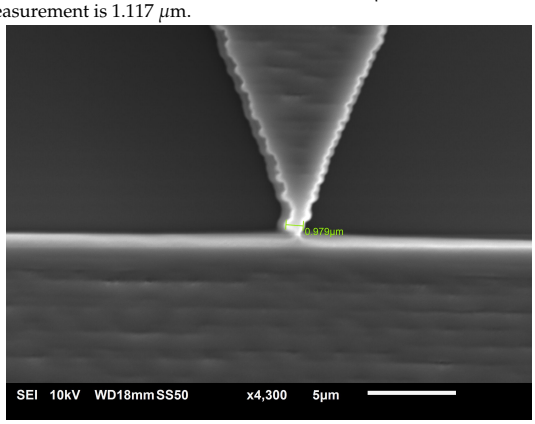

(c) Zoom-in on a nozzle with desired width of 1 μm. The width measurement is 0.979 μm.

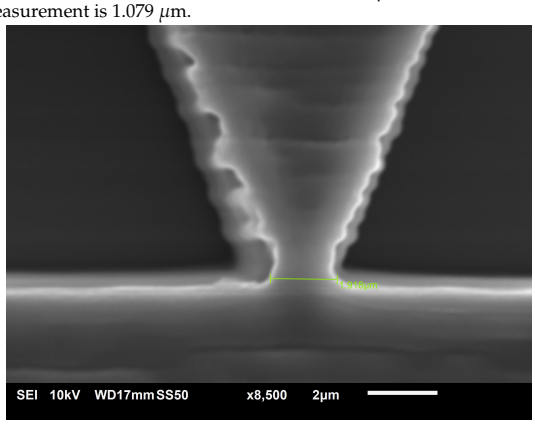

(d) Zoom-in on a nozzle with desired width of 2 μm. The width measurement is 1.918 μm.

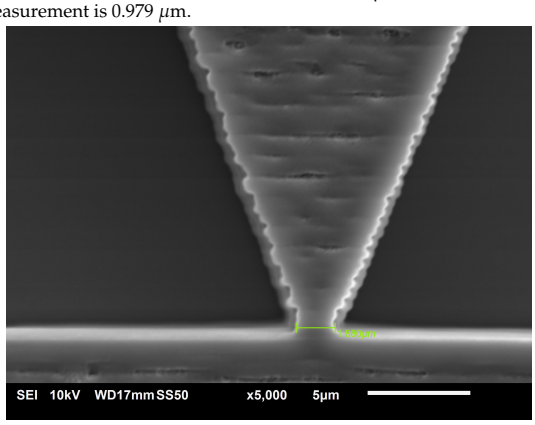

(e) Zoom-in on a nozzle with desired width of 2 μm. The width measurement is 1.880 μm.

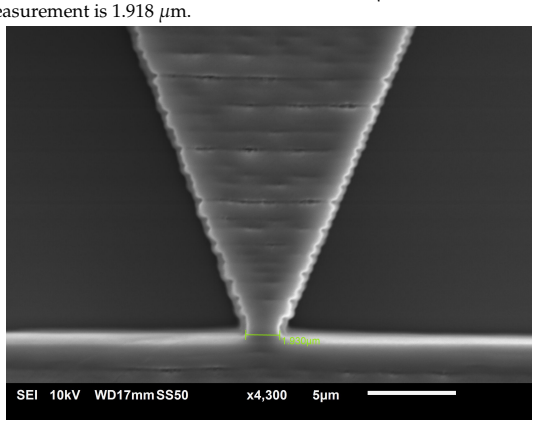

(f) Zoom-in on a nozzle with desired width of 2 μm. The width measurement is 1.930 μm.

Figure C.9: Scanning Electron Microscope (SEM) images of a 2PP test print, continued (3/4).

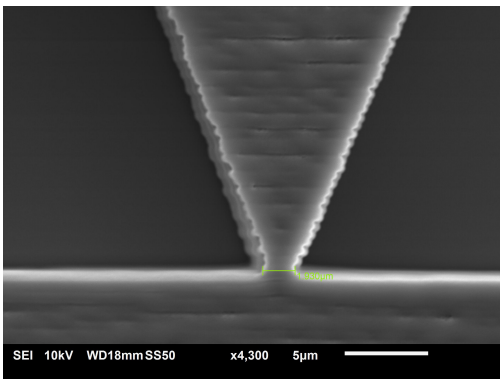

(a) Zoom-in on a nozzle with desired width of 2 μm. The width measurement is 1.930 μm.

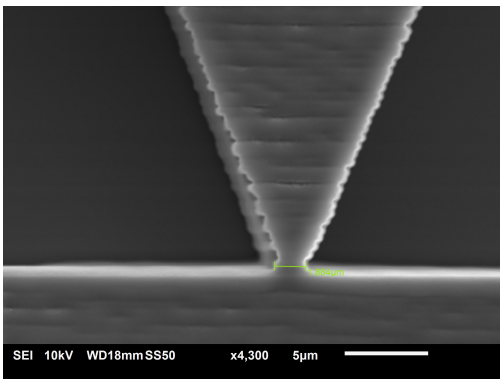

(b) Zoom-in on a nozzle with desired width of 2 μm. The width measurement is 1.844 μm.

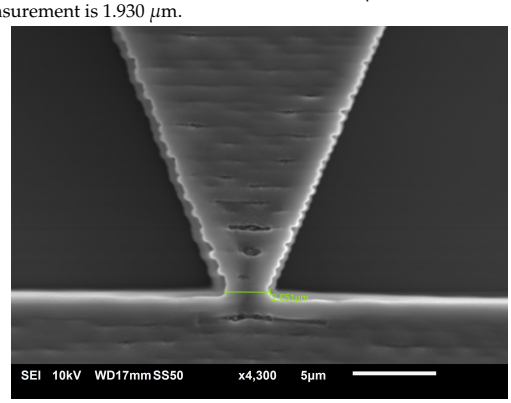

(c) Zoom-in on a nozzle with desired width of 3 μm. The width measurement is 2.651 μm.

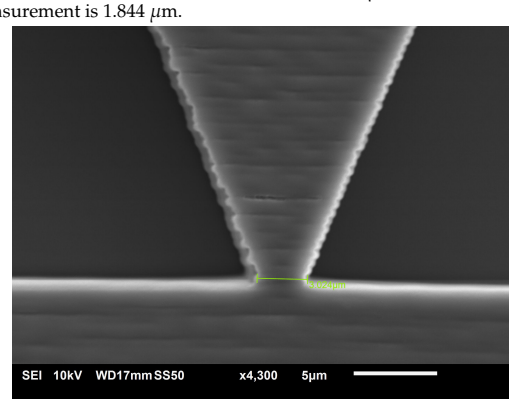

(d) Zoom-in on a nozzle with desired width of 3 μm. The width measurement is 3.024 μm.

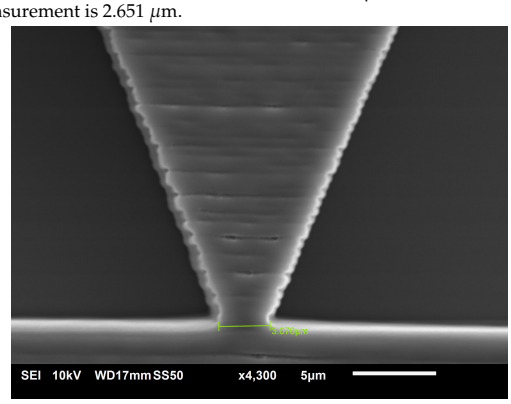

(e) Zoom-in on a nozzle with desired width of 3 μm. The width measurement is 3.070 μm.

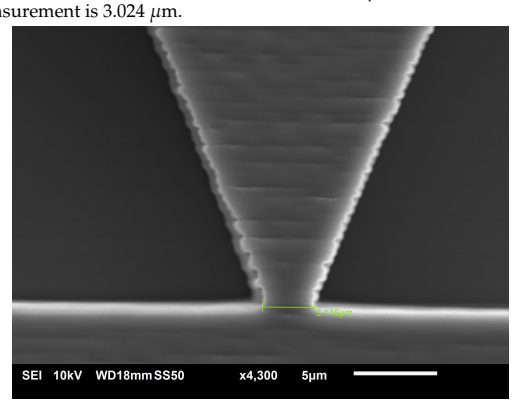

(f) Zoom-in on a nozzle with desired width of 3 μm. The width measurement is 3.116 μm.

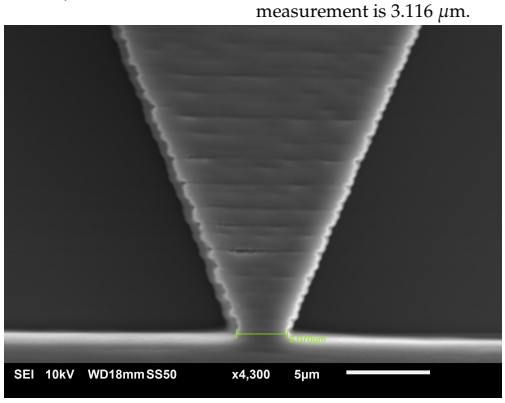

(g) Zoom-in on a nozzle with desired width of 3 μm. The width measurement is 3.070 μm.

Figure C.10: Scanning Electron Microscope (SEM) images of a 2PP test print, continued (4/4).

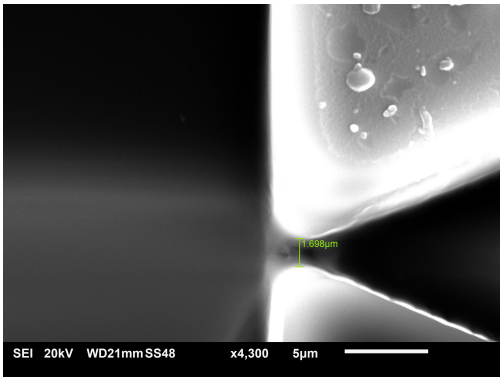

(a) Zoom-in on a nozzle with desired width of 0.2 μm. The width measurement is 1.698 μm.

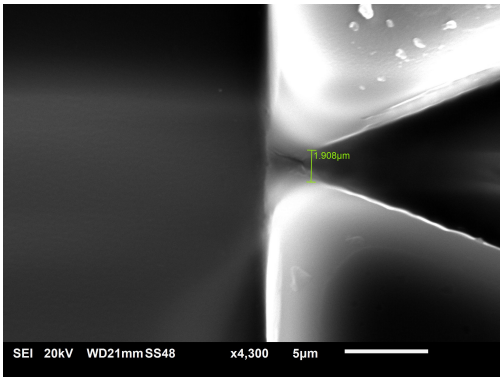

(b) Zoom-in on a nozzle with desired width of 0.2 μm. The width measurement is 1.908 μm.

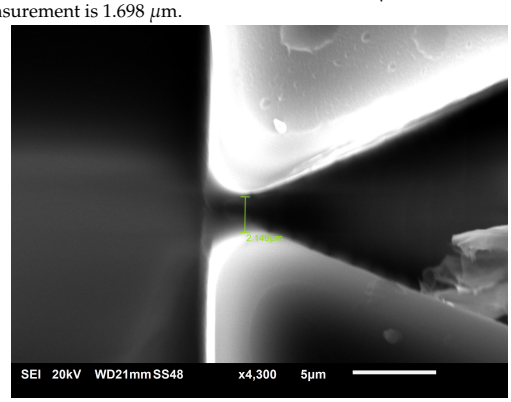

(c) Zoom-in on a nozzle with desired width of 0.2 μm. The width measurement is 2.140 μm.

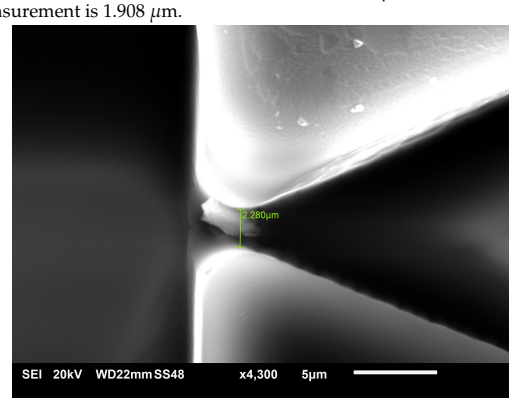

(d) Zoom-in on a nozzle with desired width of 0.2 μm. The width measurement is 2.280 μm.

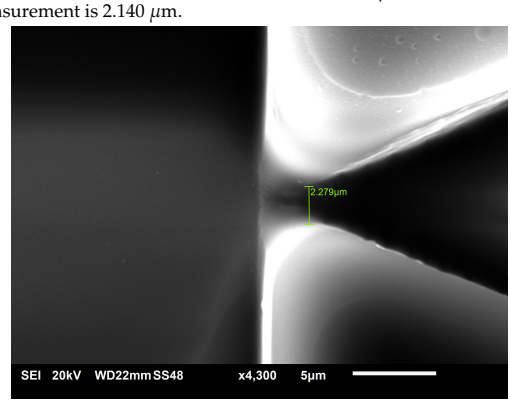

(e) Zoom-in on a nozzle with desired width of 0.2 μm. The width measurement is 2.279 μm.

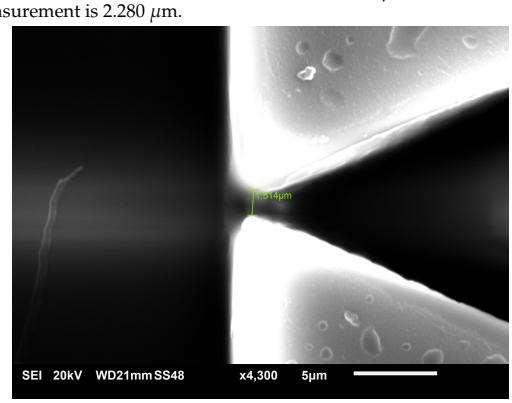

(f) Zoom-in on a nozzle with desired width of 0.5 μm. The width measurement is 1.514 μm.

Figure C.11: Scanning Electron Microscope (SEM) images of a Soft Lithography test (1/4).

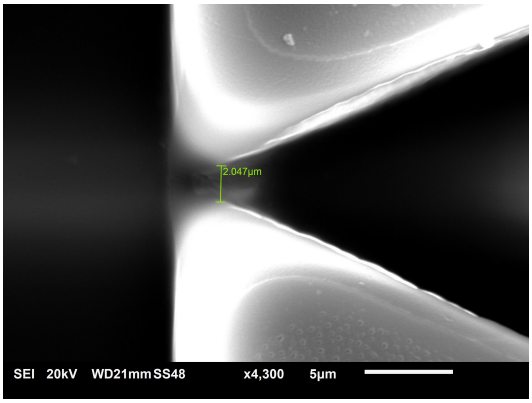

(a) Zoom-in on a nozzle with desired width of 0.5 μm. The width measurement is 2.047 μm.

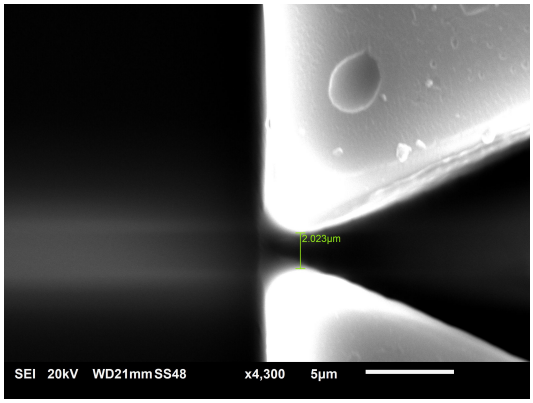

(b) Zoom-in on a nozzle with desired width of 0.5 μm. The width measurement is 2.023 μm.

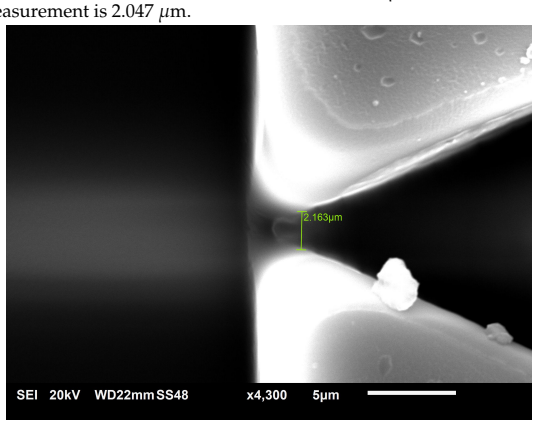

(c) Zoom-in on a nozzle with desired width of 0.5 μm. The width measurement is 2.163 μm.

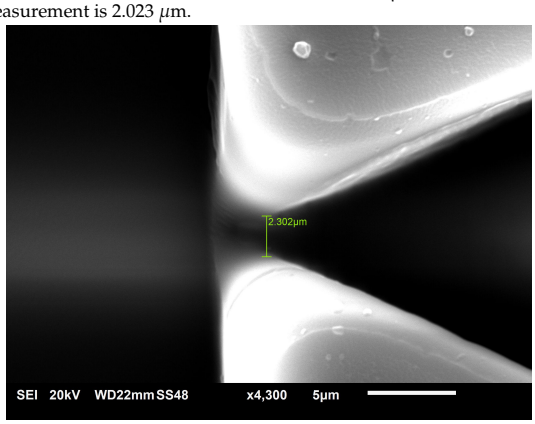

(d) Zoom-in on a nozzle with desired width of 0.5 μm. The width measurement is 2.302 μm.

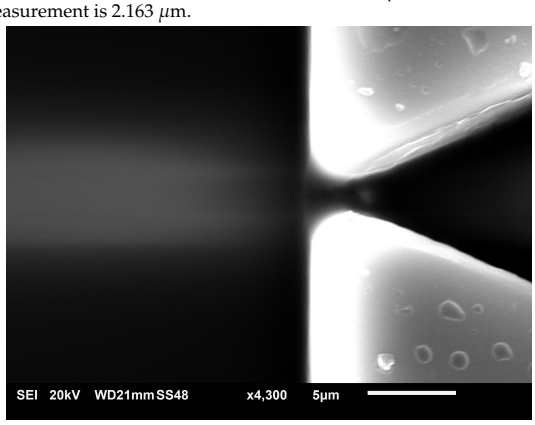

(e) Zoom-in on a nozzle with desired width of 1 μm. The width measurement is 2.093 μm.

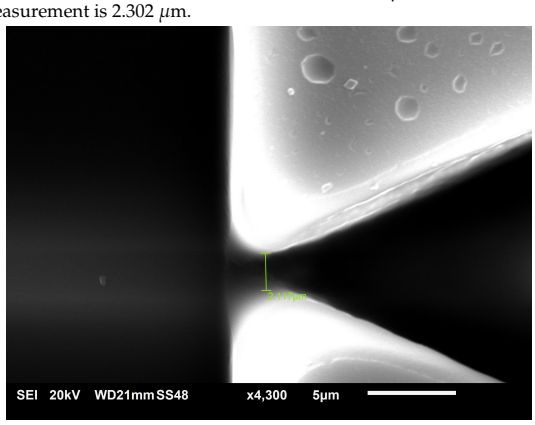

(f) Zoom-in on a nozzle with desired width of 1 μm. The width measurement is 2.117 μm.

Figure C.12: Scanning Electron Microscope (SEM) images of a Soft Lithography test, continued (2/4).

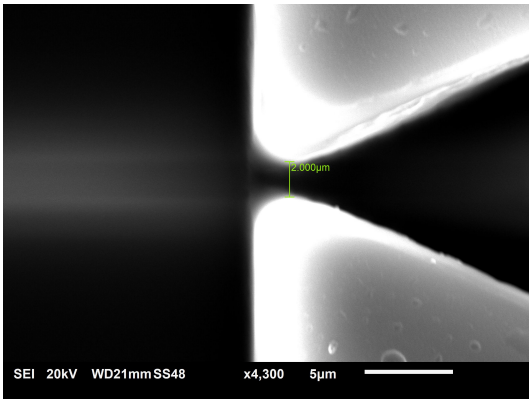

(a) Zoom-in on a nozzle with desired width of 1 μm. The width measurement is 2.000 μm.

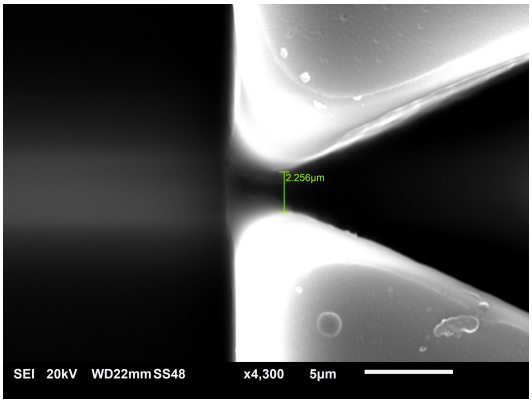

(b) Zoom-in on a nozzle with desired width of 1 μm. The width measurement is 2.023 μm.

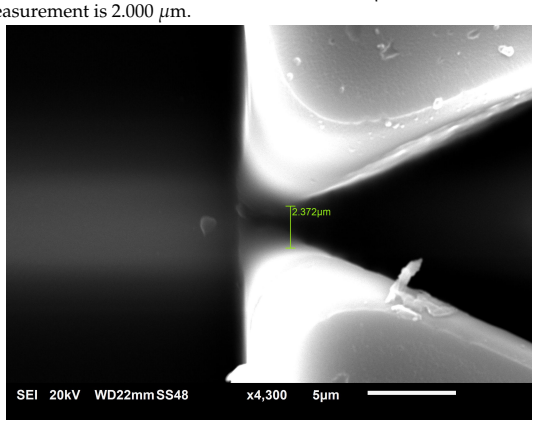

(c) Zoom-in on a nozzle with desired width of 1 μm. The width measurement is 2.302 μm.

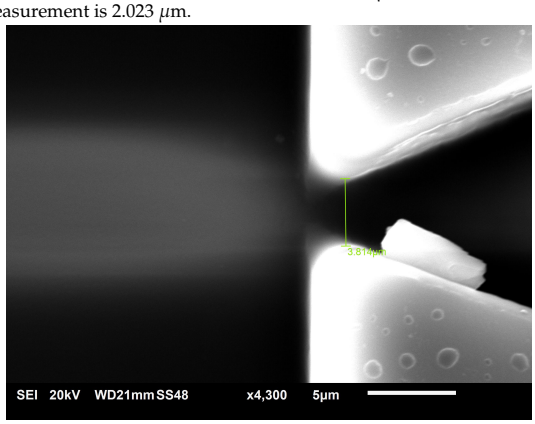

(d) Zoom-in on a nozzle with desired width of 2 μm. The width measurement is 3.814 μm.

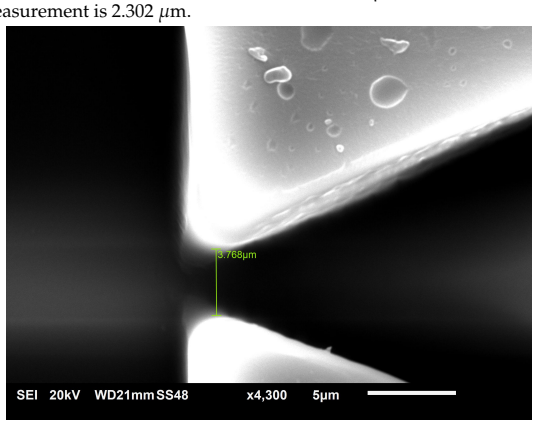

(e) Zoom-in on a nozzle with desired width of 2 μm. The width measurement is 3.768 μm.

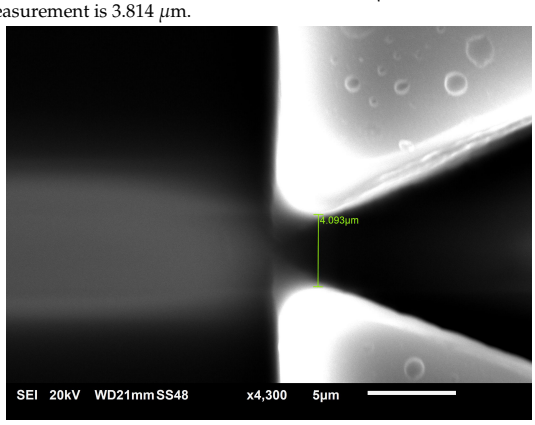

(f) Zoom-in on a nozzle with desired width of 2 μm. The width measurement is 4.093 μm.

Figure C.13: Scanning Electron Microscope (SEM) images of a Soft Lithography test, continued (3/4).

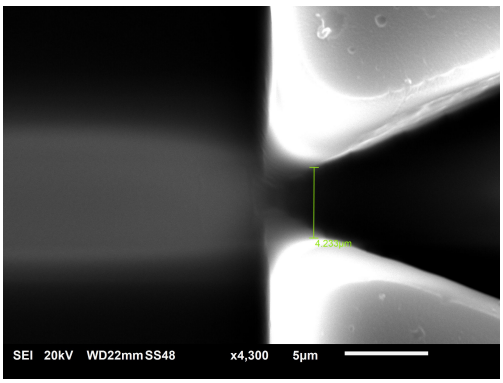

(a) Zoom-in on a nozzle with desired width of 2 μm. The width measurement is 4.223 μm.

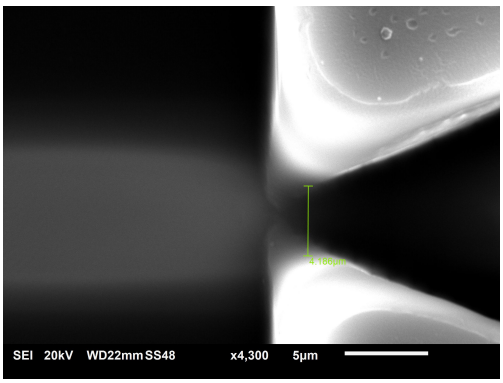

(b) Zoom-in on a nozzle with desired width of 2 μm. The width measurement is 4.186 μm.

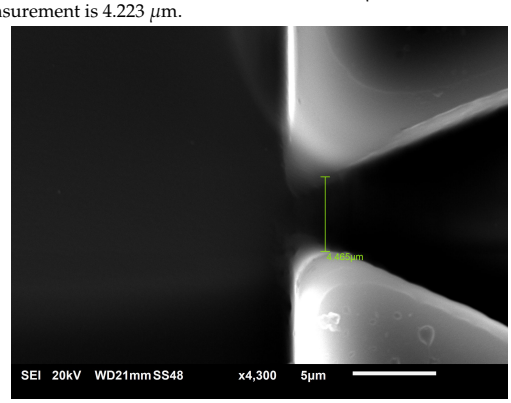

(c) Zoom-in on a nozzle with desired width of 3 μm. The width measurement is 4.465 μm.

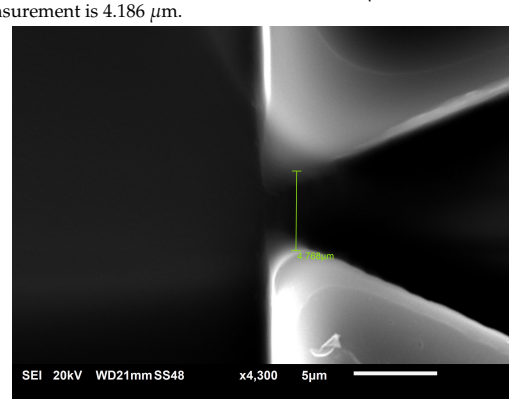

(d) Zoom-in on a nozzle with desired width of 3 μm. The width measurement is 4.768 μm.

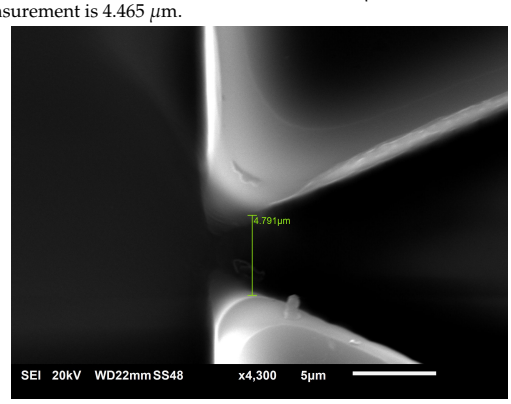

(e) Zoom-in on a nozzle with desired width of 3 μm. The width measurement is 4.791 μm.

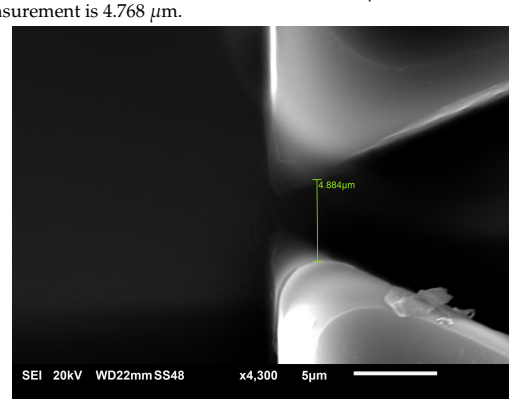

(f) Zoom-in on a nozzle with desired width of 3 μm. The width measurement is 4.884 μm.

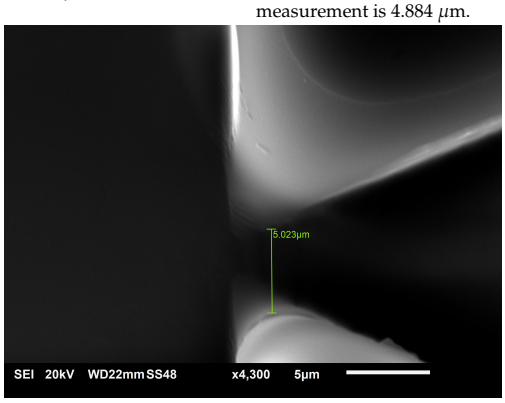

(g) Zoom-in on a nozzle with desired width of 3 μm. The width measurement is 5.023 μm.

Figure C.14: Scanning Electron Microscope (SEM) images of a Soft Lithography test, continued (4/4).

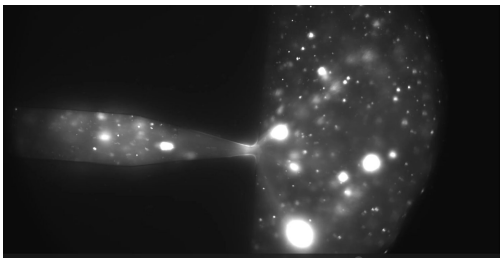

(a) Test 1: release at h = 5 mm. No lysis.

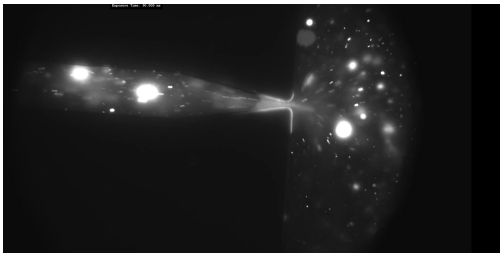

(b) Test 2: release at h = 15 mm. No lysis.

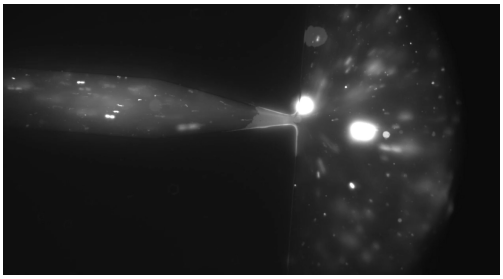

(c) Test 3: release at h = 25 mm. Both no lysis.

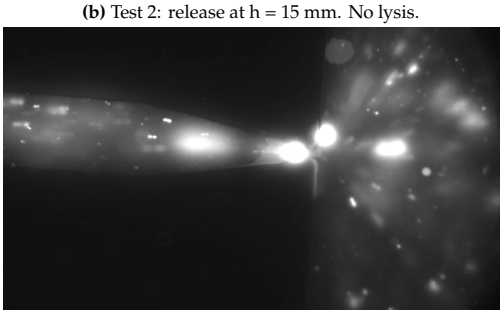

(d) Test 4: release at h = 25 mm. No lysis.

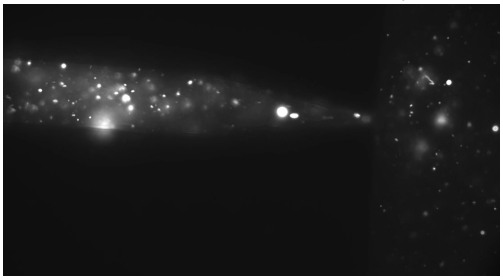

(e) Test 5: release at h = 15 mm. No lysis.

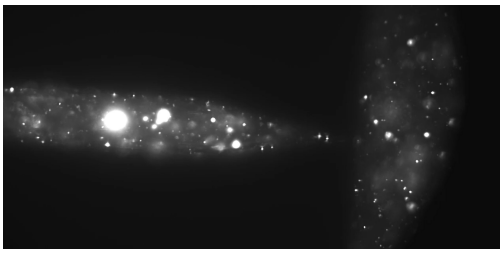

(f) Test 6: release at h = 15 mm. Sample 1. Both no lysis.

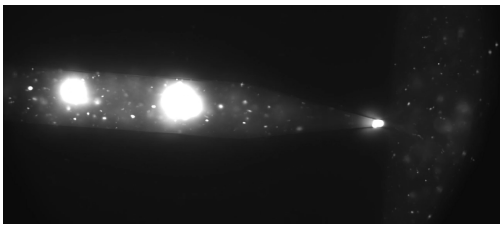

(g) Test 6: release at h = 15 mm. Sample 2. Both lysis.

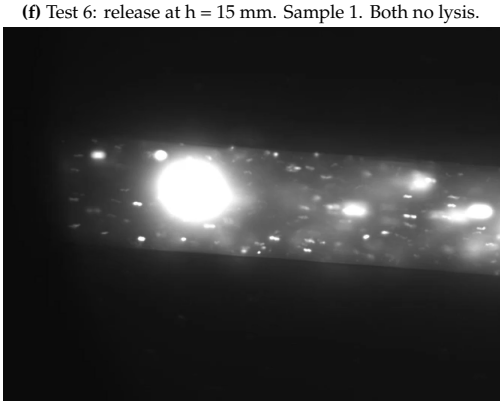

(h) Test 6: release at h = 15 mm. Sample 3. Lysis.

Figure C.15: Fluorescent Microscope images of a the trapping experiments (1/2).

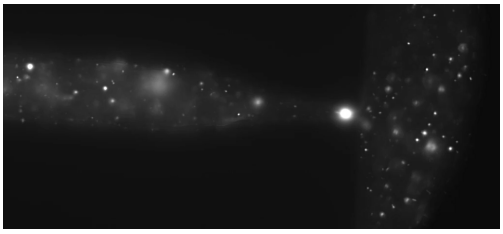

(a) Test 7: release at h = 15 mm. Sample 1. No lysis.

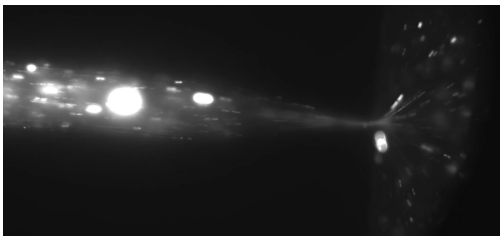

(b) Test 7: release at h = 15 mm. Sample 2. Lysis.

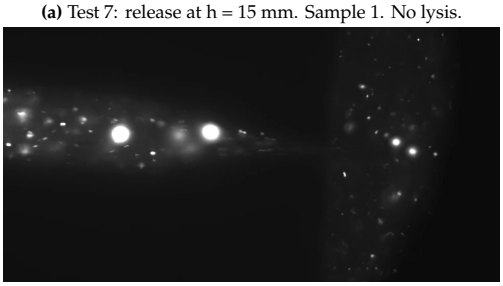

(c) Test 8: release at h = 15 mm. Sample 1. Left lysis, right no lysis.

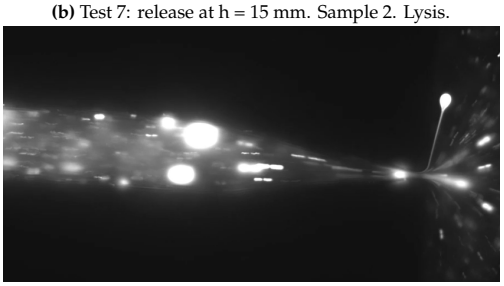

(d) Test 8: release at h = 15 mm. Sample 2. Top lysis, bottom no lysis.

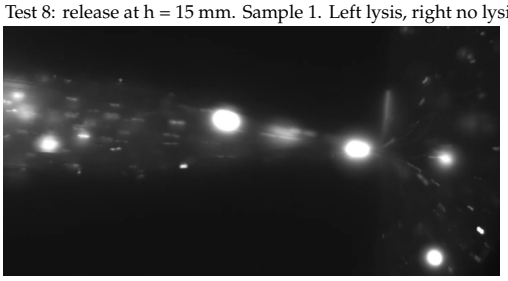

(e) Test 9: release at h = 20 mm. Sample 1. Left no lysis, right lysis.

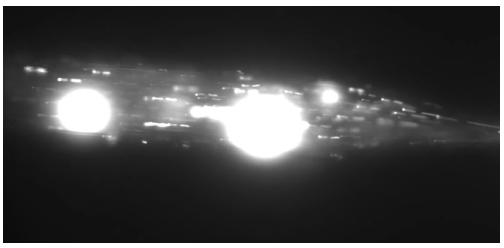

(f) Test 9: release at h = 20 mm. Sample 2. Big lysis.

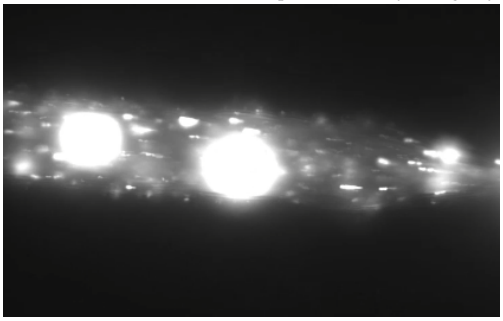

(g) Test 9: release at h = 20 mm. Sample 3. Left no lysis, right lysis.

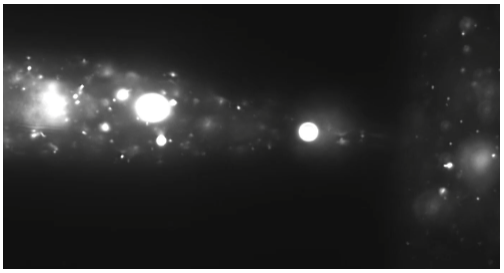

(h) Test 10: release at h = 10 mm. Both no lysis.

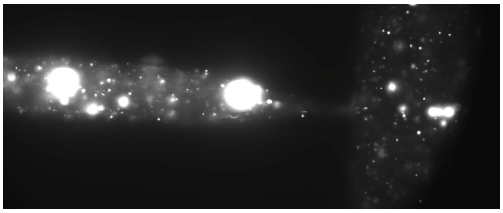

(i) Test 11: release at h = 20 mm. Sample 1. Both lysis.

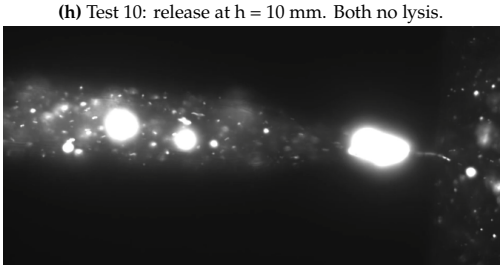

(j) Test 11: release at h = 20 mm. Sample 2. Both (left, not in trap yet) no lysis.

Figure C.16: Fluorescent Microscope images of a the trapping experiments (2/2).

D

Version history

Table D.1: Version history of the design throughout the project timeline.

Version	Date	Comments	Results
1	05/01/2024	First iteration for Micro2 and Nanoscribe printing	Micro2 not okay around critical feature + minimal channel diameter around 10 micron, Nanoscribe better but stitching errors
2	10/01/2024	Micro2 test print	Tolerances not good enough
3	22/01/2024	With integration of slander edge for bubble dissipation electro-osmotic flow	During bonding to glass, shallow structures collapsed
4	31/01/2024	Addition of poles to prevent collapsing during PDMS bonding, removal of lines in sketch to improve STL output	With oxygen plasma bonding looks good, but bonding not strong
5	29/01/2024	Negative instead of positive to reduce PDMS sticking to master)	Good results, especially around nozzle, bad bonding
6	05/02/2024	Removal of round circles for better printing time	Fast print (47 minutes), good bonding strength with air plasma but again collapsing
7	12/02/2024	Channel height angled around connection to prevent collapsing during the punching of holes	Demolding failed, print sticks to the PDMS after removal causing contamination, the collapsing was prevented
8	26/02/2024	Larger structure for electrode connection, experiment with nozzle limits	Nozzle 2 micron good print, but closed during soft lithography. Unreliable connection electrode.
9	8/03/2024	Extension tube, chamber	Never printed
10	10/04/2024	Addition of characteristic nozzle design parameters	Final design for testing
Brain 1	07/05/2024	First version for the multipore experiment, based on designs from the literature.	losses at the nozzles; due to placement in series, the flow becomes negligible at the last nozzles.
Brain 2	13/06/2024	Parallel approach to ensure that losses do not have a significant impact on concept.	Final version of the multipore design.

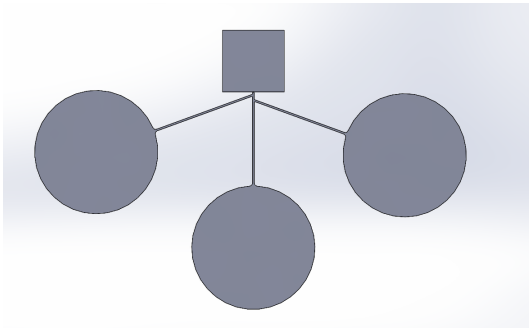

(a) Trapping V1.

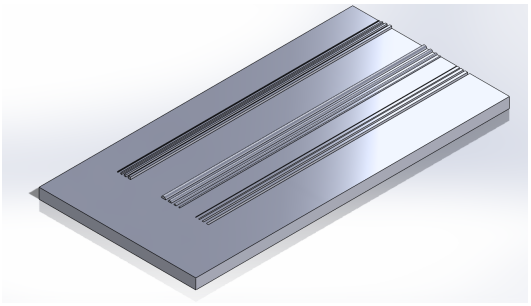

(b) Trapping V2.

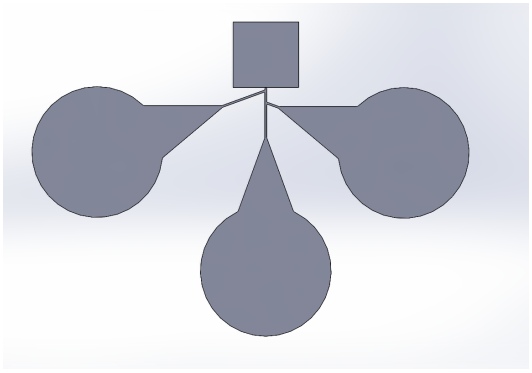

(c) Trapping V3.

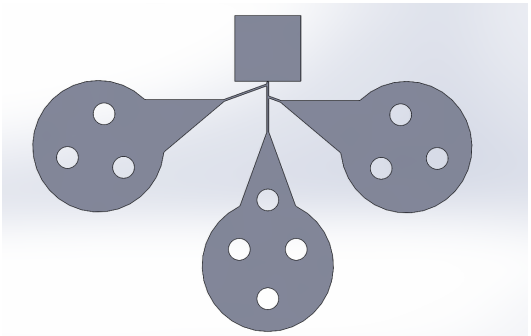

(d) Trapping V4.

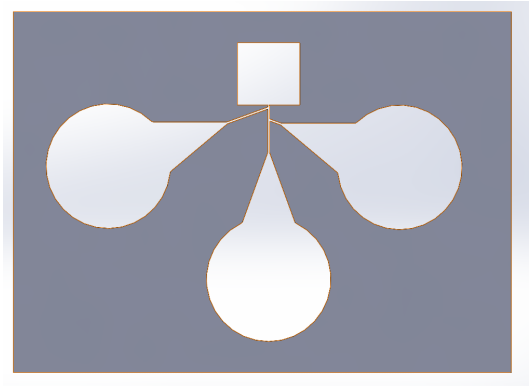

(e) Trapping V5.

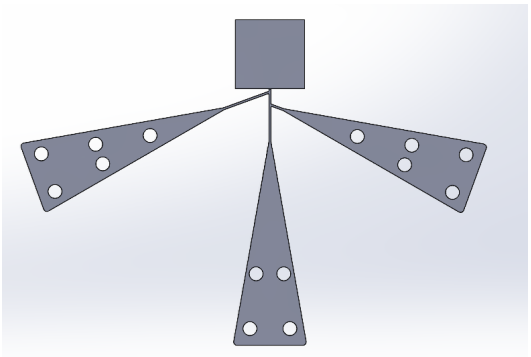

(f) Trapping V6.

Figure D.1: Screenshots from Solidworks showing the design versions (1/2).

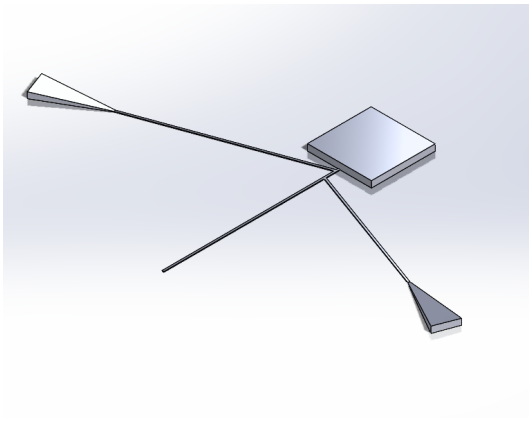

(a) Trapping V7.

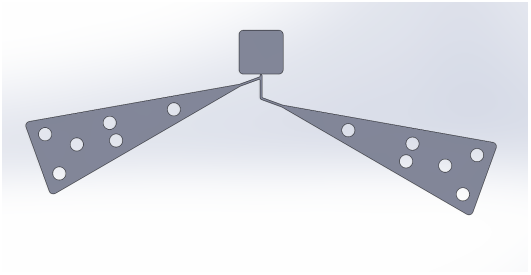

(b) Trapping V8.

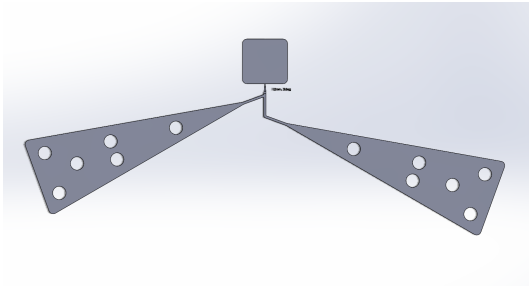

(c) Trapping V10.

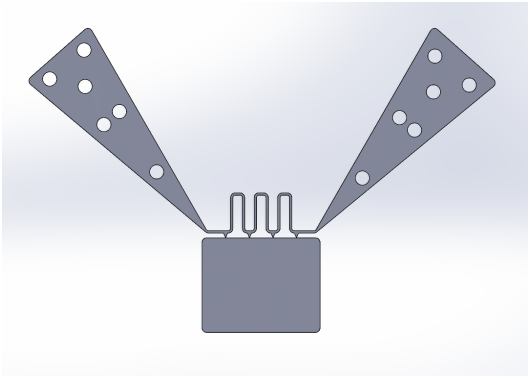

(d) Brain V1.

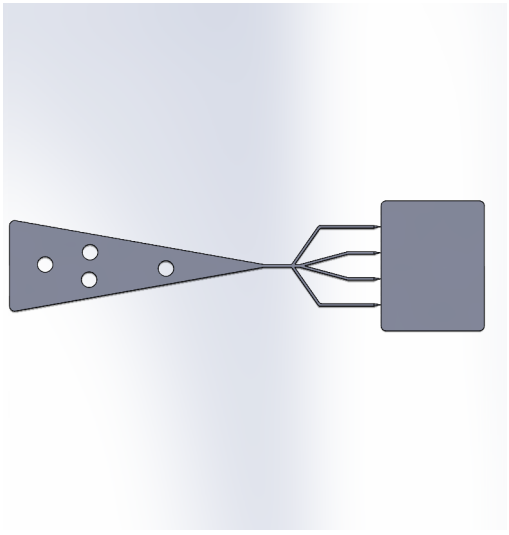

(e) Brain V2.

Figure D.2: Screenshots from Solidworks showing the design versions (2/2).

E

Project proposal and planning

In order to develop a robust project proposal, a structured approach is necessary. This begins in subsection E.1.1, where goals have been established for each function of the DDS based on the literature gaps provided in Table E.1. Next, section E.2 presents a Work Breakdown Structure (WBS) offering a systematic overview and prioritization of these goals. Each goal is then broken down into detailed activities that are integrated into the WBS. The next step, detailed in section E.3, involves a thorough risk analysis. Finally, section E.4 brings together the prioritized activities of the WBS and the assessed risks into a comprehensive plan. This section makes use of a Gantt chart, illustrating the project's planned timeline and milestones, thereby laying a solid foundation for the project's execution. Finally, section E.5 presents the updates that have been made during the course of the project.

E.1. Project Proposal

E.1.1. Goals

Trapping

Firstly, there is a gap in understanding how to efficiently trap highly deformable particles; this challenge is frequently acknowledged as one of the key obstacles in the development of microfluidic trap-and-release systems. Furthermore, there is a lack of accurate modeling to predict trapping behavior. Therefore the first sub-question is: *"How can the highly deformable liposomes be retained in pores of the DDS?"*

In order to answer this, the following goals have been determined:

- Establish effective trapping of highly deformable liposomes using passive physical methods.
- Accurately predict trapping behavior based on a model or simulation.

Releasing

The liposomes were then used only in static suspension, without the presence of microfluidic forces. Therefore, there is a lack of understanding how the newly introduced microfluidic forces affect drug release from liposomes. Furthermore, liposomes are generally exposed to light with the goal of releasing drugs omnidirectionally. However, for the DDS as proposed in this project, it is desired that the medicine is predominantly exited on the brain side of the system. Therefore, the second sub-question is: *"How should the liposomes be operated in order to efficiently release the drugs encapsulated within?"*

In order to answer this, the following goals have been determined:

- Establish efficient release from liposomes using light.
- Understand the effect of the newly introduced microfluidic environment on drug release.
- Examine potential of laser optics to achieve unidirectional opening of the liposomes.

Table E.1: Summary of the identified literature gaps in the review and their inclusion in the final project proposal.

Hydrodynamic trapping **Literature gap**	**Inclusion**
Shape influence trap region	Yes
Trapping of deforming particles	Yes
Predictions and optimization of refill time	Yes
Selectivity of the mechanism to different sized particles	No
Impact surface roughness	No
Simplification production & handling procedures	No
Burst valve/droplets **Literature gap**	**Inclusion**
Geometry influences	Yes
Conclusive effect surface roughness & defects	No
Dynamic effects	No
Evaporation effects	No
Reusability	No
Liposomes **Literature gap**	**Inclusion**
Effect of microfluidic forces on release	Yes
Unidirectional opening	Yes
Safety implications of laser in brain environment	No
Other topics **Literature gap**	**Inclusion**
Integration of microfluidic flow generation with micropumps	No
Integration of light-actuated microvalves	No
Influence of elastofluidics on flow stability and behavior	No
Integration of release mechanisms	No

Transporting
The last research direction is related to the microfluidic transport of liposomes to the desired open pores in the DDS. Although particle transport has been extensively studied in literature, the specific control of particles such as liposomes has not been covered within our research group. Furthermore, existing literature mainly focuses on the spatial control of the particles; however, for the DDS the time necessary to fill trapping sites is an important performance indicator and remains unexplored. Therefore, the resulting third and last subquestion is the following: *"How can the microfluidic system be configured to facilitate the transport of liposomes to intended open pores?"*

In order to answer this, the following goals have been determined:

- Establish a design compatible with liposomes for selective filling of an open pore.
- Determine the relation between pressure and duration required for the microfluidic system to substitute a liposome following a drug delivery event.
- Expand the single structure to create a network of traps.

E.2. Work Breakdown Structure

The goals identified in the previous section have been prioritized in a WBS using the following categories: (1) Minimum Viable Product (MVP), (2) Addition to literature gap and (3) Increase of system performance. Ultimately, goals in category (1) are the minimal requirement for successful finishing of the project. By demonstrating effective trapping and release, the *proof-of-concept* is established. Next, goals in category (2) are highly desired to be fulfilled in order to provide substantial progress to literature and system understanding. Lastly, goals in category (3) are desired to be completed in order to show the potential of the concept and more closely reach commercial viability. However, establishing a design for selectively filling open pores has already been well-documented in literature. Since the other goals are not necessary to demonstrate the *proof-of-concept*, they will be the first tasks to be cancelled in case of delays. Next, for each of these goals, detailed activities have been added. The resulting overview of goals, accompanying tasks and prioritization can be found in the WBS in Figure E.1.

E.3. Risk analysis

A risk analysis has been performed using a Failure Mode Effect Analysis (FMEA) approach. Firstly, potential risks have been identified in a brainstorm. The severity and probability of each risk were then evaluated, using the rating criteria found in Table E.2. The initial assessment of these risks is visually represented in the risk matrix shown in Figure E.2a. For each of the risks, barriers for both probability and severity have been established, with the revised risk matrix shown in Figure E.2b. A complete overview of the risk analysis can be found in Figure E.2. The key risks identified through this analysis, along with their corresponding mitigation strategies, are as follows:

- TRAP.1: Hydrodynamic trapping is not effective. In order to reduce the probability, the creation of the COMSOL/Laplace models should take place early in the process. In order to reduce the severity alternatives trapping strategies should be included in the literature review and the planning should contain a contingency plan.
- TRAP.4: Manufacturing of design takes longer than expected. In order to reduce the probability, the production courses need to be followed early in the process. In order to reduce the severity, the planning should include a buffer.
- GEN.2: Difficulties in integrating components into test setup. In order to reduce the probability, the design of the setup should start early in the process and knowledge on test setup should be acquired from previous projects. In order to reduce the severity alternative (previous) test setups could be modified as an alternative.

E.4. Planning

The planning has been structured using a Gantt chart as found in Figure E.4. Based on section E.2, the project will begin with research on trapping of liposomes (orange track) and release of the content (blue track) from them. Because it is necessary to trap liposomes before release can be established, the

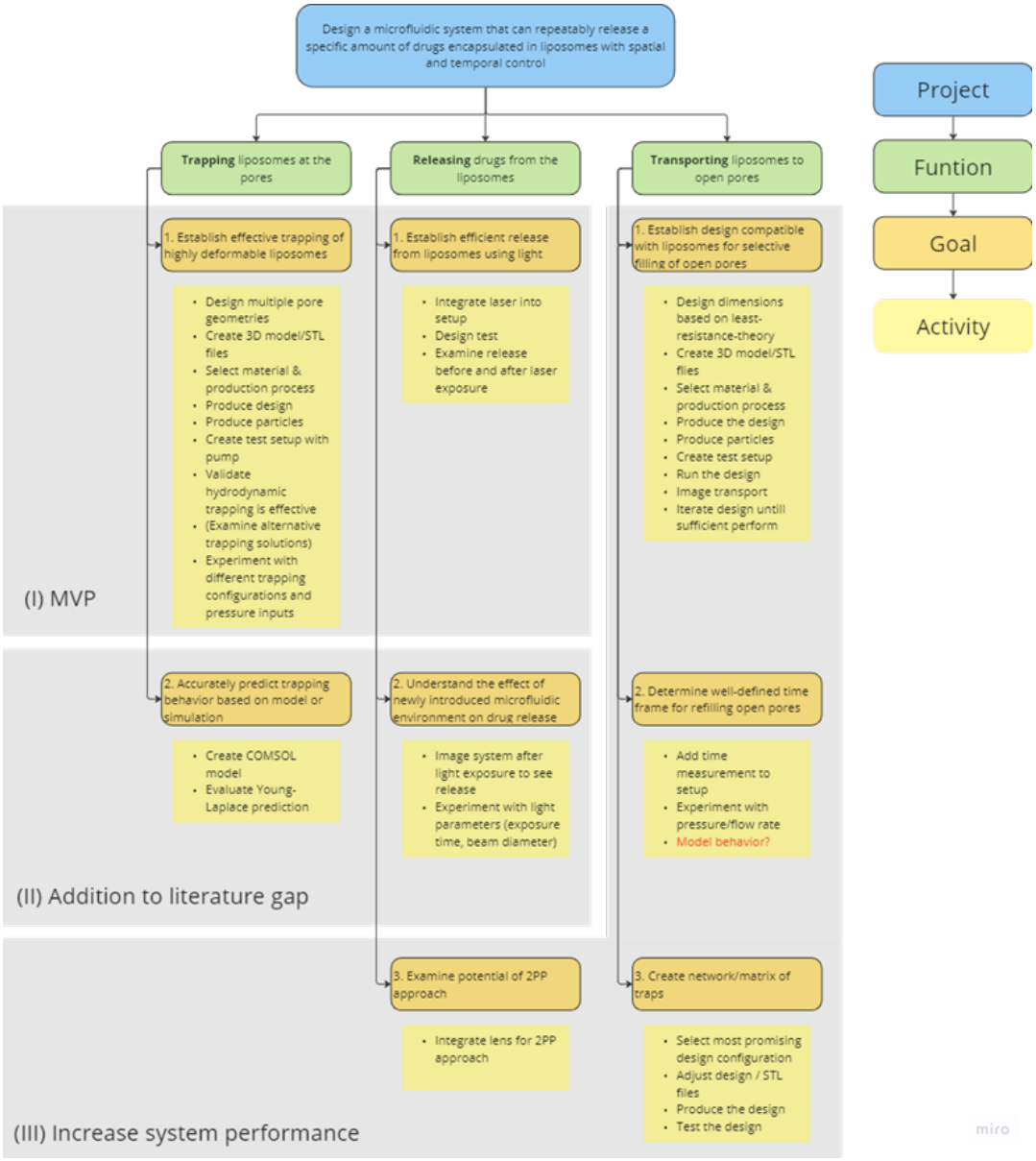

Figure E.1: The WBS used to identify and prioritize tasks.

Table E.2: The risk assessment definitions

	Probability	**Severity**
1	Almost zero chance of happening (0-10%)	Negligible: inconvenience or non-operational impact
2	Unlikely (10-50%)	Marginal: degradation of secondary mission or small reduction of performance
3	Likely (5-90%)	Critical: mission success questionable or secondary mission failure
4	Almost certain to happen (90-99%)	Catastrophic: Significant reduction of performance
5	Certain to happen (100%)	Worst case: No proof-of-concept

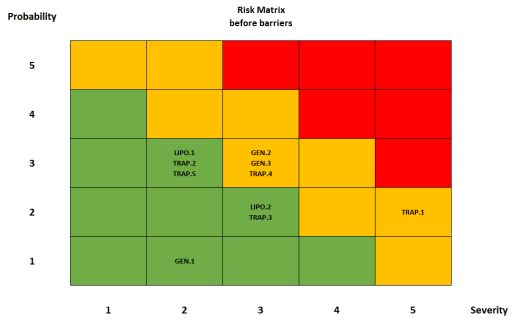

(a) Risk matrix before implementation of barriers showing some risk require significant attention (yellow).

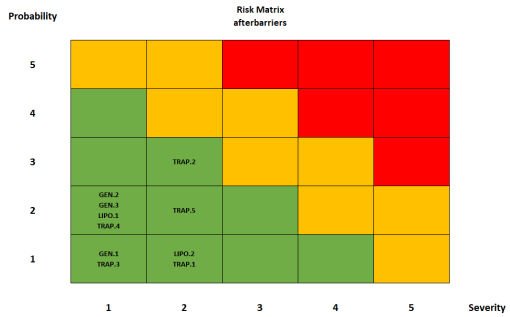

(b) Risk matrix after implementation of barriers showing all risks are in the acceptable range (green).

Figure E.2: Risks visualised on a matrix.

trapping of liposomes is the first function to be studied. The last task to be studied is transporting (the green task), which has already been well documented in previous literature.At this moment, the key decision is determining the focus for the final weeks, if time permits. For each of the tasks, the time necessary to complete it has been estimated.

Next, milestones (the dotted lines) and accompanying key decision moments (black diamonds) have been added. Based on these key decisions, different paths within the Gantt chart should be followed, indicated with the thin black arrows.

- The first milestone is the completion of the first experiment using hydrodynamic trapping. The key decision is an assessment on whether the current strategy is adequate for trapping or if alternatives, such as biochemical approaches, should be pursued.
- The second milestone, which corresponds to the midterm review, is the achievement of effective trapping. The key decision here is taken in consultation with the Chemical Engineer department, where it should be assessed if both projects are ready for integration of light to show content release.
- The third milestone is the completion of the MVP. The key decision here is if there is enough time to complete the transportation research.
- The last milestone is the achievement of transportation. At this moment, the key decision is determining the focus for the final weeks, if time permits.

Lastly, as the time budget is only an estimate and unforeseen problems can arise, it is important to keep track of the planning during the whole project and update the structure according to progress.

E.5. Planning updates during thesis

During the thesis project, the planning was updated every month. Changes were necessary due to delays and new knowledge about the process. This section provides an overview of the updates that have been made.

- February 2024: 1) Process on the 2PP-Nanoscribe printer started 2 weeks later than expected because the instructor was not available to provide training. 2) Production required more iterations than expected, adding 3 weeks to this task. 3) It was decided COMSOL simulations are not necessary as they are time consuming + models provide a sufficient estimate. Removing this task.
- March 2024: 1) The linear stage from the test-setup was required for another project, therefore the test-setup had to be redesigned. Adding 2 weeks to this task. 2) 2PP approach is not feasible to achieve in current planning + is it not part of the MVP. Removing this task.
- April 2024: 1) The needle approach to create electro-osmotic flow did not achieve a proper connection (bubbles interfere), therefore a gold electrode had to be designed and incorporated into the fabrication process. Adding 2 week to this task.

Risk Id	Probabili	Propability reduction barrier	Probability after barrier	Event	Severi	Severity reduction barrier	Severity after barrier	Consequence if risk is realised
GEN.1	1		1	Equipment malfunction	2	Use other production method	1	Delays or compromised quality
GEN.2	3	Start early with design and acquire knowledge on previous microfluidic projects	2	Difficulties in integrating components like pumps and imaging equipment into setup	3	Buffer in planning, use previous test setup?	1	Delays, unable to test
GEN.3	3	Acquire expert information on how to fix this	2	Leakage	3	Use previous test setup	1	Inconvenience with testing, unreliable results
LIPO.1	3	Produce according to experienced Chemical Engineering faculty	2	Manufacturing problem with particles of constant size	2	Add filter to liposome solution	1	Unreliable results
LIPO.2	2	Align with Yaren on planning	1	Yaren not ready for production in week 9	3	Swap planning of liposomes and transport	2	Delays
TRAP.1	2	Create both COMSOL and LaPlace model to predict trapping behavior	1	Hydrodynamic trapping is not effective	5	Look for alternatives in literature, incorporate in planning	2	Liposomes cannot be retained in DDS
TRAP.2	3		3	Trapping alternatives require more than 3 weeks	2	Buffer by starting with trapping	2	Delays
TRAP.3	2	Detailed study on production techniques	1	Manufacturing of design: difficulty with achieving high enough precision	3	2PP instead of SLA (quality up, but print speed down)	1	Precision effect on trapping efficiency, unreliable results
TRAP.4	3	Start early with production courses	2	Manufacturing of design: takes longer than expected	3	Buffer of vacation into planning	1	Delays
TRAP.5	3	Determine requirements in design, select proper pressure/flow generator	2	Pressure/flow not enough precision	2		2	Unreliable results

Figure E.3: Overview of the complete risk analysis (FMEA) from section E.3.

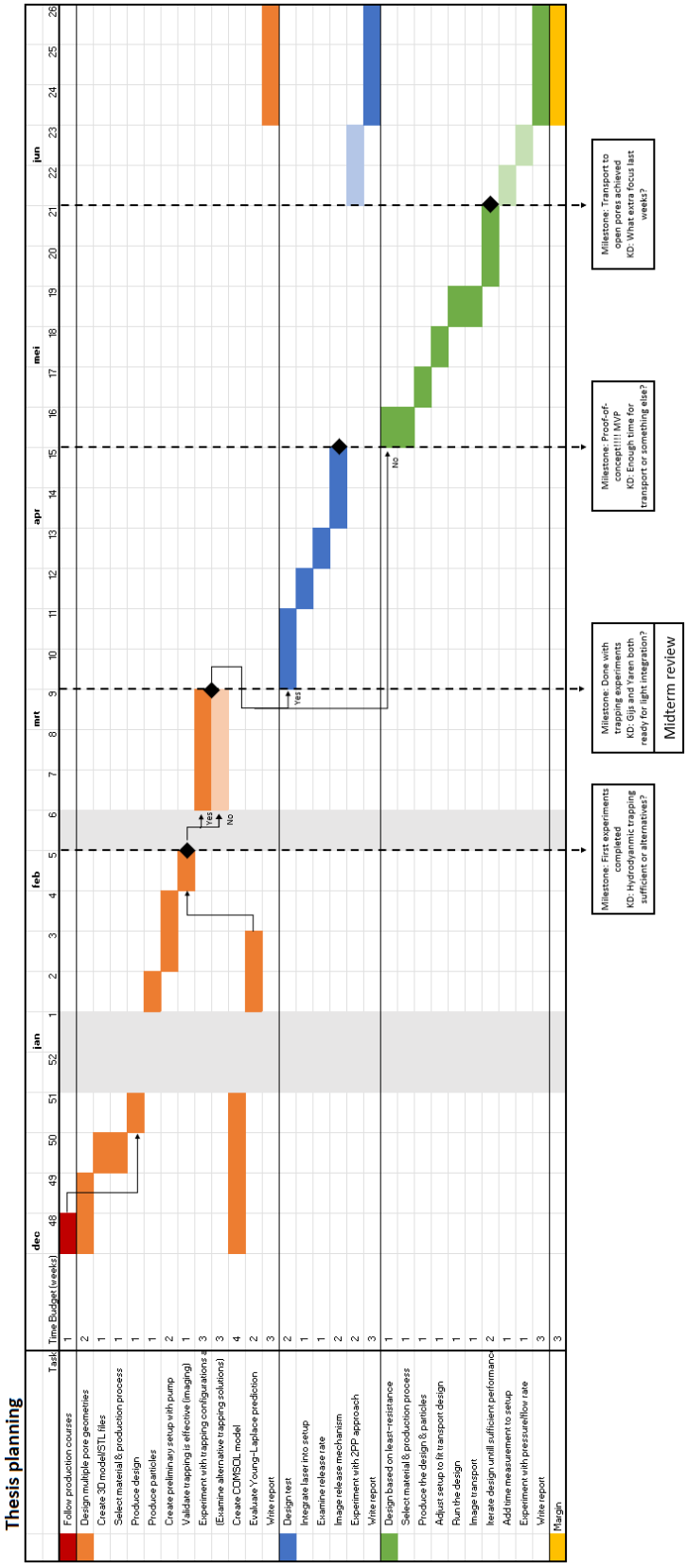

Figure E.4: Screenshot of the Excel file containing the Gantt-Chart planning of the project (flipped 90°). Orange corresponds to research on trapping, blue corresponds to research on releasing and green corresponds to research on transporting.

F

Literature review

F.1. Introduction

F.1.1. Motivation

Annually, strokes due to blood-flow blockage in the brain result in approximately 5.5 million deaths and leave survivors with long-term disabilities, amounting to 116 million disability-adjusted life years lost [1]. Current treatments are limited to acute phase management, focusing on thrombosis removal, with limited clinically available drugs for neuron protection or damage repair. This is primarily because these compounds struggle to penetrate the blood- brain barrier in sufficiently high concentrations without inducing toxicity in other parts of the body. Consequently, the dosage of drug that can be safely administered through conventional routes such as intravenous or intramuscular is limited. An implantable, on-demand drug delivery system (DDS) targeting only the brain areas most-affected by stroke will enhance the therapeutic effectiveness and minimize off-target side effects. This system would combine a detection mechanism for assessing brain tissue health and an externally-triggerable DDS to control the timing and location of on-demand drug release. Together, they form a closed-loop system with the therapeutic effects detected continuously for real-time adjustments.

This project introduces a novel implantable microsystem to dispense minute amounts of drug directly to the stroke-affected zone. By integrating the DDS with Electrocorticography (ECoG) [2], the stroke-affected zone can be identified by measuring the electrical activities of the neurons. In order to reduce interference with these measurements, no electrical signals should be used to initiate and regulate the release of the drugs. Moreover, the dosing of the drugs should be tightly controlled for safety reasons. Therefore we propose to encapsulate the drug in light-sensitive liposomes, transporting the liposomes by microfluidic means and controlling its release through light pulses. The concept foresees that each light flash opens a well-defined number of these liposomes. A graphical concept of the proposed DDS can be found in Figure F.1.

Though the primary motivation for developing the implantable DDS focuses on enhancing stroke therapy, its utility extends far beyond that singular application. The system has the potential to revolutionize targeted drug delivery which is a limiting factor in a variety of brain disorders. This includes, but is not limited to, neurological disorders such as Parkinson's disease [3] and epilepsy [4], or could even improve brain tumor chemotherapy treatment [5]. With its broad applicability, the proposed DDS opens up many possibilities for new types of medical treatment.

F.1.2. Relevance to the state-of-the-art

Drug delivery using microfluidic platforms has been research extensively. Examples include systems incorporating microneedles [6], micropumps [7] and membranes [8]. However, the specific combination of light-actuated liposomes into a microfluidic system to achieve controlled drug delivery has never been demonstrated. Furthermore, the DDS would provide significant progress in addressing two of the major challenges within the field of microfluidic controlled drug delivery as recently summarized by Sanjay *et al.* [9]. Firstly, targeted drug delivery to specific cells or tissues is challenging, as drugs tend

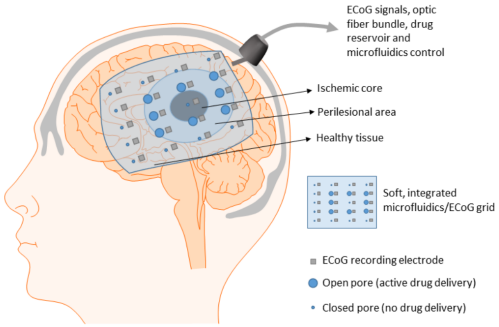

(a) Illustrative diagram of the proposed drug delivery system as integrated within the brain.

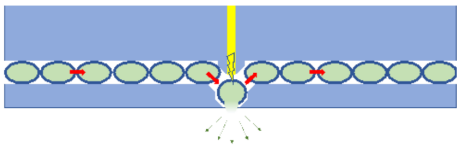

(b) Cross-section through a conceptual microfluidic system (blue) which carries liposomes (ovals) containing a drug (green) that can be released through a light flash (yellow). The red arrows indicate the liquid flow.

Figure F.1: The DDS concept as proposed in this project.

to be dispersed randomly, with only a small fraction reaching the intended sites. Secondly, existing controlled DDS' typically release drugs at fixed rates and lack the ability to adjust to changes in patient conditions once implanted.

The integration of microfluidics and liposomes has already been shown before, however such studies are focused on the production of liposomes by means of microfluidic flow principles [10–13]. Furthermore, liposomes have been utilized as on-demand DDS, although without the integration of a microfluidic control mechanism. Typically, two main strategies are employed [14]: passive targeting involves dispersing the particles within the patient exploiting their ability to accumulate at sites of increased vasculature permeability; active targeting involves biochemically altering the lipid membrane to include ligands such that it predominantly binds to specific tissues. Currently, commercially available liposomes provide passive targeting at best [15, 16]. The integration of a microfluidic system would provide substantial progress by introducing enhanced spatial and temporal control. Furthermore, the DDS would enable the delivery of drugs without having to pass the blood-brain barrier, which would significantly increase the effective dose that is delivered to the intended tissue.

F.1.3. Research problem and scope

The ambitious goal aimed at developing a *proof-of-concept* of integrating the microfluidic system with light-actuated liposomes, necessitates a collaborative approach between two different departments: the High-Tech Engineering and Chemical Engineering faculty. Firstly, the High-Tech Engineering faculty focuses on the manipulation of liposomes within the DDS. This involves designing the microfluidic system that facilitates spatial and temporal control for precise drug release. Simultaneously, the Chemical Engineering Faculty concentrates on the liposomes' chemical composition, production and characterisation. This thesis project, centering on the manipulation of liposomes and informed by literature relevance as provided before, results in the formulation of the following research question:

"How can a microfluidic system be designed such that it can repeatably release a specific amount of drugs encapsulated in liposomes with spatial and temporal control?"

In order to answer the main research question, it is important to understand what has already been achieved. Therefore an overview of relevant literature can be found in section F.2 to section F.4. Based on this state-of-the-art, numerous knowledge gaps have been identified that must be addressed for successful development of the proposed DDS. This thesis aims to bridge a selection of these gaps, acknowledging that, as only the initial phase of this broad research trajectory, certain topics have been left out of scope due to time constraints. A summary of the specific literature gaps assessed in this thesis and accompanying project proposal can be found in section E.1. Following this, section F.5 compiles literature on general design principles, materials selection, production techniques and testing methodologies. This chapter aims to provide background knowledge that can be utilized during the thesis project, rather than identifying new research directions. Lastly, section F.6 offers a detailed discussion of potential research questions and areas for future investigations that fall outside the current project's scope.

F.1.4. Methodology of Literature Review

Planning

In order to keep track of the progress of the literature review, a Gantt-chart has been used. The file was updated once a week during the process and the result was a clear overview and minimal delays. A screenshot of the planning can be found in Figure F.2. Because of the positive experience with this method, it was decided the Gantt-chart approach will be expanded into the complete thesis planning.

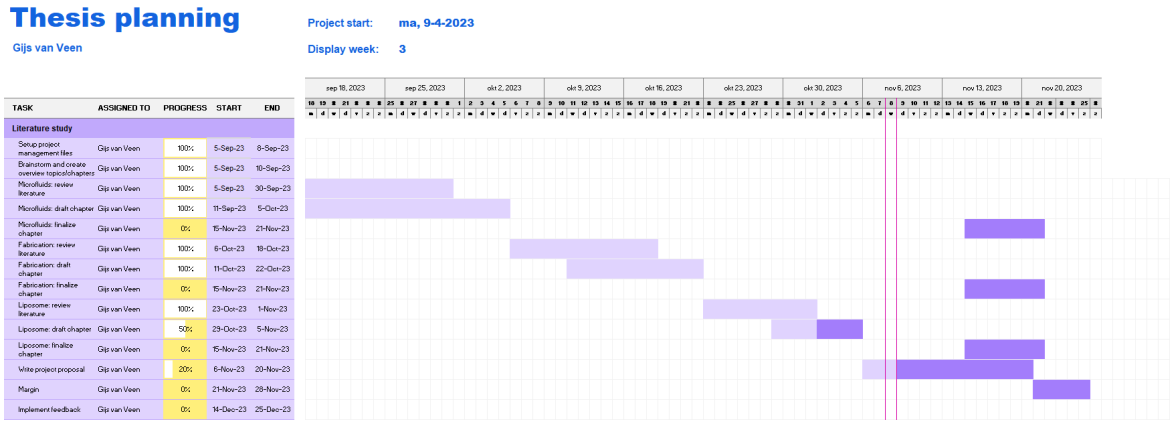

Figure F.2: Screenshot of the Gantt-chart in the Excel file, used for tracking the literature review planning.

Mind map

At the beginning of the literature review, the scope was still quite broad. In order to streamline the process, a mind map was created to cover the different topics within the project scope: microfluidics, liposomes and design/fabrication. These topics were the basis of the search strategy. Based on these topics and initial broad papers, different fields of research were added to the mind map resulting in the overview as found in Figure F.3. This map was continuously updated during the review based on literature findings. In the end, this mind map formed the basis for the structure of this paper.

Literature retrieval

During the literature review the following general strategy was used in order to retrieve new literature and find research gaps:

1. Find review papers on the topic on either Google Scholar or Scopus
2. Dive into the references of the review to gather further understanding of the topic
3. Derive search terms for the topic based on the application of the DDS
4. Check the citation map with search terms for important references
5. Check the Scopus search engine
6. Follow references (forwards and backwards)
7. Update search terms until the literature gap is found

Reference documentation

To maintain a complete overview of the literature gathered, an Excel sheet was created. This sheet documented the cited references, their relevance, and other details. A screenshot of this Excel sheet can be found in Figure F.4. The combination of ID and title was used to organize the downloaded PDFs.

F.2. Fundamentals of Microfluidics

The targeted delivery of drugs to specific regions of the brain presents numerous challenges. Microfluidic systems, with their precise control over fluid flow at the micro-scale, offer promising building blocks for addressing these challenges. Before going into the specifics of microfluidic literature, it is imperative to understand the fundamental principles that govern fluid behavior in such micro-environments. Many detailed books and lectures on the physics behind these phenomena have been published [17–21]. In this

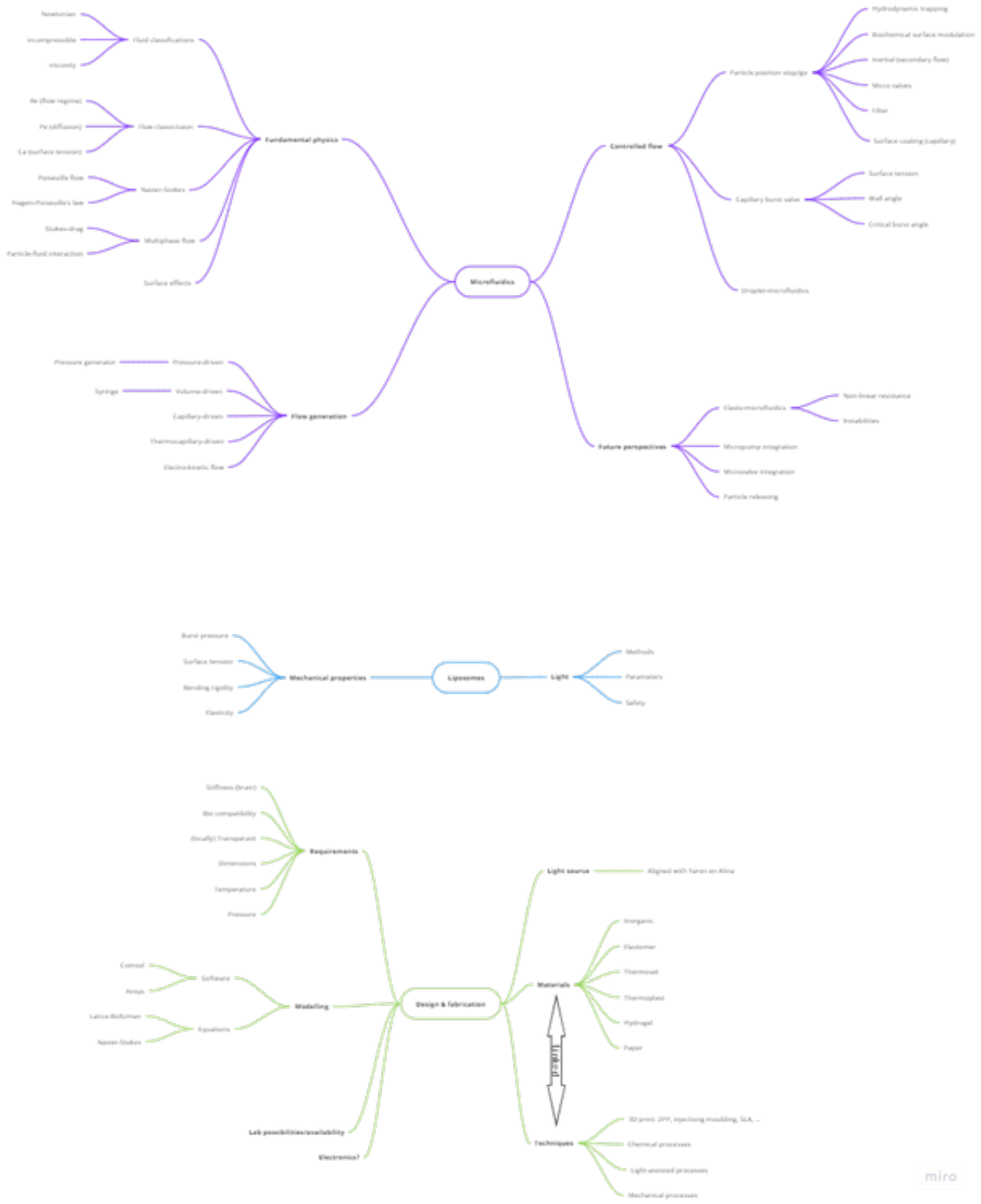

Figure F.3: Screenshot of mind map build in Miro. The file could not be exported in higher quality without payment to Miro.

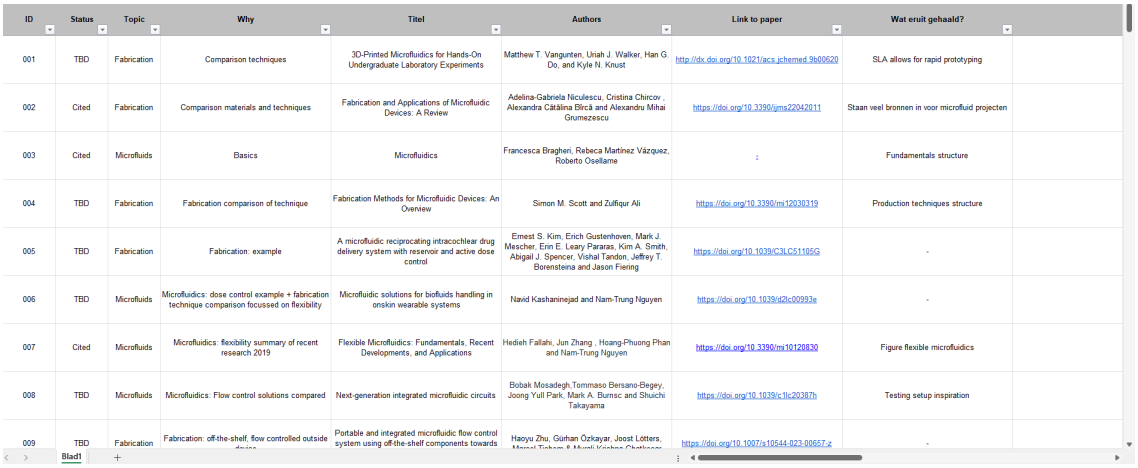

ID	Status	Topic	Why	Titel	Authors	Link to paper	Wat eruit gehaald?
001	TBD	Fabrication	Comparison techniques	3D-Printed Microfluidics for Hands-On Undergraduate Laboratory Experiments	Matthew T. Vangunten, Uriah J. Walker, Han G. Do, and Kyle N. Knust	http://dx.doi.org/10.1021/acs.jchemed.9b00620	SLA allows for rapid prototyping
002	Cited	Fabrication	Comparison materials and techniques	Fabrication and Applications of Microfluidic Devices: A Review	Adelina-Gabriela Niculescu, Cristina Chircov , Alexandra Cătălina Bîrcă and Alexandru Mihai Grumezescu	https://doi.org/10.3390/ijms22042011	Staan veel bronnen in voor microfluid projecten
003	Cited	Microfluids	Basics	Microfluidics	Francesca Bragheri, Rebeca Martínez Vázquez, Roberto Osellame	:	Fundamentals structure
004	TBD	Fabrication	Fabrication comparison of technique	Fabrication Methods for Microfluidic Devices: An Overview	Simon M. Scott and Zulfiqur Ali	https://doi.org/10.3390/mi12030319	Production techniques structure
005	TBD	Fabrication	Fabrication: example	A microfluidic reciprocating intracochlear drug delivery system with reservoir and active dose control	Ernest S. Kim, Erich Gustenhoven, Mark J. Mescher, Erin E. Leary Pararas, Kim A. Smith, Abigail J. Spencer, Vishal Tandon, Jeffrey T. Borenstein and Jason Fiering	https://doi.org/10.1039/C3LC51105G	-
006	TBD	Microfluids	Microfluidics: dose control example + fabrication technique comparison focussed on flexibility	Microfluidic solutions for biofluids handling in onskin wearable systems	Navid Kashaninejad and Nam-Trung Nguyen	https://doi.org/10.1039/d2lc00993e	-
007	Cited	Microfluids	Microfluidics: flexibility summary of recent research 2019	Flexible Microfluidics: Fundamentals, Recent Developments, and Applications	Hedieh Fallahi, Jun Zhang , Hoang-Phuong Phan and Nam-Trung Nguyen	https://doi.org/10.3390/mi10120830	Figure flexible microfluidics
008	TBD	Microfluids	Microfluidics: Flow control solutions compared	Next-generation integrated microfluidic circuits	Bobak Mosadegh,Tommaso Bersano-Begey, Joong Yull Park, Mark A. Burns< and Shuichi Takayama	https://doi.org/10.1039/c1lc20387h	Testing setup inspiration
009	TBD	Fabrication	Fabrication: off-the-shelf, flow controlled outside	Portable and integrated microfluidic flow control system using off-the-shelf components towards	Haoyu Zhu, Gürhan Özkayar, Joost Lötters,	https://doi.org/10.1007/s10544-023-00657-z	-

Blad1

Figure F.4: Screenshot of the Excel file used for reference management.

chapter the fundamentals of fluidics will be discussed with a special focus on the differences between the marco- and micro-environment.

In subsection F.2.1 and subsection F.2.2 the classification of fluids and flow as considered during this project will be discussed. Next, the equations of motion are described in subsection F.2.3. Following these equations, the relation between pressure and flow rate is discussed in subsection F.2.4. After that, the interaction between particles and flow is discussed in subsection F.2.5. Lastly, dominant effects of surface tension and clogging are described in subsection F.2.6 and subsection F.2.7 respectively.

F.2.1. Classification of fluids

In order to capture the behavior of fluid, it is essential to understand the characteristics of the fluid medium used. In this section, the assumptions around the fluid characteristics in this study have been summarized.

Newtonian

One of the primary classifications of fluids is the distinction between Newtonian and non-Newtonian fluids. The fluids are assumed to be Newtonian in this study. A Newtonian fluid is characterized by its linear relationship between the shear stress (τ) and the shear rate ($\frac{du}{dy}$). Mathematically, this relationship can be found in Equation F.1. Here, η denotes the viscosity of the fluid, which remains constant for Newtonian fluids irrespective of the shear rate. This will later be important in the Navier-Stokes equation where the viscosity will be represented by a linear term.

$$\tau = \eta \frac{du}{dy} \tag{F.1}$$

Incompressible

Another classification important for the Navier-Stokes equations is the incompressibility of fluids. The term incompressibility refers to a fluid's resistance to changes in volume when subjected to external pressures. The fluids are assumed to be incompressible in this study. An incompressible fluid maintains a nearly constant density regardless of the pressure variations it experiences. It is important to note that this assumption is usually an approximation.

Constant viscosity

Viscosity is a property that describes a fluid's resistance to flow, with fluids being categorized as either viscous or inviscid. Inviscid fluids are idealized fluids with zero viscosity. The fluids studied in this paper are assumed to be viscous. Furthermore, it has been well established that the viscosity of a fluid is a function of temperature, and many studies have been done to model the viscosity-temperature relationship [22–24]. These models however, are difficult to apply in practice and therefore another

empirical model is more generally accepted, as can be found in Equation F.2. Here, A and B are constants determined by experimental data.

$$\eta = Ae^{B/T} \tag{F.2}$$

However, since the application of the microfluidic system is under constant (controlled) temperature, for simplification the viscosity is considered a constant parameter. Other dependencies, such as pressure and rate of deformation, have also been left out of scope.

F.2.2. Classification of flow

As a result of the relatively small dimensions of the channels in the micro environment, the impact of specific forces is different compared to macro-environments. Therefore it is important to establish the scaling relations that occur. This can be done by evaluating dimensionless parameters, such as the Reynolds (Re), Péclet (Pe), and Capillary (Ca) numbers, that describe relations between different forces acting on the fluid. Other dimensionless numbers that are of less importance to the DDS include the Weissenberg, Deborah, Grashof and Rayleigh number.

Reynolds - flow regime

The Reynolds number (Re) is considered to be the most important dimensionless parameter in forced flows. By evaluating the Reynolds number, which encapsulates the relation between inertial and viscous force, the flow regime can be identified. Generally if (1) $Re < 2300$ the flow is laminar, if (2) $2300 < Re < 4000$ a non-fully developed turbulence occurs and if (3) $Re > 4000$ the flow is considered to become fully turbulent. In order to calculate the Reynolds number, in *Microfluidics: Fluid physics at the nanoliter scale* by Squires and Quake [20] summarize; a fluid element gains momentum at a rate found in Equation F.3a and viscous force densities result from gradients in viscous stress resulting in Equation F.3b. Combining these results leaves the Reynolds number as can be found in Equation F.4.

$$f_i \sim \frac{\rho u^2}{L} \tag{F.3a}$$

$$f_v \sim \frac{\eta u}{L^2} \tag{F.3b}$$

$$Re = \frac{f_i}{f_v} = \frac{\rho u L}{\eta} \tag{F.4}$$

When looking at microfluidic systems, flow rates are usually low and thus the Reynolds number often is dominated by viscous forces. Several experimental studies [25, 26] have been done in order to access the laminar flow regime in microchannels, and it can be concluded that laminar flow is established for $Re < 2000$. Therefore, only laminar flow regimes will be addressed in this review.

Péclet - diffusion

Complementing the Reynolds number, is the Péclet number (Pe), which offers insights into the balance between convection and diffusion. Under macro circumstances, mixing is mostly dominated by the presence of turbulent flows. However, given the small scales in microfluidics and the resulting laminar flow regime, the Péclet number indicates diffusion is dominant. As mentioned in [17], the Péclet number can be calculated using Equation F.5, where u is the flow velocity, L is the typical length scale for a microchannel and D_d is the molecular diffusion coefficient of the material. If relatively small particles are considered, values of Péclet number can be around 100 to 1000, meaning that a length equal to hundreds of channel widths is needed to completely diffuse over the whole microchannel cross-section.

$$Pe = \frac{uL}{D_d} \tag{F.5}$$

In the controlled microfluidic system, the importance of diffusion is negligible. However, for the application of drug delivery the situation is different as precise control over molecular transport is

crucial for drug concentrations. The Péclet number can guide the design and operation of the system by giving insight how long the liposomes need to be opened in order to properly release the drugs.

Capillary - surface tension

The Capillary number (Ca) is a dimensionless number that quantifies the relative importance of viscous forces to surface tension in a fluidic system. The definition of the Capillary number can be found in Equation F.6, where γ is the surface tension. In microfluidics, surface tension is more dominant due to the higher surface-to-volume ratio.

$$Ca = \frac{\eta u}{\gamma} \tag{F.6}$$

F.2.3. Navier-Stokes equations

At the core of (micro)fluidics lie the Navier-Stokes equations, which are partial differential equations that describe the motion of fluids. These equations have been widely used in many applications, such as predicting weather, ocean currents and Formula1 aerodynamic behavior. Interestingly, mathematically the equations have never been proven to be solvable in 3D and are even part of the Millennium Prize Problems [27]. The first equation essentially can be compared to the continuum version of the Newton's second law applied on an infinitesimal volume. The terms on the left describe the momentum. The first two terms on the right represent internal forces in the fluid and the last term are external forces acting on the body.

$$\rho\left(\frac{\partial \mathbf{u}}{\partial t} + \mathbf{u}\cdot\nabla\mathbf{u}\right) = -\nabla p + \eta\nabla^2\mathbf{u} + \mathbf{f} \tag{F.7}$$

Here ρ is the density, η is the viscosity, $\mathbf{u}$ is the velocity of the fluid, $\mathbf{f}$ is the external unit force and p is the pressure. When working at very low Reynolds numbers ($Re << 1$) and inertial forces are low compared to viscous forces, the nonlinear term can even be neglected [20]. Since this is usually the case for microfluidic systems, the resulting equation leaves Equation F.8. However, it should be noted that when working with Re in $O(0) - O(2)$, which can be the case for inertial microfluidics, this simplification will not be accurate and Equation F.7 should be followed.

$$\rho\left(\frac{\partial \mathbf{u}}{\partial t}\right) = -\nabla p + \eta\nabla^2\mathbf{u} + \mathbf{f} \tag{F.8}$$

Next, the second equation is the based on the conservation of mass and is simplified due to the incompressibility condition of the fluid and can be found in Equation F.9. Using the Navier-Stokes equations, the velocity field of the fluid can be computed.

$$\nabla\cdot\mathbf{u} = 0 \tag{F.9}$$

F.2.4. Pressure-flow rate relationship

Hagen-Poiseuille law

The theory behind flow-rate in a long channel has been explained in detail By Happel and Brenner [19]. After reaching steady-state under a constant pressure gradient, the fully developed flow in a microchannel reaches a laminar regime and has a unidirectional velocity fluid. Therefore the rate of change of momentum and external forces are zero and Equation F.8 becomes:

$$\nabla p = \eta\nabla^2\mathbf{u} \tag{F.10}$$

Considering a circular channel with radius a and no slip boundary condition ($u = 0$ at $r = a$), a velocity field which is parabolic across the diameter can be defined as:

$$u_x = \frac{a^2 - r^2}{4\eta}\left(-\frac{\mathrm{d}p}{\mathrm{d}x}\right) \tag{F.11}$$

In order to assess the flow rate Q in the channel, the law of Hagen-Poiseuille can be used. This is obtained by integrating the velocity fluid of Equation F.11 and results in the following:

$$Q = \frac{\pi a^4}{8\eta}\left(-\frac{\mathrm{d}p}{\mathrm{d}x}\right) \tag{F.12}$$

Given that the pressure gradient along the channel length is uniform, the pressure derivative can be approximated as $\Delta p/L$, where Δp is the overall pressure drop in the channel with length L. Combining this with Equation F.12, results in the pressure-flow rate relationship (also known as the Hagen-Poiseuille equation):

$$Q = \frac{\pi a^4}{8\eta}\frac{\Delta p}{L} \tag{F.13}$$

Hydraulic resistance

The relation for the Hagen-Poiseuille flow-rate as mentioned in Equation F.13 is only valid for circular channels. However, in microfluidics other shapes are commonly used such as rectangular, square and triangular. Therefore a more general approach is required. By determining the hydraulic resistance R_H of a channel, the flow rate can be calculated with Equation F.14.

$$Q = \frac{\Delta p}{R_H} \tag{F.14}$$

Research by Mortensen *et al.* [28] examines the shape dependency of the hydraulic resistance resulting in an easy evaluation for elliptical, rectangular and triangular channels. They define a dimensionless compactness number $C = P^2/A$ (where P is its perimeter and A is its area) which characterizes a given shape. Next they define a geometrical correction factor $\alpha = \frac{A^2}{\eta L}R_H$ which characterizes hydraulic resistance. They found an almost linear correlation between the two parameters C and α and conclude the hydraulic resistance correlates linearly on Equation F.15. Thus they set the first step to easily estimating flow rate based on hydraulic resistance for various shapes, which can be highly convenient when designing (micro)fluidic systems. However, shape dependent coefficients are necessary to calculate the exact hydraulic resistance.

$$R_H \propto C\frac{\eta L}{A^2} \tag{F.15}$$

H. Bruus [18] has summarized (approximated) solutions derived from the Navier-Stokes equations that can estimate the hydraulic resistance for specific geometries. An overview of the resulting hydraulic resistance approximations per shape can be found in Table F.1. Since most microfluidic systems use rectangular channels, a more detailed explanation on the derivations of the rectangular hydraulic resistance is provided next.

For rectangular (and square channels), no analytical solution has been found to the Navier-Stokes equations. However, by finding a Fourier sum representing the solution, an estimation can be made. A Fourier expansion that satisfies the no-slip boundary conditions on the channel walls can be found in Equation F.16a. When integrated over the channel dimensions, this results in the pressure-flow relationship as found in Equation F.16b. This equation can be approximated for wide rectangles ($w >> h$) and square channels ($w = h$), which results in the formulas given in Table F.1.

$$v_x(y,z) = \frac{4h^2\Delta p}{\pi^3\eta L}\sum_{n,\,\mathrm{odd}}^{\infty}\frac{1}{n^3}\left[1 - \frac{\cosh\left(n\pi\frac{y}{h}\right)}{\cosh\left(n\pi\frac{w}{2h}\right)}\right]\sin\left(n\pi\frac{z}{h}\right). \tag{F.16a}$$

$$Q = \frac{h^3 w \Delta p}{12\eta L}\left[1 - \sum_{n,\,\text{odd}}^{\infty} \frac{1}{n^5}\frac{192}{\pi^5}\frac{h}{w}\tanh\left(n\pi\frac{w}{2h}\right)\right] \tag{F.16b}$$

Table F.1: Overview of the hydraulic resistance for straight channels with different cross-sectional shapes, copied from Bruus [18].

shape	R_H **expression**
circle	$\frac{8\eta L}{\pi a^4}$
ellipse	$\frac{4\eta L}{\pi (b/a)^3 a^4}(1+(b/a)^2)$
triangle	$\frac{320\eta L}{a^3\sqrt{3}}$
two plates	$\frac{12\eta L}{h^3 w}$
wide rectangle	$\frac{12\eta L}{h w^3 (1-0.63(h/w))}$
square	$\frac{12\eta L}{h^4 (1-0.917\times 0.63)}$

Electric circuit analogy

In 2012, Kwang *et al.* [29] summarized how to use electrical circuit analogy to describe the relationship between hydraulic properties and channel dimensions/geometry in pressure-driven laminar flow. Microfluidics channels become resistors, pressure generators become batteries and flow rates become currents. The analogy can even be applied to deforming channels (capacitors) and fluid inertia (inductance). An overview of the relevant similarities is provided in Table F.2. Furthermore, using this new analogy several formulas can be compared. Firstly, the Hagen-Poiseuille law can be compared to Ohm's law. Next resistances, either hydraulic or electric, can be combined in parallel and series in the same way. Finally, conservation of mass and energy can be compared to Kirchhoff's current and voltage law, respectively. These similarities in formulation have also been included in Table F.2. With this analogy, the behavior of the pressure-driven laminar flow can be precisely engineered by defining only the channel dimensions and geometry. So it can be useful during the general design of more complex microfluidic systems. However it is important to note that there are limitations as for example Ohm's law only describes averages but does not provide detailed information about the local flow field itself.

Table F.2: The physical similarities between microfluidics and electronics: the electric circuit analogy, adapted from Kwang [29]

Fluidics	**Electronics**
Volumetric flow rate $Q[m^3 s^-1]$	Electric current $I[A]$
Pressure drop $\Delta p[Pa]$	Voltage drop $\Delta V[V]$
Hydraulic resistance $R_H[Pas^3 m^-1]$	Electric resistance $R_E[\Omega]$
Microchannel segment (fluidic resistor)	Conductive wire (electric resistance)
External pump	Battery
Atmospheric pressure p_{atm}	Floating ground
Hydraulic compliance $C_H[m^3 Pa^-1]$	Capacitance $C_E[F]$
Inertia	Inductance $L[H]$
Hagen-Poisseuille's law $\Delta p = Q R_H$	Ohm's law $V = I R_E$
Equivalent series-connected fluid resistors	Equivalent series-connected electric resistors
$R_{H,eq} = R_{H,1} + R_{H,2}$	$R_{E,eq} = R_{E,1} + R_{E,2}$
Equivalent parallel-connected fluid resistors $R_{H,eq} = \frac{R_{H,1} * R_{H,2}}{R_{H,1}+R_{H,2}}$	Equivalent parallel-connected electric resistors $R_{E,eq} = \frac{R_{E,1} * R_{E,2}}{R_{E,1}+R_{E,2}}$
Law of mass conservation (at node) $\sum Q_n = 0$	Kirchhoff's current law (at node) $\sum I_n = 0$
Law of energy conservation (in closed path) $\sum \Delta p_n = 0$	Kirchhoff's voltage law (in closed path) $\sum V_n = 0$

F.2.5. Multiphase flow

The definition of multiphase flow in fluid mechanics indicates the simultaneous flow of materials with two or more thermodynamic phases [30]. The following section will be focused on the physics driving specifically two-phase flow (transport liquid and liposomes) as is encountered in the DDS.

Analytical fluid-particle interaction

The interaction between the fluids and particles, liposomes in this case, can be determined by evaluating the Navier-Stokes equations [31]. Assuming no external forces are applied to an incompressible Newtonian fluid, the stress tensor is composed of a pressure part and a viscous part as follows:

$$\boldsymbol{\sigma} = -p\mathbf{I} + \eta\nabla\mathbf{u} \tag{F.17}$$

Where σ is the stress tensor and $\mathbf{I}$ the identity tensor. By integrating the stress tensor around the surface of the particle, the total force acting on the particle can be found. This force needs to be coupled to the equations of motion of the particle, commonly known as Newton's second law, resulting in:

$$m\frac{dv}{dt} = \int_A \boldsymbol{\sigma}\cdot\hat{n}\,dA \tag{F.18}$$

Stokes drag

If the liposome is considered a rigid spherical body in low Reynold uniform flow, the drag force acting on the particle has been shown to have a simple solution [18]. The resulting drag force is called Stokes-drag. When considering a sphere in a viscous fluid moving at a uniform speed of u_0 at low Reynolds number the Stokes drag can be calculated using Equation F.19.

$$F_{drag} = 6\pi\eta a u \tag{F.19}$$

Lateral particle migration

Besides longitudinal movement, lateral migration of particles should also be considered. The rotation of a particle and presence of channel walls creates several forces acting on the particles in flow. These forces include the rotation lift (Magnus) force, slip-shear lift (Saffman) force and wall lift force and together influence the lateral migration of particles.

The Magnus force is caused by the rotation of a particle in a uniform flow field. Assuming no-slip condition for the fluid at the boundary, the relative fluid velocity is different for each side of the particle. According to the Bernoulli principle this creates a pressure difference and associated lift force termed the Magnus lift force. The Saffman force is a lateral lift force resulting from the interaction of the velocity of the particle compared to the velocity gradient of the flow. The resulting force is exerted towards the region in which there are higher relative speeds [32]. The wall-induced lift force is caused by the change of flow field around the particle in the presence of walls. When considering only one wall, the main effect is deceleration of the particle and forcing it away from the wall [33]. When considering two walls close to the particle, the effect is significant deceleration of the particle [33].

Among them, Magnus force is often very small and negligible. The Saffman lift force directing particles toward channel walls, and wall lift force repulsing particles towards the middle of the channel, are commonly recognised as the dominant effects for the lateral migration of the particle [33]. The balance between these forces determines an equilibrium position for the particles in the channel.

Dean flow

Dean flow is another phenomenon that can cause lateral particle migration. It refers to a secondary flow pattern that arises in curved channels. When a fluid flows through a curved channel, the combination of the centrifugal force and the inertia of the fluid create a unique flow pattern. The centrifugal force pushes the fluid toward the outside, leading to higher pressure on the outer wall of the channel. To balance this, a pair of rotating vertices forms, creating the Dean flow. These vertices can influence the lateral equilibrium position of particle(s).

By assessing the Dean number, calculated using Equation F.20, the strength of the secondary dean flow can be determined. Here Re is the Reynold number, D the diameter of the channel and R_c the radius of curvature. A higher Dean number corresponds to stronger dean flow.

$$De = Re\sqrt{\frac{D}{2R_c}} \tag{F.20}$$

Deformable particles
Since liposomes are considered to be highly flexible [34], the rigid assumption made before does not apply. Assuming linear elastic behavior, the deformation can be calculated using Hooke's law, where E is the Young's modulus and ϵ is the elongation.

$$\sigma = E\epsilon \tag{F.21}$$

However, for large strain the liposomes do show that non-linear contributions from area dilatation of the shell start to dominate [34]. The newly introduced physics complicates the interaction between the fluid and the liposome. In order to capture the behavior of the liposomes in the microfluidic system, several approaches have been studied and summarized [35]. The particle could be modeled as a solid sphere which can deform with a specific elastic constant [36]. Next the particle can be modelled as a liquid drop [37]. Lastly, the particle can by considering to be a deformable capsule [38–40]. This technique considers capsules as liquid drops surrounded by thin elastic membranes. In order to make an informed choice of model which best resembles liposomes, the mechanical behavior of the liposomes needs to be examined, which will be done in section F.4.

F.2.6. Surface tension

As mentioned in subsection F.2.2 due changing surface-to-volume ratio in microfluidics surface effects, such as surface tension, play a vital role whereas they can be mostly ignored in macrofluidics. Molecules and atoms experience attractive forces due to van der Waals forces or dipole interactions. At a boundary between different media these forces are unbalanced, since the attractive forces of the second medium will likely be different than that of the first one. This difference is characterized by the surface tension γ. Since surface tension is dependent on all the surrounding media, it is generally found experimentally. It is furthermore important to note that the surface tension is also a function of temperature [41]. However, since the DDS will be in a temperature controlled environment, this effect has been left out of scope. The energy stored by surface tension can be found in Equation F.22, where S is the total surface area. This formula is the basis of the effects of surface tension as, in absence of other forces, the energy stored in surface tension is minimized.

$$E = \gamma S \tag{F.22}$$

For the DDS, it is important the filled liposomes will not leak into the brain and surface tension can be used to make sure this does not happen. Determining the pressure at which a liquid will break surface tension and flow out of a channel through an opening involves considering the Young's-Laplace equation, which relates the pressure difference across an interface to the surface tension and the curvature of the interface. The equation is as follows [42]:

$$\Delta p = -\gamma\nabla\cdot\hat{n} = -2\gamma\kappa = \gamma(\frac{1}{R_1}+\frac{1}{R_2}) \tag{F.23}$$

Where $\hat{n}$ is the unit normal pointing out of the surface, κ is the mean curvature and R_1 and R_2 the principle radii of curvature. For a circular opening or pore in the absence of external forces, the pressure required to overcome the capillary action due to surface tension can be simplified to Equation F.24.

$$\Delta p = \frac{2\gamma}{R} \tag{F.24}$$

F.2.7. Clogging

Another phenomenon that occurs due to surface effects is the adhesion of particles to the channel walls. The resulting clogging of the channels has been shown to cause problems in microfluidic systems, an overview of relevant research has been made by E. Dressaire and A. Sauret [43]. Several mechanisms can be responsible for causing clogging: sieving, bridging and aggregation of particles. See Figure F.5 for a schematic representation of the different mechanisms.

Since the ratio of the liposome diameter (d) and channel dimensions (D) will be roughly the same, mainly sieving (where $d \geq D$) will be considered in this section. During sieving liposomes will stick to the surface of the channel, which can either be exploited or cause problems. Research shows that there exists a threshold for which this occurs. If hydrogel is considered as flowing through a narrow channel the threshold value can be determined using Equation F.25 [44] where E is the Young's modulus, d is the diameter of the particle and D is the diameter of the microchannel. It is important to note that this equation is meant for a hydrogel with the linearly elastic deformation, which might not be the case for the liposomes.

$$\Delta p_{\max} \propto E \left(\frac{d}{D} \right)^{14/3} \tag{F.25}$$

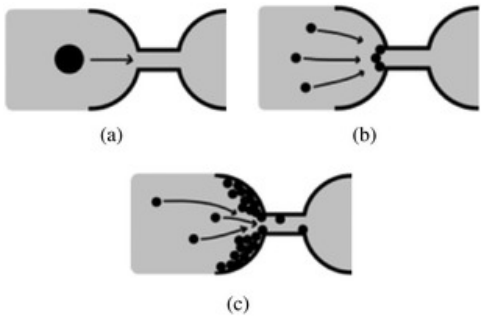

Figure F.5: Different mechanisms responsible for the clogging of microchannels: (a) sieving, (b) bridging and (c) aggregation of particles. The mechanism(s) involved depend on the size of the particle compared to the constriction, the concentration of the suspension and the particle–wall and particle–particle interactions [43].

F.3. Microfluidic Particle Manipulation

An important aspect of the DDS is to accurately control the position of liposomes, such that there is enough time for the drugs to leave the capsule and enter the brain. In order to accomplish this a stop-and-go principle is desired. This approach entails the liposome decelerating or halting entirely upon reaching an opening, allowing for a controlled release of its drugs, before proceeding, thereby making space for subsequent liposomes.

In order to realize this stop-and-go principle, the microfluidic system must ensure the following. (1) The liposomes should be selectively placed at open pores. (2) Upon reaching the opening, the liposomes should be retained inside the system. (3) After drug delivery, the liposomes should leave the pore and be replaced by a new one. Based on this functionality, different areas of research have been studied. Firstly, microfluidic single cell/particle manipulation techniques will be covered in subsection F.3.1. Next the capillary burst valve and droplet trapping will be discussed in subsection F.3.2 and subsection F.3.3 respectively as these topics could provide valuable insights on how to retain liposomes at the pores of the DDS. And finally specific liposome and other lipid vesicle trapping in combination with microfluidics will be discussed in subsection F.3.4 in order to complete the state-of-the-art. The chapter concludes with the literature gaps in subsection F.3.5.

F.3.1. Microfluidic trap-and-release techniques

Particle control in microfluidic systems has been studied extensively [45–49] and several techniques have been developed. Recently, a comparison of all different techniques has been made by Gong *et al.*

[50] and can be found in Table F.3 and Table F.4. The overview contains the complete landscape of trapping and releasing mechanisms found in literature. They can be categorized into different groups: passive physical, active physical, biochemical and hybrid mechanisms. It is important to realize that, depending on the application, a specific combination of trap and release mechanisms is favorable.

Due to time constraints not all methods are to be extensively studied in this literature review and focus would be put on passive physical and biochemical categories. This leaves the following techniques: hydrodynamic, inertial, immuno-affinity binding and aptamer-affinity binding. As the goal of this project is to develop a *proof-of-concept*, simplicity is of high importance and the best category complementing this requirement is passive physical. Biochemical methods do offer a promising building block to enhance the systems performance, however due to foreseen difficulties with selectively introducing these biochemical modifications, it is considered to be the back-up to passive physical methods in case these do not provide sufficient control. Several techniques have been excluded from this study as they introduce undesired effects to the brain such as electric fields, magnetic fields, sound or temperature control. The excluded techniques include dielectrophoresis, electrokinetic trapping, magnetic trapping, thermophoresis, optical tweezers and acoustic modulation. Furthermore, methods of viscosity modulation and intertio-elasto focusing have been left out as these exploit physics which are not considered in this study; the working fluid is considered to be of constant viscosity, incompressible and Newtonian. Finally, hybrid mechanisms such as microrobots, although offering interesting new possibilities, are deemed too complicated; uncertainty and risks involved during implementation are too high for the proof-of-concept nature of this project.

Hydrodynamic trapping

Hydrodynamic manipulation is one of the most common techniques currently used in microfluidic particle trapping. This method uses strategic obstacle placement and geometry in order to influence the path the particles are most likely to take. Its popularity is based around low costs, fabrication time and simple (passive) operation. However, in order to ensure the trapping efficiency, flow rates are often set to be small [50] and this results in low throughput being the most important disadvantage. In literature, several approaches have been studied that utilize these hydrodynamic effects to isolate particles or cells, broadly categorized into microwells, microarrays and microtraps [51].

Microwells are small cavities in a microfluidic device, designed to hold minute volumes of liquids, cells, or particles usually for analysis. An example design can be found in Figure F.6a. Since microwells form an assembly, they allow high-throughput and parallel assays, which are useful in analytical research in cell biology and medical diagnostic tests [52]. Several studied have been done in order to improve the performance and trapping efficiency of microwells. The optimal height-diameter ratio is reported to be ~ 1 for single cells [53], it has been established that cell density needs to be higher than $5.0 * 10^9$ cells per mL to achieve $> 90\%$ trapping efficiency [54] and shapes (triangle, square, circle, diamond and cone) have been compared resulting in triangles showing the highest trapping efficiency [55]. Another example is the introduction of stretchable PDMS microwells [56]. While stretching the microwell cells are loaded on the array. Next, cells can be trapped on the array by relaxation of the PDMS. This results in a system where no external force had to be applied once the cell are trapped.

Microarrays utilize an array of geometrical shapes or obstacles in order to capture particles, an example design can be found in Figure F.6b. Dino *et al.* [57] were one of the first to show the potential of this principle to capture single cells. Their device consists of arrays of physical U-shaped hydrodynamic trapping structures with geometries that are biased to trap only single cells. Later, several studies have been done in order to increase the efficiency of the method. Different shapes, circular, triangle, square and diamond, have been assessed by Kitagawa *et al.* [58] showing squares have the highest performance. Next, Mesdjian *et al.* [59] showed that the trapping efficiency can be increased by changing the flow orientation of particles w.r.t. the traps to be diagonal. And lastly, Yoon *et al.* [60] showed that adding oscillating flow can get rid of particle segregation as effect of bridging.

Microtraps generally use the principle of relative hydraulic resistance between a trap and bypass channel, see Figure F.7a for a diagram. The trap path (path 1) is designed to have a lower hydraulic resistance than the bypass channel (path 2). A particle in the flow is pushed into the trap and once it physically blocks (part of) the exit, the hydraulic resistance of path 1 is increased drastically. In this case, the resistance of the bypass channel is significantly lower compared to the trap path and flow is redirected.

Table F.3: Summary and comparisons of particle capture techniques [50] from section F.3.

Trapping technique	Advantages	Disadvantages
Hydrodynamic	• Low cost and Fabrication time • High compatibility and integrability • Minimum invasive	• Low throughput • Low specificity and selectivity • Low controllability
Inertial	• Low cost and simple fabrication • Label-free • Continuous operation	• Low throughput • Low versatility • Limited scalability
Electrical	• High controllability • Rapid and continous manipulation • Compatible with complex geometries	• Electrode fouling • Joule heating effects • Sample contamination
Optical	• Precise and high resolution • Force sensing and high controllability • Manipulation in complex environments	• Limited throughput • Challenges with irregularly shaped particles • Restricted to optically accessible samples
Acoustic	• Scalable and simple device fabrication • Continuous and parallel manipulation • Efficient and rapid manipulation	• Challenges in manipulating complex samples • High energy requirements • Challenges with acoustic field uniformity
Magnetic	• Minimal sample perturbation • High compatibility • Scalable and simple device fabrication	• Dependency on magnetic properties • Heating effects and potential sample damage • Interference from external magnetic fields
Thermophoresis	• Biocompatible • Compatible with complex environment • Relatively low energy consumption	• Potential sample degradation or alteration • Complex experimental setup • Limited manipulation range and strength
Microrobots & others	• high versatility • Programmable manipulation • Reduced human intervention and labor	• High cost • Limited sensing and feedback capabilities • Limited payload and navigation

Table F.4: Summary and comparisons of particle release techniques [50] from section F.3.

Release technique	Advantages	Disadvantages
Pulsatile flow	• High compatibility • Non-invasive particle release • High tunability	• Limited efficiency for strongly adhered particles • Potential for clogging • Limited selectivity
Microvalve	• High release efficiency • Non-invasive and gentle release • Integration with automation and robotics	• Low actuation response time • Risk of valve clogging or leaking • Limited scalability
Thermal	• Label-free • Minimal impact on fluid flow • Compatibility with many particle types	• Challenges in temperature uniformity • Limited release efficiency for strong adhesion • Limited compatibility
Electrical wetting	• Rapid and controllable release • Real-time monitoring • Selective and parallel release	• Complexity of electrode design and integration • Sensitivity to sample and liquid properties • Potential for sample damage
Acoustic, and other active-driven methods	• High efficiency • Precise spatial and temporal control • High versatility and capability	• Complexity of system setup • Dependence on particle properties • Potential of sample damage
Surface coating or pH adjustment	• Cost-effective • Compatibility with downstream analysis • Scalability and ease of use	• Lack of selectivity • Particle aggregation or agglomeration • Interference with particle functionality

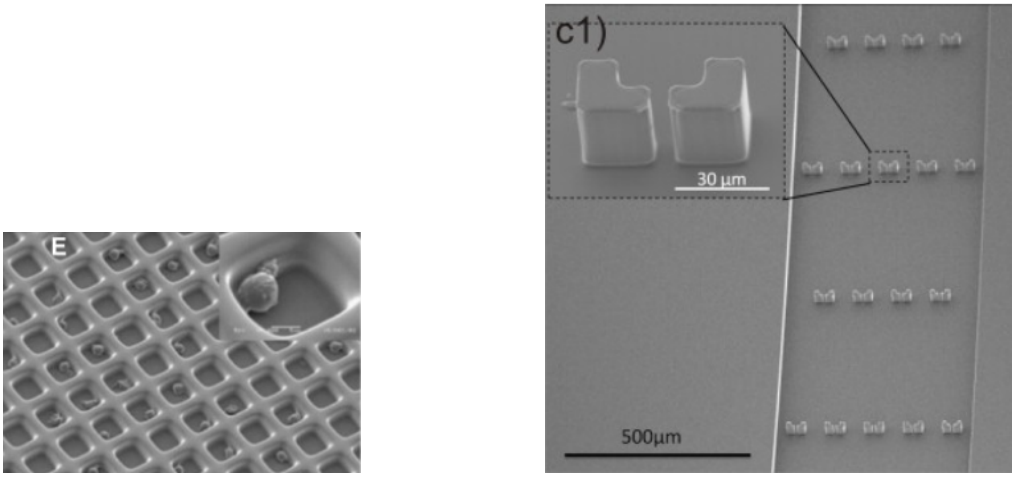

(a) Microwell design [61].

(b) Micro array design [62].

Figure F.6: Examples of designs for cell trapping using the microwell and micro array techniques.

Since this design consist of a trap with an open aperture, the situation is remarkably similar to the one encountered in the DDS. Tan and Shoji [63] were on of the first to show such a microfluidic system, the design used can be found in Figure F.7a. Later, many improvements on this design have been proposed such as minimized bypass channel length [64], deterministic cell trapping using integration of burst valves [65] and increased efficiency by introducing a matrix of cell traps [66], which can be found in Figure F.7b, Figure F.7c and Figure F.7d respectively.

In order to properly trap liposomes in the DDS is the trap region of these hydrodynamic systems is especially interesting. Research by Lawrenz *et al.* [67] focused specifically on this region and looked into the effect of different shapes (triangular, square, conical and elliptical) of the trapping site. The geometries considered can be found in Figure F.8a and trapped particles were stem cells and polystyrene micro-spheres. In order to model the fluidic behavior CFD simulations based on the Navier-Stokes equations were conducted and cell viability was assessed by investigating the induced stresses on the particles by modeling them as non-deformable spherical bodies. They conclude square shapes are best for cell variability while triangular shapes are optimal for high-speed applications. Furthermore, they noticed in their experiments that deforming cells could squeeze through holes which reduced the trapping efficiency. On the contrary, another paper [62] also experimentally examined the shape of traps (rectangular and circular) for a microarray system that was designed to capture cells. The geometries considered can be found in Figure F.8b. In this study, no difference was observed among the geometries of the traps. These contradictory results should be further investigated, with a special focus on highly deformable particles.

Biochemical trapping

Biochemical techniques involve the use of specific bio-molecular interactions. Within biochemical trapping, different approaches have been demonstrated such as immuno- [68], aptamer- [69], and lectin- [70] affinity binding. Binding affinity refers to the specific strength of interaction between two molecules and is typically measured by the equilibrium dissociation constant K_D. The smaller the K_D value, the greater the binding affinity of the molecule for its target, and vice versa.

Immuno-affinity binding is a specific type of affinity binding that involves the interaction between an antibody and its antigen. Antibodies can bind with high specificity and affinity to their corresponding antigens. By strategically introducing target surface markers, a specific region can be functionalized to achieve particle trapping. Chen *et al.* [68] were one of the first to show this principle. Their separation was based on the selective binding of exosomes to anti-CD63 IgG-coated microfluidic channel surfaces. Another approach that utilizes immuno-affinity binding is to bind nano-sized vesicles to micron-sized microbeads. Tayebi *et al.* [71] demonstrated this principle in combination with a microfluidic system and created a device used for the detection of exosomes with a size of 30-150 nm. Their design can be found in Figure F.9. Microbeads with a diameter of 20 μm are functionalized with streptavidin

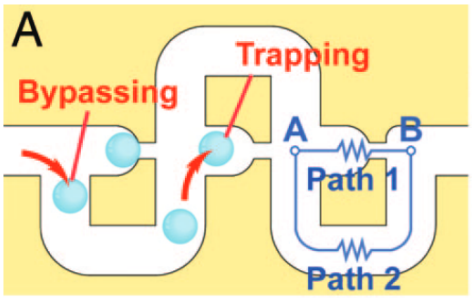

(a) Novel microtrap design based on the least-resistance-path principle [63].

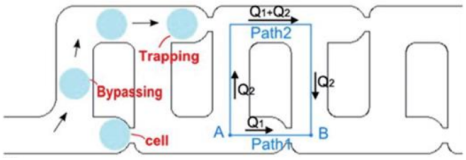

(b) Channel length optimization [64].

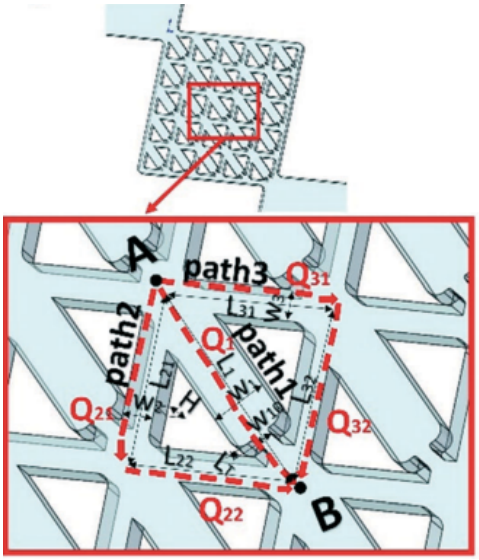

(c) Integration of matrix design for increased throughput [66].

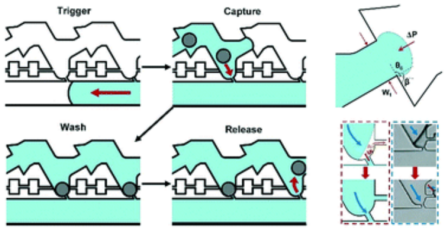

(d) Integration of burst valve into microtrap design [65].

Figure F.7: Different hydrodynamic microtraps proposed in literature.

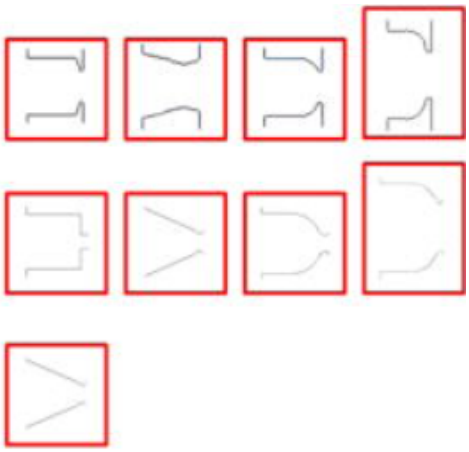

(a) Trap geometries studied by Lawrenz *et al.* [67].

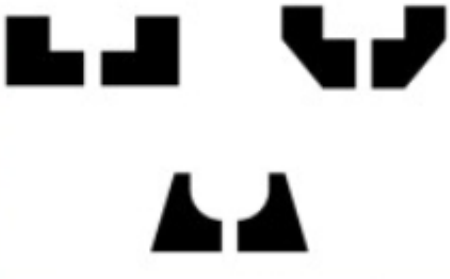

(b) Trap geometries studied by Benavente-Babace *et al.* [62].

Figure F.8: Different geometries studied for microtraps

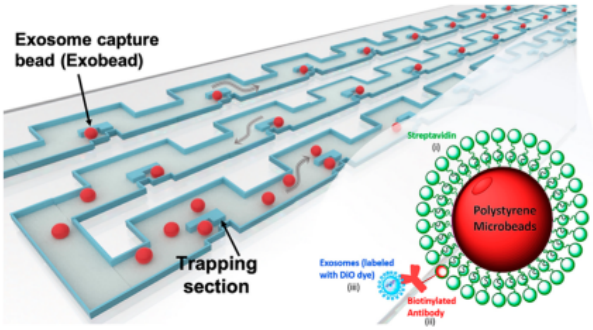

Figure F.9: Schematic diagram of the trapping mechanism by Tayebi *et al.* [71].

and biotinylated antibodies and then used to immobilize and stick exosomes on their surfaces using antigen–antibody affinity binding. By integrating these microbead particles with a passive microfluidic trap, they were able to isolate several exosomes.

Other types of bio-affinity binding include DNA or RNA derived aptamer-based binding, lectin-based binding that can capture viruses and pacteria, and many more. In general, devices that utilize biochemical affinity binding require the substrate to be coated with specific immobilized ligands, such as antibodies [50]. Additionally, it has been shown that the way these ligands are oriented significantly influences the efficiency of the binding process and the choice of substrate material for the chip is also a crucial for performance [72].

Given that biochemical trapping methods, like surface coating or microbead functionalization, involve complicated procedures that could impede the demonstration of the DDS within the thesis timeline, they are not the favored approach. Nevertheless, should hydrodynamic trapping prove inadequate to retain liposomes in the open pores, these biochemical techniques may be considered as an alternative.

Inertial

Inertial microfluidics is a technique that utilizes microchannel geometries and secondary Dean flow to manipulate particles. As notes by Gong *et al.* [50] this technique is often utilized in combination with other methods and trapping efficiency is often limited. Furthermore, they often operate at higher flow rates where inertial effects start to dominate. As the proposed DDS does not operate in this regime and the trapping efficiency is limited, no further examination of this type of system has been done.

Release techniques

For the proposed DDS releasing is assumed not to be part of this thesis [73], the detailed literature review has been left out of this chapter and is included in section F.6. The rational behind this decision is the following: After a liposome is exposed, it will likely be damaged and parts could either enter the brain environment or be carried along the microfluidic DDS. Since all substances used in the system are bio compatible, the release of small liposome parts into the brain is not an issue. If during the experiments it is found the liposomes are still intact after exposure to light, it will be much more valuable to study potential release mechanisms to reuse the liposomes.

F.3.2. Capillary burst valve

From the literature review on microfluidic particle trapping techniques, it can be concluded deformable particles can cause significant issues. In order to better understand how this problem can be solved, other research directions have been pursued. One of them being the capillary burst valve. Although the capillary burst valve is mainly used to regulate flow, the approach and methodology could be extended with regard to retaining a liposome. Capillary burst valves have been studied extensively in research, and different review papers have been published by Olanrewaju *et al.* [74], Wang *et al.* [75] and Azizian *et al.* [76]. The notation in this section is according to the schematic overview as found in Figure F.10.

One of the first to propose a model for a capillary type valve were Zeng *et al.* [77]. The model proposed was based on the Young's Laplace equation as in Equation F.23 and predicted the burst pressure for a circular opening, where θ_c is the equilibrium contact angle of the fluid. However, this model

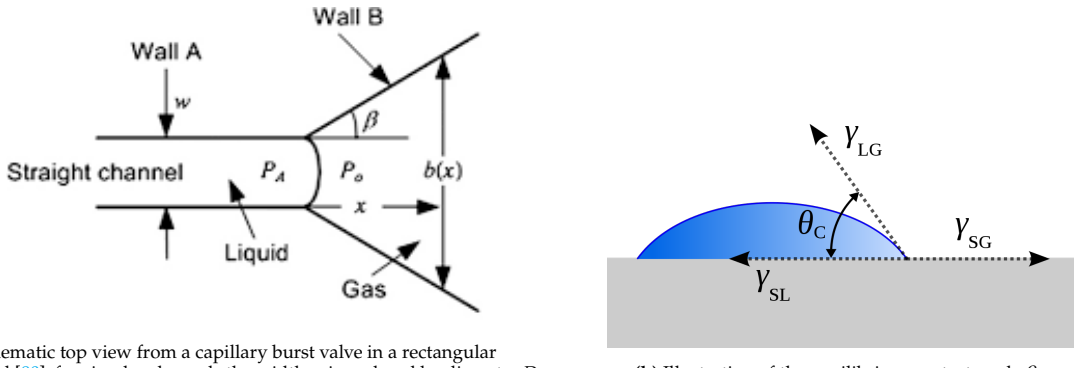

(a) Schematic top view from a capillary burst valve in a rectangular channel [80], for circular channels the width w is replaced by diameter D.

(b) Illustration of the equilibrium contact angle θ_c

Figure F.10: Notation used for burst valves.

did only prove accurate for circular openings and needed to be expended for other cross-sectional geometries. Later, Chen *et al.* [78] expanded this theory and included the expansion angle β as defined in Figure F.10a. The resulting relation between the channel dimensions D and β, surface tension γ and equilibrium contact angle θ_c can be found in Equation F.26a. The results were experimentally validated for $D = 0.1 - 0.25mm$ and $\beta = 30 - 90°$ for water and glycerin solutions on PMMA and PDMS substrates, showing good agreement.

To expand the theory to rectangular channels with height h and width w, Chen *et al.* [79] model the capillary burst pressure according to a 3-D meniscus approach and also include the expansion angle β. The resulting formula from their research can be found in Equation F.26b. This model was tested for different aspect ratios and expansion angles of $30° - 100°$. It proved to be accurate for widths up to $300\mu m$, expect for wider channels with high expansion angles ($80° - 100°$) where burst pressures was 10% lower than predicted.

$$\Delta p_{cap,cir} = \frac{4\gamma \cos\left(min\{\theta_c + \beta, \pi\}\right)}{D} \tag{F.26a}$$

$$\Delta p_{cap,rec} = -\gamma \left(\frac{2}{h} \cos\theta_c - \frac{2}{w} \cos\left(min\{\theta_c + \beta, \pi\}\right) \right) \tag{F.26b}$$

In order to better understand how to design a proper burst valve research by Agonafer *et al.* [81] can be utilized. They have studied, for both low and high surface tension, what the most important design parameters are to consider for a burst valve. Low surface tension refers to fluids with $\theta_c \sim 0°$, otherwise the fluid is considered high surface tension. The studied parameters include the effect of the edge radius of curvature and the outer diameter. They use the geometry as can be found in Figure F.11 and defined the radius of curvature R as in Equation F.27. This new radius of curvature, is combined with the Young-Laplace equation as given by Equation F.24. The results conclude that for low surface tension liquids only the outer diameter D is the important design parameter. On the other hand for high surface tension liquids, such as water, burst pressure can show dependence on r if r is significant compared to D. However, it should be noted that the model did underestimate burst pressure for high-surface tension liquids at low outer diameters ($D < 400\mu m$).

$$R(\varphi) = \frac{r\sin(\varphi) + \frac{D}{2} - r}{\sin(\theta + \varphi)} \tag{F.27}$$

Later, Agonafer *et al.* [82] implemented their findings into a silicon membrane that can retain low surface tension liquids via an array of porous micropillar structures. They experimentally find an irregular meniscus shape before the liquid spills along the micropillar edge and attribute this to highly dynamic flow conditions.

Next, different studies have been conducted in order to identify the cause of discrepancies between the theoretical and experimental values. First, research by Mo *et al.* [83], showed that for rectangular

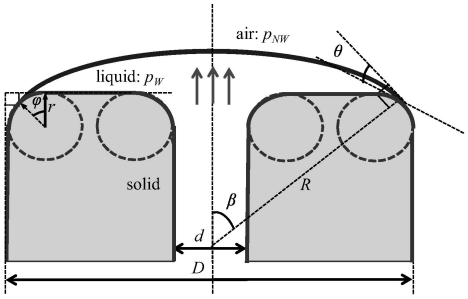

Figure F.11: Schematic of capillary model for a tip defined by outer diameter, D, and angle β defined as the angle between the center-line and the tangent edge to the meniscus radius of curvature R [81].

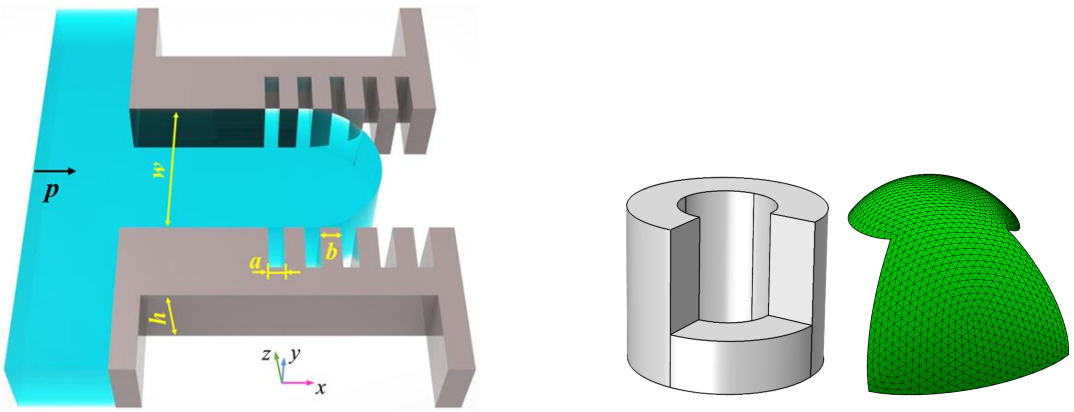

(a) Geometry used by Mo *et al.* [83] in order to examine the effect of surface roughness

(b) Geometry used by Agonafer *et al.* [82] examine the effect of surface defects.

Figure F.12: Geometries used to examine the effect of surface roughness and defects

microchannels, the discrepancies can be accounted for by modifying the Young-Laplace equation to include the effect of surface roughness. By defining surface roughness $\phi_v = \frac{a}{a+b}$, where a and b are defined as given in Figure F.12a, the Young-Laplace equation could be modified to include these effects. The resulting formula for predicting burst pressure can be found in Equation F.28. Results show good predictions for a wide range of channel sizes ($h = 160\mu m, w = 72 - 316\mu m$). However, they do note the model is only validated for the effect of a major parameter-solid fraction ($\phi_v = 0.784$). They also note the influence of other factors such as groove size and surface wettability on the capillary pressure need to be investigated in the future work. Furthermore, their research was limited to only a specific value $\phi_v = 0.784$. So in order to completely validate Equation F.28 there is a need to study different values for surface roughness. Lastly, the research focused on a rectangular channel geometry and needs to be expanded to include other dominant shapes such as a circular channel.

Another study by Agonafer *et al.* [82] tried to explain the discrepancies by examining the effect of surface defects. They did numerical simulations using the geometry as found in Figure F.12b and find surface defects on the outer edge of the micropillar can lower Laplace burst pressure up to 50%. The experimental results are in good agreement with the simulations. However, it should be noted only a single surface defect configuration has been tested. Furthermore, the depth of the particular defect ($2.75\mu m$) is significant compared to to diameter of the burst valve ($5\mu m$) and therefore not completely representative of the defects that are expected to be found in the DDS.

$$\Delta p_{cap,rec} = -\gamma \left(\frac{2}{h} \cos\theta_c - \frac{2}{w} \cos\left(\theta_c + \beta - \phi_v\right) \right) \tag{F.28}$$

Finally, research by Lee *et al.* [84] investigated the maximal burst pressure for aqueous liquids in contact with organic solvents. Their theory, also based in the Young-Laplace equation, examines burst pressure for a circular opening with expansion angle of $\beta = 90°$ and also uses Equation F.26a. They consider two

different cases of failure. The first is once the contact angle reaches 90°. The second is if the geometrical contact angle reaches the equilibrium contact angle. Since the equilibrium contact angle of the fluids tested (ethyl acetate, chloroform, cyclohexane) was lower than 90°, this was the limiting condition. This once more shows the importance of validating the equilibrium contact angle when evaluating the Young-Laplace equation.

F.3.3. Droplet microfluidics

Another field or research that might provide better understanding of highly deforming particles is droplet microfluidics. Generally this science is about generating and manipulating discrete droplets through immiscible multiphase flows in microchannels. Recently, its applications in the biomedical industry have been studied, such as: single-cell encapsulation [85] [86], cell sorting [87] and microreactors [88]. Even though the DDS does not specifically use droplets, the highly deformable liposomes could be compared to droplets.

Many studies have been found that use microfluidic platforms to trap droplets combined with the techniques as described in subsection F.3.1, for example a microarray [89] or microtrap [90]. The respective designs can be found in Figure F.13a and Figure F.13b. Next, an interesting design has been introduced by Simon *et al.* [91], which uses a skewed chamber to capture droplets using the Laplace pressure. The release could be achieved by either increasing the pressure or by fusing the droplet with another fluid from the top channel. The design can be found in Figure F.13c. Most recently, Hoang *et al.* [92] examined the effect of the angle α of the contraction using geometry as found in Figure F.13d and they find a critical value for the capillary number (Ca_{1c}) for which trapping occurs. This relation is observed to be $Ca_{1c} = a(C^M - b/\alpha)$, where M, a and b are fitted parameters.

From the literature on droplet trap designs [89–92], it can be generally concluded that the trapping behavior of the droplets is modeled using the Young's-Laplace equation as found in Equation F.23 combined with the pressure drop over the channel as found in Table F.1. In all studies incorporated in this review, the evaluation resulted in good agreement with FEM/CFD simulations and experimental results. Therefore it can be concluded that for droplets this is an effective approach, however it remains to be seen if this approach accurately predicts liposome trapping behavior.

F.3.4. Specific GUV trap-and-release systems studies

Only a handful of studies have been published that studied microfluidic manipulation of liposomes or comparable particles. This section provides an overview of what has been achieved concerning specifically giant unilamellar vesicles (GUVs). GUVs are vesicles with a size bigger than 1 μm which are comparable to the liposomes used in this project.

Firstly, Yamada *et al.* [93] have studied the trapping and releasing of GUV in a microwell trap. The geometry they used can be found in Figure F.14a. According to them, the trapping results from the reduction of the membrane elastic energy, which is stored in the GUV as it squeezes to enter into the thin channel. They consider two types of elastic energy, bending and stretching. In order to calculate the bending energy, they make use of Equation F.29a where κ is the mean curvature of the GUV and k_c is the bending rigidity. In order to calculate the stretching energy, they evaluate Equation F.29b, where K_A is a material constant that depends on the lipid composition. It is important to note this formula is only valid under the assumption of an high-tension ($\sigma > 10^{-4} N m^{-1}$) regime. In order to determine the mean curvature κ and stretching ΔA, geometric information of the shape of GUVs under different flow conditions is assessed through confocal microscopy. Furthermore, they show that GUVs can be untrapped by increasing fluid velocity beyond a critical velocity.

$$E_b = \frac{k_c}{2} \int \kappa^2 \, dA \tag{F.29a}$$

$$\Delta E_s = K_A \frac{\Delta A^2}{A_0} \tag{F.29b}$$

Next, Nuss *et al.* [94] present a micro array which is able to trap and release hundreds of GUVs with a wide range of sizes from 2 to 40 μm. The geometry they use can be found in Figure F.14b. They

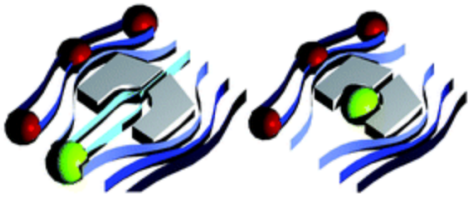

(a) Schematic diagram of the droplet trapping arrays [89].

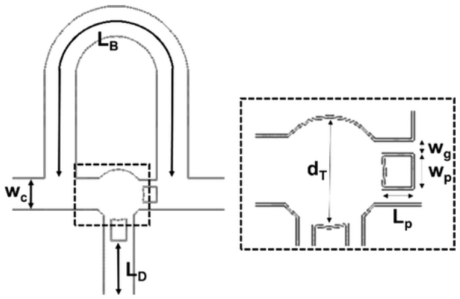

(b) Schematic diagram of the droplet microtrap design [90]. The box with dashed outlines shows a close-up view of the trap dimensions.

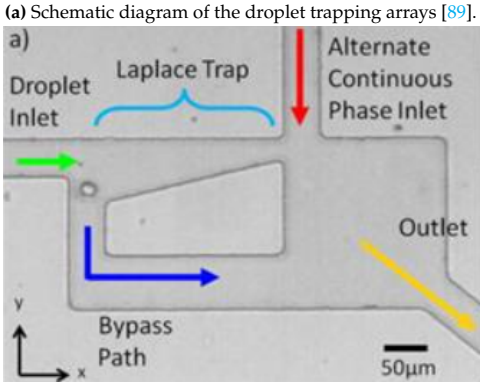

(c) Image of the Laplace trap [91].

(d) Schematic diagram of the droplet trapping design [92].

Figure F.13: Illustration of the droplet traps in this section.

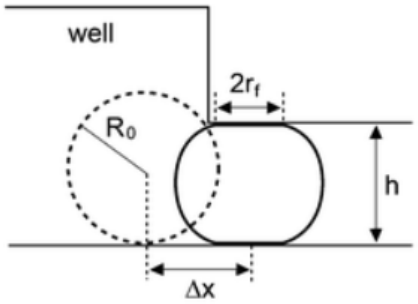

(a) Schematic diagram of the vesicle confined inside the microchannel by Yamada *et al.* [93].

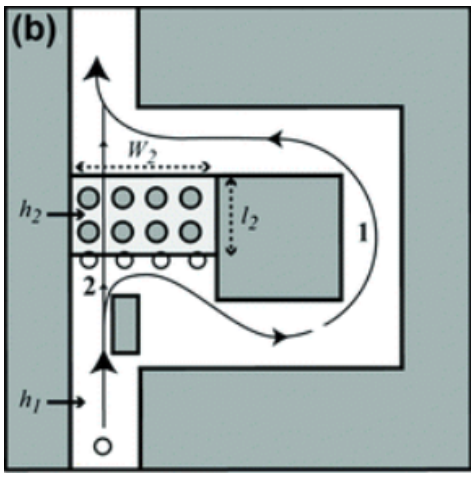

(b) Schematic diagram of the microfluidic trap by Nuss *et al.* [94].

Figure F.14: Geometries used for GUV trapping devices.

also reason the trapping ability is dependent on the deformability of the objects, however theoretical modeling is not present i.e. only experimental validation has been provided.

F.3.5. Literature gaps

Trap-and-release mechanisms

In summary hydrodynamic trapping methods offer a simple, easy to fabricate and low cost solution compared to their active alternatives such as inertial, biochemical and surface modulation. Mainly geometry and flow calculations are required to design an efficient trapping mechanism. However, since this field is still in early stage, several challenges are to be solved in order to design a functional DDS as proposed in this review. Firstly, although it has been shown that the shape of the trapping site can have a significant impact on the trapping efficiency of the system, there are contradictory claims to which is optimal [62, 67] and further optimizations within these shapes can be investigated. These optimizations include for example dimensional analysis, the angle of the triangular trap, width of the square trap, the radius of the circular trap or the implementation of completely new geometries. Secondly, since deformable particles have been identified to negatively impact trapping efficiency [52, 62, 67] as they are capable of squeezing through apertures, the impact of deformable particles on trapping efficiency should be addressed. In the state-of-the-art literature, this phenomenon has been explored exclusively through experimental methods and accurately predicting this behavior has not been done yet. Lastly, these systems are mostly used for high-volume cell capture for analysis purposes and are therefore operated for a significantly long time after which most of the traps have been filled. System performance is typically defined as trapping efficiency; the ratio between filled traps and total traps. However, compared to the conventional system performance matrix of trapping efficiency, the DDS performance is rather based on the ability to quickly refill a pore after light exposure to achieve adequate drug release. Therefore accurate predictions and optimization of the refill time are required.

Besides the gaps that need to be filled in order to create a functional prototype, other research directions have been identified that could increase the efficiency of the system or add new functionality. Firstly, specificity of the microfluidic mechanism should be addressed as this could enable the implementation of different types of liposomes for multi-drug purposes. Next, the impact of surface roughness has not been investigated yet while they could prove beneficial to trap liposomes by locally varying the surface roughness.

Predicting behavior

To summarize, the behavior of both burst valves and droplet microfluidics is modeled using the Young's-Laplace equation. Relations between design parameters and burst pressure have been examined for both circular and rectangular channels. However, still gaps in literature remain that need to be solved in order to properly predict trapping behavior for the proposed DDS. Firstly, the integration of a deformable particle in a liquid medium, instead of the fluid-fluid or fluid-air interface, has yet to be investigated. Furthermore, different geometries as proposed right now could be examined. And lastly, despite the first steps made by Mo *et al.* [83] and Agonafer *et al.* [82], the effect of surface roughness and defects is still to be included into the modeling approach for a wide range is values, different geometries and defect shapes.

Next, the modeling of trapping behavior using bending and stretching energy has shown to be effective for a specific configuration of a microwell [93]. However, as the modeling is depending on the restricted movement of the GUV, there is a need to examine if this model is accurate in the configuration of the proposed DDS.

Besides the gaps that need to be filled to predict trapping behavior, others potential research directions have been identified. The inclusion of flow momentum/dynamic effects, temperature dependence [81] and evaporation effects [81] are to be added into the modeling.

Broadly recognized literature gaps

Other topics that have been often noted in literature as possible improvements for microfluidic systems are the re-usability [75] and simplification of production and handling procedures [51, 74, 76]. Although this is not essential to establish the proposed DDS, these investigations could significantly improve the functionality and commercial viability of the DDS in the future. Therefore, results from these investigations should be closely watched and implemented into the proposed DDS.

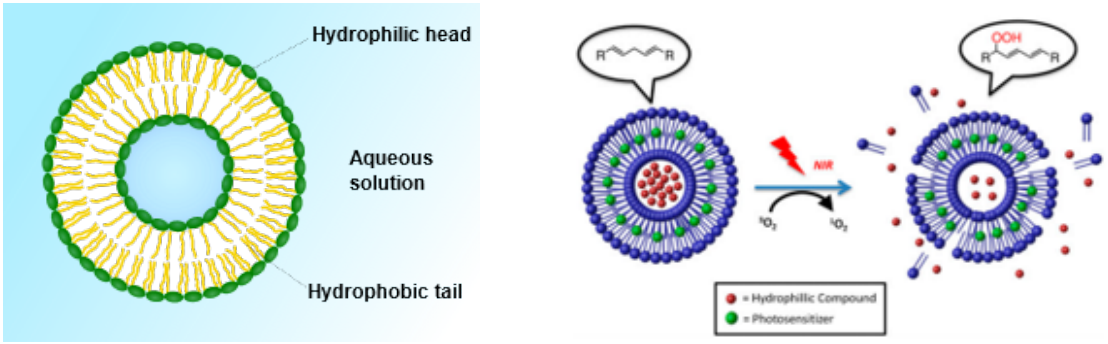

(a) Diagram of a liposome.

(b) Schematic of photo triggered cargo release from liposomes [98].

Figure F.15: Overview of light-activated liposomes.

F.4. Liposomes

Liposomes are micro- or nano scale vesicles that have an aqueous core encapsulated within lipid bi-layers. An illustrative diagram can be found in Figure F.15a. Hydrophilic drugs can be encapsulated in the aqueous core, and hydrophobic drugs can be loaded into the lipid bilayer [15]. As several liposomal formulations have already been approved by the FDA for clinical use [95, 96], they propose a promising vesicle for drug delivery. There are different triggering stimuli that can be considered to release drugs from the liposomes, recently summarized by Salkho *et al.* [97]: pH, ultrasound, light, magnetic field and hypothermia. Among them, light-triggered release is one of the most promising stimuli, as light is relatively safe and allows for accurate spatiotemporal drug release. In Figure F.15b an example schematic light-activation technique can be found. This section provides an overview of state-of-the-art liposome research, focused on the light-triggered ones. In literature, there is a strong focus on different chemical configurations to improve the performance of liposomes. However, as this thesis is on manipulation of liposomes, instead of the synthesis of the vesicles themselves, the literature review presented in this chapter is skewed towards the practical use of the liposomes. First, literature on the characterization of liposomes has been summarized in subsection F.4.1. The goal of this section is to identify the constants that are necessary to model the trapping behavior of the liposomes. Next, various light based actuation methods will be explored in subsection F.4.2, followed by a discussion on different light parameters in subsection F.4.3. Lastly the phototoxicity, an inherent side effect of using light, will be discussed in subsection F.4.4. To conclude the chapter, the literature gaps identified have been summarized in subsection F.4.5.

F.4.1. Liposome characterization

Typical research characterizes liposomes by size, drug concentration, loading efficiency. For this project, other parameters are necessary in order to model the behavior of the vesicles; namely mechanical properties such as surface tension, bending rigidity and burst pressure. Different experimental studies have been conducted in order to access these properties using techniques such as micropipetting [99] and optical tweezers [100]. Reported values of surface tension are in order of 10^{-6} $[N/m]$ [100] and reported values of bending rigidity are in order of $20 - 30$ $[\kappa_B T]$ [100]. Reported values of elasticity are in order of $0.3 - 3$ $[N/m]$ [101]. The resulting properties cannot be assumed to be valid as they are dependent on the specific chemical composition of the liposome but rather serve as an estimation during the design of the system.

F.4.2. Light-based actuation methods

Drug release from liposomes can be triggered by light through various mechanisms, primarily classified as either photochemical or photophysical. Photochemical activation works by destabilizing the lipid membrane through light-induced processes such as isomerization, cleavage, or polymerization of its components. In contrast, photophysical activation induces alterations in the membrane through non-chemical methods, leveraging thermal and/or mechanical processes to cause physical changes of the liposome. Examples of photochemical processes are photoisomerization, photopolymerization, photosensitization-induced oxidation, photo driven hydrophobicity changes and polymer backbone

photo-degradation [102]. Examples of photophysical processes are molecular absorbers and plasmonic gold nanoparticles [103]. Detailed explanations on how each of these techniques work have been summarized in several reviews [15, 103–106].

F.4.3. Light parameters

For the DDS, it is important to achieve adequate control over the opening of liposomes. In order to maximize the systems performance, the liposomes need to open quickly depending on the presence of light. As light triggers the opening of liposomes, the specific laser parameters are of influence. Recently in 2022, Yuan *et al.* [107] have summarized research on repetitive drug delivery using light-activated liposomes, including an overview of different laser parameters used. From this overview, which can be found in Table F.5, it can be deducted that in general the wavelength is in the order of $\sim 300 - 900[nm]$, laser power $\sim 0.5 - 5[Wcm^{-2}]$ and exposure time $\sim 1 - 10[mins]$.

When considering wavelength, research has shown all spectra from UV to NIR can be successfully integrated to achieve light-triggered drug release. Most of the liposomes developed to date respond most efficiently to UV or visible light [102]. However, recently NIR has been predominantly chosen over UV & visible light due to its improved safety resulting from the low adsorption by blood and water [104] and greater depth of penetration [102]. However, depending on the specific composition of the liposome, the optimal absorption wavelength might change and therefore examination of the absorption spectrum is required during the design in order to select a proper laser.

In order to enhance the tissue penetration with NIR laser, one promising development is the demonstration of two-photon approach [108], in which two photons are simultaneously absorbed by the vesicle to artificially transform NIR into UV light. This effect could be leveraged in the DDS to increase spatial resolution. When using a focused laser only a tiny volume facilitates excitation, as the probability of excitation by two-photon adsorption is proportional to the square of the intensity [109]. Although it is noted by Leung and Romanowski [104] that the delivery of focused laser pulses as required for two photon processes may create a technological challenge, it could prove useful to achieve unidirectional opening of liposomes as desired in the proposed DDS.

To expand on typical pulse duration, recent studies have experimented with pulsed nanosecond [110] and femtosecond [111] lasers instead of continuous ones. A comparison between CW and femtosecond laser has been made by Sahu *et al.* [112], showing the overall increase in temperature is lower when using the pulsed laser compared to the CW laser with the same light energy. This suggests two separate mechanisms and different potential applications according to the researchers.

In evaluating the release time in current liposomal research, the prevalent magnitude of minutes, may potentially constrain the dose that can be administered with the DDS. Most solutions propose new elements to be added in order to improve the release time. For example, Luo *et al.* [113] propose the addition of 5 molar percent of an unsaturated phospholipid such as dioleoylphosphatidylcholine (DOPC) resulting in sub-minute drug release upon NIR light radiation. Wu *et al.* [114] propose the addition of hollow gold nanoshells resulting in release in the order of seconds with NIR pulsed light.

When considering laser parameters, generally it can be concluded a minimal threshold for laser power and exposure time are necessary to start significant release [115]. However, the specific values vary considerably in each study and are hard to compare because of different variables such as chemical composition and actuation mechanisms.

F.4.4. Safety

Existing systems predominantly respond to UV or visible light as the relatively high energies are required. However, this comes with inherent concerns regarding the phototoxicity of UV radiation and resulting tissue damage. Despite significant advancements in developing photosensitizing strategies, the complexity and the associated formation of reactive oxygen species in many photosensitizers may hinder the widespread medical adoption of photochemically-controlled liposomal content release [104]. Systems sensitive to Near-Infrared (NIR) light, such as those using gold particles, offer enhanced potential due to deeper light penetration and reduced biological interference. However, challenges such as material toxicity, tissue accumulation, and cargo thermal stability remain to be addressed comprehensively [102].

Table F.5: Light parameters used for repeated drug release. Copied from [97].

Repeatability type*	Wavelength	Laser Type	Laser power	Laser duration	Laser interval	Repeat times
C	808 nm	CW	15 W/cm2	15 s	60 s	4
	1064 nm	Femtosecond	6 W/cm2	5 s	3 mins	4
D	808 nm	N/A	1 W/cm2	15 min	15 mins	6
	808 nm	CW	1 W/cm2	10 mins	20 mins	4
	860 nm	CW	2.4 W/cm2	10 mins	24 hr	2
	308 nm	Nanosecond pulse	5000 W	10 ns	2 s	6
	808 nm/ 805 nm	CW/ femtosecond pulse	1 W/cm2	10 mins	30 mins	4
	250 nm	CW	60 W	2.5 mins	5 mins	4
	350 nm/ 450 nm	CW	500 μW/cm2	120 s/ 180 s	5 mins	3
	365 nm	CW	8 W	5 mins	0**	4
	658 nm	CW	240 mW/cm2	NA	5 mins	4
	730 nm	CW	55 mW/cm2	3 mins	3 mins	5
	785 nm	CW	3.5 W/cm2	10 mins	0	4
	800 nm	CW	1.2 W/cm2	30 s	0	2
	808 nm	CW	4 W/cm2	5 mins	1 h	3
	808 nm	CW	3 W/cm2	5 mins	30 mins	3
	808 nm	CW	2 W/cm2	3 mins	4 h	5
	808 nm	CW	2 W/cm2	5 mins	4 h	2
	808 nm	CW	2 W/cm2	5 mins	1 h	8
	808 nm	CW	2 W/cm2	5 mins	4 h	5
	808 nm	CW	1.5 W/cm2	3 mins	NA	3
	808 nm	CW	1 W/cm2	5 mins	2 h	3
	808 nm	CW	1 W/cm2	4 mins	6 mins	4
	808 nm	CW	1 W/cm2	5 mins	2 h	3
	808 nm	CW	0.8 W/cm2	2 mins	58 mins	3
	808 nm	CW	42 mW/cm2	1 min	NA	4
	808 nm	CW	6 W	5 mins	4 h	2
	980 nm	CW	7.8 W/cm2	30 mins	0.5 h	6

* C and D stands for constant drug amount released and decreasing amount released, respectively.
** 0 stands for continuous irradiation with no cooling time.

Safety standards for lasers have been established in ANSI 2000 [116] regarding wavelength, power, duration and distance. Furthermore, for ocular applications Delori *et al.* [117] provided detailed insights into the application of these safety standards. Although general guidelines are provided in ANSI2000 for medical applications, it should be noted that no research has been found on guidelines for light specifically in brain applications.

In research focused on light-actuated liposomes for drug delivery, phototoxicity predominantly arises in applications necessitating deeper penetration of light into organic tissues. However, in the context of the proposed DDS, the proximity of the light source to the liposomes might alleviate the phototoxicity concerns as it is not necessary for light to significantly penetrate tissues. Due to time restraints and the proof-of-concept goal of this thesis, concerns regarding *in vivo* safety have been left out of scope. Future research could improve on this aspect.

F.4.5. Literature gaps

Firstly, in existing studies liposomes are predominantly suspended in static fluids, rendering drug release reliant on diffusion mechanisms. However, within the context of the proposed DDS, drug release could be influenced by forces introduced through microfluidic system [73], necessitating a thorough examination of the implications of this novel operational environment.

Furthermore, current research generally subjects the liposomes to light exposure to examine the omnidirectional release. In contrast, within the purview of the proposed DDS, it is desired for the medicine to predominately move out of the pores into the cerebral environment. Therefore it is necessary to investigate how light parameters such as intensity, duration of exposure, and beam diameter, influence drug release explicitly towards the brain-side of the system.

F.5. Design, Fabrication and Testing

In order to demonstrate the proof-of-concept DDS, the system needs to be correctly designed, fabricated and tested. Therefore literature on these topic has been reviewed. It should be noted that the objective of this section is not to identify literature gaps, but rather to serve as background knowledge that can be used during the MSc Thesis project.

F.5.1. Modeling techniques

As the scope of the thesis is not to develop a new modeling technique, but to develop a functional prototype DDS [73], model development has been left out of scope. However, in order to properly design a microfluidic system, numerical simulations or models will be assessed to hypothesize behavior and optimize performance. Therefore it is important to select the optimal software package, and have a comprehensive understanding of the impact of different options such as mathematical models for flow and particle interaction.

Software package

Available CFD software packages to TU Delft students are Ansys Fluent and COMSOL Multiphysics. Different software packages have been utilized in research in order to simulate flow and the interaction with deformable particles. An overview of modeling methods used in research has lately been created by Carvalho *et al.* [118], showing COMSOL Multiphysics was the most used software package, followed by Ansys software. Coincidentally, the same software packages as are available. Research comparing Ansys Fluent to COMSOL Multiphysics for multiphase flow is non-coherent in determining the more accurate, faster and memory efficient software package [119–121]. Therefore, the specific model approach and boundary conditions are likely to have more impact on simulations than the software package used. The prior experience with COMSOL Multiphysics results this software package being preferred.

Modeling approach

Carvalho *et al.* [118] highlight some important considerations for modeling flow and particle interactions. Firstly, the importance of parallel use of numerical analysis and experimental validation to improve the performance of the microfluidic device. Furthermore, to increase the accuracy of results, an often forgotten step is mesh quality and independence control. This can be ensured by doing a mesh-convergence sweep [122]. And lastly, they generally notice numerical studies do not include sufficient details in their report about the simulations making it unfeasible to reproduce the results.

F.5.2. Materials

To select the proper material for the DDS, an overview of state-of-the-art materials for microfluidic systems has been created. These materials can be organised into different groups, namely: inorganics (metal, glass, silicon, ceramics), elastomers, thermoplastics, thermosets and hydrogels. Each of these material groups have different properties, which have been summarized by Adelina-Gabriela Niculescu *et al.* [123] in Table F.6. More details about applications, advantages and drawbacks on each of these categories have been provided below. During the design of the DDS, it is important to recognize that different materials can be combined to overcome the limitations and exploit the advantages each material proposes. However, because the combination of materials often requires specific bonding techniques, special care should be taken when selecting multiple materials.

Table F.6: Comparison of several available materials for the fabrication of microfluidic platforms. Adapted from literature reference [123]

Feature	Metal	Silicon	Glass	Ceramics	Elastomers	Thermo-plastics	Hydrogel	Paper
Fabrication costs	Positive	Negative	Negative	Positive	Moderate	Positive	Positive	Positive
Ease of fabrication	Positive	Negative	Negative	Positive	Positive	Moderate	Moderate	Positive
Young's Modulus [GPa]	100-200	130-180	50-90	65-250	~ 0.0005	1.4-4.1	Low	0.0003-0.0025
Oxygen permeability		Negative	Negative	Positive	Positive	Variable	Positive	Positive
Bio compatibility	Variable	Positive	Positive	Moderate	Positive	Positive	Positive	Positive
Optical transparency	Negative	Negative	Positive	Slight auto-fluorescence	Positive	Positive	Positive	Positive
Low absorption	Positive	Positive	Positive	Positive	Positive	Positive	Moderate	Moderate
Rapid prototyping		Moderate	Negative	Negative	Negative	Positive	Moderate	Moderate

Inorganic material

Inorganic materials include metals, silicon, glass and ceramics. Although the materials in this group are generally of high stiffness and not all biocompatible, they could still help to provide valuable insights when incorporated in a test setup. Generally, inorganic materials have the advantage of broad solvent compatibility, mechanical rigidity and, for glass, optical transparency at ultraviolet & visible wavelengths [124]. Main drawbacks are that these materials are expensive, difficult to fabricate and the production techniques are difficult to scale up.

Metals are rarely used in microfluidic systems for biomedical applications because of their lack of bio-compatibility. However they do offer beneficial properties which can be exploited during the fabrication process [125]. For example, the masks used during lithography or the molding tools for polymers are often metal-based.

Since silicon was the established material used in the semiconductor industry, many of the first microfluidic devices were made from this material. Because of its ease of fabrication, design flexibility, semiconducting properties, and the possibility of surface modifications it remained a dominant material

in microfluidics [123]. However, disadvantages such as the limited optical transparency and fragile behavior resulted in other material to be explored. Among those was glass, which has great optical transparency and lower price compared to silicon [123]. Drawbacks of glass are the difficult fabrication process which can take a long time and required clean room facilities. However, devices made from glass can be washed and reused, which is highly useful if device geometries are already established [124].

Elastomer
Elastomers are made up of weakly cross-linked entangled polymer chains, they can stretch or compress when external force is applied, and return to their original shape [126]. This composition results in highly flexible materials. One of the most widely used materials of this group is polydimethylsiloxane (PDMS) because of its ease and low cost of production [127]. Due to its low surface tension, it can be easily peeled from a master after being cured. Furthermore PDMS can be bonded to another substrate made from PDMS, glass or silicon by plasma oxidizing the PDMS surface. Other beneficial properties include [126, 128]: optical transparency, permeability to gas, bio-compatibility, natural hydrophobicity and high elasticity. Because of these properties, it is often used in bio-related research. However, at the same time these properties also limit the use of PDMS [129]. For example, the permeability of gasses has side effects such as incompatibility with organic solvents, the adsorption of bio-molecules into channel walls and change in concentration of solution by water evaporation through channel walls [130]. Although mainly PDMS is used in the industry due its mechanical properties and ease of prototyping, alternative elastomers have been proposed [131]. One of those are polyester elastomers; which improves PDMS properties by incorporating low adsorption.

Thermoset
Thermosets are plastics that become rigid due to the forming of a cross-link network, which can be triggered by a chemical reaction, heat or radiation [132]. Once they are cured, they cannot be reshaped anymore. Common examples of thermosets are SU-8 and polyimide. Generally, these materials are stable even at high temperatures, resistant to most solvents, have a high stiffness and are optically transparent [126]. However, the most evident disadvantage of these materials is their high cost [123]

Thermoplastic
Thermoplastics are plastics that soften around and above their glass transition temperature. This effect is caused by the polymer chains which are not cross-linked allowing them to move inside the bulk at higher temperatures [132]. Generally, these materials have a high permeability to gas, high rigidity and are transparent [123]. Their main advantages lies in the high volume manufacturing using injection moulding or hot embossing [124]. For low volume applications the process of creating a mold is often considered to be too complicated. Furthermore, molding relies on micro-machining which uses costly machinery and has a lower resolution compared to lithography solutions. Commonly used thermoplastic materials include polymethylmethacrylate (PMMA), polycarbonate (PC) and polyvinylchloride (PVC) [124]. Bonding to other materials is typically done by strategies such as thermobonding or gluing [124]. Recently, new types of thermoplastics have been studied, such as cyclic olefin copolymers (COCs) [133]. The interest in these materials is caused by properties such as good electrical insulation, long-term stability of surface treatments, and an extremely low level of impurities [123]. Furthermore, because of their increased chemical resistance, these materials proved useful for systems containing aggressive solvents.

Hydrogel
Hydrogels are highly porous networks of hydrophilic polymer chains that allow the diffusion of small molecules/bio-particles [123]. Usually these hydrogels have an aqueous medium which can be over 90% water [134]. Advantages of hydrogels are their biocompatibility, low cytotoxicity, biodegradability, controllable pore size, high permeability and aqueous nature [123, 126, 135]. Because of their properties resembling the extracellular matrix (ECM) applications of hydrogels are mostly cell-related [136]. They are sporadically used as the main fabrication material because of their lack of structural integrity [131]. Nonetheless, hydrogels can be used in combination with a rigid material to enable new functionalities, such as semipermeable barriers and sensors [128].

Paper
Paper-based microfluidics devices where first introduced by Martinez *et al.* [137] as a means of creating a inexpensive portable biosensor. Later they demonstrated the potential to create 3D structures that can carry out analytical protocols inexpensively without external pumps [138]. Most benefits of paper-based systems are derived from the capillary effect that drives the fluid through the system and by hydrophobically modifying certain regions precise control can be achieved [123]. However, paper-based systems are limited as only a few typical microfluidic applications have been demonstrated, the reported minimum channel width is around $200\mu m$ and there is a lack of convenient strategy to integrate small-sized valves [126]. In addition, when considering the proposed DDS, the open-channel design [126] of paper-based microfluidic systems can lead to uncontrolled liposome movement out of the system.

F.5.3. Fabrication methods
For the realisation of the DDS, the choice of production technique can have a substantial impact. Besides the limitations imposed on dimensionality and feature size of the design, the concept-to-prototype time can be considerably different depending on the selected fabrication process. Therefore careful consideration can lead to better designs, faster prototyping and ultimately a better prospect on a fully functional system. This section will provide an overview of the available production processes, their applications and (dis)advantages. All insights have been summarized in Table F.7.

Chemical processes
Chemical processes have been used for a long time and their popularity originates from the possibility to simultaneously process large quantities of wafers in the semiconductor industry [123]. Commonly used techniques include Electrochemical Discharge Machining (EDM), dry etching and wet etching. Wet etching utilizes strong chemicals in order to remove material and therefore also imposes limitations based on safety and environmental hazards [140]. Dry etching achieves material removal by particle bombardment and thus removes these safety concerns, however it is slower compared to wet etching [140] and therefore often not preferred. EDM uses an electrochemically generated spark which is created by applying a voltage between two electrodes submerged in an electrolyte. The resulting high temperature environment around the spark removes materials thermally or chemically [123]. The main advantage of EDM is the material choice, allowing for both conducting and non-conducting materials as well as high hardness metals such as stainless-steel [125]. However, the speed of EDM is limited by the flushing of electrolyte. Furthermore, tool wear is difficult to predict [132], resulting in challenges in identifying the exact location and thus decreased accuracy.

Mechanical processes
Subtractive micro-machining methods, including mechanical cutting, abrasive jet machining, and ultrasonic machining, are generally effective because of their low costs and high degree of flexibility [123]. However, they are limited by their reduced precision and productivity compared to lithographic methods [124].

In abrasive jet machining (AJM), abrasive particles are injected through a nozzle at very high pressure. Material is removed by the kinetic energy of abrasive particles at the time of collision with the surface of work material [141]. Different media have been used to support the abrasive particles such as air and water. Advantages of these methods include: process control flexibility, slow tool wear and cost-effectiveness [142]. However, several drawback reduce the effectiveness: slow removal rate, unstable flow for small microparticles and residual microcracks can be present in the sub-layer of the work piece [142]. Next, another mechanical method is ultrasonic machining (USM); a process that utilizes the vibration between work piece and tools to create cracks in brittle materials [123]. However, micro machining by USM is limited by low material removal rate and fabricating microchannels via USM is still challenging [141]. Finally, xurography is the method which refers to the patterning of an adhesive film through the use of a razor blade. It is a relatively low cost method that is able to produce robust microchips within just a few minutes [143]. Furthermore, it does not require clean room facilities. On the other hand, limitations are the precision of dimensions below 300 μm and the roughness of channel walls.

These mechanical processes and others can be combined with injection molding, hot embossing and soft lithography to create a high-throughput and low cost technique to produce microchannels.

Table F.7: Overview of fabrication processes based on research from Waldbaur *et al.* [125] and combined with other references [109, 123, 132, 139].

	Feature size	**Fabrication time**	**Scalability**	**Costs**	**Dimens.**	**Materials**
EDM	5 μm	Low	Low	High	3D	Polymers, metals, ceramics
Wet etching	Sub μm	Low	Good	Low	2.5D	Metals, glass, silicon
Dry etching	Sub μm	Low	Medium	Low	2.5D	Polymers, metals, glass, silicon
AJM [123]	50 μm	Medium	Low	Low	2.5D	Metals, glass, silicon, ceramics
USM [123]	15 μm	High	Low	Low	2.5D	Metals, glass, silicon, ceramics
Xurography [123]	300 μm	Low	Good	Low	2.5D	Polymers, metals, elastomers
Injection molding [109]	Mold dependent	Low	Good	Low	3D	Polymer (Thermo-plastic)
Hot embossing [132, 139]	Mold dependent	Low	Good	Low	3D	Polymer (Thermo-plastic)
Soft lithography [139]	Mold dependent	Low	Good	Low	3D	Elastomers
Photo-lithography	Sub μm	High	Good	Low	2.5D	Photoresists, polymers
SLA	μm	Medium	Low	Low	3D	Photoresists, light curable monomers
DLP [132]	50 μm	Low	Medium	Low	3D	Photoresists, light curable monomers
SLS	100 μm	Medium	Medium	Low	3D	Metals, polymers, ceramics, glass
2PP	nm-μm	High	Low	High	3D	Photoresists, light curable monomers
FDM	Several 100 μm	Medium	Medium	Low	3D	Polymers, metals, ceramics
Inkjet printing	100 μ m	Medium	Medium	Low	3D	Wax, UV or thermally curable resins
FIB	40 nm	High	Low	High	2.5D	Polymers, metals, glass, silicon

Processes without reference have been copied from Waldbaur *et al.* [125]

Injection molding and hot embossing both use molds combined with melting thermoplastics to form microchannels. On the other hand, soft lithography uses a mold combined with a soft elastomer. During

injection molding, melted thermoplastics are injected under pressure inside a heated mold cavity [123]. The temperature is decreased and after it drops below the glass transition temperature of the polymer, the solidified material is removed from the mold. Benefits of this method are the ability to produce large numbers of parts, the small tolerances achievable and high quality surface finish [132]. Though effective to create high quantities quickly, this method is limited by material choice and high initial entry cost for low-volume prototyping [139]. Hot embossing is similar to injection molding as it uses heat and pressure to form thermoplastics, however the difference being the thermoplastic is poured and pressed against the mold. This difference allows for stress reduction in the processed materials and more delicate designs due to less shrinkage of the cast [123]. However, the same limitations as for injection molding are still valid for this method with the addition of difficulty with producing complex 3D structures [139]. Lastly, soft lithography has become one of the most popular methods to create microfluidic systems since its introduction by Xia and Whitesides [144]. The method relies on the production of a soft elastomer based replica. This replica is created by pouring a liquid-set pre-polymer on a silicon mold, heat curing it and removing it from the substrate. The soft replica that is created is bonded to a glass sheet in order to create microchannels. The popularity around this method is based on several advantages; namely the high-resolution in combination with the flexible, optically transparent and bio-compatible materials (mainly PDMS) [139]. The limitations of this method are the result of the soft materials used: pattern deformation and defects created during removal from the mold [123]. Furthermore, the process does require clean-room facilities to create high-tolerance silicon molds.

Light-assisted processes

One of the most well known fabrication techniques, often used in the MEMS industry, is photolithography. This method uses a mask to pattern the light onto a photosensitive layer, causing the illuminated area to be removed. Since these masks can be used repeatedly to produce many devices it proposes excellent reproducibility and scalability for high volume applications [125]. However, the process requires multiple sequential steps and can become complex and expensive [141]. The smallest feature size is dependent on the wavelength of the light, therefore ultra-short pulse lasers are used for nanometer sized features [141].

Additive laser assisted processes include stereolithography (SLA), digital light processing (DLP), selective laser sintering (SLS) and two-photon polymerization (2PP). SLA uses a photoresponsive polymer resin. By exposing the liquid resin to a laser the polymerization process is initiated, cross-links are formed and the material solidifies locally. By moving the substrate bed downwards, a layer-by-layer approach is used to build the desired structure. This method is ideal for generating very fine features in a short time [123]. Another method similar to SLA is DLP. This technique exposes the entire surface simultaneously though a mask [125]. Since this results in a whole layer to be printed at once, the printing speed is considerably higher compared to SLA in which the laser moves from point-to-point. However, the downside is a reduction is achievable resolution [132]. 2PP is a modified version of SLA, where two photons are required to trigger polymerization between the photo-initiator and monomers of the liquid resin. Since the absorption is a third order process, it is dependent on the light intensity squared [109]. Using a focused laser beam, polymerization is only trigger locally around the focal point. This eliminates the need for a layer-by-layer approach and allows for a higher resolution of the printed structure. However, since 2PP is a serial writing technique, the process is inherently time consuming [125]. SLS make use of a powder bed and a laser which selectively warms and fuses the powder into a solid. Compared to other powder based printing techniques, SLS has the advantage of not requiring any glue.

3D printing processes

Processed referred to as 3D-printing generally utilize a layer-on-layer technique creating structures by selectively adding material. This can be achieved by phase changes (fused deposition modeling), applying droplets of glue into a bath of the bulk material in powder form (powder printing) or droplets of light curable resin (inkjet printing) [125]. The main benefits of these techniques are rapid prototyping due to the one-step approach and allowing complicated 3D shapes to be created. Other 3D printing processes not discussed here include SLA, DLP, SLS and 2PP as these have already been discussed previously under light-assisted processes.

Fused deposition modeling (FDM) is based on consecutively melting a thermoplastic, guiding it through a nozzle and cooling it; resulting in solidification at the desired location. The process is overall

simple, affordable and allows for direct prototyping. Furthermore, FDM is also capable of printing multi-material objects, creating more complex structures with locally different properties [145]. However, due to the inadequate fusion between adjacent layers, structures are more susceptible to compressive stress fractures [123]. Besides, minimum channel dimensions are bigger compared to other techniques and surface finish is often compromised [145].

Inkjet printing was originally used to deposit colored inks, but it recently attracted interest for depositing materials such as metals, ceramics and polymers [123]. During inkjet 3D printing droplets are formed either continuously or on-demand. These droplets are ejected onto the substrate by pressure pulses that are generated with piezoelectric elements, or via rapid heating and subsequent volume expansion [146]. Other types of inkjet printing include electrospray and aerosol jetting, which use a high pressure tank and electrostatic field respectively to generate droplets. The main advantages of inkjet printing are the design freedom, process control adjustments and modularity [109]. The main drawback of inkjet printing is the limited range of potential materials due to the process requiring sufficiently low viscosity materials [125]. Besides inkjet printing there are many others types of 3D printers. Different curing mechanisms can be used, such as powder bed fusion, binder jetting (glue) and multi jet fusion (photo curing) [109].

Others

Focused ion beam uses high kinetic energy from ions to remove or add material. As the ions are far heavier than electrons, ion beams bombard the target with greater kinetic energy plus the scattering is relatively small compared to an electron beam. The FIB can engrave or deposit patterns on the work piece directly from a CAD file and is thus an relatively easy way to modify a work piece. A spot size of 5 nm is feasible with a FIB [147]. The advantages of FIB are very high resolution and the possibility to work with different materials, such as metals, inorganic semiconductors, and ceramics [132]. The drawbacks are the low processing rate, vacuum environment requirement and due to the sputtering, the machining typically roughens surfaces at the sub-micron length scales [132].

F.5.4. Generating flow

Different strategies can be used to create flow inside a microfluidic system. Since the flow-field is to be precisely regulated in the experiment, a proper source for flow generation is important. Since the focus is to demonstrate the precise control of the liposomes in the DDS, the integration of a microscale flow generator has been left out of scope. Therefore the flow-generator can be of traditional macro-size and the main focus is to select a source that is reliable and has precise control over the flow field.

Pressure driven flow

Pressure-driven flow is the most common method for generating flow in microfluidic devices. A pressure difference is created between the inlet and outlet of the microchannel, driving the fluid through the channel. The pressure can be applied using the hydrostatic effect or external pumps, such as a syringe or peristaltic pumps. Different strategies are present; using a push mechanism/overpressure, pull mechanism/underpressure or a combination of the two aforementioned. The strengths and limitations of each of these methods have been summarized by Özkayar *et al.* [148]. The results show mostly differences for multichannel and re-circulation setups. Since both of these are not required for the DDS, all methods can serve as a viable option. Due to simplicity and availability of flow generators, a push system is probably the most simple.

Next, when considering the flow generator different options are available. Elveflow [149] has created an overview of the considerations to evaluate when selecting a proper flow generator. Firstly, using hydrostatic pressure. These machines are simple but also limited by for example Laplace pressure, the lack of dynamic control, and a decreasing pressure over time. The next option is a pressure generator. The robustness and precision of these systems is highly dependent on a good compatibility of all the components. Furthermore, the response time of these systems is limited by the mechanic deformation of the tubing. Lastly a syringe could be considered. The main advantage of syringe pumps is their capability to control the flow rate across microchannels independently of the hydraulic resistance.

Research done by Sebastian *et al.* [150] compared set-flow and set-pressure approaches for delivering medicines in microneedles. In their results, it can be clearly noticed that set-pressure results in bigger

variations of flow rate, which might be undesirable for the DDS. Also, the data highlights that significant variations in delivery volumes may arise as a result of using set-pressure.

Centrifugal forces driven flow

Another way to control the flow through microfluidic channels is by using a rotating disk and resulting centrifugal forces to drive the flow, often referred to as lab-on-a-disk. Since the centrifugal force density is the quadratically proportional to the rotational speed, it can be coupled to the pressure-flow relationship [151]. The mean flow rate can be computed with Equation F.30, where r is the radial position and ω is the rotational speed. For radially oriented channels the following holds: $\Delta r = l$, making the flow independent on the channel length.

$$Q = vA = \frac{\pi\rho}{128\eta}\frac{\Delta r}{L} r D^4 \omega^2 \tag{F.30}$$

This method shows great potential to precisely measure and control forces applied to a simple microfluidic system. However, complex systems with channels in different orientations are locally exerted to specific force fields, resulting in the introduction of complicated fluid dynamics.

Out of scope

Other readily available methods to generate flow rely on the addition of other physics, such as temperature, electric or magnetic fields, to the system. Therefore the following driving techniques have been left out of consideration: electrokinetic, thermal, acoustic, magnetic and pneumatic flow generation.

F.6. Future Perspectives

To realize a commercially viable DDS within a brain environment, further developmental steps are essential. Due to time constraints in the master thesis project, not all topics from the literature review were included in the project proposal. However, in a later stage of follow-up research, these topics can be considered. Therefore, this section could serve as an overview of research gaps that still need to be filled after the proposed master thesis in order to complete the DDS.

F.6.1. Integrated microfluidic flow generation: micropumps

Although the research presented in this paper is limited to the design of the microfluidic system without integrated microscale flow generation, micropumps could in the future be implemented in order to achieve a completely independent design. Therefore, this section will provide an overview of the recent developments in micropumps and serve as a starting point for future integration of a micropump.

Over the years many papers containing a reviews of micropumps have been published [152] [153] [154] [155], these have been combined and most relevant points have been mentioned below. In order to select a proper driving mechanism, Table F.8 serves as a starting point with the different (dis)advantages found in literature summarized. Generally, micropumps are characterized as either mechanical or non-mechanical, depending on the the presence of moving parts.

Mechanical micropumps

Mechanical micropumps work by an oscillation of a thin membrane that causes flow of the working fluid. As a result of the oscillating nature of the mechanical micropumps, a pulsating flow is created, which might be undesirable for the simplicity of the DDS. Usually, they contain a driver, some chambers and one or more valves. For each of these components, different solutions have been examined. Drivers can be based on different effects such as piezoelectric [156], electrostatic [157], electromagnetic [158], thermopneumatic [159], shape memory alloys [160] or electroactive polymers [161]. Advantages and disadvantages of each method can be found in Table F.8. The chamber configuration of each of these pumps can be adjusted in order to increase the performance of the micropump related to fluid delivery. Different valve types can be included and will be discussed in detail in subsection F.6.2.

Non-mechanical micropumps
Non-mechanical micropump rely on the conversion of energy from non-mechanical sources to the working fluid. Therefore, these micropumps are able to deliver a more continuous flow of fluids, also termed as continuous micropumps. Different working principles for non-mechanical microvalves include: electrohydrodynamic [162], magnetohydrodynamic [163], electro-osmotic [164], electro-chemical [165] and acoustic [166]. Advantages and disadvantages of each method can be found in Table F.8.

Table F.8: An overview of the advantages and disadvantages of different micropumps found in literature that can be considered when designing a microfluidic system.

Type	Advantages	Disadvantages
Piezo-electric	High actuation force, Fast response time, Precise flow control	Material processing, Attachment to membrane
Electrostatic	Easy integration, High frequency response, Low power consumption	Low flow rates
Electromagnetic	High flow rates, Response time	High power consumption, Difficult to integrate driver coils
Thermopneumatic	High flow rate	High response time (especially during cooling)
Shape memory alloys	High force to volume ratio, High damping capacity, Bio-compatibility	High power consumption, Unpredictable behavior, Bad high frequency response
Electroactive polymers	High flow rates, Fast response time	Repeatability
Electrohydrodynamic	No moving parts, High reliability, Low power consumption, Minimal maintenance	Low power efficiency, Low flow rates
Magnetohydrodynamic	No moving parts, Multiple pumps driven simultaneously	Bubble generation due to ionization
Electro-osmotic	No moving parts, Easily integrated	High voltage requirements, Bubble generation, Electrode reactions
Electro-chemical	Accurate flow control, Low power consumption, Low heat generation	Long respond time
Acoustic	High-power density, No restrictions on fluids	Complicated design, Complex fabrication

F.6.2. Improving flow control by integrating microvalves

Microvalves are essential to the control of (multiphase) flow in microfluidic devices as its function includes flow regulation, on/off switching and sealing of particles [167]. The microvalves can be divided into two categories: active and passive. Active microvalves need specific control element in order to properly function and thus require energy to operate, whereas passive microvalves work in principle on the pressure field. A schematic overview of the an active and passive microvalve can be found in Figure F.16. In this section, a complete overview of the available types of microvalves will be provided, which has been summarized in Table F.9. Microvalves with high potential to be integrated into the DDS are discussed in more detail.

Active microvalves Active valves, which use external systems to control and provide power to an actuator, have been studied extensively [185]. Generally there are mechanical and non-mechanical solutions, based on the presence of moving parts. Driving mechanisms of active mechanical microvalves include designs operated by magnetic energy, electric potential, the piezo-electric effect, thermal energy,

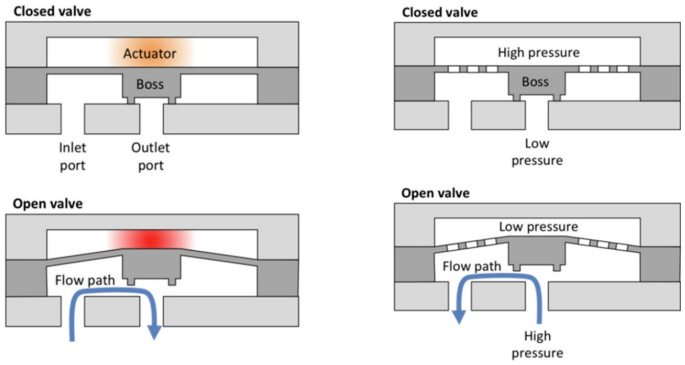

Figure F.16: Left: Schematic overview of an active microvalve, right: Schematic overview of a passive microvalve.

Table F.9: Classification of microvalves, adapted from Kwang and Chong [168] and updated for present-day literature with references.

Categories	Type	Driving mechanism	Example
Active	Mechanical	Magnetic	External magnetic fields [169]
		Electric	Electrostatic [170]
		Piezoelectric	Membrane [171]
		Thermal	Thermopneumatic [172]
		Pneumatic	Membrane [173]
		Light	Carbon Nano Tube [174]
			Polymer based [175]
	Non-mechanical	Electrochemical	Membrane [176]
		Phase change	Hydrogel [177]
		Rheological	Ferrofluids [178]
		Centrifugal	Rotary [179]
Passive	Mechanical	Check valve	Flap [180]
			Membrane [181]
	Non-Mechanical	Capillary	Burst [182]
			Stop [183]
			Hydrophobic [184]

pneumatic and light actuation. Driving mechanisms of active non-mechanical microvalves include designs operated by eletrochemical energy, phase changes, rheological and rotary energy.

In order to ensure simplicity in the *proof-of-concept* DDS, adding external components to control the flow is avoided. Therefore most of the active microvalves have not been studied in detail. However one of them, in particular the light actuated microvalve, might prove to be useful. Since there will already be a light source integrated into the system in order to release the drug, this type of microvalve might prove easy to implement. Therefore, a more detailed review of this type of microvalve will be provided next.

Light actuated microvalve are a recently developed technique in microfluidics and only a handful of paper examining such devices have been published. Most of the light actuated microvalves work with photoresponsive polymer-based hydrogels that undergo a phase change when exposed to light. Due to the phase change, dimensions of the polymer hydrogel change and a porous membrane opens or closes. One of the first systems reported using light to actuate a microvalve was by Sugiura *et al.* [186]. They used blue light irradiation to poly-N-isopropylacrylamide gels to induce shrinkage of the gels and thus causing the microvalves composed of the gels to open. While effective, this technique required more than an hour for the valve to close. Later research by Chen *et al.* [175] attempts to increase the response time by using another thermo-responsive polymer (poly-N-isopropylacrylamide), resulting

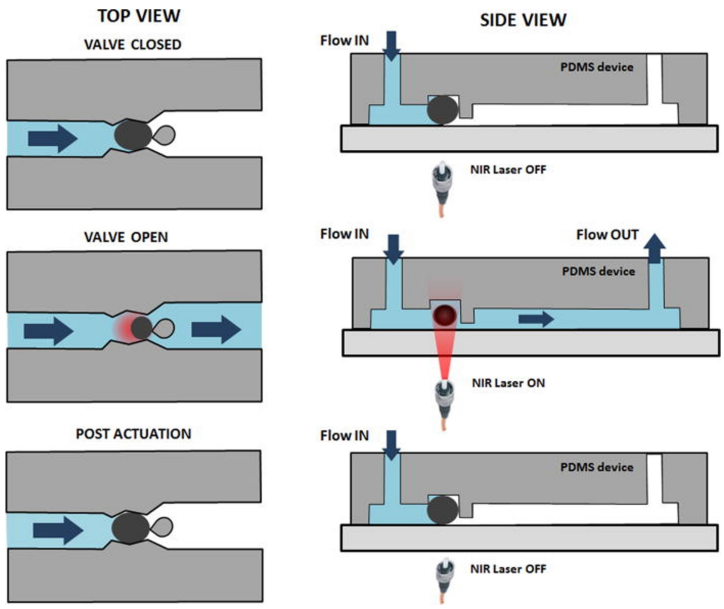

Figure F.17: Schematic representation of the light-actuated microvalve from Jadhav [187]

in response times around 4 seconds for opening and around 18 seconds for closing. Recently, such a photoresponsive hydrogel (poly-N-isopropylacrylamide combined with polypyrrole nanoparticles) irradiated by a near-infrared laser has been used with a ball-valve like approach [187]. A trapped ball of microgel is exposed to light which causes shrinking and subconsequently opening of the valve. See Figure F.17 for a schematic representation. Lastly, Cugno *et al.* [174] investigated the use of single-walled Carbon Nano Tubes (CNT) dispersed into PDMS at 1% weight percentage to create a photoresponsive actuator. Although the method was effective, the response time of the system was again slow with a cycle taking around 400 seconds.

Although limited research has been done within the field of light actuated microvalves, these approaches using light to operate the microvalve do show great potential and could be fused to selectively trap liposomes if integrated properly into the drugs delivery system. However, specific hydrogels with fast response times still need to be developed in order to be a viable solution to trap liposomes in the DDS. The review on recent developments of photoresponsive hydrogels for biomedical applications by Tomatsu *et al.* [188] serves as a promising starting point for future research.

Passive microvalves

Passive microvalves are valves whose operating state is determined by the fluid under control and do not use external systems to control and power actuators [185]. Therefore, they are a relatively simple, low cost and low power option compared to active microvalves. Passive microvalves can be categorised into either mechanical or non-mechanical, just as for active microvalves. Passive mechanical microvalves work by a movable check element, such as a ball, membrane or flap, that tightens the valve during backward flow and enables minimal resistance for forward flow. Passive non-mechanical microvalves mainly use capillary effects, for example in a burst, stop or hydrophobic valve.

F.6.3. Investigating the influence of elasto-microfluidics

Another emerging field within microfluidics is the integration of the effect of flexible walls; often referred to as elasto-, compliant- or flexible-microfluidics. Since the application of the proposed DDS is in the brain, it is likely that a flexible material will be used in the design to accommodate the environment. Therefore it is important to understand the implications of the flexible walls of the microchannels. Recent developments have been summarized by the review made by H. Fallahi *et al.* [189]. Current applications include micromixers [190], micropumps [191], on-skin wearables [192] and the study of cardiovascular-related diseases [193].

Influence on hydraulic resistance

As shown in Equation F.2.4, the hydraulic resistance is dependent on the viscosity of the fluid and the dimensions of the channel. In research by T. Gervais *et al.* [194] a model is created to predict the flow rate in a shallow channel ($W \gg h$) with a flexible top wall. The geometry used for this model can found in Figure F.18. It is shown that with deformation, the hydraulic resistance shows a nonlinear function of the applied pressure, as given by Equation F.31. where α is a proportionality constant, a fitting parameter which has to be obtained from fluid-material structure computations. This model has been validated with experiments and the effect is explained as a result of the increase in the cross-sectional area.

$$Q = \frac{h_0^4 E}{48\alpha\eta L}\left[\left(1+\alpha\frac{p_0 W}{E h_0}\right)^4 - 1\right] \tag{F.31}$$

Later research by Wang and Christov [195] creates an one-dimensional model without fitting parameter to assess the pressure-flow relationship. Research by Rai *et al.* ([196]) investigated the effect of deformable top and side walls and the thickness of the wall. In all of these research papers it is concluded that because of the effect of the deforming wall(s), the flow rate shows a nonlinear relation to pressure and higher flow rates are achieved for a given pressure drop compared to solid wall(s). Furthermore, it is observed there is an upper limit for which the walls do not deform any more. Therefore, it can be concluded the hydraulic resistance is highly impacted by deforming walls. Since it is important for the DDS to accurately control the position of liposomes, these effects have to be taken into account when working with soft materials.

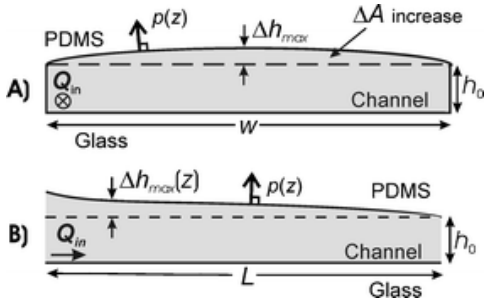

Figure F.18: Schematic representation of polymer channel deformation under an imposed flow rate. A) Channel cross-section normal to flow. B) Channel cross-section parallel to flow. [194].

Stability at lower Reynolds number

Theoretical analysis and experimental research [197] has shown that around Reynold number 200 the velocity profile in the microchannel can be disturbed, whereas for rigid channels this is around 2000. They allocate this to the fluid-structure interaction, which can disturb the laminar flow. Many models have been made in order to access the stability of flow in flexible microchannels [198] [194] [193]. Recently, X. Wang and I. Christov [195] combined the current knowledge and derived an one-dimensional model that predicts the effect on global stability and can predict the pressure drop over the channel with deforming top wall. This model also predicts that global instabilities can occur for $Re \sim O(2)$. Since turbulent flow is more difficult to predict and theory in this research is based on laminar flow, it is important to maintain in a laminar flow regime. Therefore future studies should be conducted in order to better understand the non-linear dynamics of flexible channels and examine if they have a significant impact on the DDS.

F.6.4. Integration of selectively releasing liposomes after exposure

Compared to trapping, the release of particles has seen less of an interest in research and is considered to be one of the future perspectives of single cell/particle capture [45]. However, recently the significance has started to be recognized and research is starting to pick up. An extensive summary has recently been made by Gong *et al.* and can be found in Table F.4 [50]. Some examples include release based on the formation of microbubbles [63], a multi-layer microvalve [199] and reversing flow direction [65].

Generally, it can be concluded release techniques are based on changing the environment in which the particle / cell is trapped. Passive particle release is achieved in sequential manner and is therefore not selective. In order to properly release liposomes after exposure, the literature gap that needs to be filled is to passively and selectively remove liposomes based on the changing physical properties of the liposome.

The application of the trap-and-release mechanism in the DDS is different compared to conventional cell analysis applications, as in the DDS there is no need to maintain cell viability after the drug delivery event. This allows for a completely new research area with a release technique based on changing particle properties (such as size), instead of changing environment properties. This would therefore allow for a passive and selective trap-and-release system which has not been proposed before in research.

Nomenclature

Abbreviations

Abbreviation	Definition
AJM	Abrasive Jet Machining
CAD	Computer Aided Design
CFD	Computational Fluid Dynamics
CNT	Carbon Nano Tubes
COC	Cyclic Olefin Copolymers
CW	Continuous Wave
DDS	Drug Delivery System
DiLL	Dip-in-Laser Lithography
DLP	Digital Light Processing
ECM	ExtraCellular Matrix
ECoG	ElectroCorticoGraphy
EDM	Electrochemical Discharge Machining
FDA	U.S. Food and Drug Administration
FDM	Fused Deposition Modeling
FEM	Finite Element Method
FIB	Focused Ion Beam
FMEA	Failure Mode Effect Analysis
GUV	Giant Unilamellar Vesicle
IPA	Isopropanol
ITO	Indium Tin Oxide
MVP	Minimum Viable Product
NIR	Near InfraRed
PC	PolyCarboante
PDMS	PolyDiMethylSiloxane
PGMEA	PropyleenGlycolmonoMethylEtherAcetaat
PMMA	PolyMethylMethaCrylate
PVC	PolyVinylChloride
SEM	Scanning Electron Microscopy
SLA	Stereolithography
SLS	Selective Laser Sintering
TCPFOS	Trichloro(1H,1H,2H,2H-perfluorooctyl)silane
USM	UltraSonic Machining
UV	UltraViolet
WBS	Work Breakdown Structure
2PP	Two Photon Polymerization

Symbols

Symbol	Definition	Unit
A, a, B, b, C	Parameters	[-]
A, A_0	Area, initial	[m^2]
C_H	Hydraulic compliance	[m^3/Pa]
D	Diameter of channel	[m]
D_d	Molecular diffusion coefficient	[m^2/s]
d	Diameter of particle	[m]
E	Young's modulus	[Pa]
E_b, E_s, E_m	Bending-, stretching, membrane energy	[J]
F_m, F_p	Membrane, pressure force	[N]
f_i, f_v	Inertial-, viscous force density	[N/m^3]
g	Gravitational constant	[m^2/kg/s^2]
h	Height of the microfluidic channel	[m]
K_A	Area expansion modulus	[Pa]
k_b	Bending rigidity modulus	[N m^2]
L	Length of channel/nozzle	[m]
m	Mass of particle	[m]
$\hat{n}$	Normal direction	[-]
P	Perimeter	[m]
p	Pressure	[Pa]
p_l, p_h	Laplace, hydrostatic pressure	[Pa]
Q	Flow rate	[m^3/s]
R_H	Hydraulic resistance	[Pa s/m^3]
R_1, R_2	Principle radii of curvature	[m]
$R_l ip$	Radius of liposome	[m]
r	Radius of channel	[m]
S	Surface area	[m^2]
T	Temperature	[Kelvin]
t	Time	[s]
u	Velocity of fluid	[m/s]
v	Velocity of particle	[m/s]
V_i	Volume of particle	[m^3]
w	Width of channel	[m]
W_{trap}	Width of the nozzle	[m]
x, y, z	Cartesian coordinates	[-]
$\alpha, \beta, \varphi, \phi$	Parameters, angles	[rad]
γ	Surface tension	[N/m]
ϵ	Elongation	[-]
η	Viscosity	[Pa s]
θ	Contact angle	[rad]
κ	Curvature	[1/m]
λ	Wavelength	[m]
ρ	Density	[kg/m^3]
σ	Stress tensor	[Pa]
	Continued on the next page	

	Continued from previous page	
Symbol	**Definition**	**Unit**
τ	Shear stress	[Pa]
ω	Angular frequency	[rad s^{-1}]

References - Literature review

[1] C. O. Johnson et al. "Global, regional, and national burden of stroke, 1990–2016: a systematic analysis for the Global Burden of Disease Study 2016". In: *The Lancet Neurology* 18.5 (2019), pp. 439–458. ISSN: 1474-4422. DOI: 10.1016/S1474-4422(19)30034-1.

[2] A. Palmini. "The concept of the epileptogenic zone: a modern look at Penfield and Jasper's views on the role of interictal spikes". In: *Epileptic Disorders* 8.S2 (2006), S10–S15. DOI: 10.1684/j.1950-6945.2006.tb00205.x.

[3] A. O. Pires et al. "Old and new challenges in Parkinson's disease therapeutics". In: *Progress in Neurobiology* 156 (2017), pp. 69–89. ISSN: 0301-0082. DOI: 10.1016/j.pneurobio.2017.04.006.

[4] P. Perucca and F. G. Gilliam. "Adverse effects of antiepileptic drugs". In: *The Lancet Neurology* 11.9 (2012), pp. 792–802. ISSN: 1474-4422. DOI: 10.1016/S1474-4422(12)70153-9.

[5] Y. Omidi et al. "Drug delivery and targeting to brain tumors: considerations for crossing the blood-brain barrier". In: *Expert Review of Clinical Pharmacology* 14.3 (2021), pp. 357–381. DOI: 10.1080/17512433.2021.1887729.

[6] C. Yeung et al. "A 3D-printed microfluidic-enabled hollow microneedle architecture for transdermal drug delivery". In: *Biomicrofluidics* 13.6 (Dec. 2019), p. 064125. ISSN: 1932-1058. DOI: 10.1063/1.5127778.

[7] H. Fallahi et al. "Flexible microfluidics: Fundamentals, recent developments, and applications". In: *Micromachines* 10.12 (2019), p. 830. DOI: 10.1007/s00542-019-04535-8.

[8] L. G. Aceves-Serrano et al. "Chapter 3 - Microfluidics for drug delivery systems". In: *Nanoarchitectonics in Biomedicine*. Ed. by A. M. Grumezescu. William Andrew Publishing, 2019, pp. 55–83. ISBN: 978-0-12-816200-2. DOI: 10.1016/B978-0-12-816200-2.00002-5.

[9] S. T. Sanjay et al. "Recent advances of controlled drug delivery using microfluidic platforms". In: *Advanced Drug Delivery Reviews* 128 (2018). Microfluidic Devices for Drug Delivery Systems, pp. 3–28. ISSN: 0169-409X. DOI: 10.1016/j.addr.2017.09.013.

[10] A. Jahn et al. "Microfluidic directed formation of liposomes of controlled size". In: *Langmuir* 23.11 (2007), pp. 6289–6293. DOI: 10.1021/la070051a.

[11] D. Carugo et al. "Liposome production by microfluidics: potential and limiting factors". In: *Scientific reports* 6 (May 2016), p. 25876. ISSN: 2045-2322. DOI: 10.1038/srep25876.

[12] D. van Swaay and A. deMello. "Microfluidic methods for forming liposomes". In: *Lab Chip* 13 (5 2013), pp. 752–767. DOI: 10.1039/C2LC41121K.

[13] B. Yu, R. J. Lee, and L. J. Lee. "Chapter 7 - Microfluidic Methods for Production of Liposomes". In: *Methods in Enzymology*. Vol. 465. Methods in Enzymology. Academic Press, 2009, pp. 129–141. DOI: 10.1016/S0076-6879(09)65007-2.

[14] T. M. Allen and P. R. Cullis. "Liposomal drug delivery systems: From concept to clinical applications". In: *Advanced Drug Delivery Reviews* 65.1 (2013). Advanced Drug Delivery: Perspectives and Prospects, pp. 36–48. ISSN: 0169-409X. DOI: 10.1016/j.addr.2012.09.037.

[15] A. Y. Rwei, W. Wang, and D. S. Kohane. "Photoresponsive nanoparticles for drug delivery". In: *Nano Today* 10.4 (2015), pp. 451–467. ISSN: 1748-0132. DOI: 10.1016/j.nantod.2015.06.004.

[16] U. Bulbake et al. "Liposomal Formulations in Clinical Use: An Updated Review". In: *Pharmaceutics* 9.2 (2017). ISSN: 1999-4923. DOI: 10.3390/pharmaceutics9020012.

[17] F. Bragheri, R. Martinez Vazquez, and R. Osellame. "Chapter 12.3 - Microfluidics". In: Micro and Nano Technologies (2016). Ed. by T. Baldacchini, pp. 310–334. DOI: 10.1016/B978-0-323-35321-2.00016-9.

[18] H. Bruus. *Lecture notes in Theoretical Microfluidics*. Sept. 2006.

[19] J. Happel and H. Brenner. *Low Reynolds number hydrodynamics*. 1st ed. ISBN 978-90-247-2877-0. City, State or Country: Springer Dordrecht, 1983.

[20] T. M. Squires and S. R. Quake. "Microfluidics: Fluid physics at the nanoliter scale". In: *Rev. Mod. Phys.* 77 (3 Oct. 2005), pp. 977–1026. DOI: 10.1103/RevModPhys.77.977.

[21] P. Tabeling. *Introduction to Microfluidics*. OUP Oxford, 2023. ISBN: 9780192660039. URL: https://books.google.nl/books?id=UEDHEAAAQBAJ.

[22] R. H. Ewell and H. Eyring. "Theory of the Viscosity of Liquids as a Function of Temperature and Pressure". In: *The Journal of Chemical Physics* 5.9 (Dec. 2004), pp. 726–736. ISSN: 0021-9606. DOI: 10.1063/1.1750108.

[23] H. Eyring. "Viscosity, Plasticity, and Diffusion as Examples of Absolute Reaction Rates". In: *The Journal of Chemical Physics* 4.4 (Dec. 2004), pp. 283–291. ISSN: 0021-9606. DOI: 10.1063/1.1749836.

[24] C. J. Seeton. "Viscosity-Temperature Correlation for Liquids". In: International Joint Tribology Conference Part A (Oct. 2006), pp. 131–142. DOI: 10.1115/IJTC2006-12139.

[25] C. Rands, B. Webb, and D. Maynes. "Characterization of transition to turbulence in microchannels". In: *International Journal of Heat and Mass Transfer* 49.17 (2006), pp. 2924–2930. ISSN: 0017-9310. DOI: 10.1016/j.ijheatmasstransfer.2006.02.032.

[26] D. Liu and S. V. Garimella. "Investigation of Liquid Flow in Microchannels". In: *Journal of Thermophysics and heat transfer* 8.1 (Jan. 2004). DOI: 10.2514/1.9124.

[27] C. Fefferman. "Existence and smoothness of the Navier-Stokes equation". In: *The Millennium Prize Problems* (Jan. 2006).

[28] N. A. Mortensen, F. Okkels, and H. Bruus. "Reexamination of Hagen-Poiseuille flow: Shape dependence of the hydraulic resistance in microchannels". In: *Phys. Rev. E* 71 (5 May 2005), p. 057301. DOI: 10.1103/PhysRevE.71.057301.

[29] K. W. Oh et al. "Design of pressure-driven microfluidic networks using electric circuit analogy". In: *Lab Chip* 12 (3 2012), pp. 515–545. DOI: 10.1039/C2LC20799K.

[30] C. Crowe. *Multiphase Flow Handbook*. Mechanical and Aerospace Engineering Series. CRC Press, 2005. ISBN: 9781420040470. URL: https://books.google.nl/books?id=7FDbB7VjxkQC.

[31] N. Patankar et al. "A new formulation of the distributed Lagrange multiplier/fictitious domain method for particulate flows". In: *International Journal of Multiphase Flow* 26.9 (2000), pp. 1509–1524. ISSN: 0301-9322. DOI: 10.1016/S0301-9322(99)00100-7.

[32] A. Farajpour, M. H. Ghayesh1, and H. Farokhi2. "On the Role of Saffman Force in Inertial Microfluidics". In: *Global Journal of Engineering Sciences* 2.5 (June 2019). ISSN: 2641-2039. DOI: 10.33552/GJES.2019.02.000546.

[33] J. Zhang et al. "Fundamentals and applications of inertial microfluidics: a review". In: *Lab Chip* 16 (1 2016), pp. 10–34. DOI: 10.1039/C5LC01159K.

[34] E. Schäfer et al. "Mechanical response of adherent giant liposomes to indentation with a conical AFM-tip". In: *Soft Matter* 11 (22 2015), pp. 4487–4495. DOI: 10.1039/C5SM00191A.

[35] S. C. Hur et al. "Deformability-based cell classification and enrichment using inertial microfluidics". In: *Lab Chip* 11 (5 2011), pp. 912–920. DOI: 10.1039/C0LC00595A.

[36] C. K. W. Tam and W. A. Hyman. "Transverse motion of an elastic sphere in a shear field". In: *Journal of Fluid Mechanics* 59.1 (1973), pp. 177–185. DOI: 10.1017/S0022112073001497.

[37] C. A. Stan et al. "Sheathless hydrodynamic positioning of buoyant drops and bubbles inside microchannels". In: *Phys. Rev. E* 84 (3 Sept. 2011), p. 036302. DOI: 10.1103/PhysRevE.84.036302.

[38] S. K. Doddi and P. Bagchi. "Lateral migration of a capsule in a plane Poiseuille flow in a channel". In: *International Journal of Multiphase Flow* 34.10 (2008), pp. 966–986. ISSN: 0301-9322. DOI: 10.1016/j.ijmultiphaseflow.2008.03.002.

[39] A. Kilimnik, W. Mao, and A. Alexeev. "Inertial migration of deformable capsules in channel flow". In: *Physics of Fluids* 23.12 (Dec. 2011), p. 123302. DOI: 10.1063/1.3664402.

[40] S. J. Shin and H. J. Sung. "Inertial migration of an elastic capsule in a Poiseuille flow". In: *Phys. Rev. E* 83 (4 Apr. 2011), p. 046321. DOI: 10.1103/PhysRevE.83.046321.

[41] S. Vowell. "Microfluidics Effects of Surface Tension". In: *Recovered from* (2009). URL: https://citeseerx.ist.psu.edu/document?repid=rep1&type=pdf&doi=d891806de2464d5703e36751decb47b150a51958.

[42] L. M. Siqveland and S. Skjaeveland. "Derivations of the Young-Laplace equation". In: *Capillarity* 4.2 (May 2021), pp. 23–30. DOI: 10.46690/CAPI.2021.02.01.

[43] E. Dressaire and A. Sauret. "Clogging of microfluidic systems". In: *Soft Matter* 13 (1 2017), pp. 37–48. DOI: 10.1039/C6SM01879C.

[44] Y. Li et al. "Universal behavior of hydrogels confined to narrow capillaries". In: *Scientific reports* 5.1 (2015), p. 17017. DOI: 10.1038/srep17017.

[45] X. Wang et al. "Advances in precise single cell capture for analysis and biological applications". In: *Analytical Methods* (2022). DOI: 10.1039/D2AY00625A.

[46] Y. Deng, Y. Guo, and B. Xu. "Recent Development of Microfluidic Technology for Cell Trapping in Single Cell Analysis: A Review". In: *Processes* 8.10 (2020). ISSN: 2227-9717. DOI: 10.3390/pr8101253.

[47] Y. Lan et al. "Microfluidic based single cell or droplet manipulation: Methods and applications". In: *Talanta* 265 (2023), p. 124776. ISSN: 0039-9140. DOI: 10.1016/j.talanta.2023.124776.

[48] L. Huang et al. "Microfluidics cell sample preparation for analysis: Advances in efficient cell enrichment and precise single cell capture". In: *Biomicrofluidics* 11.1 (Feb. 2017), p. 011501. ISSN: 1932-1058. DOI: 10.1063/1.4975666.

[49] J. Nilsson et al. "Review of cell and particle trapping in microfluidic systems". In: *Analytica Chimica Acta* 649.2 (2009), pp. 141–157. ISSN: 0003-2670. DOI: 10.1016/j.aca.2009.07.017.

[50] L. Gong, A. Cretella, and Y. Lin. "Microfluidic systems for particle capture and release: A review". In: *Biosensors and Bioelectronics* 236 (2023), p. 115426. ISSN: 0956-5663. DOI: 10.1016/j.bios.2023.115426.

[51] V. Narayanamurthy et al. "Microfluidic hydrodynamic trapping for single cell analysis: mechanisms, methods and applications". In: *Anal. Methods* 9 (25 2017), pp. 3751–3772. DOI: 10.1039/C7AY00656J.

[52] Q. Luan et al. "Microfluidic systems for hydrodynamic trapping of cells and clusters". In: *Biomicrofluidics* 14.3 (May 2020), p. 031502. ISSN: 1932-1058. DOI: 10.1063/5.0002866.

[53] J. R. Rettig and A. Folch. "Large-scale single-cell trapping and imaging using microwell arrays". In: *Analytical chemistry* 77.17 (Sept. 2005), pp. 5628–5634. ISSN: 0003-2700. DOI: 10.1021/ac0505977.

[54] M. C. Park et al. "High-throughput single-cell quantification using simple microwell-based cell docking and programmable time-course live-cell imaging". In: *Lab Chip* 11 (1 2011), pp. 79–86. DOI: 10.1039/C0LC00114G.

[55] J. Park et al. "Single cell trapping in larger microwells capable of supporting cell spreading and proliferation". In: *Microfluidics and Nanofluidics* 8.2 (Feb. 2010), pp. 263–268. ISSN: 1613-4982. DOI: 10.1007/s10404-009-0503-9.

[56] Y. Wang et al. "Trapping cells on a stretchable microwell array for single-cell analysis". English. In: *Analytical and Bioanalytical Chemistry* 402.3 (2012), pp. 1065–1072. DOI: 10.1007/s00216-011-5535-9.

[57] D. Di Carlo, L. Y. Wu, and L. P. Lee. "Dynamic single cell culture array". In: *Lab on a Chip* 6.11 (2006), pp. 1445–1449. DOI: 10.1039/b605937f.

[58] A. Kitagawa et al. "Microplastic particle trapping through microfluidic devices with different shaped pillars". In: *Chemical Engineering Science* 264 (2022), p. 118163. ISSN: 0009-2509. DOI: 10.1016/j.ces.2022.118163.

[59] O. Mesdjian et al. "Enhancing the capture efficiency and homogeneity of single-layer flow-through trapping microfluidic devices using oblique hydrodynamic streams". In: *Microfluidics and Nanofluidics* 25.11 (Oct. 2021), p. 91. DOI: 10.1007/s10404-021-02492-1.

[60] Y. Yoon et al. "Clogging-free microfluidics for continuous size-based separation of microparticles". English (US). In: *Scientific reports* 6 (May 2016). ISSN: 2045-2322. DOI: 10.1038/srep26531.

[61] S. Lindström and H. Andersson-Svahn. "Miniaturization of biological assays — Overview on microwell devices for single-cell analyses". In: *Biochimica et Biophysica Acta (BBA) - General Subjects* 1810.3 (2011). Nanotechnologies - Emerging Applications in Biomedicine, pp. 308–316. ISSN: 0304-4165. DOI: 10.1016/j.bbagen.2010.04.009.

[62] A. Benavente-Babace et al. "Single-cell trapping and selective treatment via co-flow within a microfluidic platform". In: *Biosensors and Bioelectronics* 61 (2014), pp. 298–305. ISSN: 0956-5663. DOI: 10.1016/j.bios.2014.05.036.

[63] W.-H. Tan and S. Takeuchi. "A trap-and-release integrated microfluidic system for dynamic microarray applications". In: *Proceedings of the National Academy of Sciences* 104.4 (2007), pp. 1146–1151. DOI: 10.1073/pnas.0606625104.

[64] D. Jin et al. "A microfluidic device enabling high-efficiency single cell trapping". In: *Biomicrofluidics* 9.1 (Jan. 2015), p. 014101. ISSN: 1932-1058. DOI: 10.1063/1.4905428.

[65] H. Chai et al. "A microfluidic device enabling deterministic single cell trapping and release". In: *Lab Chip* 21 (13 2021), pp. 2486–2494. DOI: 10.1039/D1LC00302J.

[66] L. Mi et al. "A fluidic circuit based, high-efficiency and large-scale single cell trap". In: *Lab Chip* 16 (23 2016), pp. 4507–4511. DOI: 10.1039/C6LC01120A.

[67] A. Lawrenz, F. Nason, and J. J. Cooper-White. "Geometrical effects in microfluidic-based microarrays for rapid, efficient single-cell capture of mammalian stem cells and plant cells". In: *Biomicrofluidics* 6.2 (Apr. 2012), p. 024112. ISSN: 1932-1058. DOI: 10.1063/1.4704521.

[68] C. Chen et al. "Microfluidic isolation and transcriptome analysis of serum microvesicles". In: *Lab Chip* 10 (4 2010), pp. 505–511. DOI: 10.1039/B916199F.

[69] R. Chinnappan, Q. Ramadan, and M. Zourob. "An integrated lab-on-a-chip platform for pre-concentration and detection of colorectal cancer exosomes using anti-CD63 aptamer as a recognition element". In: *Biosensors and Bioelectronics* 220 (2023), p. 114856. ISSN: 0956-5663. DOI: 10.1016/j.bios.2022.114856.

[70] F. Mi et al. "Application of lectin-based biosensor technology in the detection of foodborne pathogenic bacteria: a review". In: *Analyst* 146 (2 2021), pp. 429–443. DOI: 10.1039/D0AN01459A.

[71] M. Tayebi et al. "Exosome Purification and Analysis Using a Facile Microfluidic Hydrodynamic Trapping Device". In: *Analytical chemistry* 92.15 (Aug. 2020), pp. 10733–10742. ISSN: 0003-2700. DOI: 10.1021/acs.analchem.0c02006.

[72] M. C. Peoples and H. T. Karnes. "Microfluidic immunoaffinity separations for bioanalysis". In: *Journal of Chromatography B* 866.1 (2008). 50 Years Journal of Chromatography, pp. 14–25. ISSN: 1570-0232. DOI: 10.1016/j.jchromb.2007.08.030.

[73] U. Staufer and G. van Veen. *Weekly discussion on Literature Review and Thesis proposal*. Technical University of Delft. Sept. 2023.

[74] A. Olanrewaju et al. "Capillary microfluidics in microchannels: from microfluidic networks to capillaric circuits". In: *Lab Chip* 18 (16 2018), pp. 2323–2347. DOI: 10.1039/C8LC00458G.

[75] S. Wang et al. "A Review of Capillary Pressure Control Valves in Microfluidics". In: *Biosensors* 11.10 (2021). ISSN: 2079-6374. DOI: 10.3390/bios11100405.

[76] P. Azizian et al. "Capillary-driven microfluidics: impacts of 3D manufacturing on bioanalytical devices". In: *Analyst* 148 (12 2023), pp. 2657–2675. DOI: 10.1039/D3AN00115F.

[77] J. Zeng et al. "Fluidic Capacitance Model of Capillary-Driven Stop Valves". In: ASME International Mechanical Engineering Congress and Exposition Micro-Electro-Mechanical Systems (MEMS) (Nov. 2000), pp. 581–587. DOI: 10.1115/IMECE2000-1149.

[78] J. M. Chen, C.-Y. Chen, and C.-H. Liu. "Pressure Barrier in an Axisymmetric Capillary Microchannel with Sudden Expansion". In: *Japanese Journal of Applied Physics* 47.3R (Mar. 2008), p. 1683. DOI: 10.1143/JJAP.47.1683.

[79] J. M. Chen, P.-C. Huang, and M.-G. Lin. "Analysis and experiment of capillary valves for microfluidics on a rotating disk". In: *Microfluidics and Nanofluidics* 4 (2008), pp. 427–437. DOI: 10.1007/s10404-007-0196-x.

[80] H. Cho et al. "How the capillary burst microvalve works". In: *Journal of Colloid and Interface Science* 306.2 (2007), pp. 379–385. ISSN: 0021-9797. DOI: 10.1016/j.jcis.2006.10.077.

[81] D. D. Agonafer et al. "Burst behavior at a capillary tip: Effect of low and high surface tension". In: *Journal of Colloid and Interface Science* 455 (2015), pp. 1–5. ISSN: 0021-9797. DOI: 10.1016/j.jcis.2015.05.033.

[82] D. D. Agonafer et al. “Porous micropillar structures for retaining low surface tension liquids”. In: *Journal of Colloid and Interface Science* 514 (2018), pp. 316–327. ISSN: 0021-9797. DOI: 10.1016/j.jcis.2017.12.011.

[83] J. Mo et al. “Fluid release pressure for micro-/nanoscale rectangular channels”. In: *Journal of Applied Physics* 127.11 (Mar. 2020), p. 114302. ISSN: 0021-8979. DOI: 10.1063/1.5129411.

[84] U. N. Lee et al. “Stable biphasic interfaces for open microfluidic platforms”. In: *Biomedical Microdevices* 21.16 (Feb. 2019). ISSN: 1572-8781. DOI: 10.1007/s10544-019-0367-z.

[85] M. G. A. Mohamed et al. “Microfluidics-based fabrication of cell-laden microgels”. In: *Biomicrofluidics* 14.2 (Mar. 2020), p. 021501. ISSN: 1932-1058. DOI: 10.1063/1.5134060.

[86] D. Velasco, E. Tumarkin, and E. Kumacheva. “Microfluidic Encapsulation of Cells in Polymer Microgels”. In: *Nano Micro - Small* 8.11 (June 2012), pp. 1633–1642. DOI: 10.1002/smll.201102464.

[87] Y. Zhou et al. “Single-cell sorting using integrated pneumatic valve droplet microfluidic chip”. In: *Talanta* 253 (2023), p. 124044. ISSN: 0039-9140. DOI: 10.1016/j.talanta.2022.124044.

[88] Z. N. Linbo Liu Nan Xiang. “Droplet-based microreactor for the production of micro/nanomaterials”. In: *Electrophoresis* 41.10-11 (Nov. 2019), pp. 833–851. DOI: 10.1002/elps.201900380.

[89] A. Huebner et al. “Static microdroplet arrays: a microfluidic device for droplet trapping, incubation and release for enzymatic and cell-based assays”. In: *Lab Chip* 9 (5 2009), pp. 692–698. DOI: 10.1039/B813709A.

[90] M. Courtney et al. “Droplet Microfluidic System with On-Demand Trapping and Releasing of Droplet for Drug Screening Applications”. In: *Analytical chemistry* 89.1 (Jan. 2017), pp. 910–915. ISSN: 0003-2700. DOI: 10.1021/acs.analchem.6b04039.

[91] M. G. Simon et al. “A Laplace pressure based microfluidic trap for passive droplet trapping and controlled release”. In: *Biomicrofluidics* 6.1 (Feb. 2012), p. 014110. ISSN: 1932-1058. DOI: 10.1063/1.3687400.

[92] V. T. Hoang et al. “Effect of entry geometry on droplet dynamics in contraction microchannel”. In: *International Journal of Multiphase Flow* 167 (2023), p. 104543. ISSN: 0301-9322. DOI: 10.1016/j.ijmultiphaseflow.2023.104543.

[93] A. Yamada et al. “Trapping and release of giant unilamellar vesicles in microfluidic wells”. In: *Soft Matter* 10 (32 2014), pp. 5878–5885. DOI: 10.1039/C4SM00065J.

[94] H. Nuss et al. “Microfluidic trap-and-release system for lab-on-a-chip-based studies on giant vesicles”. In: *Lab Chip* 12 (24 2012), pp. 5257–5261. DOI: 10.1039/C2LC40782E.

[95] U. Bulbake et al. “Liposomal Formulations in Clinical Use: An Updated Review”. In: *Pharmaceutics* 9.2 (2017). ISSN: 1999-4923. DOI: 10.3390/pharmaceutics9020012.

[96] P. Liu, G. Chen, and J. Zhang. “A Review of Liposomes as a Drug Delivery System: Current Status of Approved Products, Regulatory Environments, and Future Perspectives”. In: *Molecules* 27.4 (2022). ISSN: 1420-3049. DOI: 10.3390/molecules27041372.

[97] N. M. Salkho et al. “Photo-Induced Drug Release from Polymeric Micelles and Liposomes: Phototriggering Mechanisms in Drug Delivery Systems”. In: *Polymers* 14.7 (2022). ISSN: 2073-4360. DOI: 10.3390/polym14071286.

[98] A. Y. Rwei et al. “Repeatable and adjustable on-demand sciatic nerve block with phototriggerable liposomes”. In: *Proceedings of the National Academy of Sciences* 112.51 (2015), pp. 15719–15724. DOI: 10.1073/pnas.1518791112.

[99] W. Rawicz et al. “Effect of Chain Length and Unsaturation on Elasticity of Lipid Bilayers”. In: *Biophysical Journal* 79.1 (2000), pp. 328–339. ISSN: 0006-3495. DOI: 10.1016/S0006-3495(00)76295-3.

[100] Y. Shitamichi, M. Ichikawa, and Y. Kimura. “Mechanical properties of a giant liposome studied using optical tweezers”. In: *Chemical Physics Letters* 479.4 (2009), pp. 274–278. ISSN: 0009-2614. DOI: 10.1016/j.cplett.2009.08.018.

[101] W. Rawicz et al. “Elasticity, Strength, and Water Permeability of Bilayers that Contain Raft Microdomain-Forming Lipids”. In: *Biophysical Journal* 94.12 (2008), pp. 4725–4736. ISSN: 0006-3495. DOI: 10.1529/biophysj.107.121731.

[102] N. Fomina, J. Sankaranarayanan, and A. Almutairi. "Photochemical mechanisms of light-triggered release from nanocarriers". In: *Advanced Drug Delivery Reviews* 64.11 (2012). Stimuli-responsive drug delivery systems, pp. 1005–1020. ISSN: 0169-409X. DOI: 10.1016/j.addr.2012.02.006.

[103] W. Chen, E. M. Goldys, and W. Deng. "Light-induced liposomes for cancer therapeutics". In: *Progress in Lipid Research* 79 (2020), p. 101052. ISSN: 0163-7827. DOI: 10.1016/j.plipres.2020.101052.

[104] S. J. Leung and M. Romanowski. "Light-activated content release from liposomes". In: *Theranostics* 2.10 (2012), pp. 1020–1036. ISSN: 1838-7640. DOI: 10.7150/thno.4847.

[105] A. Yavlovich et al. "Light-sensitive lipid-based nanoparticles for drug delivery: design principles and future considerations for biological applications". In: *Molecular Membrane Biology* 27.7 (2010), pp. 364–381. DOI: 10.3109/09687688.2010.507788.

[106] Y. Wang and D. S. Kohane. "External triggering and triggered targeting strategies for drug delivery". In: *Nature Reviews Materials* 2.6 (2017), pp. 1–14. DOI: 10.1038/natrevmats.2017.20.

[107] Z. Yuan et al. "Repetitive drug delivery using Light-Activated liposomes for potential antimicrobial therapies". In: *Advanced Drug Delivery Reviews* 187 (2022), p. 114395. ISSN: 0169-409X. DOI: 10.1016/j.addr.2022.114395.

[108] K. A. D. Gregersen et al. "Intracellular delivery of bioactive molecules using light-addressable nanocapsules". In: *ACS nano* 4.12 (Dec. 2010), pp. 7603–7611. ISSN: 1936-0851. DOI: 10.1021/nn102345f.

[109] M. Tichem and H. Goosen. *Lecture notes in Manufacturing for the micro and nano scale*. Published by Technical University of Delft. June 2023.

[110] M. Babincová et al. "Laser triggered drug release from magnetoliposomes". In: *Journal of Magnetism and Magnetic Materials* 194.1 (1999), pp. 163–166. ISSN: 0304-8853. DOI: 10.1016/S0304-8853(98)00553-8.

[111] S. Das et al. "Effect of laser irradiation on reversibility and drug release of light-activatable drug-encapsulated liposomes". In: *Langmuir* 36.13 (2020), pp. 3573–3582. DOI: 10.1021/acs.langmuir.0c00215.

[112] A. Sahu et al. "Nanographene oxide as a switch for CW/pulsed NIR laser triggered drug release from liposomes". In: *Materials Science and Engineering: C* 82 (2018), pp. 19–24. ISSN: 0928-4931. DOI: 10.1016/j.msec.2017.08.057.

[113] D. Luo et al. "Rapid Light-Triggered Drug Release in Liposomes Containing Small Amounts of Unsaturated and Porphyrin–Phospholipids". In: *Small* 12.22 (2016), pp. 3039–3047. DOI: 10.1002/smll.201503966.

[114] G. Wu et al. "Remotely triggered liposome release by near-infrared light absorption via hollow gold nanoshells". In: *Journal of the American Chemical Society* 130.26 (2008), pp. 8175–8177. DOI: 10.1021/ja802656d.

[115] S. Morales-Bonilla et al. "Influence of Asymmetric Agglomerations Effects over the Photothermal Release of Liposome-Encapsulated Nanodiamonds Assisted by Opto-Mechanical Changes". In: *Symmetry* 15.3 (2023). ISSN: 2073-8994. DOI: 10.3390/sym15030775.

[116] L. I. of America. "ANSI Z136.1-2000". In: *American National Standard for safe use of lasers* (2000).

[117] F. C. Delori, R. H. Webb, and D. H. Sliney. "Maximum permissible exposures for ocular safety (ANSI 2000), with emphasis on ophthalmic devices". In: *J. Opt. Soc. Am. A* 24.5 (May 2007), pp. 1250–1265. DOI: 10.1364/JOSAA.24.001250.

[118] V. Carvalho et al. "Computational Simulations in Advanced Microfluidic Devices: A Review". In: *Micromachines* 12.10 (2021). ISSN: 2072-666X. DOI: 10.3390/mi12101149.

[119] J. Crha et al. "Comparison of Two Solvers for Simulation of Single Bubble Rising Dynamics: COMSOL vs. Fluent". In: *Minerals* 11.5 (2021). ISSN: 2075-163X. DOI: 10.3390/min11050452.

[120] J. S.-R. Hysing and S. Turek. "Evaluation of commercial and academic CFD codes for a two-phase flow benchmark test case". In: *International Journal of Computational Science and Engineering* 10.4 (2015), pp. 387–394. DOI: 10.1504/IJCSE.2015.070993.

[121] D. Lopes et al. "Analysis of finite element and finite volume methods for fluid-structure interaction simulation of blood flow in a real stenosed artery". In: *International Journal of Mechanical Sciences* 207 (2021), p. 106650. ISSN: 0020-7403. DOI: 10.1016/j.ijmecsci.2021.106650.

[122] R. van Ostayen. *Lecture notes in Multiphysics Modelling using COMSOL*. Published by Technical University of Delft. Apr. 2023.

[123] A.-G. Niculescu et al. "Fabrication and Applications of Microfluidic Devices: A Review". In: *International Journal of Molecular Sciences* 22.4 (2021). ISSN: 1422-0067. DOI: 10.3390/ijms22042011.

[124] K. S. Elvira et al. "Materials and methods for droplet microfluidic device fabrication". In: *Lab Chip* 22 (5 2022), pp. 859–875. DOI: 10.1039/D1LC00836F.

[125] A. Waldbaur et al. "Let there be chip—towards rapid prototyping of microfluidic devices: one-step manufacturing processes". In: *Anal. Methods* 3 (12 2011), pp. 2681–2716. DOI: 10.1039/C1AY05253E.

[126] K. Ren, J. Zhou, and H. Wu. "Materials for microfluidic chip fabrication". In: *Accounts of chemical research* 46.11 (Nov. 2013), pp. 2396–2406. ISSN: 0001-4842. DOI: 10.1021/ar300314s.

[127] J. McDonald et al. "Fabrication of microfluidic systems in poly(dimethylsiloxane)". In: *Electrophoresis* 21.1 (Jan. 2000), pp. 27–40. ISSN: 0173-0835. DOI: 10.1002/(sici)1522-2683(20000101)21:1<27::aid-elps27>3.0.co;2-c.

[128] J. B. Nielsen et al. "Microfluidics: Innovations in Materials and Their Fabrication and Functionalization". In: *Analytical chemistry* 92.1 (Jan. 2020), pp. 150–168. ISSN: 0003-2700. DOI: 10.1021/acs.analchem.9b04986.

[129] R. MUKHOPADHYAY. "When PDMS isn't the best". In: *Analytical chemistry (Washington, DC)* 79.9 (2007), pp. 3248–3253. DOI: 10.1021/ac071903e.

[130] D. Sticker et al. "Multi-layered, membrane-integrated microfluidics based on replica molding of a thiol–ene epoxy thermoset for organ-on-a-chip applications". In: *Lab on a Chip* 15.24 (2015), pp. 4542–4554. DOI: 10.1039/C5LC01028D.

[131] S. B. Campbell et al. "Beyond Polydimethylsiloxane: Alternative Materials for Fabrication of Organ-on-a-Chip Devices and Microphysiological Systems". In: *ACS biomaterials science & engineering* 7.7 (July 2021), pp. 2880–2899. ISSN: 2373-9878. DOI: 10.1021/acsbiomaterials.0c00640.

[132] S. M. Scott and Z. Ali. "Fabrication Methods for Microfluidic Devices: An Overview". In: *Micromachines* 12.3 (2021). ISSN: 2072-666X. DOI: 10.3390/mi12030319.

[133] B. Bruijns et al. "Cyclic Olefin Copolymer Microfluidic Devices for Forensic Applications". In: *Biosensors* 9.3 (2019). ISSN: 2079-6374. DOI: 10.3390/bios9030085.

[134] K. Ren, Y. Chen, and H. Wu. "New materials for microfluidics in biology". In: *Current Opinion in Biotechnology* 25 (2014). Analytical biotechnology, pp. 78–85. ISSN: 0958-1669. DOI: 10.1016/j.copbio.2013.09.004.

[135] M. A. Mofazzal Jahromi et al. "Microfluidic Brain-on-a-Chip: Perspectives for Mimicking Neural System Disorders". In: *Molecular neurobiology* 56.12 (Dec. 2019), pp. 8489–8512. ISSN: 0893-7648. DOI: 10.1007/s12035-019-01653-2.

[136] G. Y. Huang et al. "Microfluidic hydrogels for tissue engineering". In: *Biofabrication* 3.1 (Mar. 2011), p. 012001. DOI: 10.1088/1758-5082/3/1/012001.

[137] A. W. Martinez et al. "Patterned paper as a platform for inexpensive, low-volume, portable bioassays". In: *Angewandte Chemie (International ed. in English)* 46.8 (2007), pp. 1318–1320. ISSN: 1433-7851. DOI: 10.1002/anie.200603817.

[138] A. W. Martinez, S. T. Phillips, and G. M. Whitesides. "Three-dimensional microfluidic devices fabricated in layered paper and tape". In: *Proceedings of the National Academy of Sciences* 105.50 (2008), pp. 19606–19611. DOI: 10.1073/pnas.0810903105.

[139] B. K. Gale et al. "A Review of Current Methods in Microfluidic Device Fabrication and Future Commercialization Prospects". In: *Inventions* 3.3 (2018). ISSN: 2411-5134. DOI: 10.3390/inventions3030060.

[140] C. Iliescu et al. "A practical guide for the fabrication of microfluidic devices using glass and silicon". In: *Biomicrofluidics* 6.1 (Mar. 2012), p. 016505. ISSN: 1932-1058. DOI: 10.1063/1.3689939.

[141] J. Hwang et al. “Microchannel fabrication on glass materials for microfluidic devices”. In: *International Journal of Precision Engineering and Manufacturing* 20 (2019), pp. 479–495. DOI: 10.1007/s12541-019-00103-2.

[142] R. Melentiev and F. Fang. “Recent advances and challenges of abrasive jet machining”. In: *CIRP Journal of Manufacturing Science and Technology* 22 (2018), pp. 1–20. ISSN: 1755-5817. DOI: 10.1016/j.cirpj.2018.06.001.

[143] M. Islam, R. Natu, and R. Martinez-Duarte. “A study on the limits and advantages of using a desktop cutter plotter to fabricate microfluidic networks”. English. In: *Microfluidics and Nanofluidics* 19.4 (2015), pp. 973–985. DOI: 10.1007/s10404-015-1626-9.

[144] Y. Xia and G. M. Whitesides. “Soft lithography”. In: *Annual review of materials science* 28.1 (1998), pp. 153–184. DOI: 10.1146/annurev.matsci.28.1.153.

[145] S. Waheed et al. “3D printed microfluidic devices: enablers and barriers”. In: *Lab on a Chip* 16.11 (2016), pp. 1993–2013. DOI: 10.1039/C6LC00284F.

[146] D. Fan, U. Staufer, and A. Accardo. “Engineered 3D Polymer and Hydrogel Microenvironments for Cell Culture Applications”. In: *Bioengineering* 6.4 (2019). ISSN: 2306-5354. DOI: 10.3390/bioengineering6040113.

[147] R. Ghodssi and P. Lin. *MEMS materials and processes handbook*. Vol. 1. Springer Science & Business Media, 2011. ISBN: 978-0-387-47316-1.

[148] G. Özkayar et al. “Toward a modular, integrated, miniaturized, and portable microfluidic flow control architecture for organs-on-chips applications”. In: *Biomicrofluidics* 16.2 (Apr. 2022), p. 021302. ISSN: 1932-1058. DOI: 10.1063/5.0074156.

[149] ELVEFLOW. *Flow control in microfluidics device*. https://www.elveflow.com/microfluidic-reviews/microfluidic-flow-control/flow-control-in-microfluidics-device/. Accessed: 25-09-2023).

[150] R. Sebastian et al. “A Comparison of Flow- and Pressure-Controlled Infusion Strategies for Microneedle-based Transdermal Drug Delivery”. In: (2022), pp. 2573–2576. DOI: 10.1109/EMBC48229.2022.9871582.

[151] J. Ducrée. “Centrifugal Microfluidics”. In: *Encyclopedia of Microfluidics and Nanofluidics*. Ed. by D. Li. Boston, MA: Springer US, 2008, pp. 234–245. ISBN: 978-0-387-48998-8. DOI: 10.1007/978-0-387-48998-8_203.

[152] D. J. Laser and J. G. Santiago. “A review of micropumps”. In: *Journal of Micromechanics and Microengineering* 14.6 (Apr. 2004), R35. DOI: 10.1088/0960-1317/14/6/R01.

[153] S. Mohith, P. N. Karanth, and S. Kulkarni. “Recent trends in mechanical micropumps and their applications: A review”. In: *Mechatronics* 60 (2019), pp. 34–55. ISSN: 0957-4158. DOI: 10.1016/j.mechatronics.2019.04.009.

[154] F. Amirouche, Y. Zhou, and T. Johnson. “Current micropump technologies and their biomedical applications”. In: *Microsystem technologies* 15 (2009), pp. 647–666. DOI: 10.1007/s00542-009-0804-7.

[155] Y.-N. Wang and L.-M. Fu. “Micropumps and biomedical applications – A review”. In: *Microelectronic Engineering* 195 (2018), pp. 121–138. ISSN: 0167-9317. DOI: 10.1016/j.mee.2018.04.008.

[156] W. Spencer et al. “An Electronically Controlled Piezoelectric Insulin Pump and Valves”. In: *IEEE Transactions on Sonics and Ultrasonics* 25.3 (1978). Cited by: 123, pp. 153–156. DOI: 10.1109/T-SU.1978.31006.

[157] S. Y. Jeong et al. “Peristaltic Micropump with Multi-Electrodes Using Electrostatic Force”. In: *Materials, Industrial, and Manufacturing Engineering Research Advances 2*. Vol. 1125. Advanced Materials Research. Trans Tech Publications Ltd, Nov. 2015, pp. 571–576. DOI: 10.4028/www.scientific.net/AMR.1125.571.

[158] C.-Y. Lee, H.-T. Chang, and C.-Y. Wen. “A MEMS-based valveless impedance pump utilizing electromagnetic actuation”. In: *Journal of Micromechanics and Microengineering* 18.3 (Feb. 2008), p. 035044. DOI: 10.1088/0960-1317/18/3/035044.

[159] L.-J. Yang and T.-Y. Lin. "A PDMS-based thermo-pneumatic micropump with Parylene inner walls". In: *Microelectronic Engineering* 88.8 (2011). Proceedings of the 36th International Conference on Micro- and Nano-Engineering (MNE), pp. 1894–1897. ISSN: 0167-9317. DOI: 10.1016/j.mee.2011.02.067.

[160] A. Saren, A. Smith, and K. Ullakko. "Integratable magnetic shape memory micropump for high-pressure, precision microfluidic applications". In: *Microfluidics and Nanofluidics* 22 (2018), pp. 1–10. DOI: 10.1007/s10404-018-2058-0.

[161] B. Li et al. "Design and fabrication of a microfluidic chip driven by dielectric elastomers". In: 7493 (2009). Ed. by J. Leng, A. K. Asundi, and W. Ecke, 74935S. DOI: 10.1117/12.838431.

[162] Y. Peng et al. "A Review on Electrohydrodynamic (EHD) Pump". In: *Micromachines* 14.2 (2023). ISSN: 2072-666X. DOI: 10.3390/mi14020321.

[163] A. V. Lemoff and A. P. Lee. "An AC magnetohydrodynamic micropump". In: *Sensors and Actuators B: Chemical* 63.3 (2000), pp. 178–185. ISSN: 0925-4005. DOI: 10.1016/S0925-4005(00)00355-5.

[164] D. Harrison, A. Manz, and P. Glavina. "Electroosmotic pumping within a chemical sensor system integrated on silicon". In: (1991), pp. 792–795. DOI: 10.1109/SENSOR.1991.149002.

[165] C. Zhou et al. "Chemistry pumps: A review of chemically powered micropumps". In: *Lab on a Chip* 16.10 (2016). Cited by: 91, pp. 1797–1811. DOI: 10.1039/c6lc00032k.

[166] S. Wang, X. Huang, and C. Yang. "Valveless micropump with acoustically featured pumping chamber". In: *Microfluidics and Nanofluidics* 8 (2010), pp. 549–555. DOI: 10.1007/s10404-009-0533-3.

[167] J.-Y. Qian et al. "Actuation Mechanism of Microvalves: A Review". In: *Micromachines* 11.2 (2020). ISSN: 2072-666X. DOI: 10.3390/mi11020172.

[168] K. W. Oh and C. H. Ahn. "A review of microvalves". In: *Journal of Micromechanics and Microengineering* 16.5 (Mar. 2006), R13. DOI: 10.1088/0960-1317/16/5/R01.

[169] M. Nafea, A. Nawabjan, and M. S. Mohamed Ali. "A wirelessly-controlled piezoelectric microvalve for regulated drug delivery". In: *Sensors and Actuators A: Physical* 279 (2018), pp. 191–203. ISSN: 0924-4247. DOI: 10.1016/j.sna.2018.06.020.

[170] D. Anjewierden, G. A. Liddiard, and B. K. Gale. "An electrostatic microvalve for pneumatic control of microfluidic systems". In: *Journal of Micromechanics and Microengineering* 22.2 (Jan. 2012), p. 025019. DOI: 10.1088/0960-1317/22/2/025019.

[171] A. Gunda et al. "Proportional Microvalve Using a Unimorph Piezoelectric Microactuator". In: *Micromachines* 11.2 (2020). ISSN: 2072-666X. DOI: 10.3390/mi11020130.

[172] B. Yang, B. Wang, and W. K. Schomburg. "A thermopneumatically actuated bistable microvalve". In: *Journal of Micromechanics and Microengineering* 20.9 (Aug. 2010), p. 095024. DOI: 10.1088/0960-1317/20/9/095024.

[173] D. Irimia and M. Toner. "Cell handling using microstructured membranes". In: *Lab Chip* 6 (3 2006), pp. 345–352. DOI: 10.1039/B515983K.

[174] M. Cugno, T. Stack, and J. Stolarczyk. "Light Actuated Microvalve". PhD thesis. WORCESTER POLYTECHNIC INSTITUTE, 2022. URL: https://digital.wpi.edu/downloads/9306t2767.

[175] G. Chen, F. Svec, and D. R. Knapp. "Light-actuated high pressure-resisting microvalve for on-chip flow control based on thermo-responsive nanostructured polymer". In: *Lab Chip* 8 (7 2008), pp. 1198–1204. DOI: 10.1039/B803293A.

[176] C. Das and F. Payne. "Design and characterization of low power, low dead volume electrochemically-driven microvalve". In: *Sensors and Actuators A: Physical* 241 (2016), pp. 104–112. ISSN: 0924-4247. DOI: 10.1016/j.sna.2016.01.038.

[177] D. J. Beebe et al. "Functional hydrogel structures for autonomous flow control inside microfluidic channels". In: *Nature* 404.6778 (2000), pp. 588–590. DOI: 10.1038/35007047.

[178] R. Sun, D. Li, and L. Jin. "Experimental and theoretical investigation on magnetic fluid seal in capillary tube". In: *Journal of Magnetism and Magnetic Materials* 546 (2022), p. 168869. ISSN: 0304-8853. DOI: 10.1016/j.jmmm.2021.168869.

[179] T. H. T. Hasegawa et al. “10-way micro switching valve chip with rotary mechanism for multi-directional flow control”. In: *The Seventh International Symposium on Micro Total Analysis System*. 2003, pp. 215–218. URL: https://shibaura.elsevierpure.com/en/publications/10-way-micro-switching-valve-chip-with-rotary-mechanism-for-multi.

[180] R. Walczak, K. Adamski, and D. Lizanets. “Inkjet 3D printed check microvalve”. In: *Journal of Micromechanics and Microengineering* 27.4 (Mar. 2017), p. 047002. DOI: 10.1088/1361-6439/aa6152.

[181] C. R. Daniel and T. R. Sepp. “Design and testing of a microvalve capable of precisely controlling low fluidic flow rates”. PhD thesis. Massachusetts Institute of Technology, 2011. URL: http://hdl.handle.net/1721.1/70428.

[182] K. Kistrup et al. “Fabrication and modelling of injection moulded all-polymer capillary microvalves for passive microfluidic control”. In: *Journal of Micromechanics and Microengineering* 24.12 (Nov. 2014), p. 125007. DOI: 10.1088/0960-1317/24/12/125007.

[183] Y.-J. Chang, Y.-T. Lin, and C.-C. Liao. “Chamfer-Type Capillary Stop Valve and Its Microfluidic Application to Blood Typing Tests”. In: *SLAS TECHNOLOGY: Translating Life Sciences Innovation* 24.2 (2019), pp. 188–195. DOI: 10.1177/2472630318808196.

[184] T. Ishida et al. “First-come-first-store microfluidic device of droplets using hydrophobic passive microvalves”. In: *Sensors and Actuators B: Chemical* 254 (2018), pp. 1005–1010. ISSN: 0925-4005. DOI: 10.1016/j.snb.2017.07.154.

[185] T. Ju. “Working Principle and Applications of Active and Passive Microfluidic Valves”. In: *Journal of Physics: Conference Series* 2230.1 (Mar. 2022), p. 012013. DOI: 10.1088/1742-6596/2230/1/012013.

[186] S. Sugiura et al. “Photoresponsive polymer gel microvalves controlled by local light irradiation”. In: *Sensors and Actuators A: Physical* 140.2 (2007), pp. 176–184. ISSN: 0924-4247. DOI: 10.1016/j.sna.2007.06.024.

[187] A. D. Jadhav et al. “Photoresponsive microvalve for remote actuation and flow control in microfluidic devices”. In: *Biomicrofluidics* 9.3 (June 2015), p. 034114. ISSN: 1932-1058. DOI: 10.1063/1.4923257.

[188] I. Tomatsu, K. Peng, and A. Kros. “Photoresponsive hydrogels for biomedical applications”. In: *Advanced Drug Delivery Reviews* 63.14 (2011). Hybrid nanostructures for diagnostics and therapeutics, pp. 1257–1266. ISSN: 0169-409X. DOI: 10.1016/j.addr.2011.06.009.

[189] H. Fallahi et al. “Flexible microfluidics: Fundamentals, recent developments, and applications”. In: *Micromachines* 10.12 (2019), p. 830. DOI: 10.3390/mi10120830.

[190] S. O. Hong et al. “Gear-shaped micromixer for synthesis of silica particles utilizing inertio-elastic flow instability”. In: *Lab on a Chip* 21.3 (2021), pp. 513–520. DOI: 10.1039/D0LC00834F.

[191] A. Ehsani and A. Nejat. “Conceptual design and performance analysis of a novel flexible-valve micropump using magneto-fluid–solid interaction”. In: *Smart Materials and Structures* 26.5 (2017), p. 055036. DOI: 10.1088/1361-665X/aa67c5.

[192] N. Kashaninejad and N.-T. Nguyen. “Microfluidic solutions for biofluids handling in on-skin wearable systems”. In: *Lab on a Chip* 23.5 (2023), pp. 913–937. DOI: 10.1039/d2lc00993e.

[193] A. Raj, P. P. Suthanthiraraj, and A. Sen. “Pressure-driven flow through PDMS-based flexible microchannels and their applications in microfluidics”. In: *Microfluidics and Nanofluidics* 22 (2018), pp. 1–25. DOI: 10.1007/s10404-018-2150-5.

[194] T. Gervais et al. “Flow-induced deformation of shallow microfluidic channels”. In: *Lab on a Chip* 6.4 (2006), pp. 500–507. DOI: 10.1039/B513524A.

[195] X. Wang and I. C. Christov. “Reduced modelling and global instability of finite-Reynolds-number flow in compliant rectangular channels”. In: *Journal of Fluid Mechanics* 950 (2022), A26. DOI: 10.1017/jfm.2022.802.

[196] M. K. Raj, S. DasGupta, and S. Chakraborty. “Hydrodynamics in deformable microchannels”. In: *Microfluidics and Nanofluidics* 21 (2017), pp. 1–12. DOI: 10.1007/s10404-017-1908-5.

[197] M. Verma and V. Kumaran. “Stability of the flow in a soft tube deformed due to an applied pressure gradient”. In: *Physical Review E* 91.4 (2015), p. 043001. DOI: 10.1103/physreve.91.043001.

[198] X. Wang and I. C. Christov. "Theory of the flow-induced deformation of shallow compliant microchannels with thick walls". In: *Proceedings of the Royal Society A* 475.2231 (2019), p. 20190513. DOI: 10.1098/rspa.2019.0513.

[199] Y. Zhou et al. "A microfluidic platform for trapping, releasing and super-resolution imaging of single cells". In: *Sensors and Actuators B: Chemical* 232 (2016), pp. 680–691. ISSN: 0925-4005. DOI: 10.1016/j.snb.2016.03.131.

References - Appendices

[1] M. S. Klamkin. "Elementary Approximations to the Area of N-Dimensional Ellipsoids". In: *The American Mathematical Monthly* 78.3 (1971), pp. 280–283. DOI: 10.1080/00029890.1971.11992746.

[2] M. G. Simon et al. "A Laplace pressure based microfluidic trap for passive droplet trapping and controlled release". In: *Biomicrofluidics* 6.1 (Feb. 2012), p. 014110. ISSN: 1932-1058. DOI: 10.1063/1.3687400.

[3] A. Waldbaur et al. "Let there be chip—towards rapid prototyping of microfluidic devices: one-step manufacturing processes". In: *Anal. Methods* 3 (12 2011), pp. 2681–2716. DOI: 10.1039/C1AY05253E.

[4] M. Tichem and H. Goosen. *Lecture notes in Manufacturing for the micro and nano scale*. Published by Technical University of Delft. June 2023.

[5] A.-G. Niculescu et al. "Fabrication and Applications of Microfluidic Devices: A Review". In: *International Journal of Molecular Sciences* 22.4 (2021). ISSN: 1422-0067. DOI: 10.3390/ijms22042011.

[6] S. M. Scott and Z. Ali. "Fabrication Methods for Microfluidic Devices: An Overview". In: *Micromachines* 12.3 (2021). ISSN: 2072-666X. DOI: 10.3390/mi12030319.

[7] B. K. Gale et al. "A Review of Current Methods in Microfluidic Device Fabrication and Future Commercialization Prospects". In: *Inventions* 3.3 (2018). ISSN: 2411-5134. DOI: 10.3390/inventions3030060.

[8] Nanoscribe GmbH & Co. KG. *Nanoguide - Objective Overview*. https://support.nanoscribe.com/hc/en-gb/articles/360002996413-Objective-Overview. (Accessed: 02-04-2024).

[9] S. Bhattacharya et al. "Studies on surface wettability of poly(dimethyl) siloxane (PDMS) and glass under oxygen-plasma treatment and correlation with bond strength". In: *Journal of Microelectromechanical Systems* 14.3 (2005), pp. 590–597. DOI: 10.1109/JMEMS.2005.844746.

[10] X. Jiang et al. "Polymer-on-polymer stamping: universal approaches to chemically patterned surfaces". In: *Langmuir* 18.7 (2002), pp. 2607–2615. DOI: 10.1021/la011098d.

[11] P. C. Liangcai Xiong and Q. Zhou. "Adhesion promotion between PDMS and glass by oxygen plasma pre-treatment". In: *Journal of Adhesion Science and Technology* 28.11 (2014), pp. 1046–1054. DOI: 10.1080/01694243.2014.883774.

[12] A. Borók, K. Laboda, and A. Bonyár. "PDMS Bonding Technologies for Microfluidic Applications: A Review". In: *Biosensors* 11.8 (2021). ISSN: 2079-6374. DOI: 10.3390/bios11080292.

[13] S. H. Kim et al. "Simple fabrication of hydrophilic nanochannels using the chemical bonding between activated ultrathin PDMS layer and cover glass by oxygen plasma". In: *Lab Chip* 11 (2 2011), pp. 348–353. DOI: 10.1039/C0LC00015A.

[14] F. C. A. Heuck and U. Staufer. "Low voltage electroosmotic pump for high density integration into microfabricated fluidic systems". English. In: *Microfluidics and Nanofluidics* 10.6 (2011), pp. 1317–1332. DOI: 10.1007/s10404-010-0765-2.

[15] J. Hoogvliet and W. van Bennekom. "Gold thin-film electrodes: an EQCM study of the influence of chromium and titanium adhesion layers on the response". In: *Electrochimica Acta* 47.4 (2001), pp. 599–611. ISSN: 0013-4686. DOI: 10.1016/S0013-4686(01)00793-9.

[16] L.-S. Jang and H.-J. Liu. "Fabrication of protein chips based on 3-aminopropyltriethoxysilane as a monolayer". In: *Biomedical microdevices* 11 (2009), pp. 331–338. DOI: 10.1007/s10544-008-9239-7.

[17] A. Parisi et al. "Integrated Optic Surface Plasmon Resonance Measurements in a Borosilicate Glass Substrate". In: *Sensors* 8.11 (2008), pp. 7113–7124. ISSN: 1424-8220. DOI: 10.3390/s8117113.

[18] C. L. Gonzalez-Gallardo, A. Díaz Díaz, and J. R. Casanova-Moreno. "Improving plasma bonding of PDMS to gold-patterned glass for electrochemical microfluidic applications". In: *Microfluidics and Nanofluidics* 25.2 (2021), p. 20. DOI: 10.1007/s10404-021-02420-3.

[19] J. Casanova-Moreno et al. “Fabricating devices with improved adhesion between PDMS and gold-patterned glass”. In: *Sensors and Actuators B: Chemical* 246 (2017), pp. 904–909. ISSN: 0925-4005. DOI: https://doi.org/10.1016/j.snb.2017.02.109. URL: https://www.sciencedirect.com/science/article/pii/S0925400517303362.

[20] C. Schneider, W. Rasband, and K. Eliceiri. “NIH Image to ImageJ: 25 years of image analysis.” In: *Nature Methods* 9 (2012), pp. 671–675. DOI: 10.1038/nmeth.2089.